



저작자표시-비영리-변경금지 2.0 대한민국

이용자는 아래의 조건을 따르는 경우에 한하여 자유롭게

- 이 저작물을 복제, 배포, 전송, 전시, 공연 및 방송할 수 있습니다.

다음과 같은 조건을 따라야 합니다:



저작자표시. 귀하는 원저작자를 표시하여야 합니다.



비영리. 귀하는 이 저작물을 영리 목적으로 이용할 수 없습니다.



변경금지. 귀하는 이 저작물을 개작, 변형 또는 가공할 수 없습니다.

- 귀하는, 이 저작물의 재이용이나 배포의 경우, 이 저작물에 적용된 이용허락조건을 명확하게 나타내어야 합니다.
- 저작권자로부터 별도의 허가를 받으면 이러한 조건들은 적용되지 않습니다.

저작권법에 따른 이용자의 권리는 위의 내용에 의하여 영향을 받지 않습니다.

이것은 [이용허락규약\(Legal Code\)](#)을 이해하기 쉽게 요약한 것입니다.

[Disclaimer](#)

이학박사학위논문

Prediction and control of epidemics and avalanche dynamics in complex networks

복잡계 네트워크에서 확산 현상의 예측 및 제어

2023년 8월

서울대학교 대학원

물리·천문학부

전 부 경

이학박사학위논문

Prediction and control of epidemics and avalanche dynamics in complex networks

복잡계 네트워크에서 확산 현상의 예측 및 제어

2023년 8월

서울대학교 대학원

물리·천문학부

전 부 경

Prediction and control of epidemics and avalanche dynamics in complex networks

복잡계 네트워크에서 확산 현상의 예측 및 제어

지도교수 백 용 주

이 논문을 이학박사 학위논문으로 제출함

2023년 8월

서울대학교 대학원

물리·천문학부

전 부 경

전부경의 박사 학위논문을 인준함

2023년 6월

위 원 장: _____ (인)
부위원장: _____ (인)
위 원: _____ (인)
위 원: _____ (인)
위 원: _____ (인)

Abstract

Prediction and control of epidemics and avalanche dynamics in complex networks

Bukyoung Jhun

Department of Physics and Astronomy

The Graduate School

Seoul National University

In past decades, extensive research has been done on emerging phenomena in complex systems. An important issue for such emerging phenomena is their prediction and control. Complex networks represented by graphs enable researchers to study such issues successfully. In complex systems, however, interactions among constituents can be more complex than pairwise. For instance, more than two people can collaborate on a team. Contagion through an edge in a network is called simple contagion. There are contagion processes that cannot be reduced to simple contagions. Examples are hypergraph epidemic processes, quantum spreading processes, and cascading failures in infrastructure networks.

In this dissertation, we study the prediction and control of these complex contagion processes. We study the phase transition and control strategy of the simplicial SIS model, which is an epidemic model in hypergraphs. We then study the transition of vaccination strategy in a population with heterogeneous fatality rates. Moreover, we study the phase transition of quantum spreading processes in homogeneous and heterogeneous networks. Lastly, we employ machine learning for the prediction and control of epidemic spreading and cascading failures in infrastructure networks.

Keywords: Epidemic process, Complex contagion, Hypergraph, Nonequilibrium phase transition, Vaccination strategy, Cascading failure, Graph neural network, Open quantum system, Hybrid phase transition

Student number: 2020-34297

Contents

Abstract	i
Contents	ii
List of Figures	v
List of Tables	xxiii
1 Introduction	1
1.1 Complex Network	1
1.2 Complex contagion	2
1.3 Overview of dissertation	3
2 Higher-order epidemics	5
2.1 Phase transition and critical phenomena of the simplicial susceptible- infected-susceptible (s -SIS) model	5
2.2 Static model of uniform hypergraph	7
2.3 Simplicial SIS model	9
2.4 Heterogeneous mean-field theory (annealed approximation)	11
2.4.1 Self-consistency equation	11
2.5 Phase transition and critical behavior	14
2.5.1 Order parameter	14
2.5.2 Susceptibility	18
2.5.3 Correlation size	19
2.6 Numerical simulations	22
2.6.1 Numerical methods	22
2.6.2 Numerical results	24

2.7	Degree distribution of static model	30
2.8	Asymptotic behavior of $G'(\Theta)$	30
2.9	Susceptibility	31
2.10	Containment strategy for simplicial SIS model	32
2.10.1	Hypergraph popularity-similarity optimization (h -PSO) model	35
2.10.2	Individual- and pair-based mean-field theories	37
2.10.3	Immunization strategies	41
2.10.4	Numerical Results	45
2.11	Summary and conclusion	50
3	Phase transition in vaccination strategy	53
3.1	Introduction	53
3.2	Susceptible-infected-recovered-dead (SIRD) model	55
3.3	Results	56
3.3.1	Fatality- and contact-based strategies	56
3.3.2	Transition and path-dependency of the optimal vaccination strategy	59
3.3.3	Real-world epidemic diseases	63
3.3.4	Complex epidemic stages, vaccine breakthrough infection, and reinfection	66
3.4	Conclusion	68
4	Application of graph neural network (GNN) on spreading processes . .	70
4.1	Introduction	70
4.2	Prediction and mitigation of avalanche dynamics in power grids using graph neural network	70
4.2.1	Avalanche dynamics	72
4.2.2	Avalanche mitigation strategy	75
4.2.3	Graph neural network (GNN)	78

4.2.4	Conclusion	84
4.3	Epidemic control using graph neural network ansatz	86
4.3.1	Model	88
4.3.2	Vaccination strategy	91
4.3.3	Results	97
4.3.4	Conclusion	103
5	Quantum spreading processes in complex networks	105
5.1	Introduction	105
5.2	Permutational symmetry	109
5.3	Quantum contact process	111
5.4	Dissipative Transverse Ising model	114
5.4.1	Transverse Ising model	114
5.4.2	Dissipative transverse Ising model	117
5.5	Comparison with quantum jump Monte Carlo simulation	127
5.6	Quantum contact process in scale-free networks	129
5.6.1	Annealed approximation and self-consistency equation	129
5.6.2	Phase transition and critical behavior	132
5.6.3	Numerical results	138
5.7	Summary and Discussion	141
6	Conclusion	145
	Bibliography	146
	Abstract in Korean	188

List of Figures

2.1	Degree distribution of the static model of (a) 2-uniform (graph) and (b) 3-uniform hypergraph generated with the fitness exponent $1/\mu = 1.3$. The system size N is given as $N = 10^5, 10^6$, and 10^7 . As the system size is increased, the tail part of the degree distribution is extended, and power-law behavior with exponent $\lambda = 1 + 1/\mu = 2.3$ is confirmed.	8
2.2	Schematic illustration of the simplicial contagion process through hyperedges of size 3 in (a) and (b), and 4 in (c) and (d). The susceptible and infected nodes are depicted as white open circles and red filled circles, respectively. When $d - 1$ of d nodes in a hyperedge are infected, the infection spreads to the remaining susceptible node through the hyperedge at a rate β_d .	10
2.3	Self-consistency function $G(\Theta)$ of SF 3-uniform hypergraphs with degree exponent (a) $\lambda = 2.2$, (b) 2.5, and (c) 2.8, corresponding to cases i) $\lambda < \lambda_c$, ii) $\lambda = \lambda_c$, and iii) $\lambda > \lambda_c$ in the main text. The derivative of the function with respect to Θ at $\Theta = 0$ (a) diverges, (b) is positive, and (c) is negative as Θ approaches zero.	15
2.4	Density of infected nodes versus control parameter λ for various degree exponent values λ for (a) $d = 3$ and (c) $d = 4$. Susceptibility versus control parameter λ for various λ values for (b) $d = 3$ and (d) $d = 4$. For $\lambda = 2.2$ and $\lambda = 2.4$, the transition point is $\lambda_c = 0$, and for $\lambda = 2.5, 2.6$, and 2.8 , λ_c is finite. For $\lambda = 2.2, 2.4$, and 2.8 , the transition is second-order, and for $\lambda = 2.6$ and 2.8 , the transition is hybrid. For $\lambda \leq \lambda_c$, the susceptibility converges to a finite value $1 + d(d - 2)$. For $\lambda > \lambda_c$, the susceptibility diverges as $\lambda \rightarrow \lambda_c^+$.	16

2.5	(a) Self-consistency function $G_N(\Theta)$ in finite systems versus Θ for 3-uniform hypergraphs with $\lambda = 2.8$. (b) Deviation $\lambda_c(N) - \lambda_c(\infty)$ versus system size N for various degree exponents λ . Red dotted lines denote $\lambda < \lambda_c = 2.5$; black solid lines denote $\lambda = \lambda_c$; and blue dashed lines do $\lambda > \lambda_c$	22
2.6	Finite-size scaling analysis of the s -SIS model on SF 3-uniform hypergraphs with three degree exponents: $\lambda = 2.1 < \lambda_c$ (a) and (b), $\lambda = 2.9 > \lambda_c$ (c) and (d), and $\lambda = 3.5 > \lambda_c$ (e) and (f). Scaling plots of $(\rho - \rho_c)N^{\beta/\bar{\nu}}$ versus $(\kappa - \kappa_c)N^{1/\bar{\nu}}$ are drawn, with (a) $\beta = 1.25$ and $\bar{\nu} = 1.59$, (c) $\beta = 0.52$ and $\bar{\nu} = 2.11$, and (e) $\beta = 0.5$ and $\bar{\nu} = 1.63$. Scaling plots of $\chi_2 N^{-\gamma_2/\bar{\nu}}$ versus $(\kappa - \kappa_c)N^{1/\bar{\nu}}$ are drawn, with (b) $\gamma_2 = 0.15$ and $\bar{\nu} = 1.59$, (d) $\gamma_2 = 0.62$ and $\bar{\nu} = 2.11$, and (f) $\gamma_2 = 0.62$ and $\bar{\nu} = 1.63$	25
2.7	Scaling plots of $\chi_1 N^{-\gamma_1/\bar{\nu}}$ versus $(\kappa - \kappa_c)N^{1/\bar{\nu}}$ with degree exponents (a) $\lambda = 2.9$ and (b) $\lambda = 3.5$, with (a) $\gamma_1 = 0.48$ and $\bar{\nu} = 2.11$, (b) $\gamma_1 = 0.50$ and $\bar{\nu} = 1.63$	26
2.8	Plots of $\kappa_c(N) - \kappa_c(\infty)$ versus N on double-logarithmic scale for (a) $\lambda = 2.1$, (b) $\lambda = 2.9$, and (c) $\lambda = 3.5$. Slope of each plot represents $-1/\bar{\nu}$	26
2.9	Scaling plots of the density of infection $\rho(t)$ starting from the fully infected state versus $tN^{-\bar{z}}$ (a) and (c) and $t(\kappa - \kappa_c)^{\nu_{\parallel}}$ (b) and (d) for $\lambda = 2.9$ (a) and (b) and $\lambda = 3.5$ (c) and (d). The dynamical critical exponents $\delta = 0.89$, $\bar{z} = 0.26$, and $\nu_{\parallel} = 0.56$ are obtained from (a) and (b), and $\delta = 0.86$, $\bar{z} = 0.32$, and $\nu_{\parallel} = 0.53$ are obtained from (c) and (d).	28

- 2.10 (a) The degree distribution of the 3-uniform hypergraph popularity-similarity optimization (*h*-PSO) model. The mean degree $\langle k \rangle = 6$, temperature $T = 0.5$, and the parameter $\gamma = 3$. The tail of the distribution follows a power law with an exponent of 3. (b) The clustering coefficient of 3-uniform *h*-PSO as a function of the scale parameter R . The number of nodes $N = 2000$, mean degree $\langle k \rangle = 6$, and the temperature $T = 0.5$ 35
- 2.11 Random edge immunization (Random), H-eigenscore (H-ES), EI, and SIP-based strategies tested in various synthetic and empirical networks: (a, e, i) the static model, (b, f, j) clustered power-law network, (c, g, k) an airline network, and (d, h, l) the general relativity collaboration network. Because this is a network (i.e. hypergraph with only size-two hyperedges) the H-eigenscore is identical to the usual eigenscore. (a, b, c, d) The density of infection ρ versus the removed portion of the edges p . The recovery rate $\mu = 0.2$ and the contagion rate $\beta = 0.2$. Efficient immunization strategies usually result in a higher density of infection compared to random immunization for small p but eliminate epidemics with smaller p_c . (e, f, g, h) HIT p_c , which is the minimally required portion of edges to eliminate the epidemics. The efficient strategies (i.e. H-eigenscore, EI, and SIP-based strategies) exhibit marginal differences in their HITs. To compare the HITs of efficient strategies more thoroughly, we plot the differences between the p_{cs} of EI and SIP-based strategies from the p_c of the H-eigenscore-based strategy in (i, j, k, l). The SIP-based strategy is often more efficient than EI-based strategy, despite its lower computational cost. 44

2.12 Random hyperedge immunization (Random), H-eigenscore (H-ES), EI, and SIP-based strategies tested in 3-uniform hypergraphs: (a, c) the hypergraph static model and (b, d) the hypergraph popularity-similarity optimization (*h*-PSO) model. (a, b) The density of infection ρ versus the removed portion of the edges p . The recovery rate $\mu = 0.2$ and the contagion rate $\beta = \beta_3 = 0.2$. The efficient strategies generally exhibit a higher density of infection for small p , but herd immunity is achieved at lower p_c , which is the minimally required portion of hyperedges that needs to be immunized to eliminate epidemics. (c, d) HIT p_c as a function of contagion rate $\beta = \beta_3$. The H-ES and SIP-based strategies outperform the EI-based strategy, despite their lower computational cost. 46

2.13 Random hyperedge immunization (Random) and SIP-based strategy tested in empirical hypergraphs: (a, c, e) the congressional bill cosponsorship (in 2000) hypergraph and (b, d, f) the protein interaction hypergraph. For nonuniform empirical hypergraphs, H-ES cannot be implemented due to the variety of hyperedge sizes, and EI is computationally inefficient due to the large hyperedges. (a, b) The density of infection ρ versus the removed portion of the edges p . The recovery rate $\mu = 0.2$ and the contagion rate $\beta = \beta_d = 0.2$ for all hyperedge sizes d . The efficient strategies generally exhibit a higher density of infection for small p , but herd immunity is achieved at lower HIT p_c , which is the minimally required portion of hyperedges that need to be immunized to eliminate the epidemics. (c, d) HIT p_c as a function of the contagion rate $\beta = \beta_d$. Efficient epidemic containment is achieved by the SIP-based method with low computational cost. (e, f) The immunization rate of hyperedges with size d plotted for various contagion rates. Small hyperedges are primarily targeted by the immunization strategy especially when β is low. 47

3.1 (a–b) The mortality rate as a result of various vaccination strategies. The contagion rate is (a) $\eta = 0.05$ and (b) $\eta = 0.4$, while the recovery rate is normalized $\mu = 1$. When the fraction of the population affected by the epidemic (i.e., the fraction of R and D state at the end of the dynamic) is less than 10^{-4} , we assume that herd immunity is achieved, and the epidemic is eliminated by vaccination. The point at which herd immunity is achieved is depicted as a dot. When the contagion rate is low, the contact-based strategy is more effective regardless of the vaccination rate. When the contagion rate is high, the fatality-based strategy is more effective at a low vaccination rate; however, the contact-based strategy outperforms the fatality-based strategy when the vaccine supply is sufficiently high, achieving herd immunity at a lower vaccination rate. (c) The difference between the mortality rates resulting from fatality-based and contact-based strategies. The fatality-based strategy reduces more deaths compared to the contact-based strategy when the contagion rate is high and the vaccination rate is low. However, as the vaccination rate becomes higher, the contact-based strategy outperforms the fatality-based strategy. 57

3.2 (a, d) Fraction of recovered population, (b, e) average fatality of the vaccinated population, and (c, f) average contact rate of the vaccinated population of the synthetic metapopulation model with heterogeneous fatality and contact rates. The recovery rate is normalized to $\mu = 1$, and contagion rates are (a–c) $\eta = 0.05$ and (d–f) $\eta = 0.4$. The increasing (decreasing) curve, where the locally optimal vaccination strategies are found by iteratively increasing (decreasing) the vaccination rate, is depicted as solid red (dashed blue) lines. The globally optimal strategies are found by simulated annealing (SA). There is no abrupt transition nor separation of the curves for a low contagion rate, $\eta = 0.05$, and the optimal vaccination strategy prefers to vaccinate individuals with high contact rates regardless of the vaccination rate. For a large contagion rate, $\eta = 0.4$, there is an abrupt transition in the globally optimal strategy. The separation of the increasing and decreasing curve indicates the path-dependency of the vaccination strategy which is analogous to hysteresis. For a small (0–0.56) or large (0.67–1) vaccination rate, the increasing and decreasing curves coincide; however, near the transition point, the increasing curve tends to vaccinate individuals with high fatality rates (high-fatality strategy) and the decreasing curve vaccinates individuals with high contact rates (high-contact strategy). The High-fatality strategy results in a higher number of recovered population than the high-contact strategy because the high-fatality strategy aims to protect high-risk groups, while the high-contact strategy aims to contain the infection. 60

3.3	The mortality rate of a mixed strategy that combines the high-fatality and high-contact strategies. The contagion rate is $\eta = 0.4$, and vaccine supply is, from top to bottom, 58%, 60%, 62%, 64%, and 66%. There is a barrier of mortality rate between the high-fatality and high-contact strategies, which is the cause of the path-dependency and discontinuous transition of the vaccination strategy.	61
3.4	The age contact matrix of the (a) United Kingdom and (b) United States, and (c) contact rate of each age group. The population is divided into 17 groups: aged 0–4, 5–9, . . . , 75–79, and above 80. The interaction strength between groups of similar age is disproportionately higher, and the groups of ages 10–29 show the highest number of contacts. (d) The fatality rates of TB in the United Kingdom (UK) and COVID-19 in the United States (US). The fatality rate is highly heterogeneous and monotonically increases with age, with the sole exception of children below age five in TB. Therefore, the senior population is primarily vaccinated by the fatality-based strategy, and individuals of age 10–29 are primarily vaccinated by the contact-based strategy. . . .	64

- 3.5 Average age of vaccinated individuals for (a) TB, (b) COVID-19, and (c) COVID-19 with reinfection and finite vaccine efficacy. The contagion rates are $\eta = 0.25$, and the recovery rate is normalized to $\mu = 1$. The total amount of vaccine is increased (solid red line) and decreased (dashed blue line) while keeping the vaccination strategy at its local optimum. For a small vaccination rate, the increasing curve and decreasing curve coincide; however, for a sufficiently large vaccination rate, the two curves show a largely unequal average age of the vaccinated population. The increasing curve has a higher average age. The globally optimal strategy, which is calculated by the simulated annealing, undergoes an abrupt transition from the high-fatality to the high-contact strategies. The separation of the increasing and decreasing curve indicates the path-dependency of the vaccination strategy which is analogous to hysteresis. 65
- 3.6 The mortality rate of the mixed strategy of high-fatality and high-contact strategies for (a) TB and (b) COVID-19. The contagion rate is $\eta = 0.25$, and the vaccine supply is, from top to bottom, 52%, 54%, 56%, 58%, and 60%. There is a barrier of mortality rate between the high-fatality and high-contact strategy, which is the cause of the discontinuous transition and path-dependency of the optimal vaccination strategy. The mortality rate of the high-contact strategy drops faster than the high-fatality strategy as the level of vaccine supply increases, and herd immunity is achieved at a lower vaccine supply. 65

4.1	Computation time of ML model as a function of network size. The Schultz–Heitzig–Kurths (SHK) random power grid model was used. The computation time is proportional to $N^{3.3}$; thus, if the network size doubles, the computation time increases by approximately tenfold. More than a year of computation is required to simulate the process in a network of size $N = 25000$ using the CPU of model i7-10700.	72
4.2	Avalanche size distribution of SHK network with various numbers of nodes for the ML model. The control parameter a is taken as 0.25, at which the avalanche sizes have a scale-free distribution with exponent $\tau \approx 1.6$.	73
4.3	Paradoxical effect of reinforcement in electric power grid of France. Red square (indicated by A) represents the initial failure, red dots represent secondary failures, and blue triangle (indicated by B) represents a reinforced node. (a) and (b) If no node is reinforced, the avalanche ends at $t = 2$ with avalanche size $S = 5$. (c)–(f) If node B (\blacktriangle) is reinforced, the avalanche lasts until $t = 4$, and the avalanche size increases to 33. Because the reinforced node does not fail, heavy traffic through route via node B (blue arrow) is maintained, causing other nodes on the route to fail. Reinforcement thus may result in a significantly larger global cascade.	75
4.4	Performance of avalanche mitigation strategies in the SHK network of size $N = 1000$. Degree, eigenvector centrality (EC), betweenness centrality (BC), avalanche fraction (s), failure fraction (f), avalanche centrality (AC), and GNN estimation of avalanche centrality (AC-GNN) are employed for avalanche mitigation strategies. Nodes are reinforced in descending order of the corresponding centrality measure. The area under each curve is the performance measure R_m .	79

4.5	Structure of GNN. Only the adjacency matrix of the network is input, and the features of all nodes are initially constant. Batch normalization and ReLU activation are applied between each pair of adjacent GIN layers, but they are omitted from the diagram for simplicity. A short skip connection is applied between each pair of adjacent GIN layers, and an elementwise average is obtained before the regressor. The regressor is implemented as a single-layer perceptron followed by a sigmoid function for normalization.	81
4.6	The cumulative fraction $C_\sigma(n)$ of AC as a function of n on an SHK network of size $N = 1000$. The mean cumulative fraction $\langle C_\sigma \rangle$ is the area under the cumulative fraction $C_\sigma(n)$ curve. A large $\langle C_\sigma \rangle$ means that the ranking estimation performs well. Red solid curve is obtained by taking the estimated rank σ as the graph degree, i.e., the number of connections, of each node. The estimated curve lies between those of the descending order (best case) and ascending order (worst case). . .	83
4.7	Performance of the GNN prediction in large networks in the range $N = 1000 - 8000$, which is trained in various network sizes from 100 to 999. All the results are averaged over 4 different GNNs with different random seed. (a) R^2 scores for different system sizes: the R^2 score is not appropriate to predict the performance because the AC values are distributed very skewed. (b) and (c) $\langle C_{\sigma,N} \rangle$ and Kendall's tau for different sizes, respectively. (Blue, dark bars) the GNN predicts ranks of ACs using a quantile scaled dataset. (Orange, light bars) the GNN predicts values of ACs using a raw dataset. Rank prediction using the quantile scaling marked in blue is better and more consistent than value prediction marked in orange. The representation by $\langle C_{\sigma,N} \rangle$ in (b) is more appropriate compared with that by the Kendall's Tau in (c).	85

- 4.8 Density of infection of SIS model calculated by MMCA as the function of weight parameter $w_r^{(\ell)}$ of GNNA. The plot illustrates the loss surface projected on the $w_1^{(1)}$ - $w_2^{(2)}$ plane. The value is flat everywhere except on certain lines. The flat regions each correspond to an identical vaccination strategy; therefore, the objective function does not vary in the region. The vaccination is tested in the airline network with the contagion rate $\beta = 0.2$, recovery rate $\mu = 0.5$, and vaccination rate $q/N = 0.1$ 96
- 4.9 Performance of GNNA compared to centrality-based vaccination strategies. (a) Largest connected component size of network dismantling and the density of infection ρ of (b) MMCA SIS model, (c) SIS model, (d) SIS model with heterogeneous contagion and recovery rate, (e) edge immunization of SIS model, and (f) mortality rate D/N of SIRD model. A multiplex network constructed from the human contact pattern is used for the SIRD model and DBLP Coauthorship network for the others. The number of nodes in the network is N , the number of edges is L , the number of vaccinated nodes is q , and the number of immunized edges is q_L . The vaccination strategy obtained by GNNA outperforms all centrality measures at all vaccination levels. 98

4.10 Transition of the optimal vaccination strategy in the SIRD model. (a) Phi coefficient between the nodes vaccinated by GNNA and high-BC/IFR vaccination strategies. The point where herd immunity is achieved by GNNA-based strategy (but not necessarily by other methods) is depicted by the dashed black line. When the total vaccination rate q/N is low, the set of nodes vaccinated by GNNA has a large overlap with the high-IFR strategy. As the vaccination level approaches the state where herd immunity is possible, GNNA adjusts its strategy, wherein it becomes similar to the high-BC strategy. (b) Vaccination rate of four age groups when GNNA-based vaccination is applied. Yellow, green, and blue represent high, moderate, and low vaccination rates, respectively. When the total vaccination rate q/N is low, the senior age group whose IFRs are the highest is primarily vaccinated. However, when the vaccination rate becomes high and approaches herd immunity, which is depicted by the dashed white line, the individuals below age 50 who have high contact rates are primarily vaccinated. 102

- 5.1 (a) Phase diagram of the QCP model on a fully connected graph in the parameter space (κ, ω) , determined by direct numerical enumeration of the Liouville equation based on the PI states. Discontinuous (dashed curve) and continuous transitions (dotted and solid lines) occur, and they meet at a tricritical point (TP). On the dotted critical line in $\omega \in [\omega_*, 1]$, the critical exponent α varies continuously, whereas on the solid line, it has the DP value. The color means the average order parameter $\langle n \rangle$ defined in Eq. (5.10). (b) The distribution of the order parameters n for $(\kappa, \omega) = (0, 1.8)$. This shows that the system is bistable at $n = 0$ and ≈ 0.45 . (c) Plot of the order parameter n as a function of ω for $\kappa = 0.0$ in the steady state. This shows that the transition is first-order. (d) Plot of the order parameter n as a function of κ at $\omega = 0.0$ in the steady state. This shows that the transition is second-order. Data are obtained by direct enumerations from the system of size $N = 256$. We set $\Gamma = 1$ for all figures. In (c) and (d), the color means the probability that the order parameter n exists. 110
- 5.2 Plots of the order parameter $\langle n(t) \rangle$ of the QCP model as a function of time t for fixed $\kappa = 1$ but different (a) $\omega = 0.0$, (b) 0.6 , (c) 0.8 , and (d) 1.0 . As N is increased, the data exhibit a power-law behavior in large- t regime. Guide lines (dashed lines) are drawn to show the power-law behavior, indicating $\langle n(t) \rangle \sim t^{-\alpha}$. The exponent α is estimated as (a) $\alpha = 1.0$ for $\omega = 0$, (b) $\alpha = 0.92$ for $\omega = 0.6$, (c) $\alpha = 0.70$ for $\omega = 0.8$, and (d) $\alpha = 0.50$ for $\omega = 1.0$. Figures (a)–(d) show that the critical exponent α varies continuously depending on ω . The data are obtained for $\Gamma = 1$ and $\kappa = 1$. Insets: Scaling plots of $\langle n(t) \rangle t^\alpha$ versus tN^{-z} 113

- 5.3 FSS analysis for the transverse Ising model on fully connected graphs.
- (a) Plot of the order parameter m as a function of $\Delta_c - \Delta$ for different system sizes. We set $J = 1$ and $\Delta_c = 1$. The auxiliary dashed line with slope 0.5 means the power-law behavior $m \sim (\Delta_c - \Delta)^{0.5}$. Inset: Scaling plot of the magnetization $mN^{\beta/\bar{\nu}}$ versus $(\Delta_c - \Delta)N^{1/\bar{\nu}}$ with $\bar{\nu} = 1.5$ and $\beta = 0.5$. (b) Plot of the susceptibility as a function of $\Delta_c - \Delta$ for different system sizes. $\chi = N^{1+\bar{z}} \left(\langle (\hat{\sigma}^z)^2 \rangle - \langle \hat{\sigma}^z \rangle^2 \right)$, where $\bar{z} = z/d_c = 1/3$. The black dashed line is a guide line indicating $\chi \sim (\Delta_c - \Delta)^{-1}$. Inset: Scaling plot of the susceptibility $\chi N^{-\gamma/\bar{\nu}}$ versus $(\Delta_c - \Delta)N^{1/\bar{\nu}}$. The critical exponents $\bar{\nu} = 1.5$ and $\gamma = 1.0$ are used for the FSS analysis. (c) Plot of χ versus N at Δ_c . The slope represents the value of the critical exponent $\gamma/\bar{\nu}$ 117
- 5.4 (a) Phase diagram of the DTI model on fully connected graphs in the parameter space (Δ, Γ) . A continuous transition occurs across the solid white curve. The brightness represents the magnitude of magnetization m . (b) The density of the order parameter in the steady state as a function of Γ at $\Delta = 0.1$. System size is taken as $N = 128$. The brightness represents the probability that the order parameter exists. Data are obtained from the Liouville equation with $J = 1$ based on the PI states. . 122

- 5.5 FSS analysis for the DTI model at $\Delta = 0.5$ and $J = 1$ on fully connected graphs. (a) Plot of the order parameter m as a function of $\Gamma_c - \Gamma$ for different system sizes. The auxiliary dashed line with slope 0.5 means the power-law behavior $m \sim (\Gamma_c - \Gamma)^{0.5}$. Inset: Scaling plot of the magnetization $mN^{\beta/\bar{\nu}}$ versus $(\Delta_c - \Delta) N^{1/\bar{\nu}}$ with $\bar{\nu} = 1.75$ and $\beta = 0.5$. (b) Plot of χ as a function of $\Gamma_c - \Gamma$ for different system sizes. The auxiliary dashed line with slope -1.0 means the power-law behavior $\chi \sim (\Gamma_c - \Gamma)^{-1.0}$. Inset: Scaling plot of the susceptibility $\chi N^{-\gamma/\bar{\nu}}$ versus $(\Gamma_c - \Gamma) N^{1/\bar{\nu}}$. The critical exponents $\bar{\nu} = 1.75$ and $\gamma = 1.0$ are used for the FSS analysis. 123
- 5.6 (a) Phase diagram of the DTI model on fully connected graphs in the parameter space (Δ, J) . A continuous transition occurs across the solid white curve. The brightness represents the magnitude of magnetization m . (b) The density of the order parameter in the steady state as a function of J at $\Delta = 0.2$. System size is taken as $N = 128$. The brightness represents the probability that the order parameter exists. Data are obtained from the Liouville equation with $\Gamma = 1$ based on the PI states. 124
- 5.7 FSS analysis for the DTI model at $\Delta = 0.2$ and $J = 1$ on fully connected graphs. (a) Plot of the order parameter m as a function of $J - J_c$ for different system sizes. The auxiliary dashed line with slope 0.5 means the power-law behavior $m \sim (J - J_c)^{0.5}$. Inset: Scaling plot of the magnetization $mN^{\beta/\bar{\nu}}$ versus $(J - J_c) N^{1/\bar{\nu}}$ with $\bar{\nu} = 1.75$ and $\beta = 0.5$. (b) Plot of χ as a function of $J - J_c$ for different system sizes. The auxiliary dashed line with slope -1.0 means the power-law behavior $\chi \sim (J - J_c)^{-1.0}$. Inset: Scaling plot of the susceptibility $\chi N^{-\gamma/\bar{\nu}}$ versus $(J - J_c) N^{1/\bar{\nu}}$. The critical exponents $\bar{\nu} = 1.75$ and $\gamma = 1.0$ are used. 125

5.8	Comparison of the data sets obtained by the direct enumerations of the Lindblad equation based on the PI state (solid curve) and the quantum jump Monte Carlo (QJMC) simulations (symbols) for the DTI model with $\Delta = 0.1$ and $J = 1$ for different system sizes.	127
5.9	(a)–(c) Plots of the <i>ad hoc</i> potential $U(\theta)$ as a function of θ for different ω values. (d)–(f) Plots of the self-consistency function $G(\theta)$ versus θ for different ω values. (g)–(i) Plot of the derivative of $G(\theta)$ versus θ for different ω values. (i) $\lambda = 2.5$ for (a), (d), and (g). (ii) $\lambda = 3$ for (b), (e), and (h). (iii) $\lambda = 3.5$ for (c), (f), and (i). Numerical values are obtained by solving Eq. (5.44) for the mean degree $\langle k \rangle = 1$	134
5.10	Numerical solutions of the self-consistency equation. (a) Solution θ of the self-consistency equation, (b) density of active sites, and (c) susceptibility of the steady state as a function of ω . Dashed blue, solid black, and dash-dotted curves represent $\lambda = 2.5$, $\lambda = \lambda_c = 3$, and $\lambda = 3.5$, respectively.	134
5.11	The phase diagram of the QCP model on SF networks. The type of PT depends on the degree exponent λ . If $\lambda < \lambda_c = 3$, the transition point becomes zero ($\omega_c = 0$), thus $n > 0$ for any $\omega > 0$. At $\lambda = \lambda_c$, the system undergoes a continuous PT at $\omega_c \approx 0.900316$. If $\lambda > \lambda_c$, the system undergoes a discontinuous PT, and n is discontinuous on the transition line.	137

5.12 Numerical simulation results for the PTs of the QCP model on the static model. Plots of (a) the density of active sites $\langle n \rangle$ and (d) the susceptibility versus the control parameter ω for $\lambda = 2.2$ (\bullet), 3.0 (\blacksquare), and 3.5 (\blacktriangle). Note that ω_c s for $\lambda = 3.0$ and $\lambda = 3.5$ are estimated to be 0.900316 and 1.246471, respectively. (b) Scaling plot of the order parameter $nN^{\beta/\bar{\nu}}$ versus $\omega N^{1/\bar{\nu}}$ for $\lambda = 2.2$. (c) Scaling plot of order parameter $(n - n_c)N^{\beta/\bar{\nu}}$ versus $(\omega - \omega_c)N^{1/\bar{\nu}}$ for $\lambda = 3.5$. (e) Scaling plot of susceptibility $\chi N^{-\gamma/\bar{\nu}}$ versus $\omega N^{1/\bar{\nu}}$ for $\lambda = 2.2$. (f) Scaling plot of order parameter $\chi N^{\gamma/\bar{\nu}}$ versus $(\omega - \omega_c)N^{1/\bar{\nu}}$ for $\lambda = 3.5$. The critical exponents $\beta = 0.5$, $\gamma = 0.5$, $\bar{\nu} = 2.05$, $\omega_c = 1.246471$, and $n_c = n(\omega_c) = 0.167748$ are used. The data points for different system sizes collapse onto a single curve. Finite-size scaling analysis is not feasible for $\lambda = \lambda_c$, because logarithmic corrections are applied to both the order parameter and the susceptibility: $n \sim (\omega - \omega_c)^2 \ln \left(\frac{1}{\omega - \omega_c} \right)$ and $\chi \sim \ln \left(\frac{1}{\omega - \omega_c} \right)$ 139

List of Tables

2.1	Analytic solutions of the critical exponents for the s -SIS model. . . .	22
2.2	Numerical list of critical exponents of the s -SIS model obtained by the FSS method. Theoretical values calculated in Sec. 2.5 are presented in parentheses.	29
2.3	Dynamic critical exponents of s -SIS model obtained using the dynamical FSS method.	30
4.1	Performance measure R_m of vaccination strategies: random vaccination, vaccination in descending order of degree, eigenvector centrality (EC), betweenness centrality (BC), avalanche size, failure fraction, avalanche centrality (AC), and GNN prediction of AC. Smaller values indicate better mitigation. The most efficient mitigation strategy is marked by bold.	80
4.2	Hyper parameters used to train GNN.	82
5.1	Summary of previous analytical results. We considered three problems with the quantum models. For each model, the system Hamiltonian (\hat{H}_S) and Lindblad operators (\hat{L}_ℓ) were defined. Semiclassical, Weiss, and Keldysh field-theoretic approaches were used for the QCP, TI, and DTI models, respectively. Among these methods, the Keldysh formalism predicts features that differ qualitatively from those of fluctuationless MF theory.	106
5.2	Critical exponent α values for different ω values.	114

5.3 Summary of universality classes for classical, closed quantum, and open quantum Ising models. The system Hamiltonian (\hat{H}_S) and Lindblad operators (\hat{L}_ℓ) were defined for each model. Our numerical results indicate that dissipation changes the upper critical dimension and dynamic critical exponent. Note that the hyperscaling relation $2\beta + \gamma = \nu(d_c + z)$ is valid for all the models. 128

Chapter 1

Introduction

1.1 Complex Network

The SIS model is the most extensively studied epidemic model along with the SIR model. These models simplify the actual mechanism of the spread of epidemic disease; however, they can qualitatively explain the essential properties of epidemics. For this reason, among others, these models have been studied in depth. In the SIS model, each node in the network is in S (susceptible) state or I (infected) state. If a node is in S state and is connected to a node in the I state, then the S node turns into the I state at a constant rate (contagion). A node in the I state turns into the S state at a constant rate. A stationary state where a finite fraction of nodes is in the I state can exist in the SIS model.

In the traditional epidemic model, the constituents of the system homogeneously interact. However, it was discovered that the number of interactions between individuals follows a highly heterogeneous distribution. The number of links connected to a node is called the degree of the node, and many real-world networks have a degree distribution that has a power-law tail ($P(d) \sim d^{-\gamma}$). Networks with such power-law tail are called *scale-free networks*.

Nodes with extremely high degrees appear in such heterogeneous networks, in contrast to homogeneous networks, these nodes work as a *superspreader*. Due to the existence of these superspreaders, when the degree exponent of a scale-free network is between 2 and 3, even when the average degree of the network is finite, the expected

degree of a randomly selected neighbor of a randomly selected node diverges. This property has a significant impact on the epidemic spreading in complex networks. For instance, in a system with heterogeneous interaction, if the contagion rate is below a certain finite threshold, the epidemics cannot perpetuate. In contrast, in a scale-free network with a degree exponent between 2 and 3, the threshold vanishes. This suggests that a worldwide pandemic can occur repeatedly despite efforts to reduce the contagion rate.

1.2 Complex contagion

A link in a network always connects two nodes. However, in the real world, more than two agents can interact simultaneously. To overcome this limitation of networks, the hypergraph has been introduced. A hypergraph consists of nodes and hyperedges, and hyperedges can connect an arbitrary number of nodes at once. For instance, if three people, A, B, and C, wrote a three-author paper, it is represented as a network where nodes A and B are connected, B and C are connected, and C and A are connected. Because of this, the situation is indistinguishable from the case where A and B coauthored a two-author paper, B and C coauthored, and C and A coauthored. In a hypergraph representation, however, the first situation is represented as a hyperedge that simultaneously connects A, B, and C, hence the two situations are distinguished. The research community is showing great interest in hypergraphs due to their capability to encode higher-order interactions.

The contagion that occurs through the links is called the simple contagion model. Simple contagion models have been used to describe the spread of epidemic diseases, dissemination of innovations, and opinion formation; however, social phenomena that cannot be reduced to simple contagion processes have been observed. Examples are the spread of bizarre urban legends, adoption of unproven new technologies, willingness to participate in risky migrations, and the appeal of avant-garde fashion, and they depend on contact with multiple early adopters. Hypergraph contagion models have

been introduced to describe such phenomena. Examples of other complex contagions include quantum spreading process and nonlocal cascading failures in electrical grids.

1.3 Overview of dissertation

In this dissertation, we study the prediction and control of complex spreading processes. In Chapter 2, we investigate the phase transition and critical phenomena of the epidemic process in hypergraphs [149]. We find that the type of the phase transition is controlled by the degree exponent of the hypergraph. If the degree exponent is lower than a certain threshold, the epidemic threshold vanishes, while the system undergoes a hybrid phase transition when the degree exponent is higher than the threshold. When the exponent is exactly the critical value, the system undergoes a continuous phase transition at a finite contagion rate. We also studied containment strategies for hypergraph epidemic processes [143]. We extended the individual- and pair-based mean-field theory to higher-order epidemic dynamics to formulate effective contagion strategies.

In Chapter 3, we study the efficient vaccination strategy to minimize epidemic mortality in a population with a heterogeneous fatality rate [146]. We discovered that when the vaccine supply is low, it is more effective to primarily vaccinate the population with a high fatality, and when there is a high vaccine supply, it is advantageous to vaccinate the population with a high contagion rate in priority. We also showed that there is a discontinuous transition between the two types of strategies.

In Chapter 4, we employed graph neural network to calculate effective control schemes for cascading failures [147]. First, we proposed an avalanche centrality of each node, a measure related to avalanche size, based on the Motter-Lai model. Then, we train a graph neural network with the avalanche centrality in small networks. Then, the trained GNN predicts the avalanche centrality ranking in much larger networks and real-world electrical grids. This result can be used effectively for avalanche mitigation. The framework we develop can be implemented in other complex processes that are

computationally costly to simulate in large networks. We also employ graph neural network ansatz to formulate effective epidemic containment strategy in complex networks [144].

In Chapter 5, we implemented an effective numerical simulation for several dissipative quantum systems [157]. The results are consistent with those predicted by the fluctuationless mean-field approach; however, inconsistent with those by the Keldysh method. We remark that for the quantum contact process, we discover that there exists a crossover region between the directed percolation class and the tricritical DP class. Finally, based on our numerical results, we discuss the strong and weak points of each analytic mean-field approach. We also studied the quantum contact process in scale-free networks [150]. We performed numerical simulations to corroborate the analytical predictions. We discovered that the types of phase transitions in this system are controlled by the degree exponent of the underlying network.

In Chapter 6, the conclusions of this dissertation are presented. The results of our other publications that are out of scope are not covered in this dissertation [145, 148, 151].

Chapter 2

Higher-order epidemics

2.1 Phase transition and critical phenomena of the simplicial susceptible-infected-susceptible (s -SIS) model

In past decades, extensive research has been done on emerging phenomena in complex networks, including the spread of epidemic diseases and innovations [164, 282, 283, 349], opinion formation [3, 113, 342], and many other topics [27, 30, 132, 248, 277]. An important issue for such emerging phenomena is to understand the origin and properties of phase transitions. Complex networks represented by graphs enable researchers to study such issues successfully. A graph is a collection of vertices and edges, where an edge represents a pairwise interaction between two vertices. In complex systems, however, interactions among constituents can be more complex than pairwise. For instance, more than two people can collaborate on a team.

A *hypergraph* is a generalization of a graph whose hyperedge connects two or more vertices. Consequently, it can be used to encode complicated social interactions that the graph representation cannot. In this hypergraph representation, a hyperedge of size n connects n researchers who collaborate on one task, for instance, d authors of a d -author paper in coauthorship networks [347]. This hypergraph representation successfully accounts for various types of collaborations [28, 29, 99, 176, 317, 327, 357, 361]. In particular, a *uniform hypergraph* is one in which all the hyperedges have the same size. If the size of these hyperedges is d , the structure is called a d -uniform hypergraph, or d -hypergraph. Uniform hypergraphs can describe systems in which a

uniform number of agents interact at the same time. Trivially, a 2-uniform hypergraph reduces to a graph. Owing to its simplicity, the uniform hypergraph enables succinct expression of diverse static and dynamic problems in terms of linear algebra using the adjacency tensor [69].

A *simplicial complex* is a particular hypergraph with an additional constraint: If a hyperedge is in a simplicial complex, any non-empty subset of vertices in the hyperedge is also a hyperedge of the simplicial complex. This requirement makes the simplicial complex an appropriate tool for studying systems with high-order interactions, i.e., interactions that involve a large number of agents, which also include lower-order interactions. A hyperedge in a simplicial complex is often called a simplex. The simplicial complex has been a topic of extensive research. Examples include the collaboration network [61,269], semantic network [310], cellular network [85], and brain network [196,275].

A simplicial contagion model was recently introduced [137] to describe a complex contagion process on simplicial complexes; however, as pointed out in the paper, the model itself was defined for general hypergraphs. The model can also be easily applied to general hypergraphs. Here, we consider this simplicial contagion process on d -uniform hypergraphs with hyperedges of the same size. Specifically, we consider the case that infection spreads only when all but one of the nodes in the hyperedge are infected. Even though this is a simple case with a maximally conservative contagion process, it provides an essential factor that leads to a hybrid epidemic transition on hypergraphs. Here, we consider a simplicial susceptible-infected-susceptible (s -SIS) model, where infection spreads by a simplicial contagion process. Each node is in either the susceptible (S) or infected (I) state. A susceptible node becomes infected at a rate β when all the other nodes in the same hyperedge are infected. If a node is infected, it changes spontaneously to the susceptible state S at a rate μ . This recovery process ($I \rightarrow S$) is defined as in the SIS model of a network because the recovery process occurs on each node independently, making it irrelevant to the structural type

of the contagion process.

Here we explore the s -SIS model on scale-free (SF) uniform hypergraphs. We use the annealed approximation for the static model of the uniform hypergraph, which is extended from the static model of the complex graph [107]. We find analytically that there exists a characteristic degree $\lambda_c = 2 + 1/(d - 1)$ such that when the exponent λ of the degree distribution is $2 < \lambda \leq \lambda_c$, a continuous transition occurs; however, when $\lambda > \lambda_c$, a hybrid phase transition occurs. In this hybrid phase transition, the order parameter jumps at a macroscopic scale and then increases continuously with criticality as a control parameter, $\eta \equiv \beta/\mu$, is increased.

2.2 Static model of uniform hypergraph

The static model of a complex network [107, 198] has been widely used to generate SF networks owing to its simplicity and analytical tractability. The model has been used to study the q -state Potts model [190], sandpile model [108], spin glasses [168], and many other topics [98, 138, 167, 200, 201, 203, 204, 311, 351, 354] involving complex networks.

A static model of a uniform hypergraph is a generalization of the static model of a complex graph. The static model of a d -uniform hypergraph is generated as follows:

- i) Set the number of nodes in the system, N .
- ii) Assign each node a weight p_i as

$$p_i = \frac{i^{-\mu}}{\zeta_N(\mu)} \simeq \frac{1 - \mu}{N^{1-\mu}} i^{-\mu}, \quad (2.1)$$

where $\zeta_N(\mu) = \sum_{j=1}^N j^{-\mu}$, and $0 < \mu < 1$. The normalization condition $\sum_{i=1}^N p_i = 1$ is satisfied.

- iii) Select d distinct nodes with probabilities $p_{i_1} \cdots p_{i_d}$. If the hypergraph does not already contain a hyperedge of the chosen d nodes, then add the hyperedge to

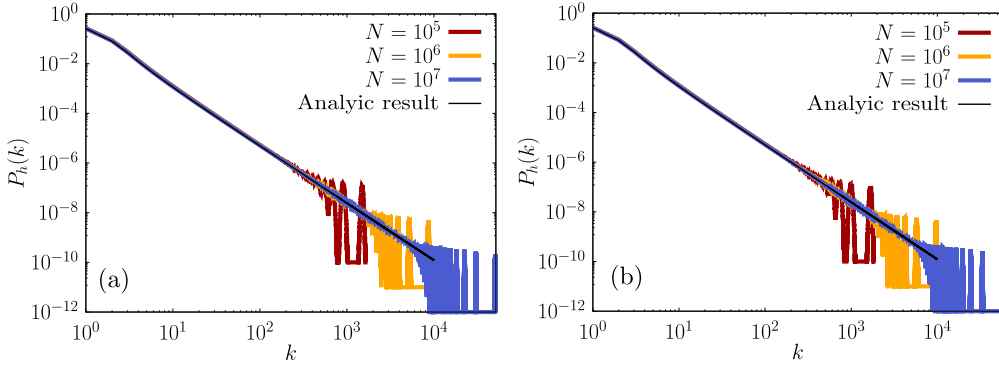


Figure 2.1: Degree distribution of the static model of (a) 2-uniform (graph) and (b) 3-uniform hypergraph generated with the fitness exponent $1/\mu = 1.3$. The system size N is given as $N = 10^5, 10^6$, and 10^7 . As the system size is increased, the tail part of the degree distribution is extended, and power-law behavior with exponent $\lambda = 1 + 1/\mu = 2.3$ is confirmed.

the hypergraph.

iv) Repeat step iii) NK times.

Then, each node i has average degree $\langle k_i \rangle$. These average degrees have a power-law distribution $P_d(k) \sim k^{-\lambda}$ with $\lambda = 1 + 1/\mu$, where the brackets of $\langle k_i \rangle$ are omitted. The details are presented in 2.7. The minimum degree is obtained as $k_{\min} = N^{1-\mu} \langle k \rangle / \sum_{j=1}^N j^{-\mu}$, which converges to a finite value, $\frac{\lambda-2}{\lambda-1} \langle k \rangle$, where $\langle k \rangle$ denotes the mean degree $\sum_k k P_d(k)$. The maximum degree is obtained as $k_{\max} = N \langle k \rangle / \sum_{j=1}^N j^{-\mu}$, which behaves as $\frac{\lambda-2}{\lambda-1} \langle k \rangle N^{1/(\lambda-1)} \sim N^{1/(\lambda-1)}$. Thus, it diverges as $N \rightarrow \infty$. Hereafter, the minimum degree is denoted as k_m . Throughout this algorithm, NK hyperedges are generated.

The probability that a hyperedge composed of d distinct nodes $\{i_1 \cdots i_d\}$ is present is given by

$$f_{i_1 \cdots i_d} = 1 - (1 - d! p_{i_1} \cdots p_{i_d})^{NK} \simeq 1 - e^{-d! NK p_{i_1} \cdots p_{i_d}}, \quad (2.2)$$

and the probability that a hypergraph G is generated is

$$P(G) = \prod_{a_{i_1 \dots i_d} \in G} \left(1 - e^{-d!NKp_{i_1} \dots p_{i_d}}\right) \prod_{a_{i_1 \dots i_d} \notin G} e^{-d!NKp_{i_1} \dots p_{i_d}}. \quad (2.3)$$

Because $d!NKp_{i_1} \dots p_{i_d} \sim N^{d\mu-d+1} / (i_1 \dots i_d)^\mu$, for $0 < \mu < \frac{d-1}{d}$, which is equivalent to $\lambda > 2 + \frac{1}{d-1}$,

$$f_{i_1 \dots i_d} \simeq d!NKp_{i_1} \dots p_{i_d}, \quad (2.4)$$

and for $2 < \lambda < 2 + \frac{1}{d-1}$,

$$f_{i_1 \dots i_d} \simeq \begin{cases} 1 & (i_1 \dots i_d)^\mu \ll N^{d\mu-d+1} \\ d!NKp_{i_1} \dots p_{i_d} & (i_1 \dots i_d)^\mu \gg N^{d\mu-d+1} \end{cases}. \quad (2.5)$$

We note that $\lambda = 2 + 1/(d-1)$ is a characteristic degree and is denoted as λ_c , which reduces to $\lambda_c = 3$ for an SF graph ($d = 2$) and $\lambda_c < 3$ for an SF hypergraph ($d > 2$). The fraction of nodes that satisfies the second case of Eq. (2.5) is proportional to $1 - AN^{d\mu-d}$, where A is a constant, which converges to one as $N \rightarrow \infty$. For $d = 2$, the static model of the hypergraph reduces to the static model of the graph. For $\mu = 0$, i.e., $\lambda = \infty$, the expected degree of all the nodes is identical, and the model reduces to an Erdős–Renyi-like hypergraph.

2.3 Simplicial SIS model

A contagion process through an edge on a graph is called a simple contagion process. Simple contagion processes on complex graphs have been extensively studied to describe the spread of disease [251, 321], adoption of innovation [283, 325], and opinion formation [3, 113, 342]. However, social phenomena that cannot be reduced to simple contagion processes have been observed, for instance, belief in bizarre urban legends [125], adoption of unproven new technologies [64], willingness to participate

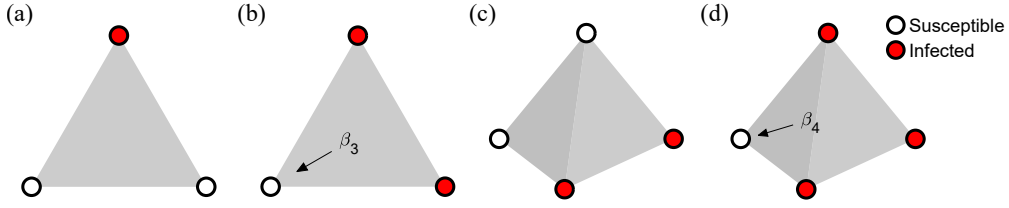


Figure 2.2: Schematic illustration of the simplicial contagion process through hyperedges of size 3 in (a) and (b), and 4 in (c) and (d). The susceptible and infected nodes are depicted as white open circles and red filled circles, respectively. When $d - 1$ of d nodes in a hyperedge are infected, the infection spreads to the remaining susceptible node through the hyperedge at a rate β_d .

in risky migrations [219], and the appeal of avant-garde fashion [70], and they depend on contact with multiple early adopters. Adoption of behaviors that are costly, risky, or controversial often requires affirmation or reinforcement from an independent source. More complicated models of contagion, namely, a complex contagion process, have been proposed to describe such social phenomena. Examples include the threshold model [114, 341] and a generalized epidemic model [58, 141].

A recently introduced simplicial contagion model [137] represents a complex contagion process on a hypergraph. It applies a maximally conservative contagion process on the hypergraph, in which contagion through a hyperedge of size d occurs only when all but one of the nodes in the hyperedge are infected. When this condition is met, the remaining susceptible node is infected at a rate β_d per unit time. For instance, when nodes j and k are infected in the hyperedge $\{i, j, k\}$, node i is infected with probability $\beta_3 \delta t$ in duration δt . If only node j is infected and the other node, k , is not, the infection does not spread to node i through the hyperedge.

The complex contagion process in a d -uniform hypergraph is described by an adjacency tensor of dimension d . The rate equation is written as follows:

$$\frac{d}{dt}q_{i_1} = -\mu q_{i_1} + \frac{1}{(d-1)!} (1 - q_{i_1}) \beta_d \sum_{i_2 \dots i_d} a_{i_1 \dots i_d} q_{i_2} \dots q_{i_d}, \quad (2.6)$$

where q_{i_1} is the probability that a node i_1 is infected, and $a_{i_1 \dots i_d}$ is the adjacency tensor,

where $a_{i_1 \dots i_d} = 1$ if nodes $\{i_1 \dots i_d\}$ are fully connected, and otherwise, it is zero.

2.4 Heterogeneous mean-field theory (annealed approximation)

We use the heterogeneous mean-field theory to study the stationary states of the SIS model on SF d -uniform hypergraphs. This theoretical approach has been successful for examining the SIS [264, 266] and susceptible-infected-recovered [235] models on SF graphs. It represents well the significant effect of a small portion of nodes with large degrees. Here, we consider the SIS model on SF d -dimensional uniform hypergraphs. We set up a differential equation for the density of infected nodes of degree k and then obtain the self-consistency equation for the stationary solution. We solve a self-consistency equation to calculate the density of infected nodes as a function of infection rate. We investigate the properties of the epidemic transition.

2.4.1 Self-consistency equation

The density of infected nodes with degree k , denoted as ρ_k , evolves with time as follows:

$$\frac{d}{dt}\rho_k = -\mu\rho_k + \beta(1 - \rho_k)k\Theta^{d-1}. \quad (2.7)$$

The first term on the r.h.s. of the above equation is a loss term associated with the recovery process $I \rightarrow S$. The second term is a gain term associated with the contagion process $(d-1)I + S \rightarrow dI$. That is, a given node i in state S is changed to state I by contagion from $d-1$ infected nodes in a hyperedge of size d at a rate β , which is equivalent to β_d in the previous notation, in which node i is included. Θ is given by

$$\Theta = \frac{\sum_{k=k_m}^{\infty} k P_h(k) \rho_k(t)}{\langle k \rangle}, \quad (2.8)$$

where $kP_h(k)\rho_k/\langle k \rangle$ is the probability that a node connected to a randomly chosen hyperedge has degree k and is infected at time t . We are interested in the behavior of ρ_k in the stationary state, in which $d\rho_k/dt = 0$, and we set $\eta \equiv \beta/\mu$ for convenience.

The stationary solution of ρ_k is obtained as

$$\rho_k = \frac{\eta k \Theta^{d-1}}{1 + \eta k \Theta^{d-1}}. \quad (2.9)$$

This solution implies that the infection probability ρ_k always increases and approaches one as $k \rightarrow \infty$ for $\eta > 0$, and that it is controlled by a single factor, $\eta \Theta^{d-1}$. The density of infected nodes becomes $\rho \equiv \sum_k P_h(k)\rho_k$, which serves as the order parameter of the epidemic transition.

To obtain ρ , we set up a self-consistency equation for Θ in the stationary state as follows:

$$\Theta = \frac{1}{\langle k \rangle} \sum_k k P_h(k) \rho_k = \frac{1}{\langle k \rangle} \sum_k k P_h(k) \frac{\eta k \Theta^{d-1}}{1 + \eta k \Theta^{d-1}}. \quad (2.10)$$

We define the self-consistency function $G(\Theta)$ as

$$G(\Theta) = \frac{1}{\langle k \rangle} \sum_k k P_h(k) \frac{\eta k \Theta^{d-1}}{1 + \eta k \Theta^{d-1}} - \Theta \quad (2.11)$$

and then obtain a solution Θ_0 of $G(\Theta_0) = 0$.

For the power-law degree distribution, $P_h(k) = (\lambda - 1)k_m^{\lambda-1}k^{-\lambda}$ for $k \geq k_m$, and the mean degree $\langle k \rangle = \frac{\lambda-1}{\lambda-2}k_m$,

$$G(\Theta) = (\lambda - 2)k_m^{\lambda-2} \sum_k k^{1-\lambda} \frac{\eta k \Theta^{d-1}}{1 + \eta k \Theta^{d-1}} - \Theta. \quad (2.12)$$

We treat k as a continuous variable and recast the summation $\sum_{k=k_m}^{\infty} \dots$ as the inte-

gration $\int_{k_m}^{\infty} dk \dots$.

$$G(\Theta) = (\lambda - 2)k_m^{\lambda-2} \int_{k_m}^{\infty} dk k^{-\lambda+1} \left(1 + \frac{1}{\eta k \Theta^{d-1}}\right)^{-1} - \Theta \quad (2.13)$$

$$= (\lambda - 2) \int_0^1 dz z^{\lambda-3} \left(1 + \frac{z}{\eta k_m \Theta^{d-1}}\right)^{-1} - \Theta \quad (2.14)$$

$$= {}_2F_1 \left(\lambda - 2, 1; \lambda - 1; -\frac{1}{\eta k_m \Theta^{d-1}} \right) - \Theta, \quad (2.15)$$

where we changed the variable k to z as $z = k_m/k$ in Eq. (2.14), and ${}_2F_1(a, b; c, d)$ in Eq. (2.15) is the Gauss hypergeometric function, which is defined as [1]

$${}_2F_1(a, b; c, z) = \frac{\Gamma(c)}{\Gamma(b)\Gamma(c-b)} \int_0^1 dz z^{b-1} (1-z)^{c-b-1} (1-tz)^{-a}. \quad (2.16)$$

To obtain a solution Θ_0 of $G(\Theta_0) = 0$, we first note that the self-consistency function has the following properties: $G(0) = 0$, and $G(1) < 0$. Second, we examine the derivative with respect to Θ , which can be written as

$$G'(\Theta) = \frac{(d-1)(\lambda-2)}{k_m \eta \Theta^d (\lambda-1)} {}_2F_1 \left(\lambda - 1, 2; \lambda; -\frac{1}{k_m \eta \Theta^{d-1}} \right) - 1. \quad (2.17)$$

If $\lim_{\Theta \rightarrow 0} G'(\Theta) > 0$, there exists at least one nonzero solution Θ_0 . Using the asymptotic properties of the hypergeometric function, we find that there exists a characteristic degree exponent $\lambda_c = 2 + 1/(d-1)$ such that

$$\lim_{\Theta \rightarrow 0} G'(\Theta) = \begin{cases} +\infty & \text{for } \lambda < \lambda_c \\ \frac{\pi/(d-1)}{\sin(\pi/(d-1))} (k_m \eta)^{1/(d-1)} - 1 & \text{for } \lambda = \lambda_c \\ -1 & \text{for } \lambda > \lambda_c \end{cases}. \quad (2.18)$$

See 2.8 for details.

After we obtain Θ_0 , the density of infection ρ , which serves as the order parameter

for the epidemic transition, is calculated as follows:

$$\rho = \int_{k_m}^{\infty} dk P_h(k) \frac{\eta k \Theta_0^{d-1}}{1 + \eta k \Theta_0^{d-1}} = {}_2F_1 \left(\lambda - 1, 1; \lambda; -\frac{1}{k_m \eta \Theta_0^{d-1}} \right). \quad (2.19)$$

We will determine the solution Θ_0 and ρ for each case in Eq. (2.18) in the next section.

2.5 Phase transition and critical behavior

The type of phase transition and the epidemic threshold are determined by the behavior of $G(\Theta)$, which in turn is determined by $\lim_{\Theta \rightarrow 0} G'(\Theta)$. Accordingly, we consider the epidemic transition separately for each case in Eq. (2.18).

2.5.1 Order parameter

To solve Eqs. (2.15) and (2.19), we use a Taylor expansion of the hypergeometric function

$$\begin{aligned} {}_2F_1 \left(\lambda - 2, 1; \lambda - 1; -\frac{1}{k_m \eta \Theta^{d-1}} \right) &= \frac{(\lambda - 2)\pi}{\sin(\pi\lambda)} (k_m \eta \Theta^{d-1})^{\lambda-2} \\ &+ (\lambda - 2) \sum_{n=1}^{\infty} (-1)^n \frac{(k_m \eta \Theta^{d-1})^n}{n - (\lambda - 2)}. \end{aligned} \quad (2.20)$$

i) For $\lambda < \lambda_c$, $\lim_{\Theta \rightarrow 0} G'(\Theta) = \infty$. Because $G(0) = 0$ and $G(1) < 0$, there exists at least one solution $\Theta_0 > 0$ for $\eta > 0$. Here, we find one such nontrivial stable solution $\Theta > 0$, leading to $\rho > 0$. Therefore, a transition occurs at $\eta_c = 0$. As η is increased, both ρ and Θ increase, and the transition is continuous. Analytically, we find that as $\eta \rightarrow 0$,

$$G(\Theta_0; k_m \eta) \simeq \frac{(\lambda - 2)\pi}{\sin(\pi\lambda)} \left(k_m \eta \Theta_0^{d-1} \right)^{\lambda-2} - \Theta_0 = 0, \quad (2.21)$$

$$\Theta_0 \sim \eta^{\frac{\lambda-2}{1-(d-1)(\lambda-2)}}. \quad (2.22)$$

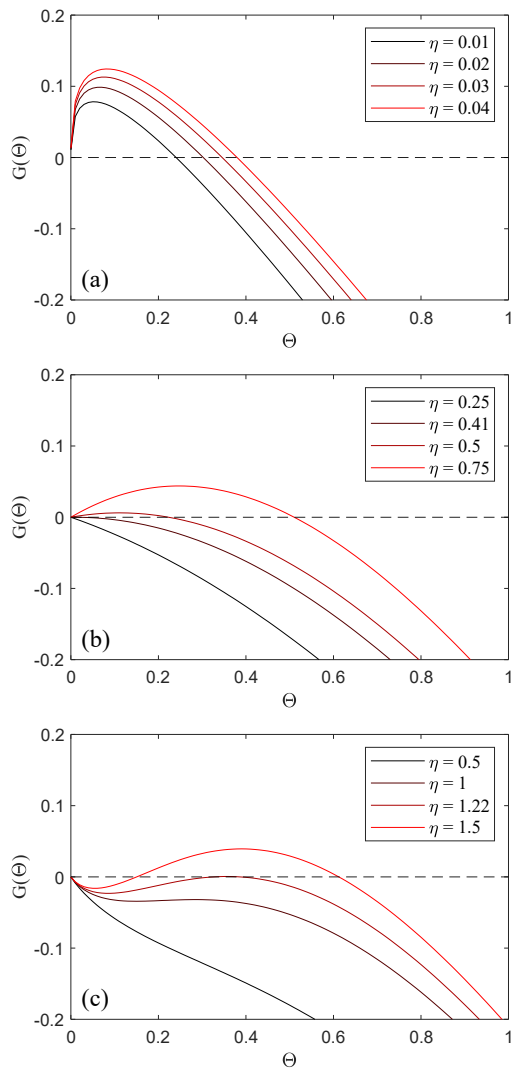


Figure 2.3: Self-consistency function $G(\Theta)$ of SF 3-uniform hypergraphs with degree exponent (a) $\lambda = 2.2$, (b) 2.5, and (c) 2.8, corresponding to cases i) $\lambda < \lambda_c$, ii) $\lambda = \lambda_c$, and iii) $\lambda > \lambda_c$ in the main text. The derivative of the function with respect to Θ at $\Theta = 0$ (a) diverges, (b) is positive, and (c) is negative as Θ approaches zero.

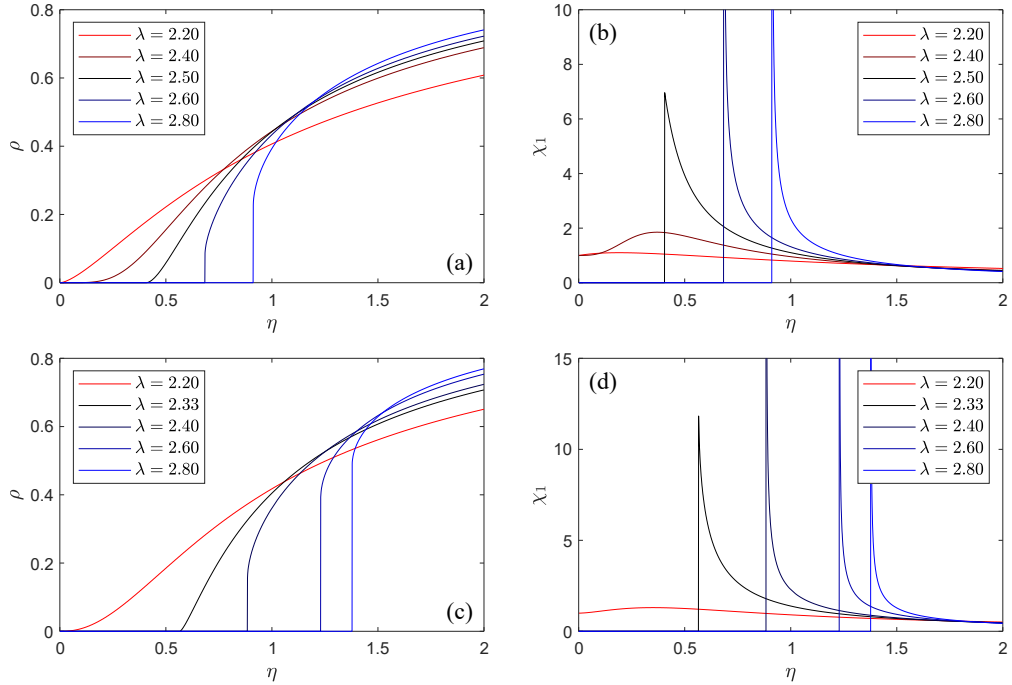


Figure 2.4: Density of infected nodes versus control parameter λ for various degree exponent values λ for (a) $d = 3$ and (c) $d = 4$. Susceptibility versus control parameter λ for various λ values for (b) $d = 3$ and (d) $d = 4$. For $\lambda = 2.2$ and $\lambda = 2.4$, the transition point is $\lambda_c = 0$, and for $\lambda = 2.5, 2.6$, and 2.8 , λ_c is finite. For $\lambda = 2.2, 2.4$, and 2.8 , the transition is second-order, and for $\lambda = 2.6$ and 2.8 , the transition is hybrid. For $\lambda \leq \lambda_c$, the susceptibility converges to a finite value $1 + d(d - 2)$. For $\lambda > \lambda_c$, the susceptibility diverges as $\lambda \rightarrow \lambda_c^+$.

The density of infection ρ can also be calculated from Eq. (2.19):

$$\rho \sim \eta \Theta_0^{d-1} \sim \eta^{\frac{1}{1-(d-1)(\lambda-2)}}. \quad (2.23)$$

Thus, the exponent $\beta = 1/[1 - (d - 1)(\lambda - 2)]$. In particular, when $d = 2$, $\rho \sim \eta^{1/(3-\lambda)}$ [264].

ii) For $\lambda = \lambda_c$, the epidemic threshold is finite as $\eta_c = \frac{1}{k_m} \left[\frac{\sin(\pi/(d-1))}{\pi/(d-1)} \right]^{d-1}$. Above η_c , $G'(\Theta) > 0$, and thus there exists a finite Θ_0 satisfying $G(\Theta_0) = 0$. As $\eta \rightarrow \eta_c^+$, both ρ and Θ_0 decrease to zero. Thus, a second-order transition occurs at η_c . Specifically, the self-consistency function $G(\Theta)$ is written in Eq. (2.21). In this case, we need to consider higher-order terms of $G(\Theta)$ as

$$\begin{aligned} G(\Theta; k_m \eta) &\simeq \left[\left(\frac{\eta}{\eta_c} \right)^{1/(d-1)} - 1 \right] \Theta - \frac{k_m \eta \Theta^{d-1}}{d-2} \\ &\simeq \frac{1}{d-1} \left(\frac{\eta - \eta_c}{\eta_c} \right) \Theta - \frac{k_m \eta \Theta^{d-1}}{d-2}. \end{aligned} \quad (2.24)$$

Therefore,

$$\Theta_0 \sim (\eta - \eta_c)^{\frac{1}{d-2}}, \quad (2.25)$$

$$\rho \sim (\eta - \eta_c)^{\frac{d-1}{d-2}}. \quad (2.26)$$

Consequently, the critical exponent $\beta = (d - 1)/(d - 2)$ for $d > 2$. When $d = 2$, $\rho \sim e^{-1/k_m \eta}$ was obtained [264].

iii) For $\lambda > \lambda_c$, $\lim_{\Theta \rightarrow 0} G'(\Theta) < 0$, and thus η_c is finite. In this case, Θ_0 and ρ do not decrease to zero but are finite as $\eta \rightarrow \eta_c^+$. We calculate the asymptotic behaviors of $\Theta_0(\eta) - \Theta_0(\eta_c)$ and $\rho(\eta) - \rho(\eta_c)$. At the transition point, $G = 0$ and $\partial_\Theta G = 0$;

thus, near this point,

$$G(\Theta; k_m \eta) = \frac{1}{2} \frac{\partial^2 G}{\partial \Theta^2} (\Delta \Theta)^2 + \frac{\partial G}{\partial \eta} \Delta \eta + \dots, \quad (2.27)$$

$$\Theta_0(\eta) - \Theta_0(\eta_c) \sim (\eta - \eta_c)^{1/2}, \quad (2.28)$$

$$\rho(\eta) - \rho(\eta_c) \sim (\eta - \eta_c)^{1/2}, \quad (2.29)$$

where $\Theta_0(\eta_c)$ and $\rho(\eta_c)$ are calculated using Eqs. (2.15) and (2.19), respectively. Therefore, the transition is hybrid with the exponent $\beta = 1/2$.

2.5.2 Susceptibility

The susceptibility is defined as the response of the order parameter, that is, the density of infection, to a conjugated field h :

$$\frac{d}{dt} \rho = -\rho + \eta \langle k \rangle (1 - \rho) \Theta^{d-1} + (1 - \rho) h. \quad (2.30)$$

The conjugated field h is implemented using the rate of spontaneous infection $S \rightarrow I$, i.e., the rate at which a susceptible node is changed to an infected state independently of the contagion process. The susceptibility is defined as the sensitivity of the density of infection to the conjugated field:

$$\chi_1 = \frac{\partial \rho}{\partial h}. \quad (2.31)$$

The differential equation for ρ_k is written as

$$\frac{d\rho_k}{dt} = -\rho_k + \eta k (1 - \rho_k) \Theta^{d-1} + (1 - \rho_k) h. \quad (2.32)$$

The steady-state solution is obtained as

$$\rho_k = \frac{h + \eta k \Theta^{d-1}}{1 + h + \eta k \Theta^{d-1}}. \quad (2.33)$$

The self-consistency equation is modified as follows:

$$G(\Theta, h) = {}_2F_1\left(\lambda - 2, 1; \lambda - 1; -\frac{1+h}{k_m \eta \Theta^{d-1}}\right) + h \frac{\lambda - 2}{\lambda - 1} \frac{1}{k_m \eta \Theta^{d-1}} {}_2F_1\left(\lambda - 1, 1; \lambda; -\frac{1+h}{k_m \eta \Theta^{d-1}}\right) - \Theta. \quad (2.34)$$

The susceptibility is obtained using the following relation:

$$\chi_1 = \left. \frac{\partial \rho}{\partial h} \right|_{\eta, \Theta_0} - \left. \frac{\partial \rho}{\partial \Theta} \right|_{\eta, h} \left. \frac{\partial G}{\partial h} \right|_{\eta, \Theta_0} \left(\left. \frac{\partial G}{\partial \Theta} \right|_{\eta, h} \right)^{-1}. \quad (2.35)$$

Detailed calculations of the susceptibility are presented in 2.9.

The results are as follows: i) For $\lambda \leq \lambda_c$, the susceptibility converges to a finite value near the critical point, and therefore the critical exponent $\gamma_1 = 0$.

ii) For $\lambda > \lambda_c$, the susceptibility diverges as $(\eta - \eta_c)^{-\gamma_1}$ with $\gamma_1 = 1/2$.

2.5.3 Correlation size

In the static model, the maximum degree diverges as $k_{\max} \sim N^{1/(\lambda-1)}$, which is called the natural cut-off [198]. We assign a weight p_i to each node using Eq. (2.1).

The exponent of the hyperedge degree distribution is $\lambda = 1 + 1/\mu$.

The self-consistency equation for finite systems reduces to

$$G_N(\Theta) = \frac{1}{N \langle k \rangle} \sum_{i=1}^N \frac{\eta \Theta^{d-1} k_i^2}{1 + \eta \Theta^{d-1} k_i} - \Theta, \quad (2.36)$$

where $k_i = \frac{N i^{-\mu}}{\sum_j j^{-\mu}}$. Further,

$$\frac{1}{N} \sum_{i=1}^N \frac{\eta \Theta^{d-1} k_i^2}{1 + \eta \Theta^{d-1} k_i} P(k_i) dk_i \simeq \int_{k_{\min}}^{k_{\max}} \frac{\eta \Theta^{d-1} k_i^2}{1 + \eta \Theta^{d-1} k_i} P(k_i) dk_i, \quad (2.37)$$

where

$$k_{\min} = \left[\frac{1}{N} \sum_{j=1}^N \left(\frac{j}{N} \right)^{-\mu} \right]^{-1} \simeq \int_0^1 x^{-\mu} dx - \int_0^{1/N} x^{-\mu} dx \quad (2.38)$$

$$= \frac{\lambda - 2}{\lambda - 1} \langle k \rangle \left(1 - N^{-\frac{\lambda-2}{\lambda-1}} \right), \quad (2.39)$$

$$k_{\max} = k_{\min} N^{\frac{1}{\lambda-1}}. \quad (2.40)$$

Therefore,

$$G_N(\Theta) \simeq \frac{\lambda - 2}{k_m^{-\lambda+2}} \int_{k_{\min}}^{k_{\max}} dk \frac{\eta k^{-\lambda+2} \Theta^{d-1}}{1 + \eta k \Theta^{d-1}} - \Theta \quad (2.41)$$

$$\simeq G(\Theta) + k_m N^{-\frac{\lambda-2}{\lambda-1}} \frac{\eta k_m^{-\lambda+2} \Theta^{d-1}}{1 + \eta k_m \Theta^{d-1}} - N^{-\frac{\lambda-2}{\lambda-1}} {}_2F_1 \left(\lambda - 2, 1; \lambda - 1; -\frac{1}{k_m N^{1/(\lambda-1)} \eta \Theta^{d-1}} \right), \quad (2.42)$$

where $G(\Theta)$ is the self-consistency function of the infinite system provided in Eq. (2.15). The solution of $G_N(\Theta) = 0$ yields the density of infected nodes in finite systems. This function is illustrated in Fig. 2.5(a) for a 3-uniform hypergraph with $\lambda = 2.8$.

By expanding the finite-size self-consistency function in Eq. (2.42) for large N , we can calculate the critical exponent of the correlation size, $\bar{\nu}$, which is defined by the relation $\eta_c(N) - \eta_c(\infty) \sim N^{-1/\bar{\nu}}$.

i) For $\lambda < \lambda_c$, $\lambda_c = 0$, and thus $\lambda_c(N)$ is expected to be close to zero for large N . Therefore, for large N ,

$$N^{-(\lambda-2)/(\lambda-1)} {}_2F_1 \left(\lambda - 2, 1; \lambda - 1; -\frac{1}{k_m N^{1/(\lambda-1)} \lambda \Theta^{d-1}} \right) \simeq N^{-(\lambda-2)/(\lambda-1)}, \quad (2.43)$$

because the hypergeometric function converges rapidly to 1. The finite-size epidemic threshold is obtained when the maximum value of the function given by Eq. (2.21) is

equal to that given by Eq. (2.43). Therefore,

$$\eta_c(N) \sim N^{-[1-(d-1)(\lambda-2)]/(\lambda-1)}. \quad (2.44)$$

The inverse of the correlation size exponent is $1/\bar{\nu} = [1 - (d - 1)(\lambda - 2)] / (\lambda - 1)$, which approaches zero as $\lambda \rightarrow \lambda_c = 2 + 1/(d - 1)$.

ii) For $\lambda = \lambda_c$, $(\lambda - \lambda_c) \rightarrow 0$, and $\Theta \rightarrow 0$ with $\lambda_c > 0$. The self-consistency function near the critical point is

$$G_N(\Theta) = A(\lambda - \lambda_c)\Theta - B\Theta^{d-1} - N^{-(\lambda-2)/(\lambda-1)}, \quad (2.45)$$

where A and B are positive constants. Therefore,

$$(\eta - \eta_c) \sim N^{-\frac{d-2}{(d-1)^2(\lambda-1)}}. \quad (2.46)$$

The inverse of the correlation size exponent becomes $1/\bar{\nu} = (d-2)/[(d-1)^2(\lambda-1)]$.

iii) For $\lambda > \lambda_c$, the self-consistency function in finite systems becomes

$$G_N(\Theta) = G(\Theta) + \frac{\partial G}{\partial \lambda}(\lambda - \lambda_c) - N^{-(\lambda-2)/(\lambda-1)}. \quad (2.47)$$

Therefore,

$$(\eta - \eta_c) \sim N^{-\frac{\lambda-2}{(\lambda-1)}}. \quad (2.48)$$

The inverse of the correlation size exponent is $1/\bar{\nu} = (\lambda - 2)/(\lambda - 1)$.

In this section, we obtained the critical exponents through the heterogeneous mean-field theory. The results are summarized in Tab. 5.2. Continuous (Discontinuous) transition occurs for $\lambda \leq \lambda_c$ ($\lambda > \lambda_c$). At $\lambda = \lambda_c$, this is the boundary point where transition type and universality class are changed. Thus, $\lambda = \lambda_c$ can be regarded as the tricritical point.

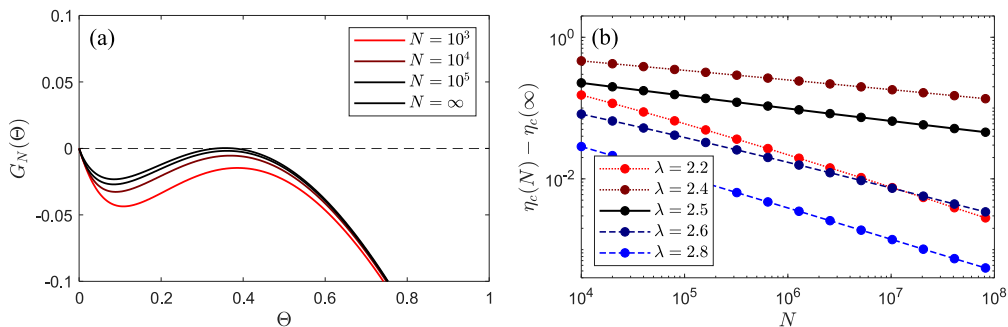


Figure 2.5: (a) Self-consistency function $G_N(\Theta)$ in finite systems versus Θ for 3-uniform hypergraphs with $\lambda = 2.8$. (b) Deviation $\lambda_c(N) - \lambda_c(\infty)$ versus system size N for various degree exponents λ . Red dotted lines denote $\lambda < \lambda_c = 2.5$; black solid lines denote $\lambda = \lambda_c$; and blue dashed lines do $\lambda > \lambda_c$.

λ	η_c	ρ_c	β	γ_1	$1/\bar{\nu}$
$\lambda < \lambda_c$	0	0	$\frac{1}{1-(d-1)(\lambda-2)}$	0	$\frac{1-(d-1)(\lambda-2)}{\lambda-1}$
$\lambda = \lambda_c$	finite	0	$\frac{d-1}{d-2}$	0	$\frac{d-2}{(d-1)^2(\lambda-1)}$
$\lambda > \lambda_c$	finite	finite	$\frac{1}{2}$	$\frac{1}{2}$	$\frac{\lambda-2}{\lambda-1}$

Table 2.1: Analytic solutions of the critical exponents for the s -SIS model.

2.6 Numerical simulations

2.6.1 Numerical methods

We perform numerical simulations using the sequential updating algorithm. The s -SIS model is simulated on an SF uniform hypergraph with N nodes. Initially, all the nodes are assigned to fully infected states. At each time step t , the following processes are applied:

- i) With probability $\kappa \equiv \eta/(1 + \eta)$, we attempt the contagion process. We select a random hyperedge, and if the hyperedge satisfies the contagion condition, i.e., if all but one node of the hyperedge is in the infected state, the susceptible node in the hyperedge enters the infected state.

- ii) With the remaining probability $1 - \kappa = 1/(1 + \eta)$, by contrast, we attempt the recovery process. A node is chosen at random, and if the chosen node is in the infected state, we change it to the susceptible state.
- iii) If the number of active sites is zero, the simulation ends. Otherwise, the time t is updated as $t \rightarrow t + 1/N$ in each step. Hereafter, we use the rescaled control parameter κ instead of η .

A Markov process with an absorbing state in a finite-size system will ultimately reach the absorbing state. If the system has a nonzero probability of reaching the absorbing state after some time, the probability that the system remains active decreases exponentially and therefore converges to zero. To investigate the stationary state in a finite-size system in an absorbing state, samples surviving after a sufficiently long time are often taken as averages [226]. This method is not computationally efficient, because the samples that have reached the absorbing state cannot be used to calculate the statistical properties of the stationary state. An alternative method is the quasistationary method [90, 91]. In this method, if the system reaches an absorbing state, it reverts to an active configuration selected randomly from the history of the simulation. After a sufficiently long time, the system and the history simultaneously reach the stationary ensemble. In simulations, a list of 100 previously visited configurations, is tracked and updated at each time step.

We performed the simulations in *annealed hypergraphs*. An annealed hypergraph is a mean-field theoretical treatment of an ensemble of hypergraphs. We replaced the adjacency tensor with its ensemble average:

$$a_\alpha = \bar{a}_\alpha = f_{i_1 \dots i_d}. \quad (2.49)$$

The probability of a particular hyperedge $f_{i_1 \dots i_d}$ in the static model of a uniform hypergraph was introduced in Sec. 2.2. For the probability of a hyperedge, we used $NK p_{i_1} \dots p_{i_d}$, which is a valid approximation, even in the thermodynamic limit, as

long as it is finite. This is a generalization of an annealed network. The annealed network, which was introduced as a randomly selected neighboring network [47], has been widely used to study dynamical processes because heterogeneous mean-field theory and other mean-field theoretical approaches are exact in annealed networks [91, 202, 262, 335].

2.6.2 Numerical results

Static exponents

From Sec. 2.5, the order parameter behaves as

$$\rho(\kappa) = \begin{cases} 0 & \text{for } \kappa < \kappa_c, \\ \rho_c + r(\kappa - \kappa_c)^\beta & \text{for } \kappa \geq \kappa_c, \end{cases} \quad (2.50)$$

where ρ_c is zero (finite) for $\lambda \leq \lambda_c$ ($> \lambda_c$) and κ_c is zero (finite) for $\lambda < \lambda_c$ ($\geq \lambda_c$) in the thermodynamic limit. Moreover, two types of susceptibilities are defined as follows: $\chi_1 \equiv \partial\rho/\partial h \sim (\kappa - \kappa_c)^{-\gamma_1}$ and $\chi_2 = N(\langle\rho^2\rangle - \langle\rho\rangle^2)/\langle\rho\rangle \sim (\kappa - \kappa_c)^{-\gamma_2}$. The correlation size exponent $\bar{\nu}$ is defined as $\kappa_c(N) - \kappa_c(\infty) \sim N^{-1/\bar{\nu}}$.

We performed simulations on a hypergraph with $d = 3$ and the characteristic degree $\lambda_c = 2.5$. Because the simulation results should be sensitive near λ_c , we chose $\lambda \in \{2.1, 2.9, 3.5\}$. We note that for the static model, a degree-degree correlation exists for $2 < \lambda < 3$. Thus, the exponent $\bar{\nu}$ is expected to be different for $\lambda = 2.9$ and 3.5 , whereas the other critical exponents, β and γ , would be similar. Using finite-size scaling (FSS) analysis, we obtain the following:

i) For $\lambda = 2.1 < \lambda_c$, we plot $\rho N^{\beta/\bar{\nu}}$ versus $\kappa N^{1/\bar{\nu}}$ for different system sizes but a fixed $d = 3$ in Fig. 5.6(a). We find that the data points for different system sizes collapse onto a single curve for $\beta = 1.25 \pm 0.02$ and $\bar{\nu} = 1.59 \pm 0.01$. β corresponds to the analytical result of Eq. (2.23), but $\bar{\nu}$ is different with the analytical

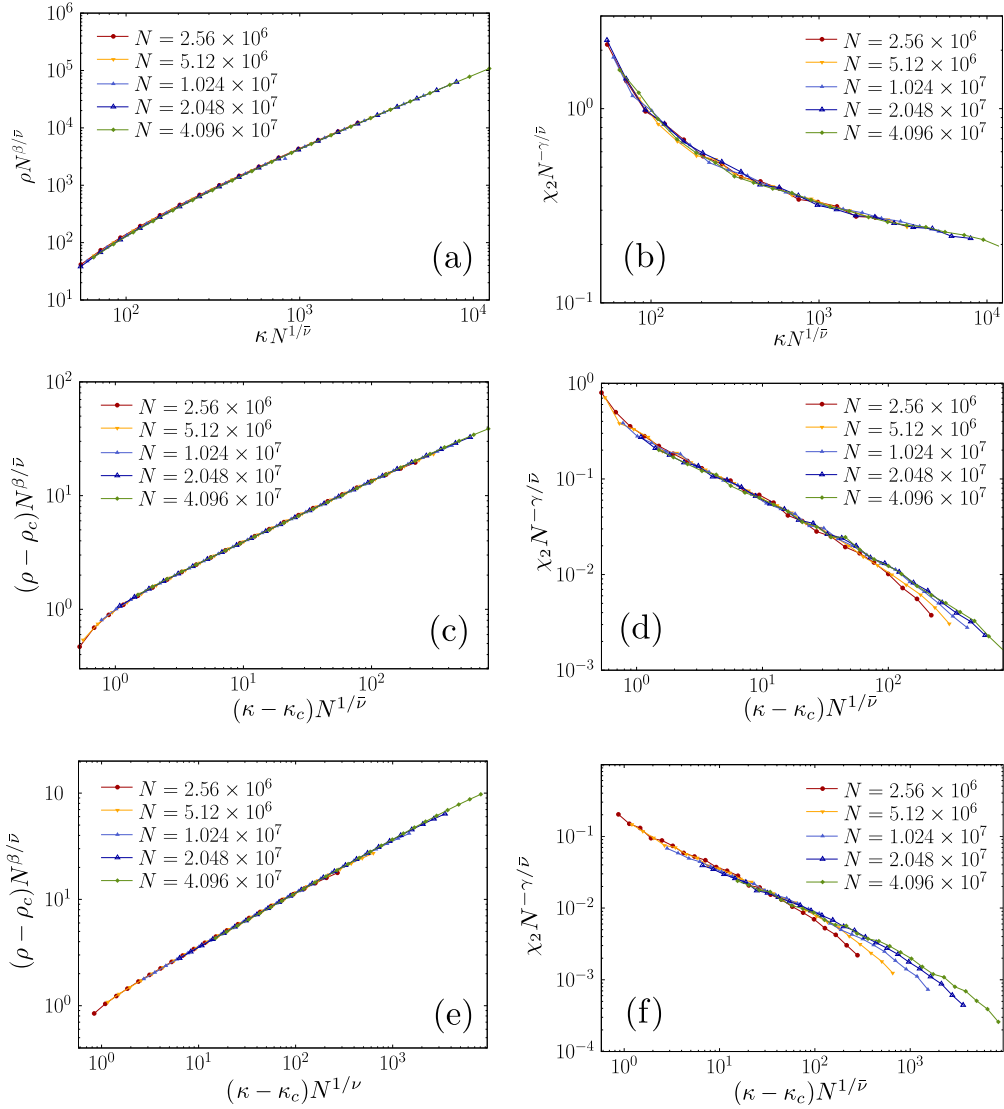


Figure 2.6: Finite-size scaling analysis of the s -SIS model on SF 3-uniform hypergraphs with three degree exponents: $\lambda = 2.1 < \lambda_c$ (a) and (b), $\lambda = 2.9 > \lambda_c$ (c) and (d), and $\lambda = 3.5 > \lambda_c$ (e) and (f). Scaling plots of $(\rho - \rho_c)N^{\beta/\bar{\nu}}$ versus $(\kappa - \kappa_c)N^{1/\bar{\nu}}$ are drawn, with (a) $\beta = 1.25$ and $\bar{\nu} = 1.59$, (c) $\beta = 0.52$ and $\bar{\nu} = 2.11$, and (e) $\beta = 0.5$ and $\bar{\nu} = 1.63$. Scaling plots of $\chi_2 N^{-\gamma/\bar{\nu}}$ versus $(\kappa - \kappa_c)N^{1/\bar{\nu}}$ are drawn, with (b) $\gamma_2 = 0.15$ and $\bar{\nu} = 1.59$, (d) $\gamma_2 = 0.62$ and $\bar{\nu} = 2.11$, and (f) $\gamma_2 = 0.62$ and $\bar{\nu} = 1.63$.

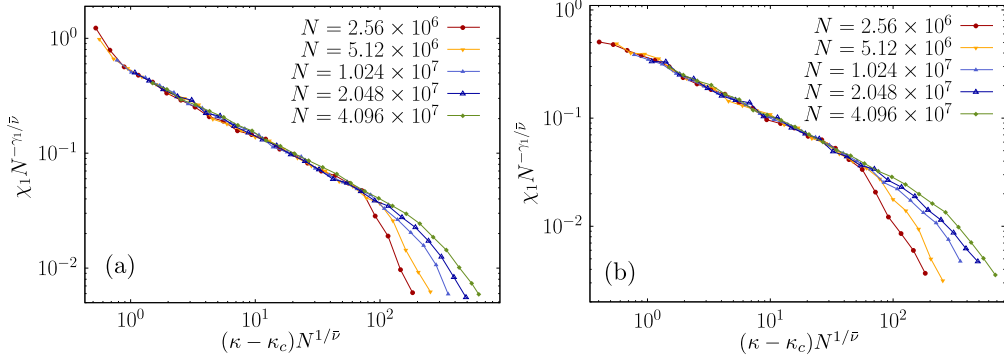


Figure 2.7: Scaling plots of $\chi_1 N^{-\gamma_1/\bar{\nu}}$ versus $(\kappa - \kappa_c) N^{1/\bar{\nu}}$ with degree exponents (a) $\lambda = 2.9$ and (b) $\lambda = 3.5$, with (a) $\gamma_1 = 0.48$ and $\bar{\nu} = 2.11$, (b) $\gamma_1 = 0.50$ and $\bar{\nu} = 1.63$.

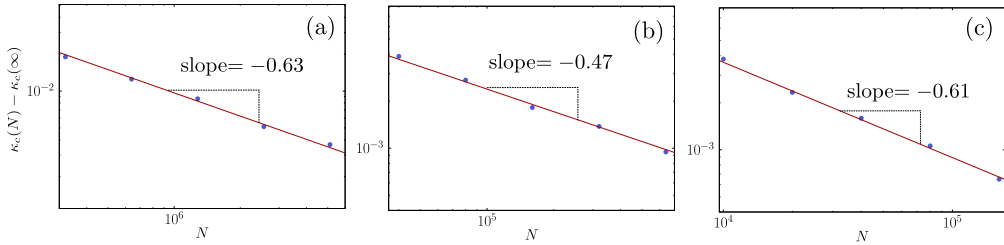


Figure 2.8: Plots of $\kappa_c(N) - \kappa_c(\infty)$ versus N on double-logarithmic scale for (a) $\lambda = 2.1$, (b) $\lambda = 2.9$, and (c) $\lambda = 3.5$. Slope of each plot represents $-1/\bar{\nu}$.

result of Eq. (2.44). This discrepancy will be discussed in Sec. 3.4. For $\chi_2(\kappa)$, we plot $\chi_2 N^{-\gamma_2/\bar{\nu}}$ versus $(\kappa - \kappa_c) N^{1/\bar{\nu}}$ for $\gamma_2 = 0.15 \pm 0.01$ and $\bar{\nu} = 1.59$ in Fig. 5.6(b). Data points for systems of different sizes collapse well onto a single curve.

ii) For $\lambda = 2.9 > \lambda_c$, the transition point κ_c and ρ_c are numerically estimated to be ≈ 0.49462 and ≈ 0.53877 , respectively, by solving the self-consistency equation [Eq. (2.15)] and using Eq. (2.19). On the basis of these values, we plot $(\rho - \rho_c) N^{\beta/\bar{\nu}}$ versus $(\kappa - \kappa_c) N^{1/\bar{\nu}}$ for $\beta = 0.52 \pm 0.02$ and $\bar{\nu} \approx 2.11 \pm 0.01$ for different system sizes N in Fig. 5.6(c). Thus, we confirm that the numerically estimated values are marginally consistent with the theoretical values from Eqs. (2.29) and (2.48). In Fig. 5.6(d), we plot the rescaled quantity $\chi_2 N^{-\gamma_2/\bar{\nu}}$ versus $(\kappa - \kappa_c) N^{1/\bar{\nu}}$ for different system sizes. We estimated $\gamma_2 = 0.62 \pm 0.01$ and $\bar{\nu} = 2.11$ using FSS analysis. Using the plot of $\chi_1 N^{-\gamma_1/\bar{\nu}}$ versus $(\kappa - \kappa_c) N^{1/\bar{\nu}}$ for different system sizes in Fig. 5.7, we estimated $\gamma_1 = 0.48 \pm 0.02$.

iii) For $\lambda = 3.5$, we plot $(\rho - \rho_c) N^{\beta/\bar{\nu}}$ versus $(\kappa - \kappa_c) N^{1/\bar{\nu}}$ for different system sizes N for $\beta = 0.50 \pm 0.01$ and $\bar{\nu} = 1.63 \pm 0.01$ in Fig. 5.6(e). For $\chi_2(\kappa)$, we plot $\chi_2 N^{-\gamma_2/\bar{\nu}}$ versus $(\kappa - \kappa_c) N^{1/\bar{\nu}}$ for $\gamma_2 = 0.62 \pm 0.01$ and $\bar{\nu} = 1.63$. The data collapse well onto a single curve, as shown in Fig. 5.6(f). We plot $\chi_1 N^{-\gamma_1/\bar{\nu}}$ versus $(\kappa - \kappa_c) N^{1/\bar{\nu}}$ in Fig. 5.7. We estimated $\gamma_1 = 0.50 \pm 0.02$. The obtained values, $\beta = 0.5 \pm 0.01$, $\gamma_2 = 0.62 \pm 0.01$, and $\bar{\nu} = 1.63 \pm 0.01$, marginally satisfy the hyperscaling relation $\bar{\nu} = 2\beta + \gamma_2$.

The correlation size exponent is measured directly as $\kappa_c(N) - \kappa_c(\infty) \sim N^{-1/\bar{\nu}}$ with $1/\bar{\nu} = 0.63, 0.47, \text{ and } 0.61$ in Fig. 5.8, which correspond to $\bar{\nu} \simeq 1.59, 2.13, \text{ and } 1.64$ for $\lambda = 2.1, 2.9, \text{ and } 3.5$, respectively. These values are in reasonably good agreement with the values $\bar{\nu} = 1.59 \pm 0.01, 2.11 \pm 0.01, \text{ and } 1.63 \pm 0.01$ obtained by FSS analysis in Fig. 5.6. We summarize the numerical values in Table 2.2.

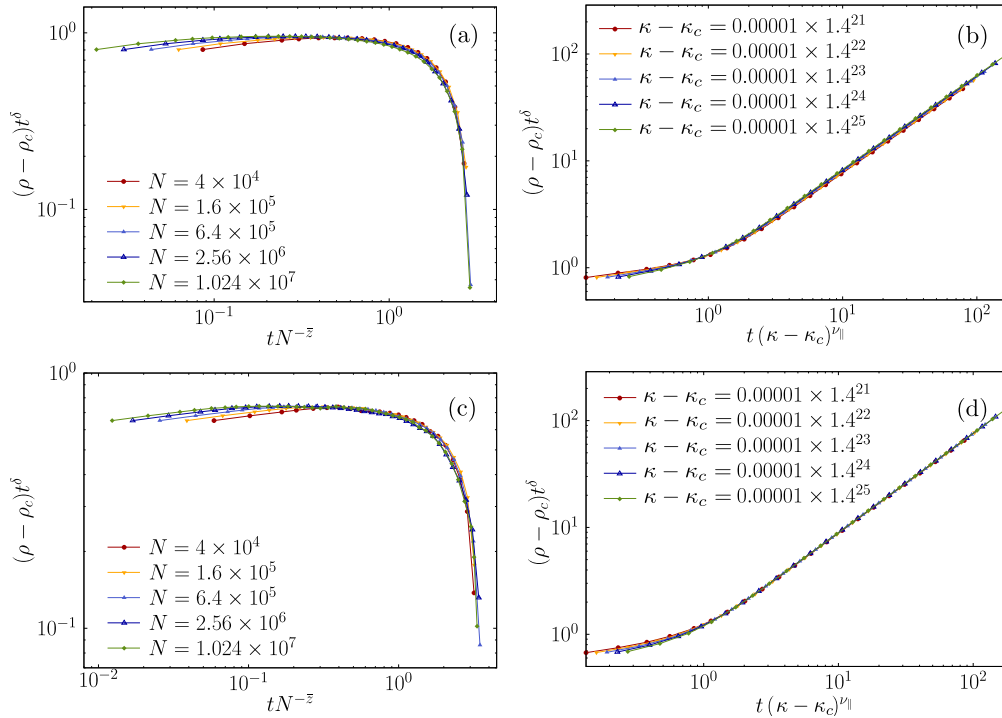


Figure 2.9: Scaling plots of the density of infection $\rho(t)$ starting from the fully infected state versus $tN^{-\bar{z}}$ (a) and (c) and $t(\kappa - \kappa_c)^{\nu_{||}}$ (b) and (d) for $\lambda = 2.9$ (a) and (b) and $\lambda = 3.5$ (c) and (d). The dynamical critical exponents $\delta = 0.89$, $\bar{z} = 0.26$, and $\nu_{||} = 0.56$ are obtained from (a) and (b), and $\delta = 0.86$, $\bar{z} = 0.32$, and $\nu_{||} = 0.53$ are obtained from (c) and (d).

λ	κ_c	ρ_c	β	γ_1	γ_2	$\bar{\nu}$
2.1	0	0	1.25 ± 0.02 (1.25)	0 (0)	0.15 ± 0.01	1.59 ± 0.01 (1.35)
2.9	0.49462	0.268306	0.52 ± 0.02 (0.50)	0.48 ± 0.02 (0.50)	0.62 ± 0.01	2.11 ± 0.01 (2.11)
3.5	0.53877	0.395602	0.50 ± 0.01 (0.50)	0.50 ± 0.02 (0.50)	0.62 ± 0.01	1.63 ± 0.01 (1.67)

Table 2.2: Numerical list of critical exponents of the s -SIS model obtained by the FSS method. Theoretical values calculated in Sec. 2.5 are presented in parentheses.

Dynamic exponents

Next, we also performed dynamical FSS analysis to obtain the dynamic exponents. We consider the temporal dynamics of the density of infection starting from a fully infected state. The average density of infection at time t over many realizations, $\rho(t)$, shows critical behavior when the contagion rate is equal to the critical value κ_c . We choose $\lambda \in \{2.9, 3.5\}$ because for $\lambda < \lambda_c$, the critical point κ_c becomes zero, and only a decay process remains. In this section, we change the notation of $\bar{\nu}$ to $\bar{\nu}_\perp$ as a counterpart of the mean survival time exponent ν_\parallel .

i) For $\lambda = 2.9$, we plot $(\rho - \rho_c)t^\delta$ versus $tN^{-\bar{z}}$ for different system sizes N in Fig. 2.9(a). Here, the dynamical critical exponents are defined conventionally as $\delta = \beta/\nu_\parallel$ and $\bar{z} \equiv \nu_\parallel/\bar{\nu} = \nu_\parallel/d\nu_\perp$. In Fig. 2.9(b), we plot the rescaled quantity $(\rho - \rho_c)t^\delta$ versus $t(\kappa - \kappa_c)N^{\nu_\parallel}$. ν_\parallel is the mean survival time exponent associated with the relaxation time. We estimated the dynamical critical exponents as $\delta = 0.89 \pm 0.02$, $\bar{z} = 0.26 \pm 0.01$, and $\nu_\parallel = 0.56 \pm 0.01$.

ii) For $\lambda = 3.5$, we used a method similar to that used in i). We estimated the dynamical critical exponents as $\delta = 0.93 \pm 0.02$, $\bar{z} = 0.32 \pm 0.01$, and $\nu_\parallel = 0.53 \pm 0.01$.

The critical exponents $\{\delta, \bar{z}, \nu_\parallel\}$ obtained using dynamical FSS and the $\{\beta, \bar{\nu}, \gamma_2\}$ values obtained using steady-state FSS are comparable.

λ	δ	\bar{z}	ν_{\parallel}
2.9	0.89 ± 0.02	0.26 ± 0.01	0.56 ± 0.01
3.5	0.93 ± 0.02	0.32 ± 0.01	0.53 ± 0.01

Table 2.3: Dynamic critical exponents of s -SIS model obtained using the dynamical FSS method.

2.7 Degree distribution of static model

Throughout this construction algorithm, a node is selected with probability $1 - (1 - p_i)^d \simeq dp_i$. Therefore, the probability that a node i has degree k follows the Poisson distribution: $P_i^{(R)}(k) = \langle k_i \rangle^k \exp(-\langle k_i \rangle) / k!$. The degree distribution is then

$$P^{(R)}(k) = \frac{1}{N} \sum P_i(k) \simeq \int_{k_{\min}}^{k_{\max}} d\langle k_i \rangle P(\langle k_i \rangle) \frac{\langle k_i \rangle^k \exp(-\langle k_i \rangle)}{k!} \quad (2.51)$$

$$= \frac{(\lambda-1)}{\langle k_i \rangle_{\min}^{-\lambda+1} - \langle k_i \rangle_{\max}^{-\lambda+1}} \frac{1}{k!} \int_{\langle k_i \rangle_{\min}}^{\langle k_i \rangle_{\max}} d\langle k_i \rangle \langle k_i \rangle^{-\lambda+k} \exp(-\langle k_i \rangle). \quad (2.52)$$

In the thermodynamic limit, $\langle k_i \rangle_{\max} \rightarrow \infty$ and $\langle k_i \rangle_{\min} \rightarrow \frac{\lambda-2}{\lambda-1} \langle k \rangle$. Further,

$$\lim_{N \rightarrow \infty} P^{(R)}(k) = (\lambda-1) k_m^{\lambda-1} \frac{\Gamma(-\lambda+k+1, k_m)}{\Gamma(k+1)} \sim k^{-\lambda} \quad (2.53)$$

for sufficiently large k . Therefore, the tail of the degree distribution of a static model of a uniform hypergraph follows a power law.

2.8 Asymptotic behavior of $G'(\Theta)$

Using the identity

$$\begin{aligned} {}_2F_1(a, b; c; -z) &= \frac{z^{-a} \Gamma(c) \Gamma(b-a) {}_2F_1(a, a-c+1; a-b+1; -\frac{1}{z})}{\Gamma(b) \Gamma(c-a)} \\ &+ \frac{z^{-b} \Gamma(c) \Gamma(a-b) {}_2F_1(b, b-c+1; -a+b+1; -\frac{1}{z})}{\Gamma(a) \Gamma(c-b)}, \end{aligned} \quad (2.54)$$

we can obtain the asymptotic behavior of the hypergeometric function ${}_2F_1(a, b; c; -z)$ as $z \rightarrow \infty$:

$${}_2F_1(a, b; c; -z) \sim \begin{cases} \frac{\Gamma(c)\Gamma(b-a)}{\Gamma(b)\Gamma(c-a)} z^{-a} & a < b \\ \frac{\Gamma(c)\Gamma(a-b)}{\Gamma(a)\Gamma(c-b)} z^{-b} & a > b \end{cases}. \quad (2.55)$$

The formula also allows us to calculate the next dominant terms proportional to z^{-a-1} , z^{-a-2} , \dots and z^{-b-1} , z^{-b-2} , \dots . As $\Theta \rightarrow 0$,

$$G'(\Theta) \sim \begin{cases} \frac{\pi(d-1)(\lambda-2)^2}{\sin(\pi\lambda)} (k_m \lambda)^{\lambda-2} \Theta^{(d-1)\lambda-(d-1)-d-1} - 1 & \lambda < 3 \\ \frac{(d-1)(\lambda-2)}{(\lambda-3)} k_m \lambda \Theta^{d-2} - 1 & \lambda > 3 \end{cases}. \quad (2.56)$$

Then we obtain Eq. (2.18).

2.9 Susceptibility

To calculate Eq. (2.35), we first take the derivatives and then set $h = 0$ and $\Theta = \Theta_0$:

$$\begin{aligned} \left. \frac{\partial \rho}{\partial h} \right|_{\eta, \Theta} &= 1 - {}_2F_1\left(\lambda - 1, 1; \lambda; -\frac{1}{k_m \eta \Theta_0^{d-1}}\right) \\ &\quad - \frac{\lambda - 1}{\lambda} \frac{1}{k_m \eta \Theta_0^{d-1}} {}_2F_1\left(\lambda, 2; \lambda + 1; -\frac{1}{k_m \eta \Theta_0^{d-1}}\right), \end{aligned} \quad (2.57)$$

$$\left. \frac{\partial \rho}{\partial \Theta} \right|_{\eta, h} = \frac{(d-1)(\lambda-1)}{\lambda} \frac{1}{k_m \eta \Theta_0^d} {}_2F_1\left(\lambda, 2; \lambda + 1; -\frac{1}{k_m \eta \Theta_0^{d-1}}\right), \quad (2.58)$$

$$\begin{aligned} \left. \frac{\partial G}{\partial h} \right|_{\eta, \Theta} &= \frac{\lambda - 2}{\lambda - 1} \frac{1}{k_m \eta \Theta_0^{d-1}} \left[{}_2F_1\left(\lambda - 1, 1; \lambda; -\frac{1}{k_m \eta \Theta_0^{d-1}}\right) \right. \\ &\quad \left. - {}_2F_1\left(\lambda - 1, 2; \lambda; -\frac{1}{k_m \eta \Theta_0^{d-1}}\right) \right], \end{aligned} \quad (2.59)$$

$$\left. \frac{\partial G}{\partial \Theta} \right|_{\eta, h} = \frac{(d-1)(\lambda-2)}{\lambda-1} \frac{1}{k_m \eta \Theta_0^d} {}_2F_1\left(\lambda - 1, 2; \lambda; -\frac{1}{k_m \eta \Theta_0^{d-1}}\right) - 1. \quad (2.60)$$

Using Eq. (2.20), we obtain the following:

i) For $\lambda < \lambda_c$, Eq. (2.57) becomes 1, and all other terms vanish in the limit $\Theta_0 \rightarrow 0$

and $\eta \rightarrow 0$. Therefore, $\chi_1 = 1$ near the critical point, and the critical exponent of the susceptibility, γ_1 , is zero.

ii) For $\lambda = \lambda_c$, Eqs. (2.57)–(2.60) in the limit $\Theta_0 \rightarrow 0$ and $\eta \rightarrow \eta_c$ are given as

$$\left. \frac{\partial \rho}{\partial h} \right|_{\eta, \Theta_0} = 1, \quad \left. \frac{\partial \rho}{\partial \Theta} \right|_{\eta, h} \sim d(d-2) \frac{\eta - \eta_c}{\eta_c}, \quad (2.61)$$

$$\left. \frac{\partial G}{\partial h} \right|_{\eta, \Theta_0} \sim 1, \quad \left. \frac{\partial G}{\partial \Theta} \right|_{\eta, h} \sim -\frac{d-2}{d-1} \frac{\eta - \eta_c}{\eta_c}. \quad (2.62)$$

The susceptibility is given by $\chi_1 \sim 1 + d(d-1)$.

iii) For $\lambda > \lambda_c$, Eq. (2.60) exhibits singular behavior, and Eqs. (2.57)–(2.59) are finite. Hence, the susceptibility diverges near the critical point. Eq. (2.60) is calculated as

$$\frac{\partial G}{\partial \Theta} \sim \frac{\partial^2 G}{\partial \Theta^2} (\Delta \Theta_0). \quad (2.63)$$

Inserting Eq. (2.28) into Eq. (2.63) yields $\chi_1 \sim (\eta - \eta_c)^{-1/2}$, and therefore $\gamma_1 = 1/2$.

2.10 Containment strategy for simplicial SIS model

In the past two decades, extensive research has been devoted to spreading processes in complex networks [80, 81, 177, 244, 360] to model the spread of epidemic diseases [263] and innovations [164, 282], opinion formation [3, 50, 113, 342], and many other physical and social phenomena [27, 132, 142, 247, 329]. Researchers now have access to large-scale datasets of interactions, such as mobility, collaborations, and temporal contacts that were unavailable in the past [95, 153, 205], and complex network representations of interactions enable the researchers to effectively study various dynamical processes. The large body of research devoted to spreading processes on complex networks provided quantitative analysis for policy-making especially in the public-health domain. Furthermore, the epidemic processes provide deeper understanding of critical phenomena and phase transition behaviors, such as the effect of structural heterogene-

ity on the transition point [236, 267] and discontinuous phase transitions induced by cascade dynamics [11, 59, 192].

A hypergraph is a generalization of network that can describe higher-order interactions between more than two agents, which widely appear in both natural and social systems, that networks cannot [16, 24, 129, 187]. A hypergraph consists of nodes and hyperedges, and a hyperedge of size d connects d nodes simultaneously. The hyperedges of a hypergraph can have various sizes, but if all the hyperedges in a hypergraph have the same size d , it is called a d -uniform hypergraph. In a collaboration hypergraph [21, 269], for instance, a hyperedge of size d encodes a d -author paper, and the nodes of the hyperedge encodes the authors of the paper. Hypergraphs have been used to describe neural and biological interactions [179, 275], evolutionary dynamics [7, 35], and other dynamical processes [38, 89, 204, 315]. Recently, the simplicial susceptible-infected-susceptible (s -SIS) model [137] was introduced to describe higher-order epidemic process in hypergraphs. The model has attracted extensive interest from the research community due to its simplicity and novel phase transition behavior [60, 149, 188, 232, 337].

An important topic in epidemiology is immunization, and it has been studied for various epidemic models in complex networks [52, 63, 68, 220, 227, 230, 268, 304, 326]. If a node in the network is immunized, the node cannot turn into the infected state, and if an edge is immunized, the infection does not spread through the immunized edge. Edge immunization models epidemic containment measures such as travel regulation and social distancing. If a node or edge is immunized, it does not only prevent nodes directly connected to them from being infected. If a portion of nodes or edges greater than a threshold p_c is immunized, the epidemic state in the network vanishes. This effect is called *herd immunity*, and the threshold is called the *herd immunity threshold* (HIT). The objective of an efficient immunization strategy is to achieve herd immunity by immunizing a minimal portion of nodes or edges, i.e. minimizing HIT p_c . Such strategies can be used to vaccinate people with limited resources or prevent a pandemic

by minimally regulating air traffic or social gatherings. The same theory can be used to promote spreading processes. If the spreading process models information flow, for instance, the objective is usually to optimize the spreading of information in a system. In such cases, we buttress the nodes or edges targeted by the efficient immunization strategies instead of immunizing them. Alternatively, in a reverse point of view, an adversarial attack can be made on such nodes/edges to hamper the information flow in the system. However, the efficient immunization strategy for epidemic processes in hypergraph has not been studied, despite the topic's importance in mathematical epidemiology.

Here, we propose an immunization strategy that targets hyperedges with high simultaneous infection probability (SIP), which is the probability that all the nodes in a hyperedge are in the infected state. This probability is calculated by the individual-based mean-field (IBMF) theory [110, 353]. This strategy can be implemented to contain epidemics of s -SIS model in general hypergraphs. We also show that immunizing hyperedges with the highest H-eigenscores, which is defined as the product of the elements of the H-eigenvector of the adjacency tensor with the largest H-eigenvalue of all the nodes in the hyperedge, effectively achieves herd immunity in uniform hypergraphs. This method generalizes the edge eigenscore in a complex network and can be implemented to contain epidemics in uniform hypergraphs. However, this method cannot be implemented in arbitrary hypergraphs with various hyperedge sizes. We also generalize the EI-based method [230], which is the state-of-the-art immunization strategy for complex networks. However, we find that this method does not perform as efficiently as H-eigenscore and SIP-based strategies for hypergraphs despite its higher computational cost. If a hyperedge has a high SIP, it suggests that the hyperedge is a 'hotspot' of the epidemic process. Therefore, SIP can be used as a centrality measure to quantify a hyperedge's influence on higher-order dynamics in general hypergraphs. The effectiveness of the immunization strategies suggests the necessity of quantitative and systematic policies for epidemic containment measures.

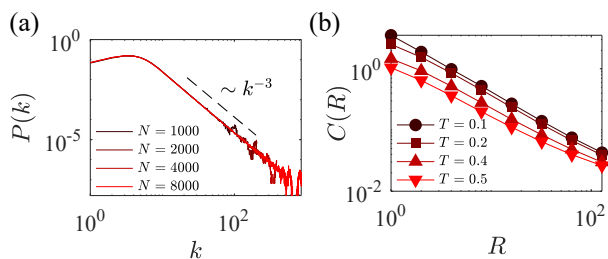


Figure 2.10: (a) The degree distribution of the 3-uniform hypergraph popularity-similarity optimization (h -PSO) model. The mean degree $\langle k \rangle = 6$, temperature $T = 0.5$, and the parameter $\gamma = 3$. The tail of the distribution follows a power law with an exponent of 3. (b) The clustering coefficient of 3-uniform h -PSO as a function of the scale parameter R . The number of nodes $N = 2000$, mean degree $\langle k \rangle = 6$, and the temperature $T = 0.5$.

2.10.1 Hypergraph popularity-similarity optimization (h -PSO) model

In addition to a highly heterogeneous degree distribution, agents in many real-world systems have a higher chance of being connected if they are similar. The similarity of two nodes is characterized by their closeness in their latent coordinates. The objective of graph node embedding algorithms [116, 259, 274] is to discover the latent coordinates of a network. For instance, hub airports are connected to a disproportionately large number of airports around the world (heterogeneous degree distribution), but two small airports can be connected by an airline if they are geographically close. Also, two researchers who are not particularly prolific can coauthor a paper if they are close. This effect is called *homophily* and results in non-vanishing clustering coefficients in both networks and hypergraphs. To account for such phenomena, a hypergraph model with a scale-free degree distribution and tunable non-vanishing clustering coefficient needs to be introduced. Furthermore, the immunization strategies need to be tested in clustered hypergraphs because it is known that epidemic dynamics and the performance of immunization strategies differ in clustered and unclustered networks [230].

The clustering coefficient $C(H)$ of a hypergraph H is defined as follows [84]:

$$C(H) = \frac{3 \times \text{number of hypertriangles}}{\text{number of undirected 2-paths}}, \quad (2.64)$$

where a hypertriangle is a set of three distinct nodes v_1, v_2, v_3 and three distinct hyperedges E_{12}, E_{23}, E_{31} that satisfies $v_1, v_2 \in E_{12}$, $v_2, v_3 \in E_{23}$, and $v_3, v_1 \in E_{31}$. A undirected 2-path is a set of three distinct nodes v_1, v_2, v_3 and two distinct hyperedges E_{12}, E_{23} that satisfies $v_1, v_2 \in E_{12}$ and $v_2, v_3 \in E_{23}$. The clustering coefficient can be greater than 1 in hypergraphs because a undirected 2-path can have multiple closures. If there are only size-2 hyperedges in the hypergraph (i.e., if the hypergraph is a network), C_2 becomes the transitivity coefficient [122], which is widely used in social network analysis. Note that there is another definition of the clustering coefficient $C_d^{(i)}$ that generalizes the local clustering coefficient of graphs [35].

To generate a scale-free hypergraph with a non-vanishing clustering coefficient, we introduce the hypergraph popularity-similarity optimization model (h -PSO), which is a hypergraph version of the popularity-similarity optimization (PSO) model in complex networks [258, 259]. The d -uniform h -PSO model is generated as follows:

- (i) Popularity parameter p_i is assigned to each node in the hypergraph. If a node has a high p_i , the node tends to have a high degree.
- (ii) Latent coordinate \mathbf{x}_i is assigned to each node in the hypergraph. If two nodes i and j are close in the latent coordinate (i.e., $|\mathbf{x}_j - \mathbf{x}_i|$ is small) two nodes will likely be connected by hyperedges.
- (iii) Pick a node i with probability p_i .
- (iv) Pick $d-1$ nodes j_1, \dots, j_{d-1} , each with probability $\left[1 + (|\mathbf{x}_{j_\ell} - \mathbf{x}_i|/Rp_i p_{j_\ell})^{1/T}\right]^{-1}$. If a hyperedge $\{i, j_1, \dots, j_{d-1}\}$ is not already present in the hypergraph, add it to the hypergraph.
- (v) Repeat steps (iii)–(iv) until the number of hyperedges reaches NK .

Here, we choose the latent coordinates on a ring; the latent coordinates are randomly chosen without replacement from $\theta \in \{1, 2, \dots, N\}$, and the distance between two nodes i and j is defined as $\min(|\theta_j - \theta_i|, N - |\theta_j - \theta_i|)$. If we set $p_i = Ni^{-\alpha}/\zeta_N(\alpha) \simeq (1 - \alpha)i^{-\alpha}/N^{-\alpha}$, the resulting hypergraph is a scale-free hypergraph with degree exponent $\gamma = 1 + 1/\alpha$. The clustering coefficient can be controlled by the scale parameter R and the temperature T ; if R and T are large, the clustering coefficient is small. The degree distribution and the clustering coefficient of the h -PSO model with hyperedge size 3 are illustrated in Fig. 2.10. The degree distribution has a power-law tail with exponent γ , and the clustering coefficient can be controlled by adjusting R .

2.10.2 Individual- and pair-based mean-field theories

In this section, we explain the individual-based mean-field (IBMF) theory and pair-based mean-field [230] (PBMF) theory for hypergraphs, which are used in immunization strategies. IBMF tracks the probability of infection p_i of each node in the network. By ignoring the statistical correlation of the probability between two nodes [$P(X_i, X_j) = P(X_i)P(X_j)$, where $X_i, X_j \in \{S, I\}$], the IBMF equation for the SIS model can be expressed as

$$p_i(t+1) = [1 - p_i(t)] \left[1 - \prod_{j \in \mathcal{N}(i)} (1 - \beta p_j(t)) \right] + (1 - \mu)p_i(t), \quad (2.65)$$

where $\mathcal{N}(i)$ is the set of nodes connected to node i (nearest-neighbors of i). For continuous phase transitions, where p_i vanishes in the vicinity of the phase transition, the equation can be linearized as $p_i(t+1) = \sum_j (\beta a_{ij} + (1 - \mu)\delta_{ij}) p_j$ and the epidemic threshold $\frac{\beta}{\mu}$ is the inverse of the largest eigenvalue of the adjacency matrix a_{ij} . Because IBMF ignores the positive correlations of the state (neighbors of infected node have greater chance of being in the infected state) in the actual system, it tends to overestimate the density of infection. The theory can be straightforwardly extended to the

s -SIS model:

$$p_i(t+1) = [1 - p_i(t)] \prod_{\{j_1, \dots, j_{d-1}\} \in \bar{\mathcal{N}}(i)} (1 - \beta_d p_{j_1}(t) \cdots p_{j_{d-1}}(t)) + (1 - \mu) p_i(t), \quad (2.66)$$

where $\bar{\mathcal{N}}(i)$ is the set of 'hyperneighbors' of i ; if a hyperedge $\{i, j_1, \dots, j_{d-1}\}$ is in the hypergraph, $\{j_1, \dots, j_{d-1}\} \in \bar{\mathcal{N}}(i)$. IBMF is often employed to describe the dynamics and phase transitions in classical stochastic processes [110, 353], as well as driven-dissipative quantum dynamics [271]. The method predicts the properties of the epidemic states more accurately than homogeneous mean-field theory or degree-based mean-field theory [267], which is often referred to as heterogeneous mean-field theory.

PBMF, often referred to as an epidemic-link equation, is known to predict the properties of the epidemic states more precisely than IBMF. In PBMF, we track the probability of the infection $p_i(t)$ of each node the same as for IBMF, and for pairs of nodes (i, j) that are connected in the network we set the differential equations for the probability that both of the nodes are infected as $\psi_{ij}(t) = P(X_i = I, X_j = I)$. Probabilities for other cases for a node pair $P(X_i = S, X_j = S)$, $P(X_i = S, X_j = I)$, and $P(X_i = I, X_j = S)$ can be expressed in terms of the p_i and ψ_{ij} :

$$P(X_i = S, X_j = S) = 1 - p_i(t) - p_j(t) + \psi_{ij}(t), \quad (2.67)$$

$$P(X_i = S, X_j = I) = p_j(t) - \psi_{ij}(t), \quad (2.68)$$

$$P(X_i = I, X_j = S) = p_i(t) - \psi_{ij}(t). \quad (2.69)$$

This method exploits the sparsity of the network (the number of variables and the equations in this method is proportional to the number of the nodes in the system); hence, it is scalable to large networks.

Then, the equations for the nodes are expressed as

$$p_i(t+1) = (1 - q_i(t))(1 - p_i(t)) + (1 - \mu)p_i(t), \quad (2.70)$$

and the equations for the pairs are expressed as

$$\begin{aligned} \psi_{ij}(t+1) &= (1 - q_{ij}(t))(1 - q_{ji}(t))(1 - p_i(t) - p_j(t) + \psi_{ij}(t)) \\ &+ (1 - (1 - \beta)q_{ij}(t))(1 - \mu)(p_j(t) - \psi_{ij}(t)) \\ &+ (1 - (1 - \beta)q_{ji}(t))(1 - \mu)(p_i(t) - \psi_{ij}(t)) + (1 - \mu)^2\psi_{ij}(t), \end{aligned} \quad (2.71)$$

where

$$q_i(t) = \prod_{j \in \mathcal{N}(i)} \left(1 - \beta \frac{p_j(t) - \psi_{ij}(t)}{1 - p_i(t)} \right), \quad (2.72)$$

$$q_{ij}(t) = \prod_{\substack{r \in \mathcal{N}(i) \\ r \neq j}} \left(1 - \beta \frac{p_r(t) - \psi_{ir}(t)}{1 - p_i(t)} \right). \quad (2.73)$$

$q_i(t)$ is the probability that node i is not infected during time step $t \rightarrow t + 1$ given that the node i is not infected at time t ; $q_{ij}(t)$ is the probability that the node i is not infected by a neighbor other than j during the time step $t \rightarrow t + 1$ given that the node i is not infected at time t .

Stationary states of the s -SIS model have been studied using both IBMF and PBMF in hypergraphs with hyperedges with sizes less than or equal to 3 [232]. Implementing the PBMF on general hypergraphs with arbitrary hyperedge sizes, the equations for the nodes are, again,

$$p_i(t+1) = (1 - q_i(t))(1 - p_i(t)) + (1 - \mu)p_i(t), \quad (2.74)$$

and the equations for the pairs that are connected by hyperedges are

$$\begin{aligned}
\psi_{ij}(t) &= (1 - q_{ij}(t)) (1 - q_{ji}(t)) (1 - p_i(t) - p_j(t) + \psi_{ij}(t)) \\
&+ (1 - q_{ij}(t)u_{ij}(t)) (1 - \mu) (p_j(t) - \psi_{ij}(t)) \\
&+ (1 - q_{ji}(t)u_{ji}(t)) (1 - \mu) (p_i(t) - \psi_{ij}(t)) + (1 - \mu)^2 \psi_{ij}(t), \quad (2.75)
\end{aligned}$$

where

$$\begin{aligned}
q_i(t) &= \prod_{\{r_1, \dots, r_{d-1}\} \in \bar{\mathcal{N}}(i)} \left(1 - \beta_d \frac{P_{ir_1 \dots r_{d-1}}^{SI \dots I}(t)}{P_i^S(t)} \right) \\
&= \prod_{\{r_1, \dots, r_{d-1}\} \in \bar{\mathcal{N}}(i)} \left(1 - \beta_d \frac{\prod_{\ell=1}^{d-1} (p_{r_\ell}(t) - \psi_{ir_\ell}(t)) \prod_{\ell \neq m} \psi_{r_\ell r_m}(t)}{(1 - p_i(t))^{d-1} \left(\prod_{\ell=1}^{d-1} p_{r_\ell}(t) \right)^{d-2}} \right), \quad (2.76)
\end{aligned}$$

$$\begin{aligned}
q_{ij}(t) &= \prod_{\substack{\{r_1, \dots, r_{d-1}\} \in \bar{\mathcal{N}}(i) \\ r_1, \dots, r_{d-1} \neq j}} \left(1 - \beta_d \frac{P_{ir_1 \dots r_{d-1}}^{SI \dots I}(t)}{P_i^S(t)} \right) \\
&= \prod_{\substack{\{r_1, \dots, r_{d-1}\} \in \bar{\mathcal{N}}(i) \\ r_1, \dots, r_{d-1} \neq j}} \left(1 - \beta_d \frac{\prod_{\ell=1}^{d-1} (p_{r_\ell}(t) - \psi_{ir_\ell}(t)) \prod_{\ell \neq m} \psi_{r_\ell r_m}(t)}{(1 - p_i(t))^{d-1} \left(\prod_{\ell=1}^{d-2} p_{r_\ell}(t) \right)^{d-2}} \right), \quad (2.77)
\end{aligned}$$

$$\begin{aligned}
u_{ij}(t) &= \prod_{\{j, r_1, \dots, r_{d-2}\} \in \bar{\mathcal{N}}(i)} \left(1 - \beta_d \frac{P_{ijr_1 \dots r_{d-2}}^{SI \dots I}(t)}{P_{ij}^{SI}(t)} \right) \\
&= \prod_{\{j, r_1, \dots, r_{d-2}\} \in \bar{\mathcal{N}}(i)} \left(1 - \beta_d \frac{\prod_{\ell=1}^{d-2} (p_{r_\ell}(t) - \psi_{ir_\ell}(t)) \prod_{\ell=1}^{d-2} \psi_{jr_\ell}(t) \prod_{\ell \neq m} \psi_{r_\ell r_m}(t)}{(1 - p_j(t))^{d-1} p_j(t)^{d-2} \left(\prod_{\ell=1}^{d-2} p_{r_\ell}(t) \right)^{d-2}} \right), \quad (2.78)
\end{aligned}$$

where $P_{r_1 \dots r_d}^{X_1 \dots X_d}$ is the probability that nodes $r_1 \dots r_d$ are each in state $X_1 \dots X_d$. $q_i(t)$

represents the same probability in the network PBMF, $q_{ij}(t)$ is the probability that the node i is not infected by hyperedges that do not contain node j during time step $t \rightarrow t + 1$ given that node i is not infected at time t , and $u_{ij}(t)$ is the probability that node i is not infected by hyperedges that contain node j during time step $t \rightarrow t + 1$ given that node i is not infected at time t . We have used the following equation for closure:

$$P_{r_1 \dots r_d}^{X_1 \dots X_d} = \frac{\prod_{\ell \neq m} P(X_{r_\ell}, X_{r_m})}{\left(\prod_{\ell=1}^d P(X_{r_\ell})\right)^{d-2}}. \quad (2.79)$$

For $d \leq 3$, we recover the identity in Ref. [232].

2.10.3 Immunization strategies

An immunization strategy is defined as a specific rule that determines a set of nodes or edges that will be immunized to eliminate the epidemic from the network. Immunized nodes cannot be infected and the infection cannot spread along the immunized edges. The immunization of nodes/edges does not only protect the nodes directly connected to them. When a sufficiently large fraction $p > p_c$ of the nodes/edges are immune, the system cannot maintain the epidemic state with a non-vanishing density of infection. This effect is called *herd immunity*. The objective of an immunization strategy is to find an algorithm that minimizes p_c . Efficient immunization strategy that can be implemented in complex network has been extensively studied for both SIS [227, 230, 268, 326] and SIR [52, 63, 220] model. However, efficient immunization strategy for epidemics in hypergraphs has not been studied, despite the importance of the subject. Here, we develop a simultaneous infection probability (SIP)-based immunization strategy that can be used to efficiently eliminate epidemic states by immunizing edges in networks or hyperedges in hypergraphs. The strategy immunizes the edges or hyperedges in the descending order of the SIP, which is the probability that all the nodes in the edge/hyperedge are infected at the same time. The probability

is calculated by IBMF in both networks and hypergraphs. In networks, the strategy is as efficient as the EI-based strategy [230], which is the state-of-the-art immunization strategy, while incurring a lower computational cost. This method can be implemented in general nonuniform hypergraphs. We compare the efficiency of the strategy with several other methods in networks, uniform hypergraphs, and nonuniform hypergraphs. However, only the proposed SIP-based strategy can be efficiently implemented in general nonuniform hypergraphs.

The EI of an edge is defined as $I_{ij} = g_{ij} + g_{ji}$, where

$$g_{ij} = \beta P(X_i = S, X_j = I) \sum_{r \in \mathcal{N}(i)} \beta P(X_r = S | X_i = I). \quad (2.80)$$

The probabilities are calculated by means of PBMF; $\beta P(X_i = S, X_j = I)$ is the probability that the infection spreads from j to i along the edge (i, j) , and $\sum_{r \in \mathcal{N}(i)} \beta P(X_r = S | X_i = I)$ quantifies the impact of such an event. For the s -SIS model in hypergraphs, the epidemic importance is expressed as

$$I_{\{i_1, \dots, i_d\}} = \sum_{\sigma \in S(\{i_1, \dots, i_d\})} g_{\sigma}, \quad (2.81)$$

where $S(\{i_1, \dots, i_d\})$ is the set of all the permutations of the set $\{i_1, \dots, i_d\}$, and

$$\begin{aligned} g_{i_1 \dots i_d} &= \beta_d P(X_{i_1} = S, X_{i_2} \dots X_{i_d} = I) \\ &\sum_{\{j_1 \dots j_{d-1}\} \in \mathcal{N}(i_1)} \beta^{d'} \sum_{\ell=1}^{d'-1} P(X_{j_1} = I, \dots, X_{j_{\ell-1}} = I, X_{j_{\ell}} = S, X_{j_{\ell+1}} = I, \\ &\dots, X_{j_{d'-1}} = I | X_{i_1} = I). \end{aligned} \quad (2.82)$$

It was shown that immunizing edges with high EI efficiently eliminates epidemic states in various synthetic and empirical networks. Because we use PBMF, as the size of hyperedge d increases, the number of pairs whose probability should be tracked by

ψ_{ij} rapidly increases, and the computational cost of the method diverges.

The eigenscore [326], which is widely used as a centrality measure, of a node i is the element of the largest eigenvector e_i of the adjacency matrix, and the eigenscore of an edge (i, j) is the product of the eigenscores of the two nodes of the edge $e_i e_j$. By immunizing the edges with the highest eigenscore, the spectral radius of the network is effectively reduced, and the epidemics in the network can efficiently be contained. The eigenscore-based strategy can be generalized for implementation in hypergraphs; however, there are multiple types of eigenvectors and eigenvalues in a uniform hypergraph. We find that the H-eigenvector is more suitable than the Z-eigenvector [211, 278] for s -SIS dynamics. The H-eigenvector e_i of a d -uniform hypergraph is defined as a vector that satisfies

$$\left(\mathbf{a}\mathbf{e}^{d-1}\right)_{i_1} \sum_{i_2, \dots, i_d=1}^n a_{i_1 i_2 \dots i_d} e_{i_2} \cdots e_{i_d} = \lambda e_{i_1}^{d-1}, \quad (2.83)$$

where \mathbf{a} is the hypergraph adjacency tensor. We define the H-eigenscore of the hyperedge $\{i_1, \dots, i_d\}$ as the product of the elements of the H-eigenvector with the largest H-eigenvalue: $e_{i_1} \cdots e_{i_d}$. For networks where $d = 2$, the H-eigenscore becomes the traditional eigenscore. Because the adjacency tensor is symmetric and hence diagonalizable [67], the H-eigenvector with the largest H-eigenvalue can be computed by an iterative power method:

$$\tilde{e}_{i_1}^{(m+1)} = \left(\sum_{i_2, \dots, i_d=1}^n a_{i_1 i_2 \dots i_d} e_{i_2}^{(m)} \cdots e_{i_d}^{(m)} \right)^{\frac{1}{d-1}}, \quad (2.84)$$

$$e_i^{(m+1)} = \frac{\tilde{e}_i^{(m+1)}}{\sqrt{\sum_{j=1}^n |\tilde{e}_j^{(m+1)}|^2}}. \quad (2.85)$$

Then, $\mathbf{e}^{(m)}$ converges to the H-eigenvector with the largest H-eigenvalue as $m \rightarrow \infty$. We show that removing high H-eigenscore hyperedges leads to effective epidemic containment in uniform hypergraphs. However, for nonuniform hypergraphs, the adjacency tensor is not defined, and the method cannot be implemented in general nonuni-

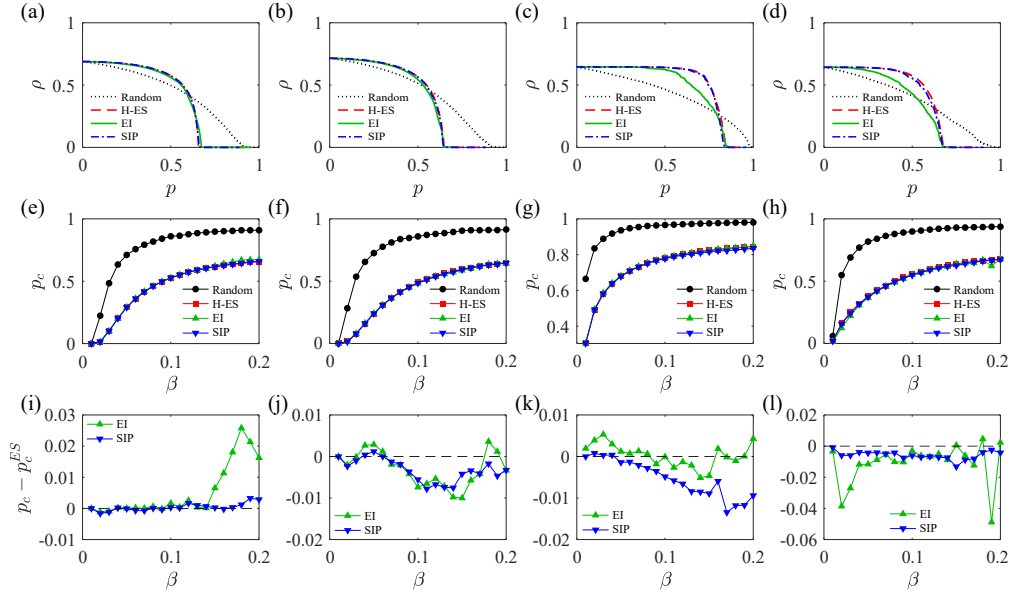


Figure 2.11: Random edge immunization (Random), H-eigenscore (H-ES), EI, and SIP-based strategies tested in various synthetic and empirical networks: (a, e, i) the static model, (b, f, j) clustered power-law network, (c, g, k) an airline network, and (d, h, l) the general relativity collaboration network. Because this is a network (i.e. hypergraph with only size-two hyperedges) the H-eigenscore is identical to the usual eigenscore. (a, b, c, d) The density of infection ρ versus the removed portion of the edges p . The recovery rate $\mu = 0.2$ and the contagion rate $\beta = 0.2$. Efficient immunization strategies usually result in a higher density of infection compared to random immunization for small p but eliminate epidemics with smaller p_c . (e, f, g, h) HIT p_c , which is the minimally required portion of edges to eliminate the epidemics. The efficient strategies (i.e. H-eigenscore, EI, and SIP-based strategies) exhibit marginal differences in their HITs. To compare the HITs of efficient strategies more thoroughly, we plot the differences between the p_c s of EI and SIP-based strategies from the p_c of the H-eigenscore-based strategy in (i, j, k, l). The SIP-based strategy is often more efficient than EI-based strategy, despite its lower computational cost.

form hypergraphs.

We introduce SIP as a measure of a hyperedge’s contribution to the continuation of epidemics in the hypergraph. The SIP of a size- d hyperedge $\{r_1, \dots, r_d\}$ is the probability that all nodes in the hyperedge are infected, which is calculated by the IBMF

$$P_{r_1 \dots r_d}^{I \dots I} \simeq P_{r_1}^I \dots P_{r_d}^I. \quad (2.86)$$

Each infection probability $P_{r_\ell}^I$ can be numerically calculated by solving Eq. (2.65) for its fixed point. Because this method uses IBMF, it incurs less computational cost than the EI-based strategy. This measure can be calculated in arbitrary nonuniform hypergraphs whose hyperedges have various sizes. We test the strategies in Sec. 5.6.3.

Other centrality measures have been tested for immunization strategies; however, they were found to be inefficient. Immunizing high edge-betweenness edges is ineffective, sometimes less efficient than randomly immunizing edges [230]. The node-infectivity-based method has been tested as well, but it is not as efficient as the eigen-score or EI-based methods.

2.10.4 Numerical Results

To test the immunization strategies, we implement the quasistationary method [90,91], which is a standard simulation method used to study stationary states of stochastic processes with absorbing states. An absorbing state has zero probability of transitioning to other states. In this case, because both the contagion and recovery process involves an infected node, if all the nodes are in the susceptible state, it cannot turn into any other state: it is the absorbing state of the s -SIS model. The quasistationary method constrains the system in the active states. We keep track of a set of configurations of the system, which is referred to as the *history*. With a certain probability, we replace one of the configurations in the history, randomly selected at each time step with the current state of the system. When the absorbing state is reached, the state of the system is replaced by a configuration randomly selected from the history. Here, we track 50

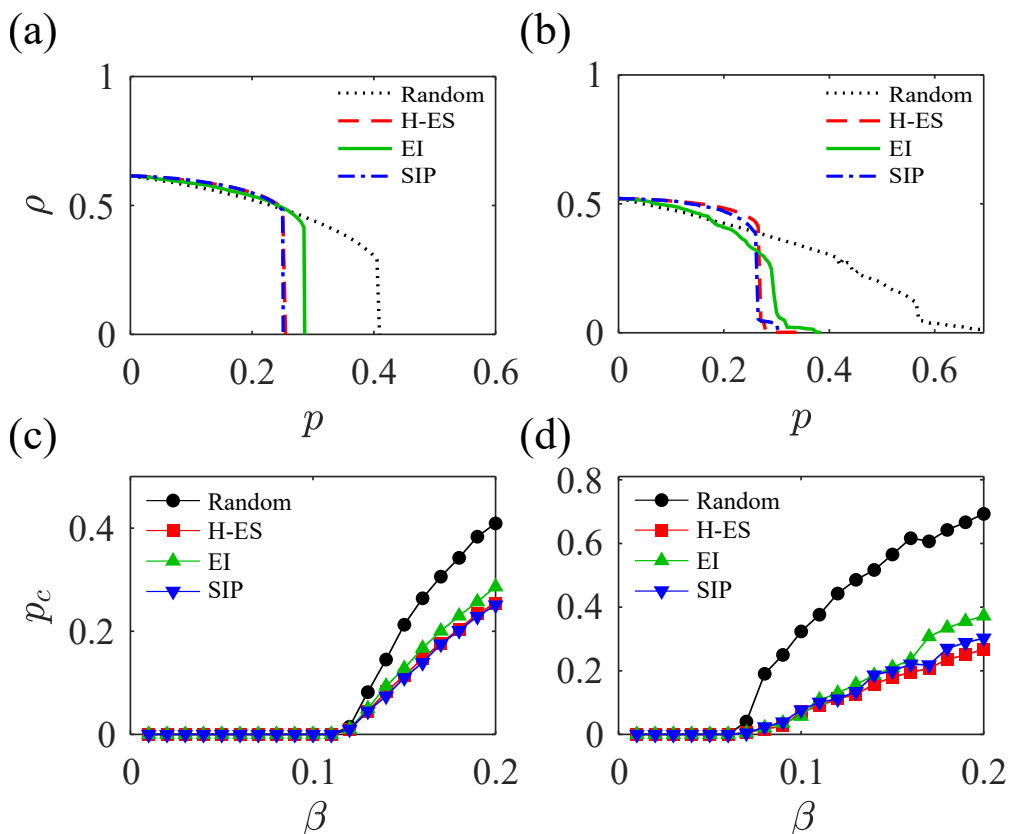


Figure 2.12: Random hyperedge immunization (Random), H-eigenscore (H-ES), EI, and SIP-based strategies tested in 3-uniform hypergraphs: (a, c) the hypergraph static model and (b, d) the hypergraph popularity-similarity optimization (h -PSO) model. (a, b) The density of infection ρ versus the removed portion of the edges p . The recovery rate $\mu = 0.2$ and the contagion rate $\beta = \beta_3 = 0.2$. The efficient strategies generally exhibit a higher density of infection for small p , but herd immunity is achieved at lower p_c , which is the minimally required portion of hyperedges that needs to be immunized to eliminate epidemics. (c, d) HIT p_c as a function of contagion rate $\beta = \beta_3$. The H-ES and SIP-based strategies outperform the EI-based strategy, despite their lower computational cost.

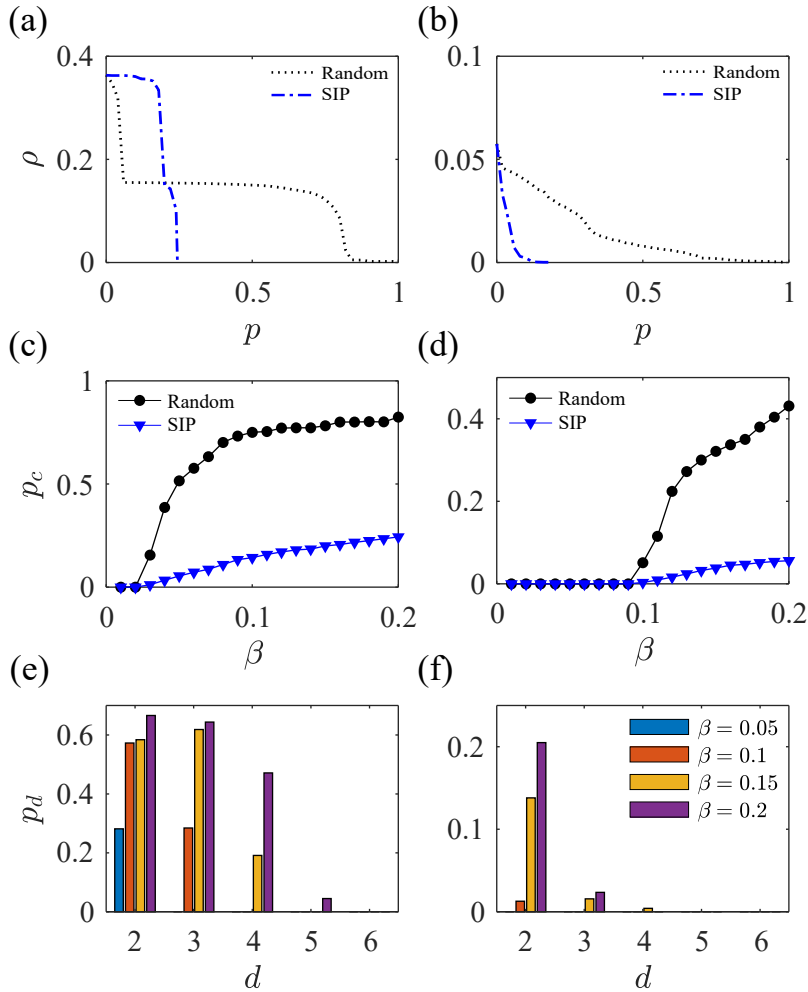


Figure 2.13: Random hyperedge immunization (Random) and SIP-based strategy tested in empirical hypergraphs: (a, c, e) the congressional bill cosponsorship (in 2000) hypergraph and (b, d, f) the protein interaction hypergraph. For nonuniform empirical hypergraphs, H-ES cannot be implemented due to the variety of hyperedge sizes, and EI is computationally inefficient due to the large hyperedges. (a, b) The density of infection ρ versus the removed portion of the edges p . The recovery rate $\mu = 0.2$ and the contagion rate $\beta = \beta_d = 0.2$ for all hyperedge sizes d . The efficient strategies generally exhibit a higher density of infection for small p , but herd immunity is achieved at lower HIT p_c , which is the minimally required portion of hyperedges that need to be immunized to eliminate the epidemics. (c, d) HIT p_c as a function of the contagion rate $\beta = \beta_d$. Efficient epidemic containment is achieved by the SIP-based method with low computational cost. (e, f) The immunization rate of hyperedges with size d plotted for various contagion rates. Small hyperedges are primarily targeted by the immunization strategy especially when β is low.

configurations and update with probability 0.2 at each time step.

We first test the strategies in synthetic and empirical networks. These networks are selected as examples, and the relative effectiveness of the immunization strategies generally do not strongly vary from network to network. For the unclustered scale-free network, we use the static model [106, 199] with 5000 nodes, 15000 edges, and degree exponent 3. For the clustered scale-free network, we implement the model proposed in Ref. [133] with 5000 nodes, 15000 edges, degree exponent 3, and the parameter $p = 0.8$, which makes the clustering coefficient 0.6. For empirical networks, we use the largest connected component of the airline network [153] which has 3354 nodes and 19162 edges. Each node represents an airport, and if there exists an airline between two airports, they are connected by an edge in the network. Another empirical network we use is the largest connected component of the general relativity and quantum cosmology collaboration network [205]. There are 4158 nodes and 13428 edges in the network. Each node represents an author of a paper submitted to the General Relativity and Cosmology category in arXiv, and if two authors coauthored a paper in the arXiv category from January 1993 to April 2003, they are connected by an edge in the network.

The results of the strategies in the networks are illustrated in Fig. 2.11. We plot the density of infection versus the immunization rate p for $\beta = \mu = 0.2$ [Figs. 2.11(a–d)]. The density of infection of efficient strategies is often higher than that of random edge immunization for small immunization rate p , but for sufficiently large p , the density of infection drops quickly and achieves herd immunity at a lower p_c . The HIT p_c is illustrated in Figs. 2.11(e–h). One way to calculate the effective HIT of is to calculate the minimally required immunization rate to lower the density of infection below $1/N$. However, when simulating the stationary states of epidemic processes, if the system reaches its absorbing state, we arbitrarily adjust the system by reverting it back to one of its histories (quasistationary method) or activating a single site [158]. Therefore, the state whose *number* of infected nodes is close to zero is highly influenced by the

choice of the simulation method which is not part of the epidemic model. To solve this problem, one can choose the herd immunity condition as the density of infection of 1%, which is sometimes used as a threshold to be considered as *subextensive* in networks [138]. However, in real-world situations, an epidemic prevalence of 1% is still an alerting scenario, and the epidemics cannot be considered under control. By choosing the density of infection of $\min\left(0.01, 1/\sqrt{N}\right)$ as the herd immunity condition, this dilemma can be resolved. In the thermodynamics limit $N \rightarrow \infty$, the epidemic density of the herd immunity condition converges to zero while the number of the infected nodes approaches infinity.

The recovery rate is fixed to $\mu = 0.2$. The HITs of the three efficient strategies are almost identical. To compare the HITs of efficient strategies more thoroughly, we plot the differences between the eigenscore strategy and two other strategies in Figs. 2.11(i–l). The EI-based strategy is generally slightly more efficient than the eigenscore strategy, but it does not have an advantage over the SIP-based strategy, despite its higher computational cost. Rather, the SIP-based strategy has a small advantage in the networks studied here, although the differences are marginal.

Then, we test the strategies in 3-uniform hypergraphs. We use two synthetic models of 3-uniform hypergraphs: a static model with 2000 nodes, 4000 hyperedges, and degree exponent 3, and the h -PSO model introduced in Sec. 2.10.1 with the same number of nodes, hyperedges, and degree exponent. The temperature $T = 0.5$ and $R = 1$ result in the clustering coefficient $C(H) = 1.0430$. We illustrated the results in Fig. 2.12. The density of infection ρ of the strategies versus the immunization ratio p for $\beta = \beta_3 = \mu = 0.2$ is depicted in Figs. 2.12(a, b). The H-eigenscore and SIP-based method result in a higher density of infection for small immunization ratios, but eventually yield a smaller HIT p_c for herd immunity [Figs. 2.12(c, d)]. The recovery rate is fixed to $\mu = 0.2$.

We test the SIP-based strategy in two empirical hypergraphs with various hyperedge sizes. One is the congressional bill cosponsorship hypergraph [21, 95], which has

536 nodes and 2773 hyperedges whose mean size is 16.57 and maximum size is 323. Each node represents a US congressperson, and if a set of d congresspeople cosponsored a bill in the year 2000, they are connected by a hyperedge of size d . The other is the protein interaction hypergraph [179], which has 8243 nodes and 6688 hyperedges whose mean size is 10.12 and maximum size is 421. Each node in the hypergraph represents a protein, and each hyperedge represents a type of multiprotein complex. Due to the large and heterogeneous size of hyperedges, only the SIP-based strategy can efficiently be implemented in these systems. We compare the density of infection of the strategy with random immunization in Figs. 2.13(a, b). The recovery rate $\mu = 0.2$ and the contagion rate for hyperedges are set $\beta_d = \beta = 0.2$ independently of their sizes. While random immunization requires the majority of hyperedges to be immune to eliminate the epidemics, the SIP-based strategy achieves it with small p_c . The HITs are plotted for various contagion rates $\beta = \beta_d$ in Figs. 2.13(c, d). The immunization rate of hyperedges of each size are illustrated in Fig. 3(e, f). Although removing large hyperedges affect large number of nodes, small hyperedges are primarily immunized especially when the contagion rate β is low. This is because the nodes that are connected by a small hyperedge interact more strongly. It is interesting to point out that an epidemic containment strategy that immunizes groups in descending order of their size was effective in the localized regime [315] of higher-order epidemics [316].

2.11 Summary and conclusion

In summary, we investigated the phase transitions and critical phenomena of the s -SIS model in SF uniform hypergraphs. We proposed a static model of the uniform hypergraph, which is a generalization of the static model of a complex network. We showed that the model indeed exhibits a degree distribution with a power-law tail.

Using the heterogeneous mean-field theory, we analytically studied the s -SIS model. We showed that the system exhibits rich phase transition and critical phenomena when the exponent of the degree distribution λ is larger than two. There exists a character-

istic degree $\lambda_c = 2 + 1/(d - 2)$. For $\lambda < \lambda_c$, the epidemic threshold vanishes. Thus, there exists a stationary state for an arbitrarily small contagion rate in the thermodynamic limit. The susceptibility χ_2 , the fluctuations of the order parameter, diverges as $\kappa \rightarrow 0$. Thus, a second-order contagion transition occurs at $\kappa_c = 0$. For $\lambda = \lambda_c$, the epidemic threshold becomes finite and the susceptibility χ_2 diverges as $\kappa \rightarrow \kappa_c$. Thus, a second-order contagion transition occurs. For $\lambda > \lambda_c$, the system undergoes a hybrid phase transition at a finite transition point κ_c . The susceptibility diverges at the transition point. We note that in a previous study [137], a discontinuous contagion transition was observed owing to higher-order interactions in a different model; however, we observed a hybrid phase transition, which exhibits a discontinuous transition with criticality at the same transition point. We also notice that for the static model, when the degree exponent is $2 < \lambda \leq 3$, a degree-degree correlation exists. Consequently, the correlation size exponent $\bar{\nu}_\perp$ differs from that for $\lambda > 3$. Accordingly, whereas the measured critical exponents β and γ are close to each other for $\lambda_c < \lambda < 3$ and $\lambda > 3$, the dynamic exponents δ and \bar{z} associated with $\bar{\nu}_\perp$ and ν_\parallel are different.

We performed numerical simulations of annealed SF 3-uniform hypergraphs with $\lambda_c = 2.5$ and the degree exponents $\lambda = 2.1, 2.9$, and 3.5 . Using dynamical FSS and steady-state FSS, the critical exponents $\{\delta, \bar{z}, \nu_\parallel\}$ and $\{\beta, \bar{\nu}_\perp, \gamma_1, \gamma_2\}$ are listed in Tables 2.2 and 2.3, respectively. The two methods are consistent within the error bars. Finally, the numerical values of the critical exponents $\{\beta, \bar{\nu}_\perp, \gamma_2\}$ are consistent with the theoretical values based on the heterogeneous mean-field theory in Sec. 2.5. They are listed in Table 5.2.

Moreover, we proposed an effective immunization strategy that immunizes hyperedges with high SIP that can be used in general hypergraphs, including networks. Hyperedges with high SIP are "hotspots" of the epidemics, and they can be identified and immunized. In case of information spreading processes, such hyperedges can be fostered to boost the information flow in the system. We also show that H-eigenscore is a natural generalization of the eigenscore for hypergraphs. If all the hyperedges in a

hypergraph have a size of 2, the H-eigenscore becomes identical to the eigenscore used in networks. Immunizing hyperedges with a high H-eigenscore effectively contains the epidemics, but the method can only be implemented in uniform hypergraphs.

We tested the performance of the method and compared it with the state-of-the-art immunization strategy of the EI-based method in networks and hypergraphs. In networks, the HIT p_c of the SIP-based strategy is marginally smaller than that of the EI-based strategy, despite its lower computational cost. In hypergraphs, the SIP-based strategy yields significantly smaller HIT p_c with lower computational cost. This suggests that SIP can serve as a centrality measure for hyperedges in general hypergraphs. The large disparity between the p_c of an efficient immunization strategy and random immunization calls for scientific, data-driven, systematic policy-making for containment measures to eliminate epidemics with the minimum use of resources for vaccination and minimal regulation of air traffic and social gatherings.

The IBMF used to calculate the SIP tend to overestimate the infection probability of the nodes (and, as a consequence, overestimate the global prevalence) because it ignores the correlations between the neighboring nodes. Recently introduced microscopic epidemic clique equations (MECLE) [34], which generalizes the epidemic-link equation to higher-order group interactions, predicted the density of infection and epidemic thresholds by taking the dynamic correlations between the neighboring nodes into account. An interesting work for the future might be to see how the performance of the SIP-based immunization strategy would be affected if the dynamical correlations are considered. Accounting for such correlations rapidly becomes unfeasible as the size of the hyperedges grow, therefore, it should be studied in hypergraphs whose hyperedges are not too large.

Chapter 3

Phase transition in vaccination strategy

3.1 Introduction

The spreading process in complex systems, such as networks [80, 81, 177, 244, 360] and metapopulation [65, 66, 213, 228, 343], has been an active field of research for modeling many physical and social phenomena [27, 132, 247]. This research has included opinion formation in social groups [3, 27, 113, 342], the spread of epidemic diseases [89, 152, 229, 235, 265, 343], and the diffusion of innovations [143, 149, 164, 282]. Current access to a plethora of data [95, 153, 205] on human mobility, collaboration, the contagion of epidemic disease, and temporal contacts, all of which were previously unavailable to researchers, now enable effective research into various dynamic processes in social systems. Extensive research devoted to the spreading processes has provided quantitative analyses for policy-making, especially in the public health domain. Moreover, study of the spreading process has provided a deeper understanding of phase transitions and critical behaviors, such as the effect of structural heterogeneity on epidemic thresholds [265, 267, 343] and the hybrid phase transition induced by cascades [59, 191, 192].

One of the most important topics in mathematical epidemiology is vaccination strategy, which has been extensively studied with various epidemic models [52, 62, 63, 68, 78, 97, 126, 220, 227, 231, 253, 268, 296, 326, 350]. If an individual is vaccinated for certain epidemic disease, that individual acquires immunity to the disease. Actual vaccines have less than perfect efficacy, which means that there is a small probability that

a vaccinated individual can be infected by the disease (i.e., a vaccine breakthrough). It is often modeled that vaccinated individuals do not turn into the infected state even in contact with infected individuals. In such a model, when a sufficient fraction of individuals in a system are vaccinated, the infection is unable to spread throughout the system, and the epidemic state is eliminated by the vaccination. This effect is called *herd immunity*. Vaccination strategies frequently aim to achieve herd immunity with the smallest number of vaccine shots.

The SARS-CoV-2 pandemic is ongoing worldwide and has caused more than five million deaths to date. Due to the development of effective vaccines for the disease, the epidemic damage of the disease can be greatly reduced. However, in most countries, especially developing countries, the number of vaccine shots available is less than the total population [318]. Therefore, it is important to formulate a vaccination strategy that minimizes the damage caused by the disease, such as the number of deaths, with the limited supply of vaccines available. Currently, many countries are vaccinating their populations in descending order of age, since the infection fatality rate (IFR) for the COVID-19 increases with age [13, 22, 169, 206, 209, 223, 304]. However, the effectiveness of this strategy needs to be quantitatively assessed.

Here, we employ the susceptible-infected-recovered-dead (SIRD) model, which is a minimal model to study epidemic mortality. We evaluate the effectiveness of fatality-based and contact-based vaccination strategies in a metapopulation model with heterogeneous contact and fatality rates. We find that the fatality-based strategy is more effective than the contact-based strategy for a high contagion rate and low vaccination supply, but the contact-based strategy outperforms the fatality-based strategy when a sufficiently large amount of vaccine is available. Simulated annealing is implemented to find the globally optimal vaccination strategy. We find that there is a discontinuous transition of the optimal strategy and path-dependency analogous to hysteresis. Further, we demonstrate that these phenomena occur in the vaccination of real-world epidemic diseases, such as tuberculosis (TB) and COVID-19.

3.2 Susceptible-infected-recovered-dead (SIRD) model

The susceptible-infected-recovered (SIR) model is a minimal model of epidemic spreading and the most extensively studied model both in complex networks [152, 235, 267, 291] and in the metapopulation model [65, 66, 213, 228, 343], together with its variants [23, 36, 51, 55, 56, 59, 208, 212, 292, 314]. In the SIR model, each individual is in either the susceptible (S), infected (I), or recovered (R) state. A susceptible individual can turn into an infected state if it comes into contact with an infected individual. If a susceptible individual and an infected individual are in contact, the susceptible individual is turned into the I state at rate η (it turns with probability $\eta\Delta t$ in an infinitesimal time step Δt). If the S individual is in contact with n infected individuals, the rate becomes $n\eta$. Infected individuals eventually turn into the recovered state at a constant rate μ . A recovered individual obtains immunity and does not turn into the infected state again. In actual epidemic diseases, there is a probability of reinfection whose effects on the results of this research are discussed in Sec. 3.3.4.

Vaccination strategy is one of the core topics in mathematical epidemiology; therefore, considerable research has been devoted to the subject [52, 62, 63, 68, 78, 97, 126, 220, 227, 231, 253, 268, 296, 326, 350]. The objective of vaccination strategies in the SIR model is to minimize the total number of individuals affected by the disease, which can be measured by the number of recovered individuals when the infection vanishes, with limited vaccination resources. However, one of the most important objectives of vaccinations in the real world is to minimize the total number of deaths caused by a disease. Because recovery and death are not distinguished in the SIR model, it cannot be used to study vaccination strategies related to such a purpose. At this point, we employ the SIRD model, which is a minimal model that distinguishes recovery and mortality [8, 299, 338, 355].

In the SIRD model, similar to the SIR model, each individual is in either a susceptible (S), infected (I), recovered (R), or dead (D) state. The contagion occurs identically

as in the SIR model. Any individual from subpopulation α (such as an age group) that is in the I state turns into the R state at rate $(1 - \kappa_\alpha)\mu$ or into the D state at rate $\kappa_\alpha\mu$. The rate equation for the SIRD model is, therefore,

$$S + I \xrightarrow{\eta} I + I, \quad (3.1)$$

$$I \xrightarrow{(1-\kappa_\alpha)\mu} R, \quad (3.2)$$

$$I \xrightarrow{\kappa_\alpha\mu} D, \quad (3.3)$$

where η is the contagion rate, μ is the recovery rate, and κ_α is the IFR of subpopulation α . If an individual from subpopulation α is infected, the individual turns into R state or D state with probability ratio $(1 - \kappa_\alpha) : \kappa_\alpha$. We assumed that the three processes (contagion, recovery, and death) occur independently at constant rates. This assumption reasonably describes the pathology of each individual; however, complex social interventions such as quarantine and social distancing that depend on the number of epidemic cases and mortality can complicate the process.

3.3 Results

3.3.1 Fatality- and contact-based strategies

A metapopulation model consists of interacting subpopulations, which are often but not necessarily, spatially structured. The subpopulations are assumed to be well-mixed. For epidemic studies using a metapopulation model, the density of epidemic states in each subpopulation is tracked instead of tracking the epidemic states of each individual. The density of states evolves due to the interactions among subpopulations and interactions that occur within the same subpopulation. Because metapopulation models have lower dimensions compared to networks, they allow more exhaustive studies on the spread of epidemic diseases. The epidemic equation for the SIRD model in the

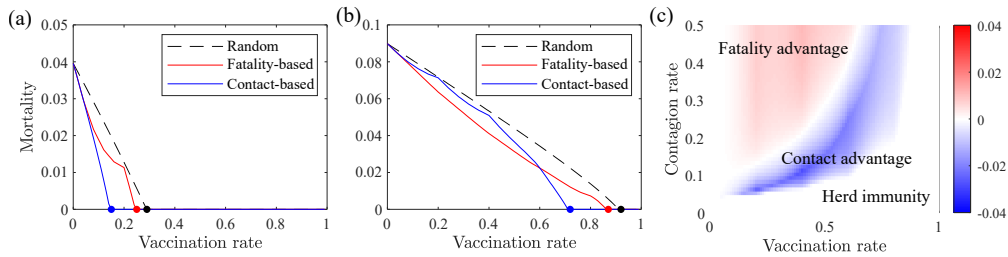


Figure 3.1: (a–b) The mortality rate as a result of various vaccination strategies. The contagion rate is (a) $\eta = 0.05$ and (b) $\eta = 0.4$, while the recovery rate is normalized $\mu = 1$. When the fraction of the population affected by the epidemic (i.e., the fraction of R and D state at the end of the dynamic) is less than 10^{-4} , we assume that herd immunity is achieved, and the epidemic is eliminated by vaccination. The point at which herd immunity is achieved is depicted as a dot. When the contagion rate is low, the contact-based strategy is more effective regardless of the vaccination rate. When the contagion rate is high, the fatality-based strategy is more effective at a low vaccination rate; however, the contact-based strategy outperforms the fatality-based strategy when the vaccine supply is sufficiently high, achieving herd immunity at a lower vaccination rate. (c) The difference between the mortality rates resulting from fatality-based and contact-based strategies. The fatality-based strategy reduces more deaths compared to the contact-based strategy when the contagion rate is high and the vaccination rate is low. However, as the vaccination rate becomes higher, the contact-based strategy outperforms the fatality-based strategy.

metapopulation model is

$$\frac{\partial}{\partial t} \rho_{\alpha}^{\text{I}}(t) = \eta (\rho_{\alpha}^{\text{S}}(t) - v_{\alpha}) \sum_{\beta} M_{\alpha\beta} \rho_{\beta}^{\text{I}}(t) - \mu \rho_{\alpha}^{\text{I}}(t), \quad (3.4)$$

$$\frac{\partial}{\partial t} \rho_{\alpha}^{\text{R}}(t) = (1 - \kappa_{\alpha}) \mu \rho_{\alpha}^{\text{I}}(t), \quad (3.5)$$

$$\frac{\partial}{\partial t} \rho_{\alpha}^{\text{D}}(t) = \kappa_{\alpha} \mu \rho_{\alpha}^{\text{I}}(t), \quad (3.6)$$

where ρ_{α}^{S} , ρ_{α}^{I} , ρ_{α}^{R} , and ρ_{α}^{D} are the probabilities that an individual in group α is in the S, I, R, and D state, respectively; v_{α} is the fraction of vaccinated individuals in subpopulation α ; and $M_{\alpha\beta}$ is the contact matrix, which is defined as the average contacts that an individual in group α has with the individuals in group β .

Initially, an infinitesimal fraction, $n_0 = 10^{-8}$ of each group α of the population, is in the I state, and all the rest of the population, $1 - n_0$, is in the S state. As long as n_0 is small enough, the value of n_0 and how these initially infected individuals are distributed among the subpopulations do not affect the final states ρ^{R} and ρ^{D} . The differential equations are then solved by the fourth order Runge-Kutta method [185, 286] until the total fraction of infected individuals, $\rho^{\text{I}} = \sum_{\alpha} P_{\alpha} \rho_{\alpha}^{\text{I}}$, becomes less than a certain threshold, 10^{-12} , and the epidemic process ends (P_{α} is the fraction of individuals in subpopulation α). We then calculate the total fraction of the deceased population $\rho^{\text{D}} = \sum_{\alpha} P_{\alpha} \rho_{\alpha}^{\text{D}}$.

We constructed a metapopulation model with heterogeneous contact and fatality rates. The population has fatality rates $\kappa_i = 5\%$, 7.5% , 10% , 12.5% , and 15% and relative contact rates $c_j = 0.5, 0.75, 1, 1.25, \text{ and } 1.5$. The population is equally divided into 25 subpopulations according to the five fatalities and five contact rates ($5 \times 5 = 25$). The contact rate between groups (i, j) and (i', j') is $M_{ijj'i'} = c_j c_{j'}$.

We investigated the effectiveness of random, fatality-based, and contact-based strategies for various levels of vaccine supply. In the random strategy, the vaccine is randomly distributed and each subpopulation is uniformly vaccinated. In the fatality-

based strategy, the subpopulations are vaccinated in descending order of fatality rates, and if two subpopulations have identical fatality rates, the one with a higher contact rate is vaccinated. In the contact-based method, an infinitesimal amount of vaccine is iteratively given to the age group with the highest contact rate with unvaccinated individuals until the total amount of vaccine is distributed. The contact rate of age group α with unvaccinated individuals is

$$\sum_{\beta} M_{\alpha\beta} (1 - v_{\beta}) , \quad (3.7)$$

and the value is recalculated at each iteration. This differs from the contact rate of age group α with any individual in the population, which is $\sum_{\beta} M_{\alpha\beta}$.

The mortality rate of the population when each vaccination strategy is employed is illustrated in Figs. 3.1(a) and (b). When the contagion rate is low, the contact-based strategy results in a lower mortality rate than the fatality-based strategy regardless of the vaccination rate; however, for a high contagion rate, there is a crossover between the strategies. The fatality-based strategy more effectively reduces mortality when the vaccination rate is low, but the contact-based strategy outperforms the fatality-based strategy when the vaccination rate is high. If the vaccination rate is sufficiently high, herd immunity is achieved regardless of the choice of the vaccination strategy (fatality-based, contact-based, random, etc). The difference between the mortality rates when fatality- and contact-based strategies are employed is depicted in Fig. 3.1(c). The fatality-based strategy is effective when the contagion rate is high and the vaccine supply is low.

3.3.2 Transition and path-dependency of the optimal vaccination strategy

In this section, we further investigate the vaccination rate dependency of the vaccination strategy and demonstrate that the optimal vaccination strategy undergoes a dis-

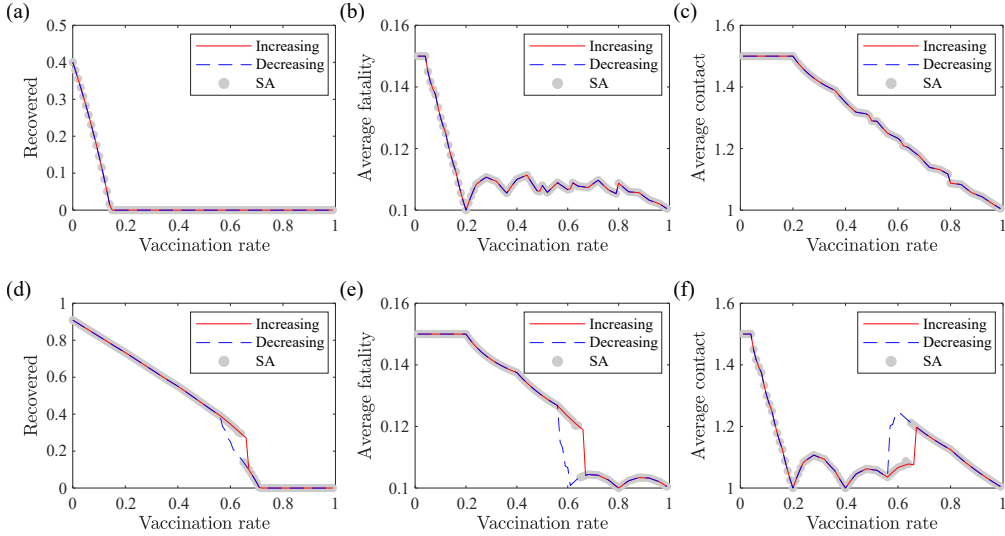


Figure 3.2: (a, d) Fraction of recovered population, (b, e) average fatality of the vaccinated population, and (c, f) average contact rate of the vaccinated population of the synthetic metapopulation model with heterogeneous fatality and contact rates. The recovery rate is normalized to $\mu = 1$, and contagion rates are (a–c) $\eta = 0.05$ and (d–f) $\eta = 0.4$. The increasing (decreasing) curve, where the locally optimal vaccination strategies are found by iteratively increasing (decreasing) the vaccination rate, is depicted as solid red (dashed blue) lines. The globally optimal strategies are found by simulated annealing (SA). There is no abrupt transition nor separation of the curves for a low contagion rate, $\eta = 0.05$, and the optimal vaccination strategy prefers to vaccinate individuals with high contact rates regardless of the vaccination rate. For a large contagion rate, $\eta = 0.4$, there is an abrupt transition in the globally optimal strategy. The separation of the increasing and decreasing curve indicates the path-dependency of the vaccination strategy which is analogous to hysteresis. For a small (0–0.56) or large (0.67–1) vaccination rate, the increasing and decreasing curves coincide; however, near the transition point, the increasing curve tends to vaccinate individuals with high fatality rates (high-fatality strategy) and the decreasing curve vaccinates individuals with high contact rates (high-contact strategy). The High-fatality strategy results in a higher number of recovered population than the high-contact strategy because the high-fatality strategy aims to protect high-risk groups, while the high-contact strategy aims to contain the infection.

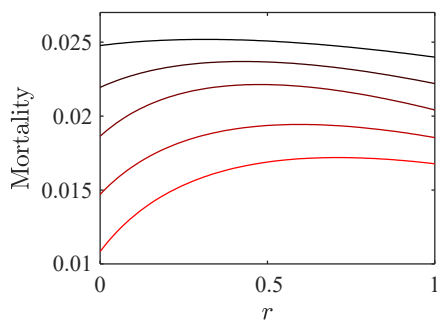


Figure 3.3: The mortality rate of a mixed strategy that combines the high-fatality and high-contact strategies. The contagion rate is $\eta = 0.4$, and vaccine supply is, from top to bottom, 58%, 60%, 62%, 64%, and 66%. There is a barrier of mortality rate between the high-fatality and high-contact strategies, which is the cause of the path-dependency and discontinuous transition of the vaccination strategy.

The mortality rate of the high-contact strategy drops faster than the high-fatality strategy as the level of vaccine supply increases, causing the crossover between the two strategies.

continuous transition. To find the globally optimal vaccination strategy, we implement a modified version of the simulated annealing technique. The simulated annealing is a probabilistic optimization algorithm inspired by spin glass [174]. First, we start with a random vaccination strategy with a given amount of vaccine supply. We set this strategy as a provisional solution. We then calculate the mortality rate of a trial strategy, which is perturbed from the provisional solution by a small amount while keeping the vaccine supply of the total population constant. If the mortality rate of the trial strategy is smaller than that of the provisional solution, we replace the provisional solution with the trial strategy. Otherwise, we replace the provisional solution with the trial strategy with probability $\exp(-1/T)$, where T is the temperature of the algorithm. In the beginning, the temperature is set at $T = 2$. We iterate this process $n_{\text{iter}} = 10^6$ times, while the temperature is dropped by a factor of $f_{\text{iter}} = 1 - 2 \times 10^{-5}$ at each step. The resulting provisional solution is the optimal vaccination strategy, given that n_{iter} is sufficiently large and f_{iter} is sufficiently close to one. To find locally optimal solutions, we use the zero-temperature simulated annealing, which is analogous to the gradient-descent method. We perturb the provisional solution by decreasing the vacci-

nation rate of group α by $\delta v/P(\alpha)$ and increasing the vaccination rate of group β by $\delta v/P(\beta)$, where δv is a small number, and $P(\alpha)$ is the fraction of the group α in the population. This way, the total vaccination rate of the entire population remains constant. Among perturbed solutions, if any solution results in a smaller mortality rate, we replace the provisional solution with the perturbed solution that results in the smallest mortality rate. Otherwise (i.e., if all the perturbed solutions result in larger mortality rates than the provisional solution), we have achieved a locally optimal solution; hence, we terminate the process.

To investigate the path-dependency of the optimal vaccination strategy, we iteratively increased and decreased the vaccination rate by a small amount, while constantly calculating the locally optimal vaccination strategy in the vicinity. To obtain the increasing curve, we first set the vaccination rate to $\Delta v = 0.01$ and find the optimal vaccination strategy $v_{\beta}^{(I)}(\Delta v)$. We then increase the vaccination rate by Δv and find the locally optimal vaccination strategy $v_{\beta}^{(I)}(2\Delta v)$ near the optimal strategy from the previous step. We repeat this process until the vaccination rate reaches one. To obtain the decreasing curve, we start from a vaccination rate of $1 - \Delta v$ and repeat the process.

The results are illustrated in Fig. 3.2. Fraction of the recovered population ρ^R , average fatality, and contact rates of the vaccinated individuals are depicted as characteristics of vaccination strategies. These values are analogous to the order parameters of the phase transition in thermal systems and the vaccination rate is the control parameter. The order parameters of the two local mortality minima are depicted in the curves similarly to the magnetization of the two free energy minima is depicted in the hysteresis curve of the magnetic systems. The global mortality minimum corresponds to the global free energy minimum where the system lies in the Boltzmann distribution. For a low contagion rate, there is no abrupt transition of the optimal vaccination strategy. For a high contagion rate, an abrupt transition of the globally optimal vaccination strategy, which is obtained by simulated annealing, discontinuously changes. Moreover, there is a path-dependency in the vaccination strategy. When locally optimal

vaccination strategies are found by slowly increasing the vaccination rate from zero, the strategies vaccinate individuals with high fatality rates in the middle region (high-fatality strategy). If the strategies are found by slowly decreasing the vaccination rate from one, they primarily vaccinate individuals with high contact rates (high-contact strategy). A high-fatality strategy results in a higher fraction of recovered individuals than the high-contact strategy, even though the strategies' mortality rates are similar or the same in the vicinity of the transition point.

The path-dependency of this transition implies that a moderate strategy that combines the high-fatality and high-contact strategy can be less effective than either strategy. The vaccination rate of the moderate strategy is $v_{\alpha}^{\text{mod}} = rv_{\alpha}^f + (1 - r)v_{\alpha}^c$, where v_{α}^f and v_{α}^c are the vaccination rates of subpopulation α in the high-fatality and high-contact strategy, respectively. The performance of the moderate strategy for various levels of vaccine supply is depicted in Fig. 3.3. There is a barrier of mortality rate between the high-fatality and high-contact strategies, and the moderate strategy is never more effective than both of the strategies, and in some regions, it is less effective than either of the two strategies. Hence, it is inadvisable to mix the two strategies or change from one to the other in the middle. The mortality rate of the high-contact strategy ($r = 0$) decreases faster than the high-fatality strategy ($r = 1$), which results in an abrupt transition of the optimal vaccination strategy from a high-fatality to a high-contact strategy.

3.3.3 Real-world epidemic diseases

In this section, we show that the discontinuous transition and path-dependency of the optimal vaccination strategy illustrated in the previous section occur in the vaccination of actual epidemic diseases, such as tuberculosis (TB) and COVID-19. Contact data between each age group in the various countries have been studied utilizing surveys [234]. To model TB, we employed a contact matrix calculated from the UK data along with the incidence risk ratio of TB in the UK [270]. The population is divided

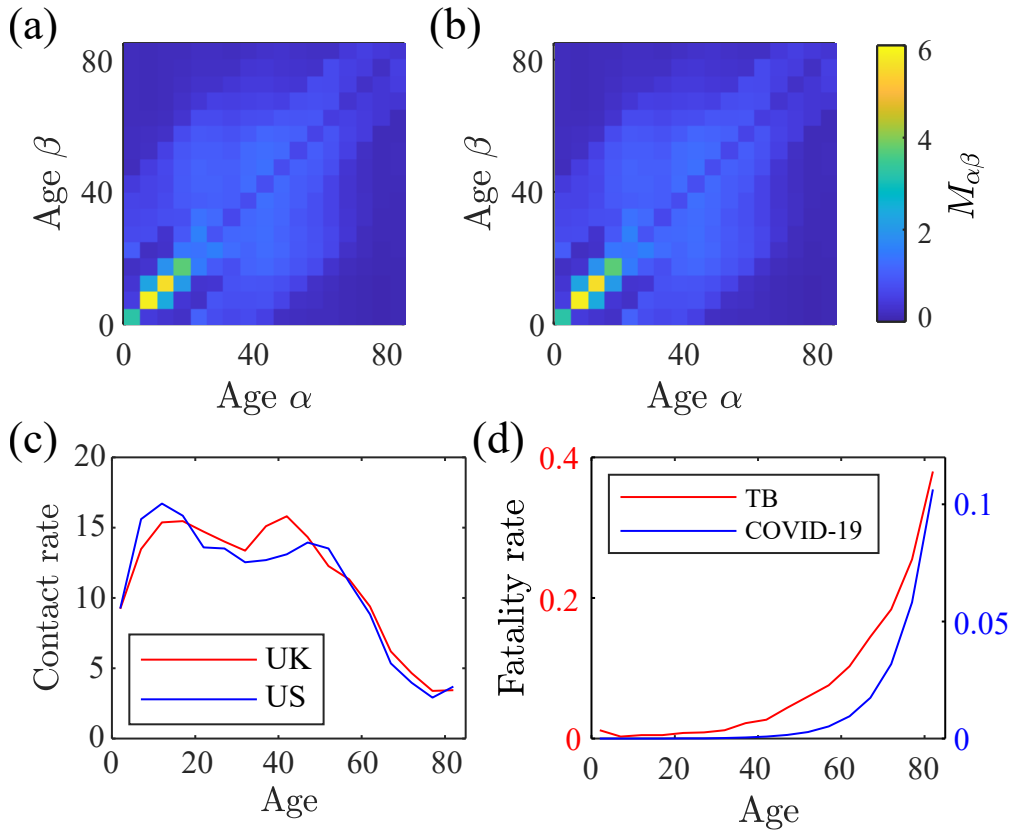


Figure 3.4: The age contact matrix of the (a) United Kingdom and (b) United States, and (c) contact rate of each age group. The population is divided into 17 groups: aged 0–4, 5–9, . . . , 75–79, and above 80. The interaction strength between groups of similar age is disproportionately higher, and the groups of ages 10–29 show the highest number of contacts. (d) The fatality rates of TB in the United Kingdom (UK) and COVID-19 in the United States (US). The fatality rate is highly heterogeneous and monotonically increases with age, with the sole exception of children below age five in TB. Therefore, the senior population is primarily vaccinated by the fatality-based strategy, and individuals of age 10–29 are primarily vaccinated by the contact-based strategy.

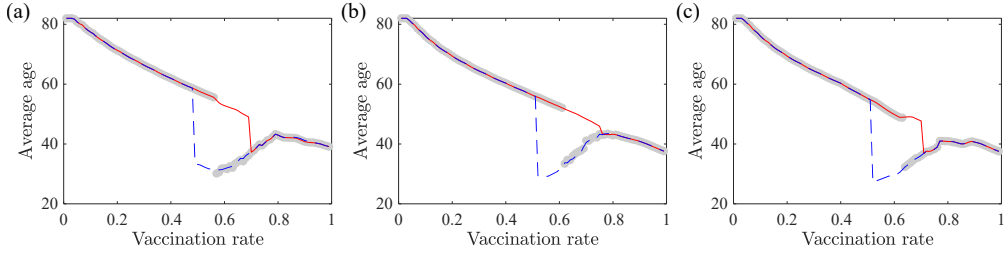


Figure 3.5: Average age of vaccinated individuals for (a) TB, (b) COVID-19, and (c) COVID-19 with reinfection and finite vaccine efficacy. The contagion rates are $\eta = 0.25$, and the recovery rate is normalized to $\mu = 1$. The total amount of vaccine is increased (solid red line) and decreased (dashed blue line) while keeping the vaccination strategy at its local optimum. For a small vaccination rate, the increasing curve and decreasing curve coincide; however, for a sufficiently large vaccination rate, the two curves show a largely unequal average age of the vaccinated population. The increasing curve has a higher average age. The globally optimal strategy, which is calculated by the simulated annealing, undergoes an abrupt transition from the high-fatality to the high-contact strategies. The separation of the increasing and decreasing curve indicates the path-dependency of the vaccination strategy which is analogous to hysteresis.

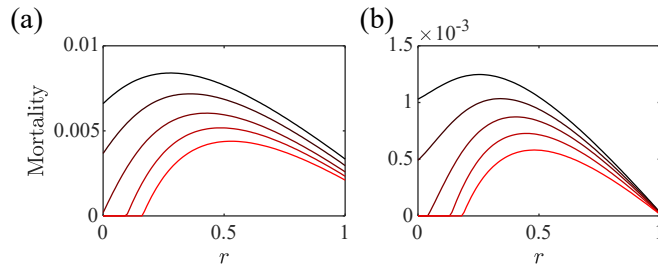


Figure 3.6: The mortality rate of the mixed strategy of high-fatality and high-contact strategies for (a) TB and (b) COVID-19. The contagion rate is $\eta = 0.25$, and the vaccine supply is, from top to bottom, 52%, 54%, 56%, 58%, and 60%. There is a barrier of mortality rate between the high-fatality and high-contact strategy, which is the cause of the discontinuous transition and path-dependency of the optimal vaccination strategy. The mortality rate of the high-contact strategy drops faster than the high-fatality strategy as the level of vaccine supply increases, and herd immunity is achieved at a lower vaccine supply.

into 17 groups: aged 0–4, 5–10, ..., 75–79, and above 80. For COVID-19, we use the contact matrix of the US and the age-dependent IFR obtained from a meta-analysis of medical literature [206]. The latter is calculated as

$$\log_{10} \text{IFR} = (-3.27 \pm 0.07) + (0.0524 \pm 0.0013) \text{ age}. \quad (3.8)$$

The contact matrices and the fatality rates of the diseases are illustrated in Fig. 3.4. Contact within a similar age group is disproportionately intense (Figs. 3.4(a, b)), and contacts between teenagers exhibit the highest strength. Fatality rates of the diseases monotonically increase with age, except for children below age five for TB. As a result, the fatality-based strategy primarily vaccinates the senior population, while the contact-based strategy vaccinates the teenagers first.

The average age of the vaccinated individuals are presented for TB (Fig. 3.5(a)) and COVID-19 (Fig. 3.5(b)). Both figures exhibit the discontinuous transition and path-dependency of the optimal vaccination strategy. The increasing curve vaccinates the senior population more than the decreasing curve, which corresponds to the phenomenon depicted in Fig. 3.2(e), where the increasing curve has a greater preference to vaccinate individuals from groups with high fatality rates than the decreasing curve. Also, there are barriers of mortality rate between the high-fatality and high-contact strategies (Fig. 3.6), suggesting that mixing the two strategies is ineffective. As the vaccination rate increases, the mortality associated with the high-contact strategy decreases faster than that of the high-fatality strategy to achieve herd immunity at a lower vaccine supply.

3.3.4 Complex epidemic stages, vaccine breakthrough infection, and re-infection

The previous results are obtained in simplified models. In this section, we demonstrate that the more complicated behaviors of the actual diseases do not significantly alter the

findings of this research. First, in the real world, actual infectious diseases progress in a series of epidemic stages, such as the incubation period, prodromal period, and acute period. Each of these stages has a distinct rate of spreading the disease. These stages have complicated effects on the temporal dynamics of epidemics, but in this study, only the fraction of population in each epidemic state (R and D) at the end of the epidemic is relevant. In this sense, the complex stages of a disease can be reduced to a simplified model. For instance, suppose there multiple infectious stages I_k ($k = 1, \dots, K$) of a disease, each with contagion rate η_k and progression rate μ_k (i.e., $S + I_k \rightarrow I_1 + I_k$ occurs with rate η_k , $I_k \rightarrow I_{k+1}$ occurs with rate μ_k , and $I_K \rightarrow R$ occurs with rate μ_K). The total recovered population at the end of the epidemic disease is then identical to that of the SIR model with contagion rate $\eta^* = \sum_k \eta_k / \mu_k$ and $\mu = 1$. To model an incubation stage, we can set $\eta_I = 0$ and $\mu_I = 1/\tau_I$, where τ_I is the incubation period of the disease.

Also, we assumed that vaccinated individuals never become infected even in contact with infected individuals. However, people who are vaccinated still can get infected by COVID-19. An infection of a vaccinated individual is referred to as a vaccine breakthrough infection. To include vaccine breakthrough infection, we can suppose a vaccine efficacy of $\theta < 1$, and the vaccinated individuals turn into the infected state at a rate of $(1 - \theta)\eta$ instead of η . Additionally, even when an infected individual recovers and obtains immunity to the disease, there is a small probability that the individual can be infected by the disease again. Such reinfection can be modeled as some individuals losing immunity [252, 288, 290]. Hence, individuals in state R turn into S state at rate ν . The typical time for an individual to lose immunity is $1/\nu$. Individuals in the D state remain in the D state.

We included vaccine breakthrough infections and reinfections to COVID-19 and illustrated the average age of the vaccinated population in Fig. 3.5(c). The vaccine efficacy is $\theta = 0.9$, and the rate of immunity loss is $\nu = 0.05$. This means that typically the immunity of a vaccine is lost over a duration 20 times the average recovery time

of the disease (~ 200 days). The discontinuous transition of the optimal strategy and path-dependency still manifests themselves in the model with these modifications.

3.4 Conclusion

In summary, we employed the SIRD model to investigate the effectiveness of vaccination strategies to minimize the mortality rate in a population with heterogeneous fatality rates. We constructed a synthetic metapopulation model with heterogeneous fatality and contact rates to investigate how the effectiveness of vaccination strategies relates to the amount of vaccine available. Vaccinating individuals with high fatality rates is effective when the contagion rate is high and the vaccine supply is low. We found the discontinuous transition and path-dependency, which is analogous to hysteresis in statistical physics, of the optimal vaccination strategy. The path-dependency of the vaccination strategy implies that combining high-fatality and high-contact strategies is ineffective in reducing the mortality rate of the epidemic disease. We also demonstrated that such phenomena occur in real-world epidemic diseases, such as TB and COVID-19. These conclusions are valid even when complex stages of a disease, vaccine breakthrough infection, and reinfection are considered.

In conclusion, the effectiveness of vaccination strategies is closely related to the amount of vaccine available. Hence, the quantity of vaccine supply should be estimated before the design of the vaccination strategies. Precise estimation of the contact matrix, basic reproduction number, and the IFR of the population is also important. In the survey data used in this paper, all types of contacts were treated equally. However, the contagion rate of disease among individuals who live in the same house, work in the same place, or shop in the same grocery store should differ from each other. If more accurate contagion tree data of the disease are collected and implemented, the relative strength of such interactions can be taken into account. Although the effectiveness of the strategies at specific vaccination rates will be modified if the precision of the dataset is improved, because the discontinuous transition and path-dependency of the

optimal vaccination strategies occur in various epidemic models with a wide range of parameters, the conclusions of this research should still be valid.

Chapter 4

Application of graph neural network (GNN) on spreading processes

4.1 Introduction

4.2 Prediction and mitigation of avalanche dynamics in power grids using graph neural network

Small, local disturbances in a complex networks can trigger consecutive failures of other nodes in the network. Most failures remain local and do not last for an extended period [44,86,154]. However, there is a small probability that they will spread throughout the network, resulting in catastrophic global failure. This type of failure in infrastructure networks such as the Internet and electrical grids can result in tremendous financial damage and even the loss of human lives. For example, in the Northeast blackout of 2003, an initial disturbance in Ohio triggered the largest blackout in North American history, which affected more than 50 million people and lasted for up to 15 hours in the US and Canada.

The prediction and control of cascading failures in complex networks is a central topic of research in network science. Conventional epidemic models [262] based on local contact process, propagating in branching process, fail to capture the unique features of cascading failures that propagate nonlocally [131,255]. Therefore, several models have been proposed to simulate such nonlocal cascading failures, and this sub-

ject has been extensively studied.

Most studies of cascading failures have used numerical simulations and enumeration. In this study, computational complexity is an important issue. The computational complexity of the local cascading failure dynamics is generally somewhat lower than that of the nonlocal dynamics. For instance, for the k -core percolation [193], cascading failure occurs at nodes with a degree of less than k . Thus, cascading failures propagate locally. The calculation of a single cascade step has a time complexity of $O(N)$ in a network with N nodes and can be simulated even in large-scale networks. By contrast, the random resistor network model [74], in which cascading failures propagate nonlocally, has a time complexity of $O(N^2)$ because of a critical slowdown near the critical point. To overcome this problem, Batrouni et al. [14] proposed the Fourier acceleration algorithm, which decreased the computation complexity dramatically, to $O(N \log N)$. In the Motter–Lai (ML) model [241], cascading failure propagates nonlocally, and the time complexity is higher, $O(N^2 \log N)$, because the shortest paths must be identified for a single cascade step. Therefore, the ML model has been simulated only for small networks.

The ML model [241] was proposed to study data packet transport along the shortest paths between two routers on the Internet. When heavily loaded nodes break down, network traffic is rerouted, causing load redistribution; consequently, cascading failure can occur at nodes distant from the failed nodes. This simple dynamics of the ML model makes it possible to understand the propagation of cascading failure in detail; thus, the model has been widely implemented [87, 123, 134, 181, 186, 195, 240, 295, 336, 345, 358, 359].

In this study, we addressed the problem of avalanche mitigation. We define the avalanche centrality (AC) of each node and show that this quantity can be used to effectively suppress avalanches. To reduce the time complexity of the AC calculation, which exceeds $O(N^3 \log N)$, we used a graph neural network (GNN) approach. The GNN is a deep learning model for analyzing graph data; it was introduced by Scarselli

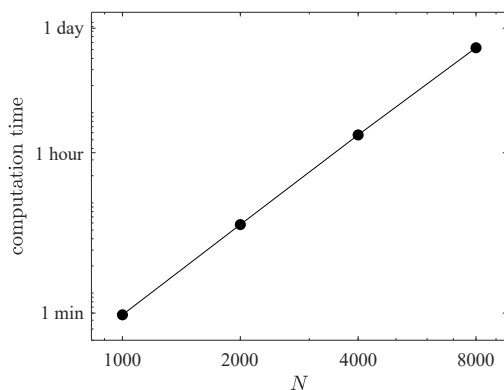


Figure 4.1: Computation time of ML model as a function of network size. The Schultz–Heitzig–Kurths (SHK) random power grid model was used. The computation time is proportional to $N^{3.3}$; thus, if the network size doubles, the computation time increases by approximately tenfold. More than a year of computation is required to simulate the process in a network of size $N = 25000$ using the CPU of model i7-10700.

et al. [293]. In particular, we constructed a scalable GNN structure that is independent of network size using an inductive learning scheme that is applicable to various type of networks. The GNN structure was designed to be effective for modeling a large network, even if it is trained using the simulation results for a small network. An avalanche mitigation strategy that uses this methodology and is applicable to large-scale networks, which are impractical to simulate, is proposed.

4.2.1 Avalanche dynamics

Many models of cascading failure dynamics have been proposed, for example, random fuse networks [74], k -core percolation [20, 79, 109, 193], dynamically induced cascades [294], and others [19, 33, 48, 71, 172, 191, 281]. Among them, the ML model [241] is one of the simplest models capable of capturing the avalanche dynamics of propagation through nonlocal nodes. It has been applied to power grids [181]. This simple, shortest-path-based model can be used to understand the avalanche process. Consequently, it has been extensively applied in studies of suppression strategies [123, 240], the analytic calculation of the robustness criterion [358, 359], the effect of network

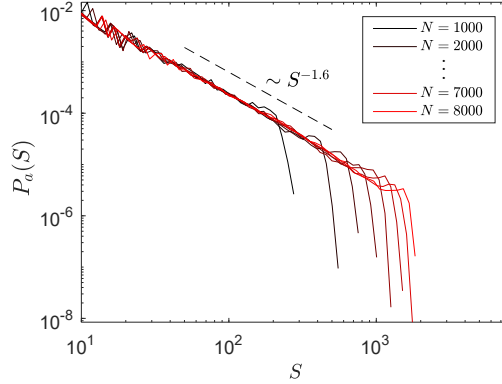


Figure 4.2: Avalanche size distribution of SHK network with various numbers of nodes for the ML model. The control parameter a is taken as 0.25, at which the avalanche sizes have a scale-free distribution with exponent $\tau \approx 1.6$.

topology [345], and other topics [87, 134, 181, 186, 195, 295, 336].

In the ML model [241], the capacity C_i of each node i is proportional to the betweenness centrality (BC), $B_i^{(0)}$, of node i , as follows:

$$C_i = (1 + a)B_i^{(0)}, \quad (4.1)$$

where $a > 0$ is a model parameter. The superscript (0) denotes that the BC is calculated in a network without any failure. The BC is the number of shortest paths that pass through the node; it is written as

$$B_i^{(0)} = \sum_{j \neq k \neq i} \frac{m_{jk}(i)}{m_{jk}}, \quad (4.2)$$

where m_{jk} is the number of shortest paths between nodes j and k , and $m_{jk}(i)$ is the number of those paths that pass through node i .

We initiate the avalanche dynamics by causing node i on the network to fail. The failed node is effectively removed from the network, as all the connected links are disconnected. Then, all the shortest paths that had passed through node i are rerouted to detours. Consequently, the excess BC is redistributed over the network. The BC of

each node j is then updated to $B_j^{(1)}$. If the updated $B_j^{(1)}$ exceeds the capacity of the preassigned node, C_j , node j is overloaded and fails. Other nodes with BCs exceeding their capacities fail simultaneously. Then the BCs of the remaining active nodes are again updated to $B_k^{(2)}$. The process is repeated until there are no overloaded nodes in the network: $B_k^{(t)} < C_k$ for all remaining nodes k .

The avalanche size S_i of each node ($i = 1, \dots, N$) has a distribution $P_a(S)$. On scale-free networks, the distribution exhibits power-law behavior as $P_a(S) \sim S^{-\tau}$, where $\tau \approx 2.1$ when a particular value of a is chosen, which is denoted as $a_c \approx 0.15$ [195]. This result may indicate that $P_a(s)$ exhibits critical behavior at a_c . The exponent τ is insensitive to the degree exponent λ of scale-free networks and seems to be closely related to the exponent of the diameter-change distribution when nodes are deleted one by one [171]. It has also been found that the average size $\langle s(k) \rangle$ of avalanches triggered by removing each node with degree k depends on k as $\langle s(k) \rangle \sim k^{(\lambda-1)/(\tau-1)}$. Note that the avalanche size distribution observed in cascading failures in real-world electric power grids has a heavy-tailed distribution [43–45, 77, 130].

In this study, we simulated the ML model on a network model proposed by Schultz, Heitzig, and Kurths (SHK), which was designed according to the essential features of real-world electric power grids [297]. This model has many control parameters. Using an appropriate set of parameter values used in Ref. [249], we obtained power-law behavior of the avalanche size distribution at $a_c \approx 0.25$. The exponent $\tau \approx 1.6$ was found as shown in Fig. 4.2, which is close to $\tau = 1.5$, the value of the sandpile model in random networks [108].

The ML model was modified for application to electric power grids by Carreras et al. [42]. In this modified ML model, each node i is characterized by an input power P_i , which has positive and negative values for power generators and consumers, respectively. To account for the avalanche failures of links rather than nodes, the capacity of each link is defined as $C_{ij} = (1 - a)F_{ij}^{\max}$, where F_{ij}^{\max} is the maximum power flow through link (ij) between nodes i and j . At each time step, the direct-current circuit

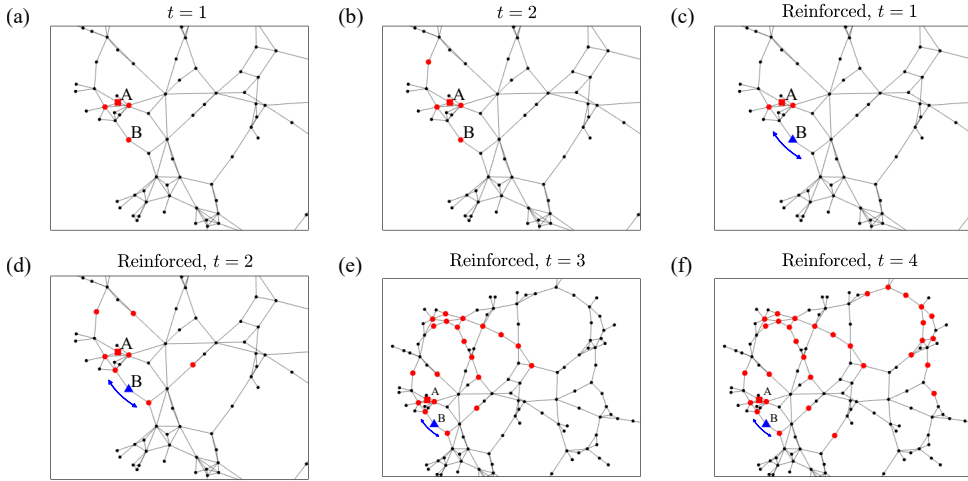


Figure 4.3: Paradoxical effect of reinforcement in electric power grid of France. Red square (indicated by A) represents the initial failure, red dots represent secondary failures, and blue triangle (indicated by B) represents a reinforced node. (a) and (b) If no node is reinforced, the avalanche ends at $t = 2$ with avalanche size $S = 5$. (c)–(f) If node B (\blacktriangle) is reinforced, the avalanche lasts until $t = 4$, and the avalanche size increases to 33. Because the reinforced node does not fail, heavy traffic through route via node B (blue arrow) is maintained, causing other nodes on the route to fail. Reinforcement thus may result in a significantly larger global cascade.

equation is solved, and the power flow F_{ij} through link (ij) is obtained. If $F_{ij} > C_{ij}$, link (ij) is disconnected, and the power flow of each link is recalculated. This link disconnection process is repeated until further link failure occurs. The avalanche size is obtained by counting the number of failed links.

4.2.2 Avalanche mitigation strategy

Various methods of reducing the avalanche size in the ML model have been implemented. For instance, after an initial failure but before the failure propagates to other nodes, selected nodes are removed to reduce the avalanche size [123, 240]. However, the initial failure often propagates so rapidly that it is impossible to remove nodes involved in significant propagation of the failure. As another strategy, a parameter a is assigned to each node under the constraint $\sum_i a_i = \text{const}$ [336]. However, there is

no way to adjust the capacity of every node to an appropriate value to minimize the avalanche size.

In this study, we compare the performance of various strategies that minimize the avalanche size when nodes are reinforced. To simplify the problem, we suppose that reinforced nodes never fail unless they are intentionally chosen as the initial failure of the cascade; however, the effectiveness of the strategies should be maintained even when reinforcement is finite.

The problem with reinforcement is analogous to the problem of vaccination against epidemic contagion, where epidemic spreading is minimized by vaccination; however, there is a crucial difference. Specifically, during epidemics, a node is eliminated after vaccination, and the centrality measures of the network are recalculated to determine the next node to be vaccinated [6, 62, 63, 230, 340]. This process is repeated until the feasible number of vaccinations is reached. In the avalanche mitigation problem, however, reinforced nodes can remain in the power flow; they simply do not fail even if the power flow increases.

Avalanche mitigation poses a novel type of vaccination problem in which the effects of reinforced nodes on the avalanche are complex. A unique feature of the avalanche mitigation problem is the paradoxical effect of reinforcement. In some cases, reinforcement of a node can increase the avalanche size. As shown in Fig. 4.3, even if one correctly predicts that node B is at risk and reinforces it, reinforcement results in a significant increase in avalanche size. Therefore, reinforcement of nodes without a systematic strategy can be counterproductive.

To characterize the role of each node in the avalanche dynamics, we define a binary variable x_j^i , which is 1 if node j fails in an avalanche triggered by node i and is 0 otherwise ($x_i^i = 1$). Then, the avalanche fraction of node i is given by $s_i = \sum_j x_j^i / N$. This quantity represents the effect of node i in cascading failures. The failure fraction f_j of node j is defined as $f_j = \sum_i x_j^i / N$ and represents the probability that node j fails in isolation or because of triggering by another node. These two quantities characterize

the role of each node in cascading failures. For instance, if $s_i \gg 0$ but $f_i \ll 1$, then node i triggers a large avalanche, but its effect on the avalanche is rather limited.

We define the AC of node i as

$$A_i = s_i \left(f_i - \frac{1}{N} \right), \quad (4.3)$$

where the factor $1/N$ accounts for the case where node i is selected as the initial trigger of the avalanche. Fig. 4.9 shows that the avalanche size can be reduced by reinforcing nodes with high ACs.

We define the performance measure R_m of each avalanche mitigation strategy as

$$R_m = \int_0^1 \varphi(r) dr \simeq \sum_i \frac{\varphi(r_i) + \varphi(r_{i+1})}{2} \Delta r, \quad (4.4)$$

where

$$\varphi(r) = \frac{\bar{s}(r) - 1/N}{\bar{s}(0) - 1/N}. \quad (4.5)$$

Here r denotes the fraction of reinforced nodes, and $\bar{s}(r)$ is the mean avalanche fraction; that is, $\sum_i s_i(r)/N$ when a fraction r of nodes are reinforced according to the avalanche mitigation strategy. The term $1/N$ is needed to exclude initial failure from s . Consequently, $\varphi(0) = 1$, $\varphi(1) = 0$, and $0 \leq R_m \leq 1$. As R_m decreases, the avalanche mitigation strategy becomes more efficient. To calculate R_m , we use $\Delta r = 0.01$ for small networks ($N \leq 1000$) and $\Delta r = 0.1$ for large networks ($N > 1000$) to avoid excessive computational cost.

Fig. 4.9 shows the $\varphi(r)$ values of various avalanche mitigation strategies in the SHK network. The area under each curve represents the performance measure R_m . Reinforcing nodes with high network centralities, such as degree centrality, eigenvector centrality, and BC, blocks the avalanche dynamics more effectively than random reinforcement. The strategy based on an avalanche fraction s is effective in a small r range. The strategy based on the failure fraction f is even less effective than random

reinforcement for small r . However, for sufficiently large r , strategies based on s and f both become more effective than other strategies except that based on the AC, and the cascading failure is reduced to zero at a certain value r_c . This value corresponds to the threshold of herd immunity in epidemics. The strategy based on the AC that takes into account both the avalanche and failure fractions becomes the most effective strategy among all the strategies in the broad range $r < r_c$.

Table 4.1 lists the performance measure R_m for various avalanche mitigation strategies in the SHK networks of various sizes and real-world electrical power grids. The AC-based strategy exhibits fairly good performance compared with all other methods. We remark that the BC-based strategy is also highly effective. However, it is not scalable because of the logarithmic correction of the computational complexity $O(N^2 \log N)$. Thus, strategies using scalable centrality measures such as degree centrality and eigenvector centrality can be employed in the GNN.

4.2.3 Graph neural network (GNN)

The AC can be used for effective avalanche suppression; however, it has high computational complexity as high as $O(N^3 \log N)$. Thus, it cannot be calculated directly in large networks. To overcome this problem, we apply the GNN, a deep learning algorithm that can be used for graph-structured data [293]. We constructed a GNN structure applicable to networks of different sizes. This GNN was trained using the ACs obtained by simulations of small networks. Then, the AC of each node in large networks, where simulations using the ML model are not feasible, can be predicted.

We used the SHK network, a synthetic network mimicking a power grid, to simulate avalanche failures. The network size was selected at random from 100 to 999 in uniform increments. The dataset consists of 10^4 data.

The GNN is a type of space-based convolutional GNN [346] composed of graph isomorphism network (GIN) layers [348], as shown in Fig. 4.5. In the GIN layers, the hidden feature y_i of node i is updated according to its own value and those of the

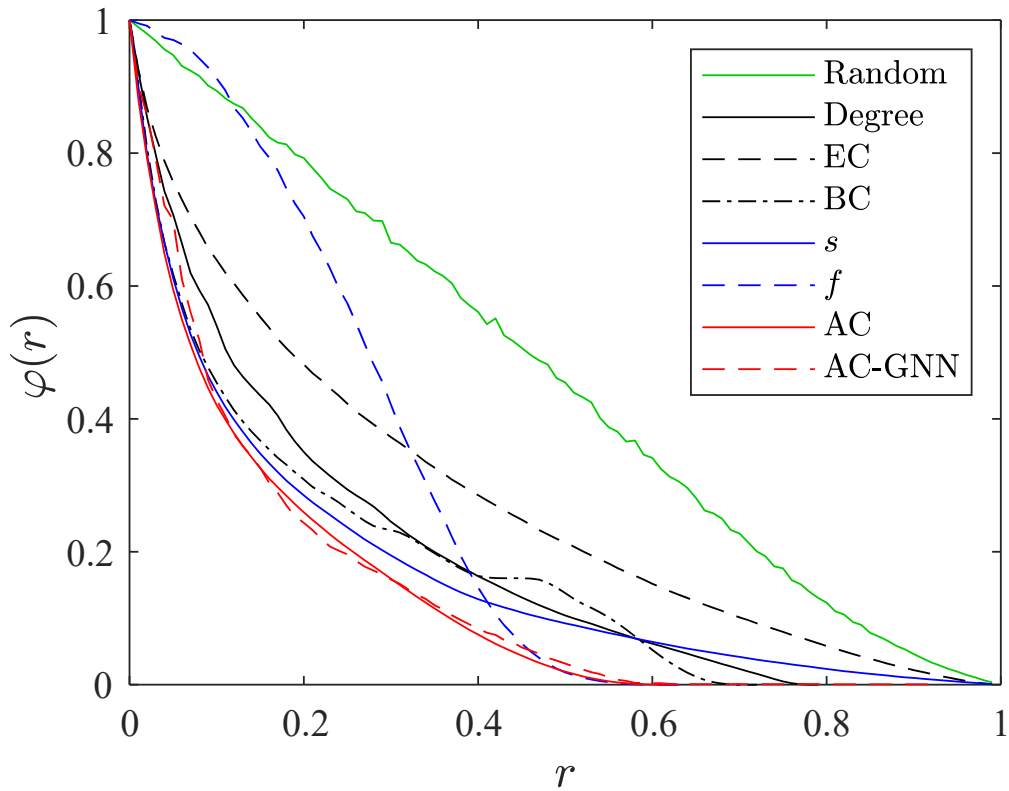


Figure 4.4: Performance of avalanche mitigation strategies in the SHK network of size $N = 1000$. Degree, eigenvector centrality (EC), betweenness centrality (BC), avalanche fraction (s), failure fraction (f), avalanche centrality (AC), and GNN estimation of avalanche centrality (AC-GNN) are employed for avalanche mitigation strategies. Nodes are reinforced in descending order of the corresponding centrality measure. The area under each curve is the performance measure R_m .

Table 4.1: Performance measure R_m of vaccination strategies: random vaccination, vaccination in descending order of degree, eigenvector centrality (EC), betweenness centrality (BC), avalanche size, failure fraction, avalanche centrality (AC), and GNN prediction of AC. Smaller values indicate better mitigation. The most efficient mitigation strategy is marked by bold.

Network	Random	Degree	EC	BC	Avalanche fraction	Failure fraction	AC	AC (GNN-pred)
SHK ($N = 1000$)	0.4593	0.1923	0.2767	0.1763	0.1691	0.2697	0.1338	0.1399
SHK ($N = 2000$)	0.4547	0.1733	0.2582	0.1624	0.1560	0.3102	0.1273	0.1423
SHK ($N = 4000$)	0.4490	0.1508	0.2423	0.1415	0.1360	0.3569	0.1126	0.1206
SHK ($N = 8000$)	0.4458	0.1322	0.2199	0.1248	0.1202	0.4431	0.1009	0.1140
Spain	0.4887	0.3347	0.3604	0.2648	0.2815	0.2410	0.2320	0.2610
France	0.4855	0.3727	0.4593	0.2477	0.2633	0.2171	0.2177	0.2263
UK	0.4619	0.4220	0.2720	0.3607	0.3203	0.2715	0.2787	0.3864

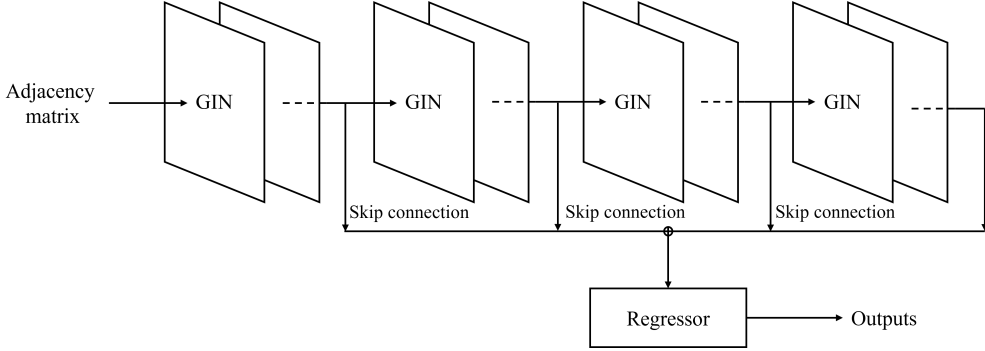


Figure 4.5: Structure of GNN. Only the adjacency matrix of the network is input, and the features of all nodes are initially constant. Batch normalization and ReLU activation are applied between each pair of adjacent GIN layers, but they are omitted from the diagram for simplicity. A short skip connection is applied between each pair of adjacent GIN layers, and an elementwise average is obtained before the regressor. The regressor is implemented as a single-layer perceptron followed by a sigmoid function for normalization.

nearest-neighbor nodes of i , that is, $\{y_j\}$, where $j \in \text{n.n. of } i$ as

$$y'_i = h_{\Theta} \left((1 + \epsilon)y_i + \sum_{j \in \text{n.n. of } i} y_j \right), \quad (4.6)$$

where ϵ is a constant and h_{Θ} is taken to be a two-layer perceptron for the trainable parameter Θ . The GNN also has a batch normalization layer [139] and a rectified linear unit (ReLU) activation function between subsequently GIN layers.

The ML model is based on the BC, which contains a global connection information of network. Therefore, the GNN must consider not only local information around a given node, but also the global information of the entire network. As shown in Eq (4.6), the GIN layer is used for one-hop calculation. y_i is updated locally. To address the global features at longer hopping distances, many layers should be stacked. This deep structure may cause the so-called vanishing gradient problem [124]. To mitigate this problem and to take into account the effect of nodes at various hopping distances [2, 328], the short skip connection algorithm [309] is applied for every pair of adjacent

Table 4.2: Hyper parameters used to train GNN.

name	value
node embedding dimension	128
batch normalization momentum	0.1
optimizer	RMSprop
learning rate	10^{-3}
loss	MAE
L2 value	10^{-5}

layers. Table. 4.2 lists the hyperparameters used to train the GNN.

To perform avalanche mitigation in the GNN framework, it is necessary to rank the ACs of the nodes. This information makes it possible to handle all reinforcement states because one can choose a node set depending on the available reinforcement resources. Because the AC distribution is highly skewed, simple node feature regression is not an appropriate approach. Instead, we applied the quantile transformation to the ACs and then the min-max scale to the obtained values for normalization. The validation and test datasets were scaled using the scaler fitted to the training dataset.

Let z_i is an observable, for example, the AC of node i . $\text{Rank}(i)$ is defined according to the relative size of z_i among others. $\sigma(i)$ is the estimated rank of z_i using the GNN. A pair of observables (z_i, z_j) is concordant if the order of their ranks is correctly estimated: for the $\text{Rank}(i) < \text{Rank}(j)$, $\sigma(i) < \sigma(j)$. The pair is discordant, otherwise.

A well-known metric for ordinal association is the Kendall rank correlation or Kendall’s tau [166], which is defined as

$$\tau = \frac{n_c - n_d}{n_c + n_d}, \quad (4.7)$$

where n_c and n_d denote the numbers of concordant and discordant pairs, respectively.

This Kendall’s tau is expressed explicitly as

$$\tau = \frac{2}{N(N-1)} \sum_{i < j} \text{sign}(z_i - z_j) \text{sign}(\sigma(j) - \sigma(i)). \quad (4.8)$$

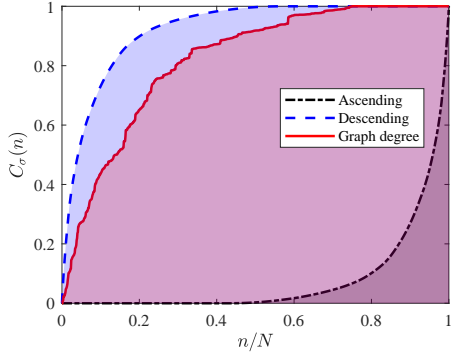


Figure 4.6: The cumulative fraction $C_\sigma(n)$ of AC as a function of n on an SHK network of size $N = 1000$. The mean cumulative fraction $\langle C_\sigma \rangle$ is the area under the cumulative fraction $C_\sigma(n)$ curve. A large $\langle C_\sigma \rangle$ means that the ranking estimation performs well. Red solid curve is obtained by taking the estimated rank σ as the graph degree, i.e., the number of connections, of each node. The estimated curve lies between those of the descending order (best case) and ascending order (worst case).

In the calculation of Kendall's tau, the incorrect ranking of two values that differ greatly receives the same penalty as the incorrect ranking of two similar values. However, the former error is likely to be disproportionately detrimental (in avalanche mitigation, for example). This problem may be more important for highly heterogeneous data.

Accordingly, we propose a new quantity, the cumulative fraction $C_\sigma(n) \equiv \sum_{i=1}^n z_{\sigma(i)} / \sum_{j=1}^N z_j$. This represents the contribution of n the most highly estimated z_i s in the sum of all values in the data. The average of $C_\sigma(n)$ over n (denoted as $\langle C_\sigma \rangle$) represents the overall performance of the σ estimation.

$$\begin{aligned}
 \langle C_\sigma \rangle &= \sum_{n=1}^N \frac{1}{N} \sum_{i=1}^n \frac{z_{\sigma(i)}}{\sum_{j=1}^N z_j} \\
 &= \sum_{i=1}^N \frac{N-i+1}{N} \frac{z_{\sigma(i)}}{\sum_{j=1}^N z_j}.
 \end{aligned} \tag{4.9}$$

Fig. 4.6 shows the behavior of $C_\sigma(n)$ as a function of n . $C_\sigma(n)$ is always between the two extremes: the descending and the ascending orders of $\text{Rank}(i)$ ($i = 1, \dots, N$).

Accordingly, we define the normalized $\langle C_\sigma \rangle$ (denoted as $\langle C_{\sigma,N} \rangle$) as

$$\langle C_{\sigma,N} \rangle \equiv \frac{\langle C_{\sigma,N} \rangle - \langle C_{\text{ascending}} \rangle}{\langle C_{\text{descending}} \rangle - \langle C_{\text{ascending}} \rangle}. \quad (4.10)$$

Then, $0 \leq \langle C_{\sigma,N} \rangle \leq 1$.

We also use R^2 score to evaluate the prediction of z_i value, which is defined as follows [104]:

$$R^2 \equiv 1 - \frac{\sum_{i=1}^N (z_i - \hat{z}_i)^2}{\sum_{i=1}^N (z_i - \bar{z})^2}, \quad (4.11)$$

where \hat{z}_i is the estimated value of z_i and \bar{z} is the average of all z_i .

Fig. 4.7 shows the performances of the R^2 score, $\langle C_{\sigma,N} \rangle$, and Kendall's tau for the prediction of z_i obtained by the GNN. Although the R^2 score decreases rapidly as the network size increases ($N = 1000 - 8000$), the $\langle C_{\sigma,N} \rangle$ and Kendall's tau values of the GNN do not change significantly as N increases. This result suggests that R^2 score fails to predict the AC values of networks larger than those in the training dataset. As shown in Fig. 4.9 and Table. 4.1, node reinforcement according to the AC predicted by the GNN is also effective for suppressing avalanches in the SHK model as well as in several real-world electric power grids of Spain, France, and UK. We remark that the GNN was trained on the SHK model, however, the real-world electrical power grids were not trained.

4.2.4 Conclusion

In summary, we introduced the concept of the avalanche centrality (AC) of each node in networks and showed that reinforcing nodes in descending order of AC is effective for suppressing the nonlocal avalanche propagation in electrical power grids. However, the calculation of the AC has a high computational cost. Therefore, we employed a GNN to address this problem. We trained the GNN with the ACs of small networks and showed that it can be used for larger networks where the direct calculation of the ACs is not feasible. The GNN predicts the descending order of AC in large networks,

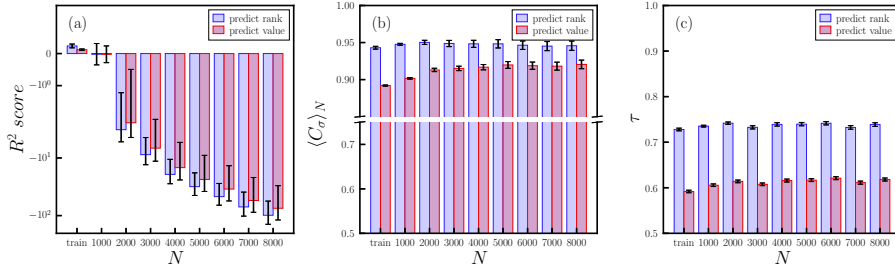


Figure 4.7: Performance of the GNN prediction in large networks in the range $N = 1000 - 8000$, which is trained in various network sizes from 100 to 999. All the results are averaged over 4 different GNNs with different random seed. (a) R^2 scores for different system sizes: the R^2 score is not appropriate to predict the performance because the AC values are distributed very skewed. (b) and (c) $\langle C_{\sigma,N} \rangle$ and Kendall's tau for different sizes, respectively. (Blue, dark bars) the GNN predicts ranks of ACs using a quantile scaled dataset. (Orange, light bars) the GNN predicts values of ACs using a raw dataset. Rank prediction using the quantile scaling marked in blue is better and more consistent than value prediction marked in orange. The representation by $\langle C_{\sigma,N} \rangle$ in (b) is more appropriate compared with that by the Kendall's Tau in (c).

allowing the effective suppression of avalanche failures in electrical power grids. Conventionally, the Kendall's tau was used as a performance measure of ranking estimation. However, this measure contains intrinsic drawback: the incorrect estimation of the order of two values that differ greatly is penalized similarly to that of the ranking of two slightly different values. To overcome such a limitation, here, we introduced a new performance measure denoted as $\langle C_{\sigma} \rangle$ for ranking prediction. This new performance measure successfully reflects the importance of the ordering of two values that differ greatly as shown in Fig 4.6.

In network epidemiology, the microscopic Markov chain approximation (MMCA) [110, 111, 232] was introduced to bypass the computationally cumbersome Monte Carlo simulation. The result of MMCA was then used to calculate epidemic prevalence or to formulate vaccination strategies [143, 144, 230]. This method, however, cannot be used to approximate avalanche dynamics that propagates nonlocally, for example, in the ML model. Therefore, we think the GNN introduced here may replace the role of the MMCA in the analysis of nonlocal avalanche dynamics and the development of

mitigation strategy, for example, for the blackout in electrical power grid.

4.3 Epidemic control using graph neural network ansatz

Epidemics do not occur randomly; instead, they spread through structured interactions among the host population. Network theory provides an integrated framework to study the effects of the structure of interactions on dynamical processes [12, 16, 26, 27, 81]. For epidemic processes, individuals are represented as nodes, and contacts between individuals are represented as edges (links) in the network. Traditional theories of epidemic spreading ignored network effects [9, 165]; however, extensive research devoted to network epidemiology demonstrated that the structural properties of network such as heterogeneity of degree (number of edges a node has) significantly affect the spreading of epidemics [90, 235, 262, 264, 266]. Such network effects have significant implications because most real-world social systems exhibit highly complex connectivity patterns characterized by heavy-tailed distributions [12, 26, 27, 81]. Network epidemiology has also been applied to social spreading processes such as the spread of innovations, rumors, and opinions [88, 164, 237, 342].

Containing, mitigating, and preventing the spread of epidemics is a crucial goal in mathematical epidemiology, therefore, extensive research has been devoted to developing effective vaccination strategies in complex networks [52, 62, 63, 126, 143, 220, 230, 262, 268, 296, 326, 339, 340]. Effective vaccination strategies aim to vaccinate the optimal set of nodes in the network to minimize the damage caused by epidemic diseases such as the total number of infections or epidemic mortality. It has been found that the effectiveness of a vaccination highly depends on which nodes we choose to vaccinate even if we choose the same number of nodes. This problem is relevant to the current situation where the number of effective SARS-CoV-2 vaccine shots is less than the total population in most countries, especially in developing countries [318]. Moreover, the vanishing epidemic threshold of scale-free networks [264, 266] suggests that such a pandemic will presumably occur repeatedly; therefore, it is crucial to be

prepared for another vaccine shortage.

Graph neural networks (GNNs) are deep learning–based methods that operate on graphs or networks where other types of machine-learning methods such as convolutional neural networks (CNNs) or recurrent neural networks (RNNs) cannot be implemented because of the irregular and non-Euclidean nature of the complex network. GNN has become a widely used method for network analysis because of its convincing performance in various fields, such as estimation of molecular properties [121, 356], drug discovery [112], and traffic forecasting [32, 285]. In the epidemic field, GNNs have been employed for the prediction of disease prevalence [75, 242, 256], identification of patient zero [300], and estimation of epidemic state using limited information [323]. Few studies have developed dynamic epidemic control schemes that identify epidemic hotspots from the partially observed epidemic state of each individual [233, 313].

Here, we propose a framework for vaccination strategy in complex networks based on GNN. By employing graph neural network ansatz (GNNA) and microscopic Markov chain approach (MMCA) [110, 111, 232], we can determine the optimal strategy through few mean-field calculations. Note that comparing the performances of two similar vaccination strategies generally requires an excessive number of Monte Carlo epidemic simulations. This framework can be implemented to formulate effective vaccination strategies, tailored to the available amount of vaccine shots, for various epidemic processes in a complex network. If the properties of each node, such as contagion rate, recovery rate, or fatality rate, are distinct, the GNNA can systematically consider this information to formulate an optimal strategy. Such a situation wherein the nodes of a network possess distinctive characteristics is relevant in real-world epidemics. For instance, the case fatality rate of COVID-19 varies significantly according to age [13, 22, 169, 206, 209, 223, 303]; hence, it is not trivial to determine whether senior population with high fatality rate or young population with high contact rate should be primarily vaccinated to minimize the epidemic mortality [146]. The age-

dependent efficacy and probability of severe reaction to vaccines further complicate the issue [184, 280]. However, there has been no vaccination strategy that systematically takes the epidemic properties of each node into account.

To prove the validity of our algorithm, we test this method for network dismantling, the susceptible-infected-susceptible (SIS) model with homogeneous and heterogeneous epidemic parameters, and the susceptible-infected-recovered-dead (SIRD) model in many real-world networks with up to 320K nodes and 1M edges. We also extend this framework to edge immunization, which represents non-pharmaceutical epidemic containment measures such as travel regulations and social distancing. We compare the performance of the proposed framework with the existing centrality-based methods. The proposed method outperforms the centrality-based vaccination strategies at all levels of vaccine supply. Moreover, because GNNA considers the properties of each node and tailors the vaccination strategy to the specific amount of vaccine available, it allows us to find new phenomena such as the transition of optimal strategies from high-fatality to high-BC strategies according to the level of vaccine supply.

4.3.1 Model

SIS model with homogeneous and heterogeneous contagion/recovery rate

The SIS model and contact process are among the most extensively studied epidemic models in complex network [15, 90, 91, 137, 149, 230, 262, 264]. Recently, the SIS model where the recovery rate varies from node to node was introduced [53, 89, 279]. We extend this model and let the contagion rate that each node infects others to be varying as well. Such variability of epidemic parameters is a natural assumption because the prognosis of an epidemic disease depends on the age and other factors of each individual.

In the SIS model, each node is either in the susceptible (S) or infected (I) state. At each time step, each infected node j infects its neighbors with probability β_j , hence

susceptible node i turns into the infected state with probability

$$P_i = 1 - \prod_{j \in \text{n.n. of } i} (1 - \beta_j), \quad (4.12)$$

where the index j runs over all the nearest neighbors of node i . An infected node turns into the susceptible state with probability μ_i . If $\beta_i = \beta$ and $\mu_i = \mu$, the equation is reduced to the traditionally studied SIS model with homogeneous contagion and recovery rate. For heterogeneous cases, the distribution of the contagion and recovery rates can be arbitrary, but in this study, the contagion rate and recovery rate of node i are uniformly distributed between 0 and β , and 0 and μ , respectively.

We start the simulation with the fully infected system and evolve the system for $t_{\text{relax}} = 2 \times 10^4$ so that the system reaches its stationary state. Then, the density of infection is sampled for $t_{\text{sample}} = 2 \times 10^4$. Quasistationary method [90, 91] and other approaches [158] have been employed to obtain the steady-state of the epidemic dynamics in previous studies. Here, we apply a small conjugated field $h_i = 10^{-3}\mu_i$ on each node i to keep the system in the active state [217]. The intensity of the conjugated field is irrelevant as long as the value is very low.

SIRD model

Although mortality is one of the significant damage caused by epidemic diseases, the susceptible-infected-recovered (SIR) model cannot be used to study the vaccination strategy to minimize epidemic mortality, because recovery and death are not distinguished in the SIR model. The SIRD model was therefore introduced as a minimal epidemic model to study epidemic mortality.

In the SIRD model, each node is in either susceptible (S), infected (I), recovered (R), or dead (D) states. The infection occurs by the same rule with the SIS model. A

susceptible node turns into the infected state with probability

$$P_i = 1 - (1 - \beta)^{n_i^I}, \quad (4.13)$$

where n_i^I is the number of infected neighbors of node i . At each time step, an infected node turns to the R state with probability $(1 - \text{IFR}_i)\mu$ and to D state with probability $\text{IFR}_i \cdot \mu$.

Recovery and death occur with ratio $(1 - \text{IFR}_i) : \text{IFR}_i$, therefore, the infection fatality rate (IFR) of node i is IFR_i . IFR is defined as the ratio of deaths caused by disease to the total number of people infected with the disease. The fatality rate of epidemic diseases such as COVID-19 significantly depends on age and other morbidity factors [161,210]. Therefore, it is important to study the SIRD model where the fatality rate varies from node to node. We start the simulation after infecting a small fraction 10^{-3} of nodes in the network. All the reactions (infection, recovery, and death) include an infected node; therefore, if the number of infected nodes becomes zero, then the epidemic dynamics ends. In this study, we sampled the mortality rate for $n_{\text{sample}} = 2 \times 10^4$.

Construction of a multiplex network from contact data

To investigate the effectiveness of the vaccination strategies on real-world epidemic diseases, we construct a multiplex network from human contact patterns between age groups and the degree distribution, and the age-dependent IFR of COVID-19 was implemented. The network is constructed [5] from the contact matrix $M_{\alpha\beta}$, which is the average number of contacts that an individual in group α has with individuals in group β , obtained by survey [234]. The human contact degree distribution follows negative binomial distribution NB (r, p) with $r \simeq 0.36$ [239]. The parameter p_β of age group β is determined by the average degree $\langle k \rangle_\beta = \sum_\alpha M_{\alpha\beta}$: $p_\beta = 1 - \langle k \rangle_\beta / (r + \langle k \rangle_\beta)$.

The data was collected for people of age 0 to 84, and people of age 85 and above

were aggregated. We extend the data to people of age 99 by assuming that people of age 85 and above exhibit identical contact patterns. First, we draw the degree of each node from the degree distribution $\text{NB}(r, p_\beta)$ of the corresponding age group, and place "stubs" of that number. We then select a stub with equal probability and connect it with another stub, which is selected with probability proportional to $M_{\alpha\beta}$, where α is the age group of the first selected stub and β is that of the second selected stub. This iteration is repeated until only one or no stub is left (If only one stub is left, it cannot be matched with any other stub).

The IFR of each node is calculated based on meta-analysis of medical literature [206], where the age dependent IFR is calculated as

$$\log_{10} \text{IFR} = (-3.27 \pm 0.07) + (0.0524 \pm 0.0013) \text{ age}. \quad (4.14)$$

4.3.2 Vaccination strategy

Graph neural network ansatz (GNNA)

We aim to vaccinate the optimal set of q nodes to minimize the damage caused by an epidemic process, such as the total number of infections or infectious deaths. A vaccinated node does not get infected even if it has contact with infected nodes. We suppose that each node's fitness to be vaccinated in the network can be expressed by an L -layered GNN, namely GNNA.

$$\mathbf{s}_i^{(\ell)} = \text{Agg} \left(\mathbf{s}_i^{(\ell-1)}, \cup_{j \in \text{n.n. of } i} \mathbf{s}_j^{(\ell-1)} \right), \quad (4.15)$$

and

$$\mathbf{s}_i^{(0)} = \mathbf{x}_i, \quad (4.16)$$

$$\mathbf{z}_i = \mathbf{s}_i^{(L)}, \quad (4.17)$$

where Agg is the function that aggregates the information from the neighbors of each node, \mathbf{x}_i is the vector of node features of node i such as its contagion rate, recovery rate, fatality rate, efficacy of vaccine, or probability of having a severe reaction to the vaccine. $s_i^{(\ell)}$ is the vector of hidden state of node i in layer ℓ , and \mathbf{z}_i is the output of the GNN. Various functions have been used for the aggregation function [120, 173, 330]. Here, we take the form

$$s_i^{(0)} = \sigma \left(w_0^{(0)} + w_1^{(0)} x_{i1} + w_2^{(0)} x_{i2} + \dots \right), \quad (4.18)$$

$$s_i^{(1)} = \sigma \left(w_0^{(1)} + w_1^{(1)} s_i^{(0)} + w_2^{(1)} k_i^{w_4^{(1)}-1} \sum_{j \in \text{n.n. of } i} (s_j^{(0)} + w_3^{(1)}) \right), \quad (4.19)$$

\vdots

$$s_i^{(L)} = \sigma \left(w_0^{(L)} + w_1^{(L)} s_i^{(L-1)} + w_2^{(L)} k_i^{w_4^{(L)}-1} \sum_{j \in \text{n.n. of } i} (s_j^{(L-1)} + w_3^{(L)}) \right) \quad (4.20)$$

where k_i is the degree of node i , and we choose leaky rectified linear unit (ReLU) for the activation function $\sigma(\cdot)$. The introduction of $w_4^{(\ell)}$ allows GNN to include both the summation ($w_4^{(\ell)} = 1$) and average ($w_4^{(\ell)} = 0$) for the aggregation. The permutational invariance among neighboring nodes is retained. In this study, we use $L = 2$. The output $s_i^{(L)} = s_i^{(2)}$ is the fitness of node i to be vaccinated. This fitness effectively works as a centrality measure tailored to the epidemic process of the interest. We vaccinate q nodes with the highest fitness.

The ansatz Eqs. 4.18–4.20 includes various vaccination strategies. For instance, if

$$w_{r_0}^{(0)} = 1, \quad (4.21)$$

$$w_r^{(0)} = 0 \quad \forall r \neq r_0, \quad (4.22)$$

$$w_1^{(\ell)} = 1 \quad \forall \ell > 0, \quad (4.23)$$

$$w_r^{(\ell)} = 0 \quad \forall r \neq 1, \ell > 0, \quad (4.24)$$

the fitness of each node becomes equal to its node feature x_{ir_0} , and we vaccinate the

nodes in descending order of their feature (fatality rate of the node, for instance). If

$$w_0^{(0)} = 1, \quad (4.25)$$

$$w_r^{(0)} = 0 \quad \forall r > 0, \quad (4.26)$$

$$w_0^{(1)} = w_1^{(1)} = w_3^{(1)} = 0, \quad (4.27)$$

$$w_2^{(1)} = w_4^{(1)} = 1, \quad (4.28)$$

$$w_1^{(\ell)} = 1 \quad \ell > 1, \quad (4.29)$$

$$w_r^{(\ell)} = 0 \quad \forall r \neq 1, \ell > 1, \quad (4.30)$$

the fitness equals the degree of each node. Other strategies such as averaging the node features of the nearest or second-nearest neighbors of a node can be represented by the Eqs. 4.18–4.20.

Because the weights $w_r^{(\ell)}$ are shared over the entire network, the number of parameters of GNNA is $5L + m + 1$, where m is the number of node features. Moreover, the actual dimension of the manifold represented by GNNA is lower. The output of GNNA, which is the vaccination strategy, is invariant under the following transforms for each $0 \leq \ell \leq L$ (because if the input of leaky ReLU scales by a factor of α , so does the output):

$$w_r^{(\ell)} \rightarrow \alpha w_r^{(\ell)} \quad \forall r, \quad (4.31)$$

$$w_0^{(\ell')} \rightarrow \alpha w_0^{(\ell')} \quad \forall \ell' > \ell, \quad (4.32)$$

$$w_3^{(\ell')} \rightarrow \alpha w_3^{(\ell')} \quad \forall \ell' > \ell, \quad (4.33)$$

while other weights are kept unchanged. Additionally, because we are only interested in the rank of $s_i^{(L)}$, the parameter $w_0^{(L)}$ is irrelevant. The dimension of the manifold is, therefore, $4L + m$. Moreover, when there is no node feature, $w_3^{(1)}$ becomes irrelevant because $s_j^{(0)}$ is constant, and the dimension is $4L - 1$. Therefore, GNNA is highly scalable to large networks.

We can extend GNNA to edge immunization by aggregating the fitness of nodes in each edge. Because an edge is always connected to two nodes, we employ two-dimensional Taylor series expansion for the aggregation function. The fitness $s_{(i,j)}$ of an edge (i, j) is then

$$s_{(i,j)} = w_0^{(L+1)} \left(s_i^{(L)} + s_j^{(L)} \right) + w_1^{(L+1)} \left(s_i^{(L)2} + s_j^{(L)2} \right) + w_2^{(L+1)} s_i^{(L)} s_j^{(L)} + \dots, \quad (4.34)$$

where the coefficients are chosen so that there is a symmetry between i and j . Here, we only use quadratic terms $w_0^{(L+1)}$, $w_1^{(L+1)}$, and $w_2^{(L+1)}$. Therefore, three additional parameters are required for the edge immunization.

Microscopic Markov chain approach (MMCA)

The stochasticity of the epidemic processes brings a challenge to the optimization problem. Because of the fluctuation in the results of the epidemic simulations, the average of the sampled density of infection can exhibit a low value even if the expectation value is not low. If the gradient descent method is directly implemented, the trajectory of the optimization may be forever affected by a low value once obtained because of the fluctuation. Also, to compare the performances of two similar vaccination strategies, which likely have similar expectation values of the density of infection, an excessive number of Monte Carlo simulations have to be performed. A point with high fluctuation can be selected as the optimal point even if the expectation value is not low.

To avoid such issues, we employ MMCA [110, 111, 232], to analytically estimate the performance of the vaccination strategies. MMCA solves the mean-field equation for each node in the network to provide more accurate predictions of the epidemic prevalence than heterogeneous mean-field (HMF) theory [235, 264, 266]. Because there is no fluctuation in the result of the MMCA, the aforementioned problem

can be avoided. We show that even when the GNNA is optimized with MMCA, the resulting vaccination strategies effectively minimize the density of infection of the stochastic epidemic model.

The MMCA tracks the probability $P_i^X(t)$ of each node i being in state X at time t [110, 111, 232]. For SIS model, we track $P_i^I(t)$. The MMCA equations of the SIS model with heterogeneous contagion/recovery rate is expressed

$$P_i^I(t+1) = P_i^S(t) \left[1 - \prod_{j \in \text{n.n. of } i} (1 - \beta_j P_j^I(t)) \right] + (1 - \mu_i) P_i^I(t), \quad (4.35)$$

and $P_i^S(t) = 1 - P_i^I(t)$. For the traditionally studied SIS model with homogeneous contagion and recovery rate, $\beta_i = \beta$ and $\mu_i = \mu$. We solve Eq. 4.35 for its fixed point to determine the stationary state.

For SIRD model, we track $P_i^I(t)$, $P_i^R(t)$, and $P_i^D(t)$. The MMCA equations of the SIRD model is expressed

$$P_i^I(t+1) = P_i^S(t) \left[1 - \prod_{j \in \text{n.n. of } i} (1 - \beta P_j^I(t)) \right] + (1 - \mu) P_i^I(t), \quad (4.36)$$

$$P_i^R(t+1) = (1 - \text{IFR}_i) \mu P_i^I(t), \quad (4.37)$$

$$P_i^D(t+1) = \text{IFR}_i \cdot \mu P_i^I(t), \quad (4.38)$$

and $P_i^S(t) = 1 - P_i^I(t) - P_i^R(t) - P_i^D(t)$. We solve Eqs. 4.36–4.38 until $\sum_i P_i^I(t) < \epsilon = 10^{-4}$, then calculate the mortality rate $\sum_i P_i^D/N$.

Gaussian random walk–based optimization

The loss surface of GNNA is distinct from the loss landscape of usual neural networks [207]. The loss, which is the density of infection calculated by MMCA in this case, is illustrated in Fig. 4.8 for the SIS model. It is flat almost everywhere; at certain lines, there is a leap. This is because the parameters of the GNNA are continuous but the vaccination strategy is discrete. For a small perturbation of the weights, except for

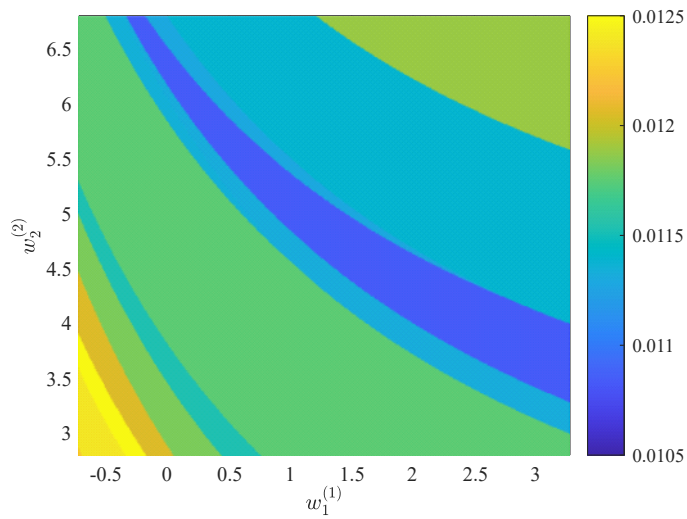


Figure 4.8: Density of infection of SIS model calculated by MMCA as the function of weight parameter $w_r^{(\ell)}$ of GNN. The plot illustrates the loss surface projected on the $w_1^{(1)}-w_2^{(2)}$ plane. The value is flat everywhere except on certain lines. The flat regions each correspond to an identical vaccination strategy; therefore, the objective function does not vary in the region. The vaccination is tested in the airline network with the contagion rate $\beta = 0.2$, recovery rate $\mu = 0.5$, and vaccination rate $q/N = 0.1$.

special cases, the vaccination strategy formulated by the GNNA is invariant, as is the objective function. Therefore, the gradient descent and other gradient descent–based optimization algorithms such as SQP [100] and the Nelder–Mead method [245] cannot be used in this case.

GNNA reduces the exponentially large dimension of the space of the vaccination to 7–10 and allows Gaussian random walk to effectively optimize the vaccination strategies. Initially, the weights of the provisional solution are set as $w_0^{(0)} = 1$, $w_1^{(\ell)} = 1$ for all $\ell > 0$, and zero if otherwise. This way, the fitnesses of all nodes are equal to one. At each step, we perturb the weights $w_r^{(\ell)} \rightarrow w_r^{(\ell)} + \omega_r^{(\ell)}$, where $\omega_r^{(\ell)}$ independently follows the Gaussian distribution with zero mean: $\omega_r^{(\ell)} \sim \mathcal{N}(0, \sigma^2)$. The standard deviation σ is initially 0.5 and decreases by a factor of $1 - 5/n_{\text{iter}}$ at each step (the standard deviation becomes 0.003 at the end of the iteration). This way, as the iteration progresses, we can focus on finding a more detailed position of the minimum in the loss landscape. There is a probability that the perturbed weight returns the same set of nodes as the provisional solution. In such cases, we find another position without calculating the objective function again (Because the result is the same as the provisional solution).

4.3.3 Results

Effectiveness of the vaccination strategy

Vaccinating nodes with high centrality measures has been reported to effectively reduce epidemics in complex networks. One example of such centrality measure is *betweenness centrality* (BC), or *load* [105,246]. This measure is related to the number of shortest paths passing through the node or edge. It was found that immunizing nodes or edges with high BC is effective in containing epidemics [63, 296]. However, the computational complexity for calculating the BC is $O(N^2 \log N)$. This significantly limits its capability to be used in large networks.

As an alternative to BC, collective influence (CI) was introduced [238]. The CI

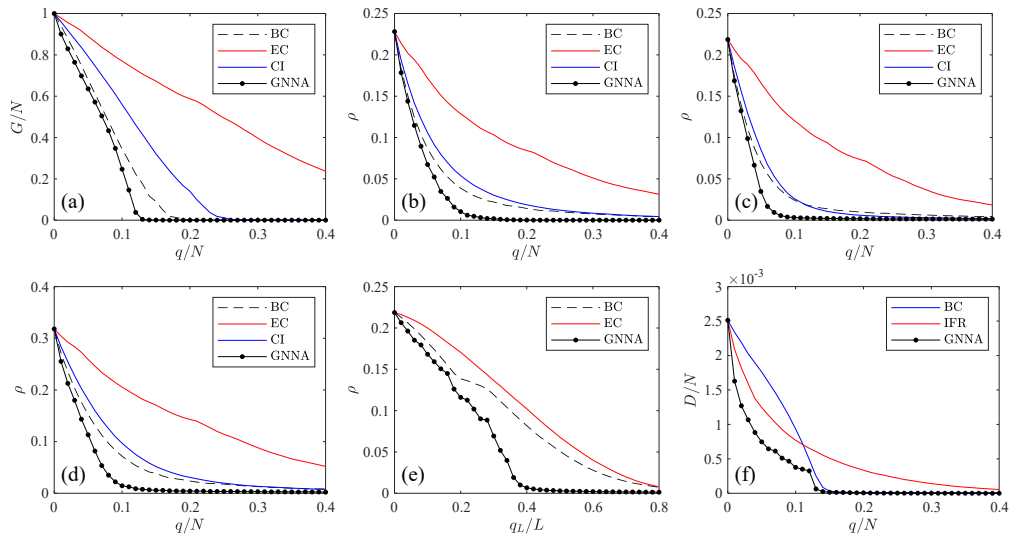


Figure 4.9: Performance of GNA compared to centrality-based vaccination strategies. (a) Largest connected component size of network dismantling and the density of infection ρ of (b) MMCA SIS model, (c) SIS model, (d) SIS model with heterogeneous contagion and recovery rate, (e) edge immunization of SIS model, and (f) mortality rate D/N of SIRD model. A multiplex network constructed from the human contact pattern is used for the SIRD model and DBLP Coauthorship network for the others. The number of nodes in the network is N , the number of edges is L , the number of vaccinated nodes is q , and the number of immunized edges is q_L . The vaccination strategy obtained by GNA outperforms all centrality measures at all vaccination levels.

provides a scalable centrality measure that considers the local stability of message-passing equations. Vaccinating (or eliminating) nodes with the highest CI leads to effective dismantling (or herd immunity) of a network. The collective influence of a node i is

$$C_\ell(i) = (k_i - 1) \sum_{j \in \partial \text{Ball}(i, \ell)} (k_j - 1), \quad (4.39)$$

where $\partial \text{Ball}(i, \ell)$ is the set of nodes that have distance ℓ from node i (surface of a ball with radius ℓ). Although the algorithm becomes exact as $\ell \rightarrow \infty$ for treelike networks, a small ℓ yields good results in general complex networks. In this study, we take $\ell = 2$. CI can be calculated within a time complexity of $O(N \log N)$. Eliminating nodes with high CI effectively reduces the size of the largest connected component in the network and contains epidemics.

Further, vaccinating nodes with high eigenvector centrality (EC), which has a computational complexity of $O(N \log N)$, is effective in reducing epidemics [326]. Other centrality measures such as K-core index [178], closeness [49], K-shell [175], and H-index [82] have been used to formulate vaccination strategies; however, one cannot conclude which of these strategies is the most effective because the efficiency of the strategies varies depending on the network and level of vaccine supply. In this study, we show the performance of BC, which is believed to be effective in a wide class of networks [262, 339, 340], and CI as benchmarks. Recalculating these centrality measures after each node vaccination enhances the performance of the vaccination; however, this increases the time complexity of the algorithm by a factor of N , and makes the method no longer scalable. Other vaccination strategies that can be implemented when the entire network structure is not available have been researched [63, 78, 289]; however, these strategies are not as effective as the centrality-based methods.

We tested and compared GNNA-based vaccination with centrality-based strategies for network dismantling, SIS models with homogeneous and heterogeneous contagion/recovery rate, edge immunization of SIS model, and SIRD model. The strategies

were tested in various networks [117,204,230,352], with the number of nodes ranging from 1K to 320K and number of edges from 5K to 1M (the specifics of the networks are provided in the Supplementary Table S1). We only show the result from one network for each epidemic process (a multiplex network constructed from the human contact pattern for the SIRD model and DBLP Coauthorship network for the others); the rest is provided in Supplementary Figures S2–S6.

Network dismantling is a problem of finding an optimal set of q nodes that breaks the largest connected component of a network into small components with *subextensive* size. It can be mapped to the optimal vaccination strategy for the spreading process [62,238]. For the network dismantling, we directly calculate the size of the largest connected component instead of employing MMCA because there is no stochasticity in this process. The size of the largest connected component of the DBLP Coauthorship network dismantled by GNNA is illustrated in Fig. 4.9(a). For comparison, we plotted the performance of the BC-, EC-, and CI-based strategies. GNNA-based strategy outperforms all centrality-based strategies at all vaccination levels.

Further, we tested the performance of GNNA-based vaccination for the SIS model. The density of infection calculated by MMCA is illustrated in Fig. 4.9(b), and the result of the Monte Carlo simulation is illustrated in Fig. 4.9(c). GNNA-based strategy outperforms all centrality-based strategies at all vaccination levels. The results for the SIS model with heterogeneous contagion and recovery rates are illustrated in Fig. 4.9(d). The disparity between the performance of GNNA-based strategy and centrality-based strategies is greater than the homogeneous case because GNNA considers the epidemic properties of each node whereas centrality-based methods do not.

For edge immunization, vaccinating edges with high edge BC or high edge EC is effective [230,296]. The edge EC is calculated as the product of the ECs of the two nodes in the edge. It has been shown that iteratively eliminating edges with the highest link epidemic importance is effective [230]; however, the complexity of the algorithm is $O(N^2)$. The results of the edge immunization are illustrated in Fig. 4.9(e). The per-

performances of high edge BC and high edge EC vaccinations are plotted as benchmarks. GNNA-based strategy outperforms all the edge centrality-based methods at all vaccination levels.

For the SIRD model, the results are illustrated in Fig. 4.9(f). Vaccinating nodes with high IFR is effective in reducing the number of deaths; hence, a high-IFR vaccination strategy has been employed in many countries to minimize the mortality due to COVID-19. The performances of high-BC and high-IFR strategies are shown as baselines. The high-IFR strategy is more effective than the high-BC strategy when the vaccination rate is low; however, the high-BC strategy outperforms the high-IFR strategy when the vaccination rate is high. GNNA-based strategy outperforms the two strategies at all vaccination levels. The number of iterations is $n_{\text{iter}} = 10^3$ for all cases except for network dismantling is $n_{\text{iter}} = 10^4$. Because there is a small probability that weights get stuck in a local minimum, we took the best results out of eight trials.

Transition of the optimal vaccination strategy in the SIRD model

There is a crossover between the efficiency of the high-IFR and high-BC strategies in the SIRD model as illustrated in Fig. 4.9(f), which is consistent with the results of previous research [214]. Similar phenomena in the metapopulation model have been reported, and the first-order phase transition has been identified [146]. Although the crossover between the two strategies has been observed, the investigation of the transition of the optimal strategy according to the availability of vaccine has not been extended to networks due to the lack of an appropriate method to study the optimal vaccination strategy in complex networks. By considering the node features and tailoring the vaccination strategy to specific levels of vaccine supply, GNNA enables us to observe a new phenomenon in complex networks that could not be observed by the existing methods. Phi coefficient, which is identical to Pearson correlation coefficient for binary variables, of the optimal vaccination strategy identified by GNNA and BC/IFR-based strategy is illustrated in Fig. 4.10(a). When only a small fraction of

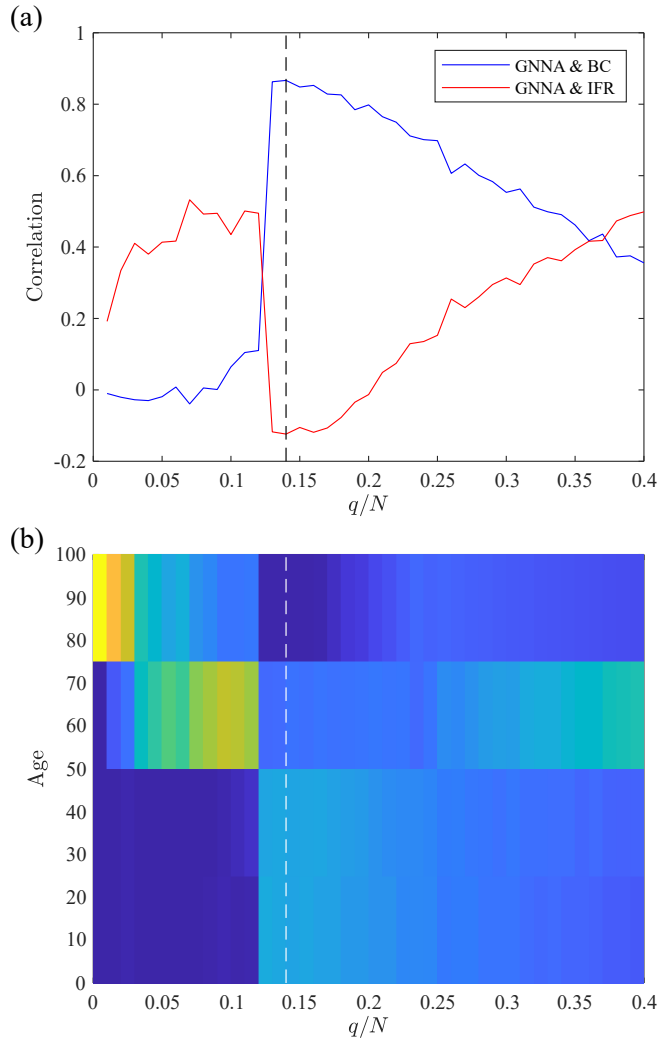


Figure 4.10: Transition of the optimal vaccination strategy in the SIRD model. (a) Phi coefficient between the nodes vaccinated by GNN and high-BC/IFR vaccination strategies. The point where herd immunity is achieved by GNN-based strategy (but not necessarily by other methods) is depicted by the dashed black line. When the total vaccination rate q/N is low, the set of nodes vaccinated by GNN has a large overlap with the high-IFR strategy. As the vaccination level approaches the state where herd immunity is possible, GNN adjusts its strategy, wherein it becomes similar to the high-BC strategy. (b) Vaccination rate of four age groups when GNN-based vaccination is applied. Yellow, green, and blue represent high, moderate, and low vaccination rates, respectively. When the total vaccination rate q/N is low, the senior age group whose IFRs are the highest is primarily vaccinated. However, when the vaccination rate becomes high and approaches herd immunity, which is depicted by the dashed white line, the individuals below age 50 who have high contact rates are primarily vaccinated.

nodes can be vaccinated, the optimal strategy is similar to that of the high-IFR strategy. However, when the vaccination rate approaches the point where herd immunity can be achieved, an abrupt transition occurs in the optimal vaccination strategy and involves vaccinating nodes with high BC. The vaccination rate of the population divided into four age groups is illustrated in Fig. 4.10(b). When the vaccination rate is low, the oldest age group 75–99, who has the highest fatality rate, is primarily vaccinated. When the vaccination rate increases to approach herd immunity, the age group primarily targeted by the optimal vaccination strategy abruptly changes, and the population below age 50 is primarily vaccinated. The senior age group is even less vaccinated than the rest of the population because they have a low contact rate (see Supplementary Figure S1).

4.3.4 Conclusion

We presented a vaccination framework based on GNNA, which can be implemented to minimize the damage, such as the total number of infections or epidemic mortality, caused by general epidemic processes. The main advantage of GNNA is that it takes node features such as contagion rate, recovery rate, and fatality rate, and tailors the vaccination strategy to the level of vaccine supply available. GNNA reduces the exponentially large dimension of the space of the vaccination to 7–10 and enables Gaussian random walk to effectively optimize vaccination strategies. The efficacy and risk of vaccine side effects vary from individual to individual [184, 280]. GNNA can consider statistical estimation of such factors along with other risks (here, we only considered the age-dependency of the fatality rate) and morbidity.

We demonstrated that the optimal vaccination strategy is closely related to the total amount of vaccines available. For instance, in the SIRD model, when vaccine supply is low, the optimal strategy primarily vaccinates nodes with high fatality rates, and when the vaccine supply is relatively high, it vaccinates nodes with high BC. Such transition of the optimal vaccination strategy based on the vaccination rate can

be identified by GNNA. This transition is of theoretical interest also with real-world implications. For instance, the hysteresis of the optimal vaccination strategy implies that mixing the fatality- and centrality-based strategies is ineffective in reducing the mortality rate [146]. The proposed framework can be implemented in future research to find other new phenomena in the optimal vaccination strategies that couldn't be observed in the current centrality-based vaccination paradigm.

Chapter 5

Quantum spreading processes in complex networks

5.1 Introduction

Phase transitions and critical phenomena in dissipative quantum many-body systems have attracted considerable attention recently because theoretical results can be realized experimentally, and vice versa [17, 18, 25, 39, 46, 92–94, 127, 135, 156, 180, 189, 197, 243, 250, 272, 362]. Mutual competition between the coherent Hamiltonian and incoherent dissipation dynamics creates unexpected emergent phenomena such as time crystals [57, 96], zero-entropy entangled states [182, 333], driven-dissipative strong correlations [218, 322], and dissipative phase transitions in the nonequilibrium steady state [72, 73, 76, 306–308, 320], including novel universal behaviors [159, 225].

Dissipative phase transitions from a disordered (absorbing) state to an ordered (active) state in dissipative quantum systems, such as the quantum contact process (QCP) and dissipative transverse Ising (DTI) model, have been exploited by developing several analytical techniques in the mean-field (MF) limit. For instance, the Keldysh (or semiclassical MF) approach and fluctuationless MF approach have been proposed. In the Keldysh approach, the spins of the DTI model are changed to bosonic operators, and an MF functional integral formalism is applied [221, 305]. Once the upper critical dimension (d_c) is determined, a transition point is obtained. In the fluctuationless MF approach, the MF concept is applied to the correlation function. The average of the product of a pair of individual field amplitudes is treated as the product of the individual average of the field amplitudes. The result is regarded as a valid approximation

Table 5.1: Summary of previous analytical results. We considered three problems with the quantum models. For each model, the system Hamiltonian (\hat{H}_S) and Lindblad operators (\hat{L}_ℓ) were defined. Semiclassical, Weiss, and Keldysh field-theoretic approaches were used for the QCP, TI, and DTI models, respectively. Among these methods, the Keldysh formalism predicts features that differ qualitatively from those of fluctuationless MF theory.

Model	Hamiltonian and Lindblad operators	Field-theoretic approach	fluctuationless MF
QCP	$\hat{H}_S = \frac{\omega}{N-1} \sum_{m \neq \ell} \hat{n}_m (\hat{\sigma}_\ell^+ + \hat{\sigma}_\ell^-),$ $\hat{L}_\ell^{(d)} = \sqrt{\Gamma} \hat{\sigma}_\ell^-, \hat{L}_{m\ell}^{(b)} = \sqrt{\kappa} \hat{n}_m \hat{\sigma}_\ell^+, \hat{L}_{m\ell}^{(c)} = \sqrt{\kappa} \hat{n}_m \hat{\sigma}_\ell^-.$	Continuous and discontinuous transitions	Continuous and discontinuous transitions
TI	$\hat{H}_S = -\frac{J}{N-1} \sum_{\ell \neq m} \hat{\sigma}_\ell^z \hat{\sigma}_m^z + \Delta \sum_\ell \hat{\sigma}_\ell^x.$	Continuous transition	Continuous transition
DTI	$\hat{H}_S = -\frac{J}{N-1} \sum_{\ell \neq m} \hat{\sigma}_\ell^z \hat{\sigma}_m^z + \Delta \sum_\ell \hat{\sigma}_\ell^x,$ $\hat{L}_\ell = \sqrt{\Gamma} \hat{\sigma}_\ell^x.$	Discontinuous transition with sufficiently strong dissipation	Continuous transition

in infinite dimensions (d_∞). In addition, noise effects are ignored. In the semiclassical approach, averaging is applied to individuals, as in the fluctuationless MF approach. However, noise effects are considered [163]. These approaches are thought to provide a general framework for exploring the critical behaviors of dissipative phase transitions in the MF limit [31, 305, 307].

According to the conventional theoretical framework of equilibrium systems, the two MF solutions at d_c and d_∞ exhibit the same universal behavior. Indeed, for the QCP model, the MF solutions obtained using the semiclassical and fluctuationless MF approaches appear to be the same, as expected. However, for the DTI model, the Keldysh solution predicts $d_c = 3$, at which a dissipative phase transition is of first order when the dissipation is strong, whereas it is of second order when the dissipation is weak [221]. By contrast, the fluctuationless MF approach predicts that the dissipative phase transition is of second order regardless of the dissipation strength. This result is regarded as the MF solution at d_∞ . Accordingly, the two solutions in the strong dissipation limit at d_c and d_∞ are inconsistent with each other. This result is also obtained numerically in three dimensions [254]. Therefore, this discrepancy remains a challenging problem.

To resolve this inconsistency, it is necessary to confirm the analytical results numerically; however, numerical approaches, including quantum jump Monte Carlo simulations [276] and the tensor network [331, 334] and its variants [183, 332, 344], are not feasible in higher dimensions because the computational complexity increases exponentially as the dimensionality is increased.

Here, we aim to show that numerical studies are possible when the quantum states can be contracted considerably. Thus, the MF solutions for the DTI model can be tested using this numerical method. To this end, we use that spin indices are permutation invariant (PI) on fully connected graphs [301], which is regarded as the networks at d_∞ . On the all-to-all graphs, the quantum states that are PI can be contracted to a single state. The contracted quantum states are called *the PI states* for simplicity. This con-

traction reduces the computational complexity considerably, from $\mathcal{O}(2^{2N})$ to $\mathcal{O}(N^3)$, which enables us to numerically study the model in large systems (up to $N = 1024$). In this paper, we test the transition type of the DTI mode. It reveals to be continuous. The critical behaviors are obtained using finite-size scaling (FSS) analysis. The critical behaviors are in agreement with those obtained using the fluctuationless MF approach.

To check the validity of the numerical method, we first consider the QCP model. This model is chosen because it is regarded as a prototypical model that exhibits a dissipative phase transition. Using the semiclassical method and fluctuationless MF approach, analytical solutions were obtained at d_c and d_∞ . Unlike those of the DTI model, the two analytical solutions exhibit a continuous transition with the same universal behavior. However, like the DTI model, the transition behaviors of the QCP model have not been numerically studied yet because of the numerical complexity. Therefore, we perform numerical studies based on the PI states and confirm that the numerical results are in agreement with the analytical solutions of d_c and critical exponents [31, 160].

Next, we consider the transverse Ising (TI) model in a closed quantum system, which corresponds to the zero limit of the dissipation strength of the DTI model in an open quantum system. Because the system is a closed quantum system, we reset the Schrödinger equation based on the PI states. We find that its complexity is reduced as $\mathcal{O}(N)$. The static critical exponents we obtain are in agreement with the previously known values. We summarize previous analytical results for the three models in Table. 5.1.

5.2 Permutational symmetry

The time evolution of an open quantum system is described by the Lindblad equation, which consists of the Hamiltonian and dissipation terms:

$$\partial_t \hat{\rho} = -i [\hat{H}_S, \hat{\rho}] + \sum_{\ell=1}^N \left[\hat{L}_\ell \hat{\rho} \hat{L}_\ell^\dagger - \frac{1}{2} \{ \hat{L}_\ell^\dagger \hat{L}_\ell, \hat{\rho} \} \right], \quad (5.1)$$

where $\hat{\rho}$ is the density matrix of the full system, \hat{H}_S is the system Hamiltonian, and \hat{L}_ℓ is the Lindblad operator at site ℓ .

Qubit systems on a fully connected structure are invariant under any permutation of the spin indices. The elements of the density matrix satisfy the relation $\rho_{v,w} = \rho_{P(v),P(w)}$, where v and w denote two states among 2^N quantum states of N spins, and P denotes a permutation operator. If both the dynamical equation and initial density matrix are PI, the density matrix would also be PI. For example, for a four-spin system, $\rho_{\uparrow\uparrow\downarrow\downarrow, \uparrow\downarrow\uparrow\downarrow} = \rho_{\uparrow\uparrow\downarrow\downarrow, \uparrow\downarrow\uparrow\downarrow} = \rho_{\uparrow\uparrow\downarrow\downarrow, \downarrow\uparrow\uparrow\downarrow} = \rho_{\downarrow\uparrow\uparrow\downarrow, \uparrow\downarrow\uparrow\downarrow} = \dots$. According to this symmetry, the elements $|v\rangle\langle w|$ of the density matrix can be classified in terms of (n_1, n_2, s) , where n_1 is the number of up spins in v , n_2 is the number of up spins in w , and s is the number of sites with up spins in both v and w states. Then the density matrix is written as

$$\hat{\rho} = \sum_{n_1, n_2, s} A_{n_1, n_2, s} |n_1, s\rangle\langle n_2, s|, \quad (5.2)$$

where $A_{n_1, n_2, s} = \langle n_1, s | \hat{\rho} | n_2, s \rangle$ is the 3-rank tensor whose components are the sum of the elements of $\hat{\rho}$. $|n_1, s\rangle$ is a PI state. Particularly, $P(n)$ denotes $A_{n_1=n_2=s=n}$, representing the probability that the system has n up spins. For convenience, we introduce a Liouvillian superoperator \mathcal{L} and rewrite the time evolution of the Lindblad equation,

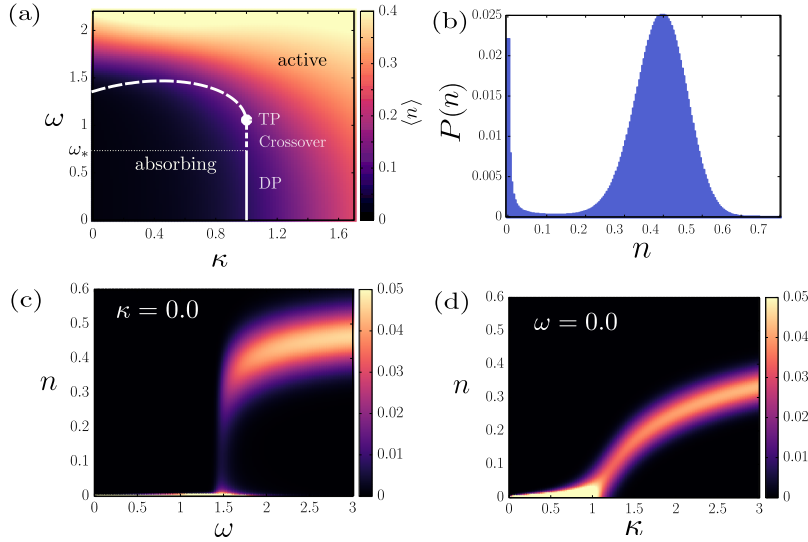


Figure 5.1: (a) Phase diagram of the QCP model on a fully connected graph in the parameter space (κ, ω) , determined by direct numerical enumeration of the Liouville equation based on the PI states. Discontinuous (dashed curve) and continuous transitions (dotted and solid lines) occur, and they meet at a tricritical point (TP). On the dotted critical line in $\omega \in [\omega_*, 1]$, the critical exponent α varies continuously, whereas on the solid line, it has the DP value. The color means the average order parameter $\langle n \rangle$ defined in Eq. (5.10). (b) The distribution of the order parameters n for $(\kappa, \omega) = (0, 1.8)$. This shows that the system is bistable at $n = 0$ and ≈ 0.45 . (c) Plot of the order parameter n as a function of ω for $\kappa = 0.0$ in the steady state. This shows that the transition is first-order. (d) Plot of the order parameter n as a function of κ at $\omega = 0.0$ in the steady state. This shows that the transition is second-order. Data are obtained by direct enumerations from the system of size $N = 256$. We set $\Gamma = 1$ for all figures. In (c) and (d), the color means the probability that the order parameter n exists.

Eq. (5.1), in the form of the Liouville equation,

$$\partial_t \hat{\rho} = \mathcal{L} \hat{\rho}, \quad (5.3)$$

This transformation is possible because the Lindblad equation is linear in ρ . Consequently,

$$\sum_{n_1, n_2, s} \partial_t A_{n_1, n_2, s} |n_1, s\rangle \langle n_2, s| \quad (5.4)$$

$$= \sum_{n_1, n_2, s} \mathcal{L} A_{n_1, n_2, s} |n_1, s\rangle \langle n_2, s|. \quad (5.5)$$

Thus, the computational complexity decreases as $\mathcal{O}(N^3)$ [301].

5.3 Quantum contact process

We consider the QCP model [40, 101–103, 159, 160, 224], a paradigmatic model exhibiting an absorbing phase transition in open quantum systems. This theoretical model has recently become attractive to scientists because it is simple and thus can be analytically solved at d_c and d_∞ . Moreover, it has been realized experimentally in ultracold Rydberg atomic systems using the antiblockade effect [119] in the classical limit. However, numerical results of this model in the MF limit have not been obtained yet because of its numerical complexity. We perform numerical studies using the Runge-Kutta algorithm for the Liouville equation (5.5) based on the PI states.

The Hamiltonian \hat{H}_S contains coherent terms for branching and coagulation and is given by

$$\hat{H}_S = \frac{\omega}{N-1} \sum_{m \neq \ell} \hat{n}_m (\hat{\sigma}_\ell^+ + \hat{\sigma}_\ell^-), \quad (5.6)$$

and the Lindblad decay, branching, and coagulation operators are given by

$$\hat{L}_{m\ell}^{(b)} = \sqrt{\kappa} \hat{n}_m \hat{\sigma}_\ell^+, \quad (5.7)$$

$$\hat{L}_{m\ell}^{(c)} = \sqrt{\kappa} \hat{n}_m \hat{\sigma}_\ell^-, \quad (5.8)$$

$$\hat{L}_\ell^{(d)} = \sqrt{\Gamma} \hat{\sigma}_\ell^-, \quad (5.9)$$

respectively. Here, $\hat{n}_\ell = |\uparrow\rangle\langle\uparrow|_\ell$ is the number operator of the active state at site ℓ , and $\hat{\sigma}_\ell^\pm = (\hat{\sigma}_\ell^x \pm i\hat{\sigma}_\ell^y)/2$. The composite operator $\hat{n}_m \hat{\sigma}_\ell^+$ or $\hat{n}_m \hat{\sigma}_\ell^-$ with $\ell \neq m$ indicates that the active state at site m activates or deactivates the state at ℓ , which represents the branching or coagulation process, respectively. κ is the rate of incoherent branching or coagulation. By contrast, $\hat{L}_\ell^{(d)}$ in Eq. (5.7) denotes the decay dynamics $|\uparrow\rangle \rightarrow |\downarrow\rangle$ at ℓ , where Γ is the decay rate. Therefore, if there is no active state, no further dynamics occurs, and the system enters an absorbing state.

According to the MF solution obtained by the semiclassical method [31, 160], the QCP exhibits three types of phase transitions: i) for $\kappa < 1$, a discontinuous transition [dashed line in Fig. 5.9(a)] occurs; ii) for $\kappa_c = 1$ and $\omega_* < \omega < \omega_c = 1$ [dotted line in Fig. 5.9(a)], a continuous transition occurs with continuously varying exponents; and iii) for $\kappa = 1$ and $\omega < \omega_*$, a continuous transition [solid line in Fig. 5.9(a)] occurs. A tricritical point (TP) appears at (κ_c, ω_c) , as shown in Fig. 5.9. The continuous transition iii) belongs to the directed percolation (DP) universality class [37]. The continuous transition at the TP belongs to the tricritical DP class [115, 158, 215].

We discuss the numerical results for the QCP model based on the PI states. The QCP model exhibits a phase transition from the absorbing state to the active state as shown in Fig. 5.9. The order parameter of the phase transition is defined as the average density of active sites (i.e. the sites of up spins), formulated as

$$\langle n(t) \rangle = \left(\sum_\ell \text{Tr}[\hat{\rho}(t) \hat{n}_\ell] \right) / N = \sum_n P(n) n. \quad (5.10)$$

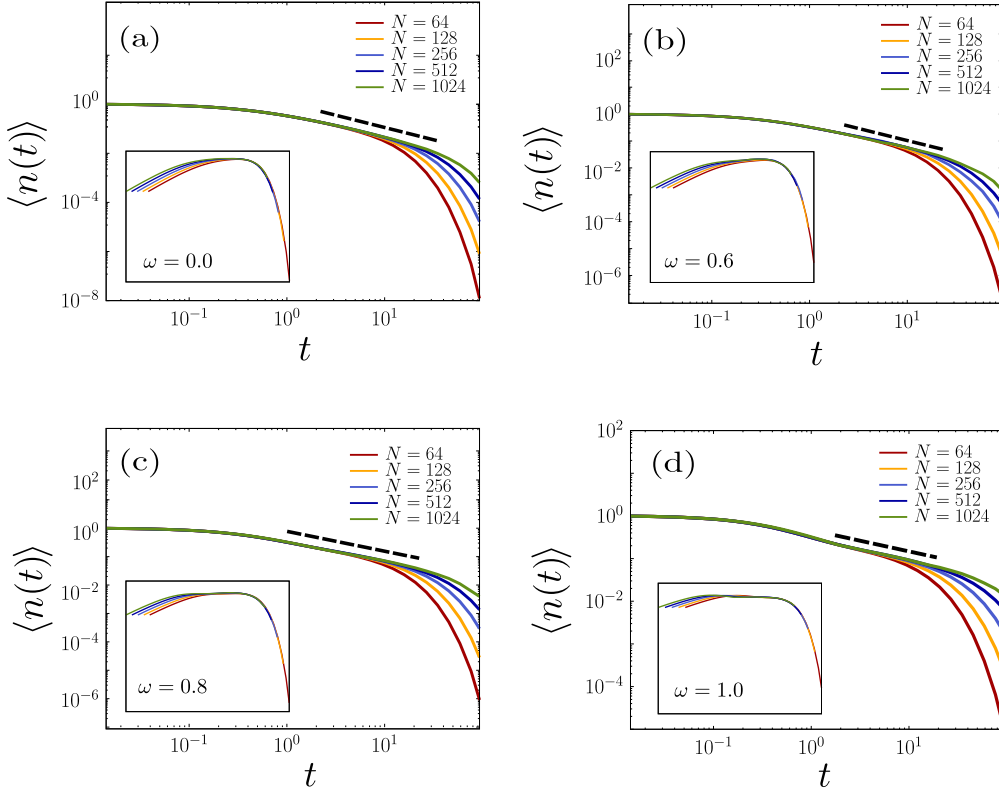


Figure 5.2: Plots of the order parameter $\langle n(t) \rangle$ of the QCP model as a function of time t for fixed $\kappa = 1$ but different (a) $\omega = 0.0$, (b) 0.6 , (c) 0.8 , and (d) 1.0 . As N is increased, the data exhibit a power-law behavior in large- t regime. Guide lines (dashed lines) are drawn to show the power-law behavior, indicating $\langle n(t) \rangle \sim t^{-\alpha}$. The exponent α is estimated as (a) $\alpha = 1.0$ for $\omega = 0$, (b) $\alpha = 0.92$ for $\omega = 0.6$, (c) $\alpha = 0.70$ for $\omega = 0.8$, and (d) $\alpha = 0.50$ for $\omega = 1.0$. Figures (a)–(d) show that the critical exponent α varies continuously depending on ω . The data are obtained for $\Gamma = 1$ and $\kappa = 1$. Insets: Scaling plots of $\langle n(t) \rangle t^\alpha$ versus $t N^{-z}$.

In the absorbing state, $\langle n(t) \rangle \rightarrow 0$ as $t \rightarrow \infty$, whereas in the active state, $\langle n(t) \rangle \rightarrow$ finite as $t \rightarrow \infty$. The phase boundaries are composed of two parts for the first-order and second-order transitions in the parameter space $[\kappa, \omega]$, and their positions are in agreement with the ones predicted by the theory using the semiclassical method.

The numerical method using the PI states enables to easily calculate $P(n)$ as a function of n for any given κ and ω as shown in Fig. 5.9(b). We find that the density of n up spins is broadly distributed around the phase boundary. This distribution

Table 5.2: Critical exponent α values for different ω values.

ω	α
1.0	0.50 ± 0.02
0.9	0.61 ± 0.02
0.8	0.70 ± 0.02
0.7	0.81 ± 0.02
0.6	0.92 ± 0.02
≤ 0.53	MF DP values

originates from the quantum effect.

The numerical results are obtained on a fully connected graph of size $N = 256$. Along the continuous transition line (solid line) at $\kappa = 1$ in Fig. 5.9(a), we examine critical behaviors under different initial conditions. For an initial state with all up spins at time $t = 0$, we measure $\langle n(t) \rangle$ as a function of time for different system sizes up to $N = 1024$. We find that $\langle n(t) \rangle$ exhibits power-law decay as $\langle n(t) \rangle \sim t^{-\alpha}$. As predicted by the theory, the exponent α is continuously varying for $\omega_* < \omega < 1$ with $\omega_* \approx 0.53$ as shown in Fig. 5.12(d)–(b)] and α is fixed as 1.0 ± 0.02 at $\omega = 0.0$ [Fig. 5.12(a)]. The value $\alpha = 1$ is the DP value. Numerical estimates for different ω values are listed in Table 5.2). Therefore, we conclude that the numerical method based on the PI states successfully reproduces the theoretical values of the QCP model.

5.4 Dissipative Transverse Ising model

5.4.1 Transverse Ising model

The Hamiltonian \hat{H}_S of the TI model at d_∞ is expressed as

$$\hat{H}_S = -\frac{J}{N-1} \sum_{\ell \neq m} \hat{\sigma}_\ell^z \hat{\sigma}_m^z + \Delta \sum_{\ell} \hat{\sigma}_\ell^x, \quad (5.11)$$

where J represents the strength of the ferromagnetic interaction of the Ising spins in the z direction. The summation runs for every pair of spins. ℓ is the spin index, $\ell = 1, \dots, N$. The parameter Δ represents the strength of the transverse field. When $\Delta/J < 1$, the ferromagnetic interaction becomes dominant, and the ground states are two-fold degenerate ordered states, whereas for $\Delta/J > 1$, the ground state is nondegenerate and disordered. Thus, the system exhibits a quantum phase transition [287] from a ferromagnetic phase ($\Delta/J < 1$) to a paramagnetic phase ($\Delta/J > 1$). Note that this Hamiltonian has \mathbb{Z}_2 symmetry under the transformation $\hat{\sigma}^z \rightarrow -\hat{\sigma}^z$.

The Liouville equation of Eq. (5.5) must be replaced by imaginary time dynamics, because the TI model is a closed quantum system. The elements of the wavefunction satisfies the relation $\psi_\nu = \psi_{P(\nu)}$, where ν denotes a state among 2^N quantum states of N spins, and P denotes a permutation operator. Therefore, the wave function is simply written as

$$|\psi\rangle = \sum_{n=0}^N B_n |n\rangle, \quad (5.12)$$

where n is the number of up spins in ν and B_n is the coefficient of the state n . Thus, we need to track only $N + 1$ complex numbers to study the system.

To obtain the ground state, we use the imaginary-time Schrödinger evolution $\partial_t |\psi\rangle = -\hat{H}_S |\psi\rangle$ under the normalization condition for the wave function $\langle\psi|\psi\rangle = 1$. Using the above expression for the wave function, we obtain the differential equations for B_n :

$$\sum_{n=0}^N \partial_t B_n |n\rangle = - \sum_{n=0}^N B_n \hat{H}_S |n\rangle. \quad (5.13)$$

Unlike the Lindblad open quantum systems, where the normalization condition $\sum_\nu \rho_{\nu\nu} = \sum_n A_{n,n,n} = 1$ holds owing to the dynamics given by Eq. (5.5), the normalization condition $\sum_{n=0}^N |B_n|^2 = 1$ is broken at each time step. Therefore, B_n s must be rescaled at each time step in the simulation to restore the normalization condition.

Using this method, we perform numerical iterations of the dynamics, Eq. (5.13), for different system sizes. FSS analysis follows to measure the critical exponents β

and $\bar{\nu}$ associated with the order parameter and correlation size, respectively. For a steady-state of B_n , the magnetization is obtained as

$$m = \sum_n |B_n|^2 |m_n|, \quad (5.14)$$

where $m_n \equiv (1/N) \langle n | \sum_i \hat{\sigma}_i^z | n \rangle$. We plot the magnetization m versus $\Delta_c - \Delta$ for different sizes N up to $N = 20480$ in Fig. 5.3(a), and obtain the critical exponent $\beta = 0.50 \pm 0.01$. We also plot $mN^{\beta/\bar{\nu}}$ versus $(\Delta_c - \Delta)N^{1/\bar{\nu}}$ in the inset of Fig. 5.3(a). In this plot, $\bar{\nu}$ is taken so that data points for various N values collapse onto a single curve. $\bar{\nu} = d_c \nu = 1.5 \pm 0.01$ is obtained.

The susceptibility χ [257], which represents the fluctuations of the order parameter in finite quantum systems, is defined as

$$\chi = N^{1+\bar{z}} (\langle m^2 \rangle - \langle m \rangle^2), \quad (5.15)$$

where $z = \bar{z}d_c$ is the dynamical critical exponent. We note that the dynamical exponent contributes to the susceptibility, because the imaginary time appears as an extra dimension at zero temperature, and the dynamic correlation function appears with the imaginary time axis [189] in a closed quantum system. Thus, the critical phenomena are described using one additional scaling variable with a single new exponent z [319]. The susceptibility diverges as $\chi \sim (\Delta_c - \Delta)^{-\gamma}$ as $\Delta \rightarrow \Delta_c^-$. Therefore, we plot χ versus $\Delta_c - \Delta$ on a double logarithmic scale and find that χ exhibits power-law decay with slope -1.00 ± 0.01 . Thus, the exponent γ is estimated as $\gamma = 1.00 \pm 0.01$. In particular, we note that in Fig. 5.3(b), the data points collapse onto a single power-law line in the subcritical region when $\bar{z} = 0.33 \pm 0.005$ is chosen. Inserting this \bar{z} value into $d_c + z = 4$, we obtain $d_c = 3.0 \pm 0.01$ and $z = 1.0 \pm 0.03$. At $\Delta = \Delta_c$, we find that $\chi \sim N^{\gamma/\bar{\nu}}$ holds, as shown in Fig. 5.3(c). A similar plot is presented in Ref. [257] for one-dimensional case with $L = 120$. Next, by plotting $\chi N^{-\gamma/\bar{\nu}}$ versus $(\Delta_c - \Delta)N^{1/\bar{\nu}}$ and taking $\bar{\nu} = 1.50 \pm 0.01$, we find that the data points collapse onto a single curve.

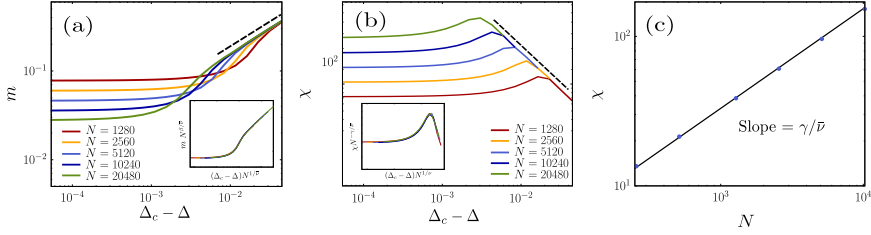


Figure 5.3: FSS analysis for the transverse Ising model on fully connected graphs. (a) Plot of the order parameter m as a function of $\Delta_c - \Delta$ for different system sizes. We set $J = 1$ and $\Delta_c = 1$. The auxiliary dashed line with slope 0.5 means the power-law behavior $m \sim (\Delta_c - \Delta)^{0.5}$. Inset: Scaling plot of the magnetization $mN^{\beta/\bar{\nu}}$ versus $(\Delta_c - \Delta)N^{1/\bar{\nu}}$ with $\bar{\nu} = 1.5$ and $\beta = 0.5$. (b) Plot of the susceptibility as a function of $\Delta_c - \Delta$ for different system sizes. $\chi = N^{1+\bar{z}} \left(\langle (\hat{\sigma}^z)^2 \rangle - \langle \hat{\sigma}^z \rangle^2 \right)$, where $\bar{z} = z/d_c = 1/3$. The black dashed line is a guide line indicating $\chi \sim (\Delta_c - \Delta)^{-1}$. Inset: Scaling plot of the susceptibility $\chi N^{-\gamma/\bar{\nu}}$ versus $(\Delta_c - \Delta)N^{1/\bar{\nu}}$. The critical exponents $\bar{\nu} = 1.5$ and $\gamma = 1.0$ are used for the FSS analysis. (c) Plot of χ versus N at Δ_c . The slope represents the value of the critical exponent $\gamma/\bar{\nu}$.

These results confirm that $\bar{\nu} = 1.50 \pm 0.01$. When \bar{z} is chosen as the classical Ising value $\bar{z} = 0$ in Eq. (5.15), we confirm that data collapse fails because the value of \bar{z} is incorrect.

Next, using the dimensional analysis of Eq. (5.15), we find the hyperscaling relation $2\beta + \gamma = \nu(d_c + z)$, or equivalently, $2\beta + \gamma = \bar{\nu}(1 + \bar{z})$ [83]. Using the numerical values $\beta = 0.50 \pm 0.01$, $\gamma = 1.00 \pm 0.04$, $\bar{\nu} = 1.50 \pm 0.01$, and $\bar{z} = 0.33 \pm 0.01$, we find that the hyperscaling relation is satisfied. Below, we examine whether this hyperscaling relation still holds in dissipative quantum systems.

5.4.2 Dissipative transverse Ising model

Model definition

We consider the DTI model [10, 136, 155, 284], which has been experimentally realized using ultracold Rydberg atoms [41, 222]. For open quantum systems, in addition to the Hamiltonian \hat{H}_S given by Eq. (5.11), we need the Lindblad operator to account for the dissipation process. For the DTI model, a spin decay is imposed from positive to

negative eigenvectors on the x axis. This operation is written as

$$\hat{L}_\ell = \sqrt{\Gamma} \hat{\sigma}_\ell^{x-} = \sqrt{\Gamma} \frac{\hat{\sigma}_\ell^z + i \hat{\sigma}_\ell^y}{2}, \quad (5.16)$$

where Γ is the decay rate. For this system, \mathbb{Z}_2 symmetry still remains under the transformation $(\hat{\sigma}^x, \hat{\sigma}^y, \hat{\sigma}^z) \rightarrow (\hat{\sigma}^x, -\hat{\sigma}^y, -\hat{\sigma}^z)$. Accordingly, it is expected that the critical exponents of the static variables remains in the Ising class [319]. Conventionally, this DTI model is known to exhibit a continuous transition according to the fluctuationless MF approach [10]. However, a recent analytical solution based on the Keldysh formalism shows that the transition at the upper critical dimension (which is calculated as $d_c = 3$) is not continuous but rather discontinuous when the dissipation is sufficiently strong [221], specifically, in the regions $\Delta/\Gamma < 0.5$ [221] and $\Delta/J < 0.22$ [254]. This result is also confirmed by numerical results using the variational method [254].

Fluctuationless MF approach

Let us consider the MF solution for the DTI model using the fluctuationless MF approach [31, 160]. To obtain the MF solution, one may explore the equation of motion of an observable O . This equation is given as the conjugate master equation:

$$\partial_t \hat{O} = i [\hat{H}_S, \hat{O}] + \sum_{\ell=1}^N \left[\hat{L}_\ell^\dagger \hat{O} \hat{L}_\ell - \frac{1}{2} \{ \hat{L}_\ell^\dagger \hat{L}_\ell, \hat{O} \} \right]. \quad (5.17)$$

Ignoring correlations and assuming uniform fields, we derive the MF equations as follows:

$$\partial_t \sigma^x = 4J \sigma^y \sigma^z - \Gamma(1 + \sigma^x), \quad (5.18)$$

$$\partial_t \sigma^y = -4J \sigma^x \sigma^z - 2\Delta \sigma^z - \frac{\Gamma}{2} \sigma^y, \quad (5.19)$$

$$\partial_t \sigma^z = 2\Delta \sigma^y - \frac{\Gamma}{2} \sigma^z. \quad (5.20)$$

We find that there exist two sets of steady-state solutions for $\{\sigma_0^x, \sigma_0^y, \sigma_0^z\}$. The first set is given as

$$\sigma_0^x = -1, \quad \sigma_0^y = \sigma_0^z = 0, \quad (5.21)$$

and the other set is given as

$$\sigma_0^x = \frac{J}{\Delta}(\sigma_0^z)^2 - 1, \quad (5.22)$$

$$\sigma_0^y = \frac{4}{\Gamma} (2J - \Delta) \left(1 + \frac{32J^2 z^2}{\Gamma^2}\right)^{-1} \sigma_0^z,$$

$$\sigma_0^z = \pm \frac{\sqrt{-\Gamma^2 + 32J\Delta - 16\Delta^2}}{4\sqrt{2}J}. \quad (5.23)$$

Next, we check the stability of the two solutions. For the first solution [Eq. (5.21)], the dynamical equations (5.18)–(5.20) are linearized around the fixed point. By inserting $\sigma^x = \sigma_0^x + \delta\sigma^x$, $\sigma^y = \sigma_0^y + \delta\sigma^y$, and $\sigma^z = \sigma_0^z + \delta\sigma^z$ into Eqs. (5.18)–(5.20) and expanding up to the linear order of perturbations, we obtain the linear equation $\dot{\delta\mathbf{a}} = \mathbf{M}\delta\mathbf{a}$, where

$$\delta\mathbf{a} = (\delta\sigma_0^x, \delta\sigma_0^y, \delta\sigma_0^z)^\top, \quad (5.24)$$

and the matrix \mathbf{M} is given by

$$\mathbf{M} = \begin{pmatrix} -\Gamma & 4J\sigma_0^z & 4J\sigma_0^y \\ -4J\sigma_0^z & -\frac{\Gamma}{2} & -2\Delta - 4J\sigma_0^x \\ 0 & 2\Delta & -\frac{\Gamma}{2} \end{pmatrix}. \quad (5.25)$$

All the eigenvalues of \mathbf{M} are negative in the region $2J - \Delta - \Gamma^2/(16\Delta) < 0$, indicating that the fixed point is stable.

For the other solution [Eq. (5.22)], all the eigenvalues of \mathbf{M} are negative in the other region, $2J - \Delta - \Gamma^2/(16\Delta) > 0$, indicating that the fixed point is unstable. Thus, a continuous phase transition occurs from the disordered phase governed by

Eq. (5.21) to the ordered phase governed by Eq. (5.22) across a transition line given by

$$2J - \Delta - \Gamma^2/(16\Delta) = 0. \quad (5.26)$$

By substituting the expression for σ_0^y in Eq. (5.22) into Eq. (5.20), one may expand the equation with respect to $\sigma_0^z \ll 1$ as

$$\partial_t \sigma^z = 0 = -u_2 \sigma_0^z - u_4 (\sigma_0^z)^3 + \mathcal{O}((\sigma_0^z)^5), \quad (5.27)$$

where u_2 and u_4 are defined as

$$u_2 = -\frac{8\Delta}{\Gamma} \left(2J - \Delta - \frac{\Gamma^2}{16\Delta} \right), \quad (5.28)$$

$$u_4 = \frac{256\Delta J^2}{\Gamma^3} (2J - \Delta). \quad (5.29)$$

Note that Eq. (5.27) implies that there exists an effective potential defined as

$$U(\sigma^z) = \frac{u_2}{2} (\sigma^z)^2 + \frac{u_4}{4} (\sigma^z)^4 + \mathcal{O}((\sigma^z)^6), \quad (5.30)$$

where $\mathcal{O}((\sigma^z)^6)$ is irrelevant because the u_4 term is always positive near the transition line. Thus, we consider the terms up to the u_4 term hereafter. Note that $U(\sigma^z) = U(-\sigma^z)$ holds because of the \mathbb{Z}_2 symmetry, and this effective potential describes the universality class of the classical Ising model. Then, the solution σ_0^z satisfying Eq. (5.27) is also the steady-state solution of the single effective equation of the order parameter, which is given by

$$\partial_t \sigma^z = -\frac{\partial U}{\partial \sigma^z}.$$

Again, we obtain the transition line of Eq. (5.26) given by $u_2 = 0$. Then the transition

line Γ_c is expressed as a function of J :

$$\Gamma_c/J = 4\sqrt{2(\Delta_c/J) - (\Delta_c/J)^2}, \quad (5.31)$$

where Δ_c denotes the Δ value at the transition line. Then, the order parameter behavior near the transition line can be obtained by taking the minimum value of the effective potential in Eq. (5.53); the resulting solution equals σ_0^z in Eq. (5.22). Expanding the order parameter for $\Gamma_c - \Gamma \ll 1$, we obtain

$$m = \frac{\sqrt{\Gamma_c}}{4J} \sqrt{\Gamma_c - \Gamma}, \quad (5.32)$$

which gives the exponent of magnetization $\beta = 0.5$. Similarly, we find the transition line for fixed Γ as follows:

$$J_c/\Gamma = \frac{1 + 16(\Delta_c/\Gamma)^2}{32(\Delta_c/\Gamma)}. \quad (5.33)$$

We also obtain the order parameter for $J - J_c \ll 1$ as

$$m = \frac{\sqrt{\Delta_c}}{J_c} \sqrt{J - J_c}. \quad (5.34)$$

Thus, the critical exponent $\beta = 0.5$ is obtained.

Numerical results

Hereafter, we consider the numerical results for the DTI model. We first consider the case where J is fixed at $J = 1$, but Δ and Γ are varied. Numerical simulations are performed by applying the Runge-Kutta method to the Liouville equation [Eq. (5.5)] based on the PI states. The phase diagram obtained numerically in the parameter space (Δ, Γ) is shown in Fig. 5.4(a). The phase boundary curve (white curve) is obtained by the analytic fluctuationless MF solution [Eq. (5.31)]. A distribution of the order parameter is shown in Fig. 5.4(b), where $J = 1$ and $\Delta = 0.1$ are fixed.

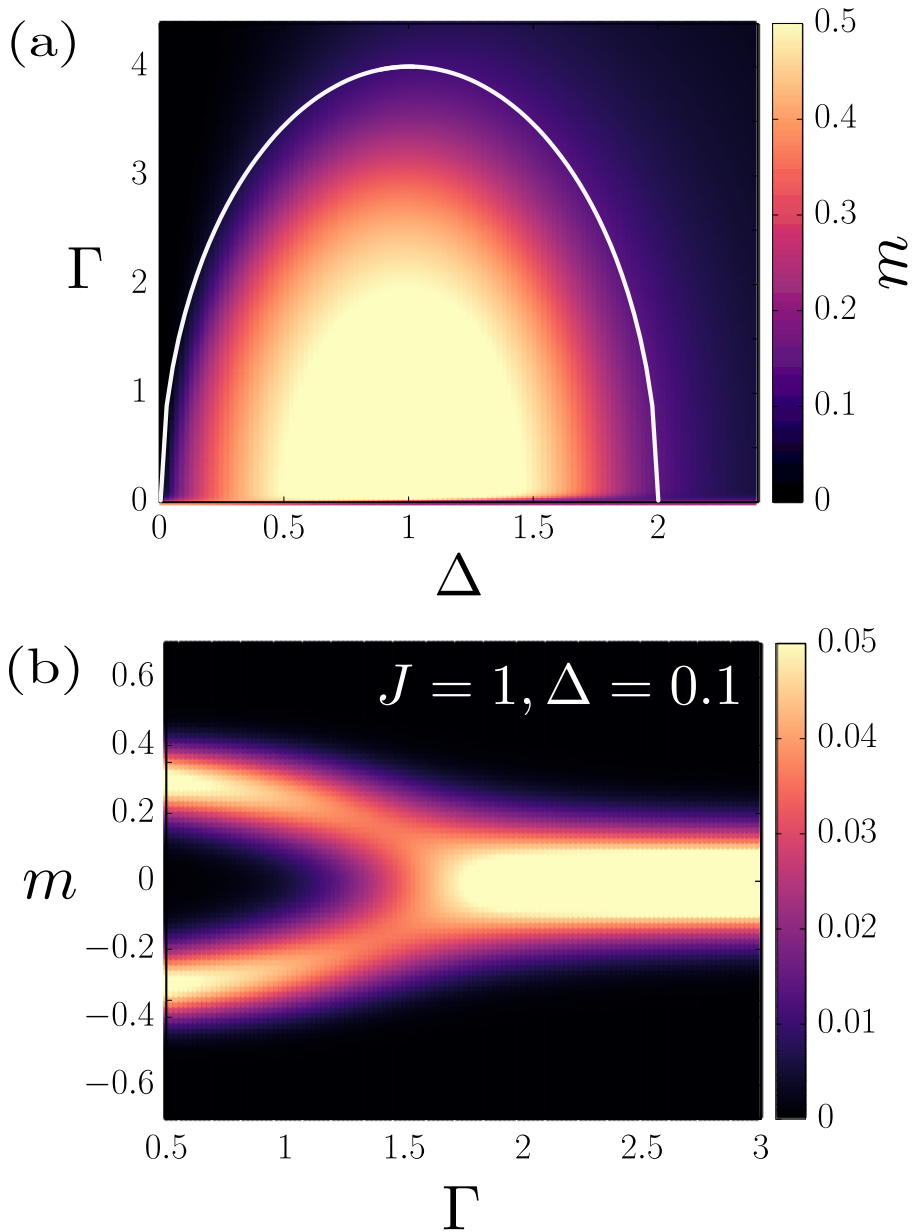


Figure 5.4: (a) Phase diagram of the DTI model on fully connected graphs in the parameter space (Δ, Γ) . A continuous transition occurs across the solid white curve. The brightness represents the magnitude of magnetization m . (b) The density of the order parameter in the steady state as a function of Γ at $\Delta = 0.1$. System size is taken as $N = 128$. The brightness represents the probability that the order parameter exists. Data are obtained from the Liouville equation with $J = 1$ based on the PI states.

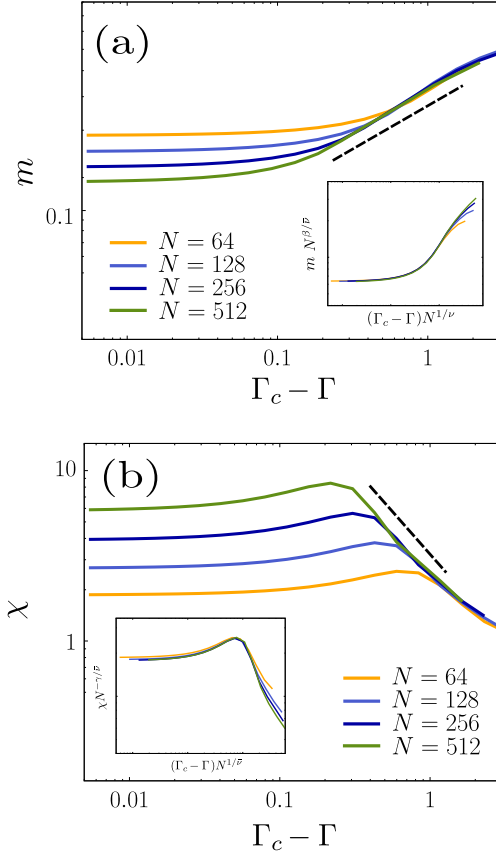


Figure 5.5: FSS analysis for the DTI model at $\Delta = 0.5$ and $J = 1$ on fully connected graphs. (a) Plot of the order parameter m as a function of $\Gamma_c - \Gamma$ for different system sizes. The auxiliary dashed line with slope 0.5 means the power-law behavior $m \sim (\Gamma_c - \Gamma)^{0.5}$. Inset: Scaling plot of the magnetization $mN^{\beta/\bar{\nu}}$ versus $(\Delta_c - \Delta)N^{1/\bar{\nu}}$ with $\bar{\nu} = 1.75$ and $\beta = 0.5$. (b) Plot of χ as a function of $\Gamma_c - \Gamma$ for different system sizes. The auxiliary dashed line with slope -1.0 means the power-law behavior $\chi \sim (\Gamma_c - \Gamma)^{-1.0}$. Inset: Scaling plot of the susceptibility $\chi N^{-\gamma/\bar{\nu}}$ versus $(\Gamma_c - \Gamma)N^{1/\bar{\nu}}$. The critical exponents $\bar{\nu} = 1.75$ and $\gamma = 1.0$ are used for the FSS analysis.

Next, we perform FSS analysis to obtain the critical exponents β and $\bar{\nu}$, which are associated with the order parameter and correlation size, respectively. We obtain the critical exponent β associated with the order parameter by directly measuring the local slope of the plot of m versus $\Gamma_c - \Gamma$ on a double logarithmic scale in Fig. 5.5(a). Then, we plot $mN^{\beta/\bar{\nu}}$ versus $(\Gamma_c - \Gamma)N^{1/\bar{\nu}}$ for different system sizes N in the inset of Fig. 5.5(a). The result confirms that $\beta = 0.50 \pm 0.01$. We also obtain a correlation

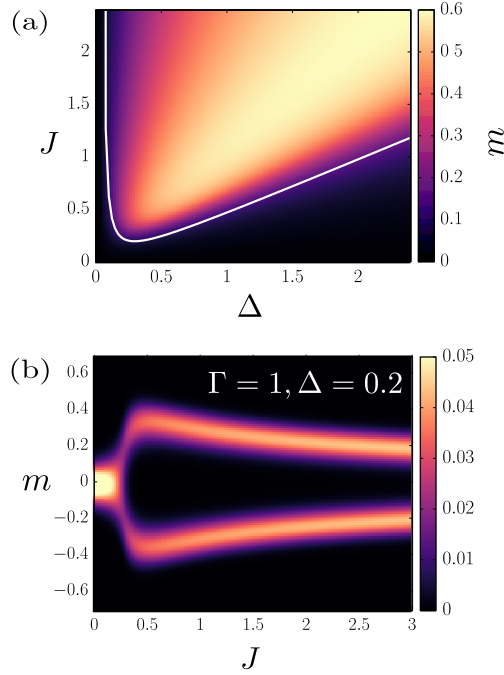


Figure 5.6: (a) Phase diagram of the DTI model on fully connected graphs in the parameter space (Δ, J) . A continuous transition occurs across the solid white curve. The brightness represents the magnitude of magnetization m . (b) The density of the order parameter in the steady state as a function of J at $\Delta = 0.2$. System size is taken as $N = 128$. The brightness represents the probability that the order parameter exists. Data are obtained from the Liouville equation with $\Gamma = 1$ based on the PI states.

size exponent $\bar{\nu}$ of $\bar{\nu} = d_c \nu = 1.75 \pm 0.01$ using FSS analysis, as shown in the inset of Fig. 5.5(a). Note that the critical exponent β is in agreement with the analytical result of Eq. (5.32).

The susceptibility χ defined in Eq. (5.15) exhibits the divergent behavior $\chi \sim (\Gamma_c - \Gamma)^{-\gamma}$ as $\Gamma \rightarrow \Gamma_c^-$. Therefore, we plot χ versus $\Delta_c - \Delta$ on a double logarithmic scale and find that χ exhibits power-law decay with slope -1.00 ± 0.01 in Fig. 5.5(b). Thus, the exponent γ is estimated as $\gamma = 1.00 \pm 0.01$. We note that the data points collapse onto a single power-law line in the subcritical region with the choice of $\bar{z} = 0.14 \pm 0.01$. Inserting this \bar{z} value into $d_c + z = 4$, we obtain $d_c = 3.5 \pm 0.02$ and $z = 0.5 \pm 0.03$. Next, by plotting $\chi N^{-\gamma/\bar{\nu}}$ versus $(\Delta_c - \Delta) N^{1/\bar{\nu}}$ and taking

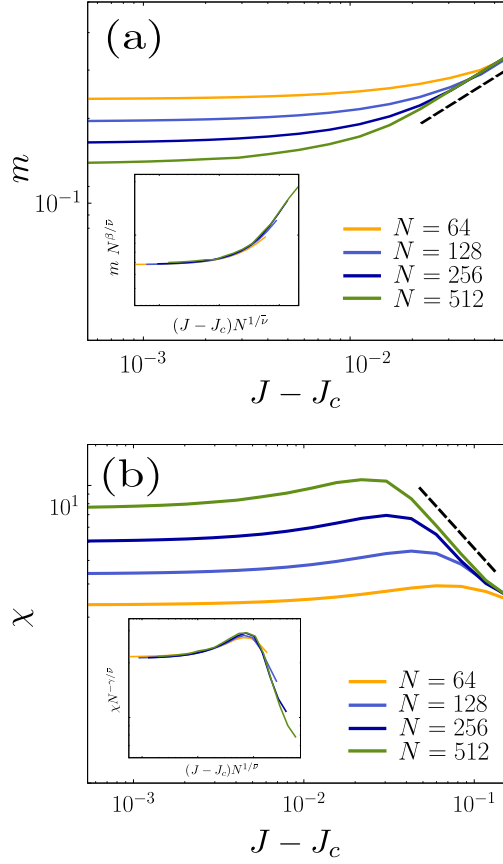


Figure 5.7: FSS analysis for the DTI model at $\Delta = 0.2$ and $J = 1$ on fully connected graphs. (a) Plot of the order parameter m as a function of $J - J_c$ for different system sizes. The auxiliary dashed line with slope 0.5 means the power-law behavior $m \sim (J - J_c)^{0.5}$. Inset: Scaling plot of the magnetization $m N^{\beta/\bar{\nu}}$ versus $(J - J_c) N^{1/\bar{\nu}}$ with $\bar{\nu} = 1.75$ and $\beta = 0.5$. (b) Plot of χ as a function of $J - J_c$ for different system sizes. The auxiliary dashed line with slope -1.0 means the power-law behavior $\chi \sim (J - J_c)^{-1.0}$. Inset: Scaling plot of the susceptibility $\chi N^{-\gamma/\bar{\nu}}$ versus $(J - J_c) N^{1/\bar{\nu}}$. The critical exponents $\bar{\nu} = 1.75$ and $\gamma = 1.0$ are used.

$\bar{\nu} = 1.75 \pm 0.01$ in the inset of Fig. 5.5(b), we find that the data points collapse onto a single curve. These results confirm that $\bar{\nu} = 1.75 \pm 0.01$.

Next, we consider the case where $\Gamma = 1$ is fixed. The phase diagram obtained numerically in the parameter space (Δ, J) is shown in Fig. 5.6(a). The heat map data are obtained by the direct enumeration of the magnetization on the basis of PI states,

whereas the phase boundary curve (white curve) is obtained by the fluctuationless MF solution. The probability of the order parameter is shown in Fig. 5.6(b), where $\Delta = 0.2$ is fixed, but J is varied. For $\Delta = 0.2$, a discontinuous transition is predicted by the Keldysh formalism; however, we obtain a continuous transition. Note that the order parameter curve does not increase monotonously but rather decreases after a point near $J \approx 0.5$. It is likely that the order parameter saturates at a constant value in the large- J limit.

Our result implies that if we simulate the DTI model at $d = 4$, the transition would be continuous with the criticality in the MF limit. These results differ from those obtained from the Keldysh formalism [221]. Because the Keldysh field theory is well justified for bosonic systems when one applies to the Keldysh formalism on the spin systems such as the DTI model, it is necessary to map spins to bosons; for instance, through a hard-core bosonization using a large on-site potential, which might not result in a valid qubit system in the infinite potential limit.

Next, we perform FSS analysis to obtain the critical exponents β and $\bar{\nu}$, which are associated with the order parameter and correlation size, respectively. From Fig. 5.7(a), for $\Delta = 0.2$, we obtain $\beta = 0.50 \pm 0.01$ by measuring the local slope of m as a function of $J - J_c$ on a double logarithmic scale. Here, J_c is the value predicted by the fluctuationless MF theory. Next, we plot $mN^{\beta/\bar{\nu}}$ versus $(J - J_c)N^{1/\bar{\nu}}$ for different system sizes in the inset of Fig. 5.7(a). In this plot, $\bar{\nu}$ is the value at which the data for different N values collapse onto the same curve. $\bar{\nu} = d_c\nu = 1.75 \pm 0.01$ is obtained. The susceptibility defined in Eq. (5.15) diverges as $\chi \sim (\Delta_c - \Delta)^{-\gamma}$ as $\Delta \rightarrow \Delta_c^-$. Therefore, we plot χ versus $\Delta_c - \Delta$ on a double logarithmic scale and find that χ exhibits power-law decay with slope -1.00 ± 0.01 in Fig. 5.7(b). We note that the data points collapse onto a single power-law line in the subcritical region with the choice of $\bar{z} = 0.14 \pm 0.01$. Next, by plotting $\chi N^{-\gamma/\bar{\nu}}$ versus $(\Delta_c - \Delta)N^{1/\bar{\nu}}$ and taking $\bar{\nu} = 1.75 \pm 0.01$, we find that the data collapse onto a single curve, as shown in the inset of Fig. 5.7(b). This result confirms that $\bar{\nu} = 1.75 \pm 0.01$.

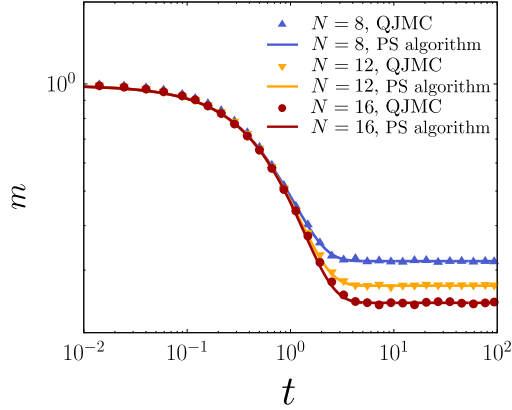


Figure 5.8: Comparison of the data sets obtained by the direct enumerations of the Lindblad equation based on the PI state (solid curve) and the quantum jump Monte Carlo (QJMC) simulations (symbols) for the DTI model with $\Delta = 0.1$ and $J = 1$ for different system sizes.

Similarly, we obtain the same critical exponents and upper critical dimension along the transition line. The obtained exponents $\beta = 0.50 \pm 0.01$, $\gamma = 1.00 \pm 0.04$, $\bar{\nu} = 1.75 \pm 0.01$, and $\bar{z} = 0.14 \pm 0.01$ satisfy the hyperscaling relation $2\beta + \gamma = \nu(d_c + z)$, or equivalently $2\beta + \gamma = \bar{\nu}(1 + \bar{z})$ [83]. Note that the Lindblad operator in Eq. (5.16) conserves \mathbb{Z}_2 symmetry, and thus the static critical exponents are the same, whereas it affects the dynamics and the related critical exponent z .

5.5 Comparison with quantum jump Monte Carlo simulation

To check the validity of the numerical method of the Lindblad equation based on the PI states, we perform quantum jump Monte Carlo simulations for the DTI model on the fully-connected graph. Simulations are performed on relatively small system sizes, $N = 8, 12$, and 16 shown in Fig. 5.8. We find the two methods are in good agreement.

Table 5.3: Summary of universality classes for classical, closed quantum, and open quantum Ising models. The system Hamiltonian (\hat{H}_S) and Lindblad operators (\hat{L}_ℓ) were defined for each model. Our numerical results indicate that dissipation changes the upper critical dimension and dynamic critical exponent. Note that the hyperscaling relation $2\beta + \gamma = \nu(d_c + z)$ is valid for all the models.

Model	Classical Ising model	TI model	DTI model
Hamiltonian	$\hat{H} = -J \sum_{\langle \ell m \rangle} \hat{\sigma}_\ell^z \hat{\sigma}_m^z$	$\hat{H} = -J \sum_{\langle \ell m \rangle} \hat{\sigma}_\ell^z \hat{\sigma}_m^z + \Delta \sum_\ell \hat{\sigma}_\ell^x$	$\hat{H} = -J \sum_{\langle \ell m \rangle} \hat{\sigma}_\ell^z \hat{\sigma}_m^z + \Delta \sum_\ell \hat{\sigma}_\ell^x$
Lindblad operator	—	—	$\hat{L}_\ell = \sqrt{\Gamma} \hat{\sigma}_\ell^x$
d_c	4	3	3.5
z	0	1	0.5
Other critical exponents	$\beta = 0.5, \gamma = 1.0, \nu = 0.5, \text{ and } d_c + z = 4.$		

5.6 Quantum contact process in scale-free networks

Studying the QCP model on complex networks provides advantages for obtaining analytical solutions. Here, we obtain an analytical solution of the PT using the annealed approximation. Furthermore, we confirm our result with numerical simulations of the static model [107, 198], which is a simple model of an SF network, allowing us to obtain analytic solutions. We find that the PTs and critical behavior depend on the heterogeneity of the network, i.e., the exponent λ of the degree distribution. We obtain the following results. If the degree exponent of the SF network is less than a critical value, $\lambda_c = 3$, the transition point becomes zero, and thus the system is always in a nontrivial stationary state. At $\lambda = 3$, the system undergoes a continuous PT at a finite transition point and the susceptibility diverges logarithmically. If $\lambda > 3$, the system undergoes a discontinuous PT [4, 11, 58, 162, 193, 194, 260, 261]. The order parameter jumps at a transition point and the susceptibility, defined as the response of the order parameter to the conjugated field [215, 216], diverges at the transition point. We discuss the similarities and differences between these phenomena and those of a classical model using hypergraphs [143, 149].

5.6.1 Annealed approximation and self-consistency equation

We introduce the annealed approximation. We average the expectation values of the observables over the nodes with the same degree k . Next, we establish a set of differential equations for the observables for each k . If we ignore fluctuations and set $\kappa = 0$, the annealed equations for the QCP become

$$\frac{\partial n_k}{\partial t} = \omega y_k k \theta - n_k, \quad (5.35)$$

$$\frac{\partial x_k}{\partial t} = -\omega y_k k \phi - \frac{1}{2} x_k, \quad (5.36)$$

$$\frac{\partial y_k}{\partial t} = \omega(2k\theta - 4n_k k \theta + x_k k \phi) - \frac{1}{2} y_k, \quad (5.37)$$

where n_k , x_k , and y_k are the expectation values of the operators over the nodes with degree k , and

$$\theta = \frac{1}{\langle k \rangle} \int_{k_m}^{\infty} dk k P_d(k) n_k, \quad (5.38)$$

$$\phi = \frac{1}{\langle k \rangle} \int_{k_m}^{\infty} dk k P_d(k) x_k, \quad (5.39)$$

where k_m denotes the minimum degree. For the steady state, we set $\frac{\partial n_k}{\partial t} = 0$, $\frac{\partial x_k}{\partial t} = 0$, and $\frac{\partial y_k}{\partial t} = 0$. The solutions are as follows:

$$n_k = \frac{4\theta^2 k^2 \omega^2}{1 + 8\theta^2 k^2 \omega^2 + 4k^2 \omega^2 \phi^2}, \quad (5.40)$$

$$x_k = -\frac{8\theta k^2 \omega^2 \phi}{1 + 8\theta^2 k^2 \omega^2 + 4k^2 \omega^2 \phi^2}, \quad (5.41)$$

$$y_k = \frac{4\theta k \omega}{1 + 8\theta^2 k^2 \omega^2 + 4k^2 \omega^2 \phi^2}. \quad (5.42)$$

Then, θ and ϕ are again expressed in terms of n_k and x_k using Eqs. (5.38) and (5.39), respectively. Inserting Eq. (5.40) into Eq. (5.38), we obtain a self-consistency function $G(\theta)$ as

$$G(\theta) \equiv \frac{1}{\langle k \rangle} \int_{k_m}^{\infty} dk k P_d(k) \frac{4\theta^2 k^2 \omega^2}{1 + 8\theta^2 k^2 \omega^2 + 4k^2 \omega^2 \phi^2} - \theta \quad (5.43)$$

and obtain a solution θ_0 of $G(\theta_0) = 0$. Similarly, inserting Eq. (5.41) into Eq. (5.39), we obtain the solution $\phi_0 = 0$. The power-law degree distribution $P_d(k) \propto k^{-\lambda}$ for $k > k_m$. Then, the self-consistency condition is rewritten as follows:

$$G(\theta_0) = \frac{1}{2} {}_2F_1 \left(\frac{\lambda}{2} - 1, 1; \frac{\lambda}{2}; -\frac{1}{8k_m^2 \omega^2 \theta_0^2} \right) - \theta_0 = 0, \quad (5.44)$$

where ${}_2F_1(a, b; c; d)$ is the Gauss hypergeometric function defined as [1]

$${}_2F_1(a, b; c; z) = \frac{\Gamma(c)}{\Gamma(b)\Gamma(c-b)} \int_0^1 dt t^{b-1} (1-t)^{c-b-1} (1-tz)^{-a}.$$

Using the Taylor expansion of the hypergeometric function near the trivial solution $\theta_0 = 0$,

$${}_2F_1\left(\frac{\lambda}{2} - 1, 1; \frac{\lambda}{2}; -\frac{1}{8k_m^2\omega^2\theta_0^2}\right) = \frac{(\lambda/2 - 1)\pi}{\sin[(\lambda/2 + 1)\pi]} (8k_m^2\omega^2\theta_0^2)^{\lambda/2-1} \quad (5.45)$$

$$+ \left(\frac{\lambda}{2} - 1\right) \sum_{i=1}^{\infty} (-1)^i \frac{(8k_m^2\omega^2\theta_0^2)^i}{i + 1 - \lambda/2}, \quad (5.46)$$

we obtain that the self-consistency function has the following properties: $G(0) = 0$ and $G(1) < 0$. Hence, $G(\theta)$ always has a trivial solution $\theta_0 = 0$. This reflects that $n = \theta_0 = 0$ is an absorbing state: the absorbing state is a steady-state of QCP whether the system is finite or infinite. If $\lim_{\theta \rightarrow 0} G'(\theta) > 0$, there exists at least one nonzero solution, because $G(1) < 0$. Using the asymptotic properties of the hypergeometric function, we find that the derivative of the self-consistency function

$$G'(\theta) = \frac{\lambda - 2}{8\lambda k_m^2\omega^2\theta^3} {}_2F_1\left(\frac{\lambda}{2}, 2; \frac{\lambda}{2} + 1; -\frac{1}{8k_m^2\omega^2\theta^2}\right) - 1 \quad (5.47)$$

reduces in the limit $\theta \rightarrow 0$ to the following:

$$\lim_{\theta \rightarrow 0} G'(\theta) = \begin{cases} +\infty & \text{for } \lambda < \lambda_c \\ \frac{\pi k_m \omega}{\sqrt{2}} - 1 & \text{for } \lambda = \lambda_c \\ -1 & \text{for } \lambda > \lambda_c \end{cases}. \quad (5.48)$$

Therefore, there exists a characteristic degree exponent $\lambda_c = 3$. These results can be confirmed numerically, as shown in Fig. 5.9.

After we obtain the solution θ_0 , we can calculate the density of active sites in the

system, which serves as the order parameter of the PT and is given by

$$\begin{aligned} n &= \int_{k_m}^{\infty} dk P_d(k) \frac{4\theta_0^2 k^2 \omega^2}{1 + 8\theta_0^2 k^2 \omega^2} \\ &= \frac{1}{2} {}_2F_1 \left(\frac{\lambda - 1}{2}, 1; \frac{\lambda + 1}{2}; -\frac{1}{8k_m^2 \omega^2 \theta_0^2} \right). \end{aligned} \quad (5.49)$$

To determine the stability of the solution θ_0 , we apply small perturbations to the steady-state solution n_k and θ_0 as δn_k and $\delta\theta$, respectively, where $n_k \rightarrow n'_k = n_k + \delta n_k$, and $\theta_0 \rightarrow \theta' = \theta_0 + \delta\theta$. Then, $y_k(\theta)$ in Eq. (5.42) becomes $y_k(\theta')$, and the equation of motion of n_k given by Eq. (5.35) becomes

$$\frac{\partial \delta n_k}{\partial t} = \frac{4\theta'^2 k^2 \omega^2}{1 + 8\theta'^2 k^2 \omega^2 + 4k^2 \omega^2 \phi^2} - n'_k. \quad (5.50)$$

By integrating the equation after multiplying both sides by $kP_d(k)/\langle k \rangle$, we obtain

$$\begin{aligned} \frac{\partial \delta\theta}{\partial t} &= \frac{1}{\langle k \rangle} \int_{k_m}^{\infty} dk k P_d(k) \frac{4\theta'^2 k^2 \omega^2}{1 + 8\theta'^2 k^2 \omega^2 + 4k^2 \omega^2 \phi^2} - \theta' \\ &= G'(\theta_0) \delta\theta, \end{aligned} \quad (5.51)$$

where we used $G(\theta_0) = 0$. Therefore, the solution θ_0 is stable when $G'(\theta_0) < 0$.

5.6.2 Phase transition and critical behavior

A PT can be determined in terms of the *ad hoc* potential, which has been employed to study a synchronization transition in nonequilibrium systems [312]. This approach is similar to approach using the Landau free energy proposed in equilibrium systems. The *ad hoc* potential can be applied to the QCP model. The *ad hoc* potential $U(\theta)$ is defined through the relation $G(\theta) = -dU(\theta)/d\theta$. In turn, $U(\theta)$ is written as

$$U(\theta) = - \int_0^\theta G(\theta') d\theta', \quad (5.52)$$

where we set $U(0) = 0$. The effective potential is illustrated in Fig. 5.9(a)–(c). Integrating the leading terms in Eq. (5.46), we obtain

$$U(\theta) = \frac{1}{2}\theta^2 - \frac{8k_m^2\omega^2}{3} \left(\frac{\lambda-2}{\lambda-4} \right) \theta^3 - \frac{(\lambda/2-1)\pi}{(\lambda-1)\sin[(\lambda/2+1)\pi]} (8k_m^2\omega^2)^{\lambda/2-1} \theta^{\lambda-1} + \text{h.o.}, \quad (5.53)$$

where h.o. represents higher-order terms. The profile of $U(\theta)$ depends on the degree exponent λ and the frequency ω as shown in Fig. 5.9(a)–(c). The transition type is determined by investigating the profile of $U(\theta)$: the solution of $dU(\theta)/d\theta = 0$ provides the behavior of the order parameter and the sign of $d^2U(\theta)/d\theta^2$ at the solution θ_0 does the stability.

Here, we determine the type of PT and investigate the critical behavior of the QCP model as a function of ω for different λ values.

Type of phase transition and order parameter

- (i) For $2 < \lambda < 3$ (Fig. 5.9(a), (d), and (g)), the term of $O(\theta^{\lambda-1})$ in Eq. (5.53) is much dominant than θ^2 . There exists a potential well at θ_0 (Fig.5.9(a)), at which $U'(\theta_0) = G(\theta_0) = 0$ (Fig.5.9(d)). $\theta_0 > 0$ for $\omega > 0$, but $\theta_0 = 0$ for $\omega = 0$. A PT occurs at $\omega_c = 0$. From $G(\theta_0) = 0$, we obtain the relation that for $\theta_0 \ll 1$,

$$\frac{(\lambda/2-1)\pi}{\sin[(\lambda/2+1)\pi]} (8k_m^2\omega^2\theta_0^2)^{\lambda/2-1} - \theta_0 = 0. \quad (5.54)$$

Therefore,

$$\theta_0 \sim \omega^{\frac{\lambda-2}{3-\lambda}}, \quad (5.55)$$

$$n \sim (\omega^2\theta_0^2)^{(\lambda-1)/2} \sim \omega^{\frac{\lambda-1}{3-\lambda}}. \quad (5.56)$$

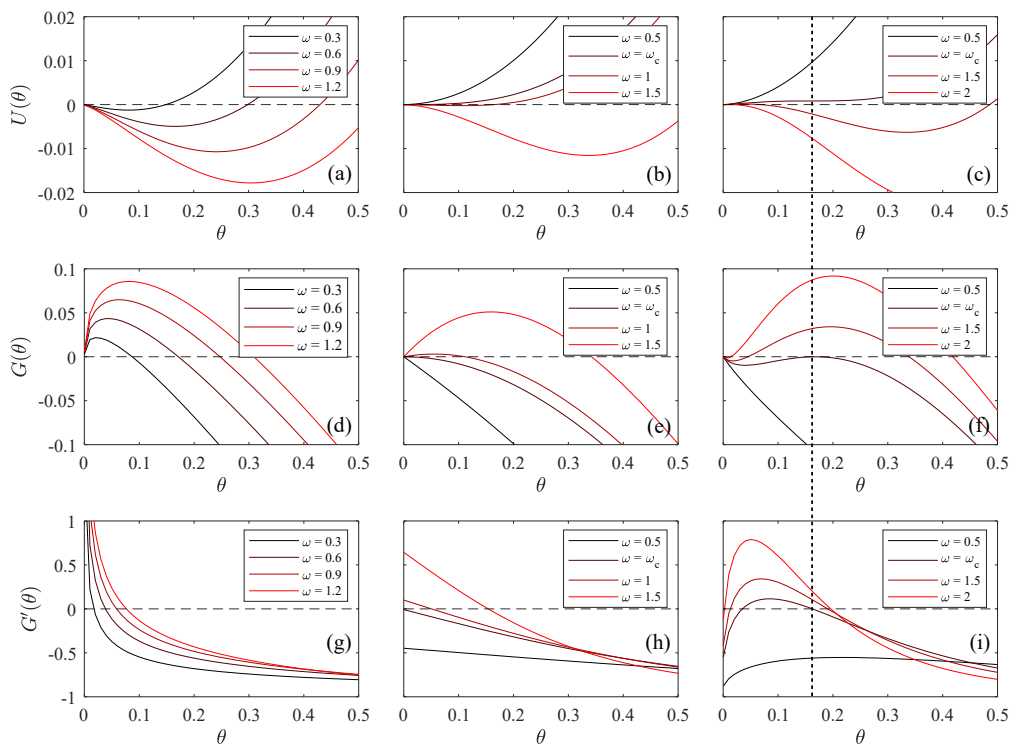


Figure 5.9: (a)–(c) Plots of the *ad hoc* potential $U(\theta)$ as a function of θ for different ω values. (d)–(f) Plots of the self-consistency function $G(\theta)$ versus θ for different ω values. (g)–(i) Plot of the derivative of $G(\theta)$ versus θ for different ω values. (i) $\lambda = 2.5$ for (a), (d), and (g). (ii) $\lambda = 3$ for (b), (e), and (h). (iii) $\lambda = 3.5$ for (c), (f), and (i). Numerical values are obtained by solving Eq. (5.44) for the mean degree $\langle k \rangle = 1$.

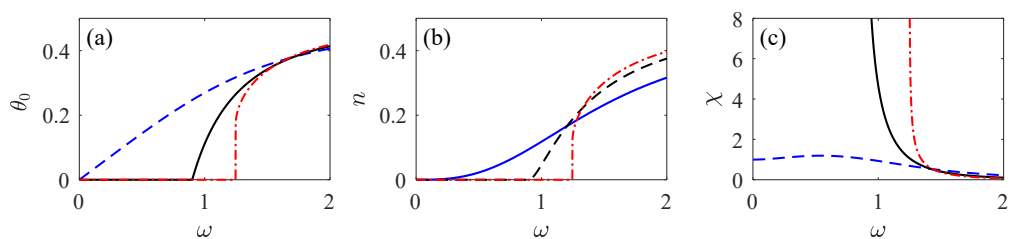


Figure 5.10: Numerical solutions of the self-consistency equation. (a) Solution θ of the self-consistency equation, (b) density of active sites, and (c) susceptibility of the steady state as a function of ω . Dashed blue, solid black, and dash-dotted curves represent $\lambda = 2.5$, $\lambda = \lambda_c = 3$, and $\lambda = 3.5$, respectively.

Thus, the critical exponent of the order parameter $\beta = (\lambda - 1)/(3 - \lambda)$. By contrast, in the classical limit ($\omega = 0$ and $\kappa \neq 0$), the transition point is also $\kappa_c = 0$ and $\beta = 1/(3 - \lambda)$.

- (ii) At $\lambda = \lambda_c = 3$ (Fig. 5.9(b), (e), and (h)), the terms of $O(\theta^{\lambda-1})$ and $O(\theta^3)$ are of the same order. For this case, the profile of $U(\theta)$ depends on ω . There exists a characteristic value ω_c , calculated as $\omega_c = \sqrt{2}/k_m\pi = 0.900316$ using Eq. (5.48) for the case $\langle k \rangle = 1$. For $\omega < \omega_c$, a potential well exists at $\theta_0 = 0$, whereas for $\omega > \omega_c$, it locates at finite θ_0 depending on ω . A PT occurs at finite ω_c .

The self-consistency function and the density of active sites are expressed as

$$G(\theta_0) = \theta_0 \sqrt{2} \omega k_m \tan^{-1} \left(\frac{1}{2\sqrt{2}\theta_0 \omega k_m} \right) - \theta_0 = 0, \quad (5.57)$$

$$n = 4\theta_0^2 \omega^2 k_m^2 \ln \left(\frac{1}{8\theta_0^2 \omega^2 k_m^2} + 1 \right), \quad (5.58)$$

where we used the properties ${}_2F_1 \left(\frac{1}{2}, 1; \frac{3}{2}; -z^2 \right) = \tan^{-1}(z)/z$ and ${}_2F_1(1, 1; 2; -z) = \ln(1+z)/z$ [1]. When $\omega > \omega_c$, $G'(\theta_0 = 0) > 0$. The absorbing state ($n = \theta_0 = 0$) becomes unstable, and a single stable nonzero solution $\theta_0 > 0$ appears (Fig. 5.9(e)). Near the transition point ω_c ,

$$G(\theta_0) \simeq \left(\frac{\omega - \omega_c}{\omega_c} \right) \theta_0 - 8k_m^2 \omega^2 \theta_0^2, \quad (5.59)$$

and the solutions are

$$\theta_0 \sim (\omega - \omega_c), \quad (5.60)$$

$$n \sim \theta_0^2 \ln \left(\frac{1}{\theta_0} \right) \sim (\omega - \omega_c)^2 \ln \left(\frac{1}{\omega - \omega_c} \right). \quad (5.61)$$

Thus, the critical exponent $\beta = 2$ but with a logarithmic correction.

- (iii) For $3 < \lambda < 4$ (Fig. 5.9(c), (f), and (i)), the term of $O(\theta^{\lambda-1})$ in $U(\theta)$ is the

second leading term and its coefficient is negative. For $\lambda > 4$, the term of $O(\theta^3)$ is the second leading term, which is negative. Therefore, the critical behavior for $\lambda > 3$ is mainly determined by the competition between the strengths of the terms of $O(\theta^2)$ and $O(\theta^{\lambda-1})$ or $O(\theta^3)$. Because $\lim_{\theta_0 \rightarrow 0} G'(\theta_0) = -1$ in Eq. (5.48), there exists a finite ω_c at which there exists a characteristic nonzero θ_0 satisfying $G(\theta_0) = 0$ (Fig. 5.9(f)). For instance, $\omega_c = 1.246471$ in Fig 5.9(f). Moreover, we find that $G'(\theta_0) = 0$ at ω_c (Fig 5.9(i)). Near the transition point θ_0 ,

$$G(\theta_0) = \frac{\partial G}{\partial \theta_0} \Delta \theta_0 + \frac{1}{2} \frac{\partial^2 G}{\partial \theta_0^2} (\Delta \theta_0)^2 + \frac{\partial G}{\partial \omega} \Delta \omega. \quad (5.62)$$

Because $G(\theta_0) = 0$ and $G'(\theta_0) = 0$, $\theta_0(\omega) - \theta_0(\omega_c) \sim (\omega - \omega_c)^{1/2}$. Therefore,

$$n(\omega) - n(\omega_c) \sim (\omega - \omega_c)^{1/2}. \quad (5.63)$$

The order parameter jumps by the amount of $n(\omega_c)$, and increases continuously as ω is increased beyond ω_c . The PT is hybrid with the critical exponent $\beta = 1/2$. The phase diagram is illustrated in Fig. 5.11. At the transition point, $G(\theta_0) = 0$ and $G'(\theta_0) = 0$. Similar behaviors appear in the epidemic model [58], synchronization [312], and colloid crystal [4] in non-equilibrium and the Ashkin-Teller model [140, 170] on complex networks in thermal equilibrium systems. Note that for the colloid crystal problem, the *ad hoc* potential is zero at the transition point for hybrid phase transitions, whereas $U(\theta_0) \neq 0$ for the QCP model on SF networks.

Susceptibility

We define the susceptibility as the response of the density of active sites n to the conjugated field H , which is realized as the time-reversed form of the decay process

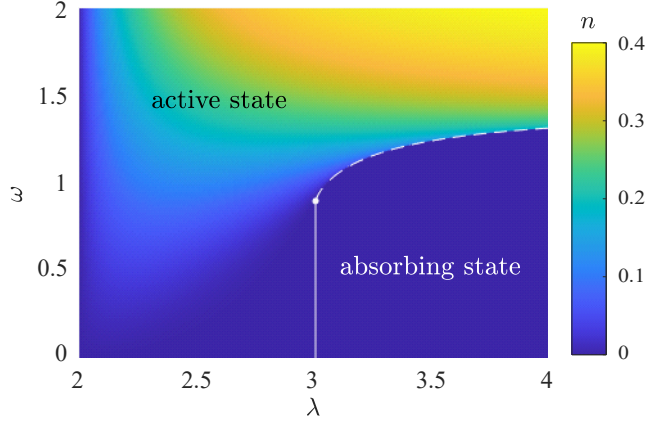


Figure 5.11: The phase diagram of the QCP model on SF networks. The type of PT depends on the degree exponent λ . If $\lambda < \lambda_c = 3$, the transition point becomes zero ($\omega_c = 0$), thus $n > 0$ for any $\omega > 0$. At $\lambda = \lambda_c$, the system undergoes a continuous PT at $\omega_c \approx 0.900316$. If $\lambda > \lambda_c$, the system undergoes a discontinuous PT, and n is discontinuous on the transition line.

$(|\downarrow\rangle \rightarrow |\uparrow\rangle)$ [215, 216]:

$$\mathcal{L}_\ell^{(h)} \hat{\rho} = H \left(\hat{\sigma}_\ell^+ \hat{\rho} \hat{\sigma}_\ell^- - \frac{1}{2} \{ (1 - \hat{n}_\ell), \hat{\rho} \} \right). \quad (5.64)$$

Then, the annealed equations, Eqs. (5.35)–(5.37), become

$$\frac{\partial n_k}{\partial t} = \omega k \theta y_k - n_k + h(1 - n_k), \quad (5.65)$$

$$\frac{\partial x_k}{\partial t} = -\omega k \phi y_k - \frac{1+h}{2} x_k, \quad (5.66)$$

$$\frac{\partial y_k}{\partial t} = \omega k (2\theta - 4\theta n_k + \phi x_k) - \frac{1+h}{2} y_k, \quad (5.67)$$

where $h = H/\Gamma$. The conjugated field affects n directly through Eq. (5.49) and indirectly through the self-consistency equation, Eq. (5.44). The susceptibility is then

$$\chi = \frac{dn}{dh} = \left. \frac{\partial n}{\partial h} \right|_{\omega, \theta} - \left. \frac{\partial n}{\partial \theta} \right|_{\omega, h} \left. \frac{\partial G}{\partial h} \right|_{\omega, \theta} \left(\left. \frac{\partial G}{\partial \theta} \right|_{\omega, h} \right)^{-1}. \quad (5.68)$$

The susceptibility for various λ is illustrated in Fig. 5.10(c). We can use the asymp-

otic properties of the hypergeometric function to calculate the behavior of the susceptibility near the transition point.

- (i) For $2 < \lambda < 3$, $\frac{\partial n}{\partial h}\Big|_{\omega, \theta} \rightarrow 1$, and $\frac{\partial n}{\partial \theta}\Big|_{\omega, h} \rightarrow 0$ as $\omega \rightarrow 0$. Therefore, the susceptibility converges to one, and the critical exponent of the susceptibility $\gamma = 0$.
- (ii) For $\lambda = \lambda_c = 3$, $\frac{\partial n}{\partial \theta}\Big|_{\omega, h} \sim \theta \ln\left(\frac{1}{\theta}\right)$, and $\frac{\partial G}{\partial \theta}\Big|_{\omega, h} \sim \theta(\omega - \omega_c)$. Thus, the susceptibility diverges logarithmically at the transition point: $\chi \sim \ln\left(\frac{1}{\omega - \omega_c}\right)$. Again, the critical exponent of the susceptibility $\gamma = 0$.
- (iii) For $\lambda > 3$, $\frac{\partial G}{\partial \theta}\Big|_{\omega, h} \sim (\omega - \omega_c)^{1/2}$, whereas all the other terms converge to a finite value at the transition point. The susceptibility diverges as $(\omega - \omega_c)^{-\gamma}$ with the critical exponent $\gamma = 1/2$.

5.6.3 Numerical results

To further confirm our results, we perform numerical simulations by tracking the expectation values of the observables n_ℓ , x_ℓ , and y_ℓ . This method has also been implemented in the quantum three-state epidemic model [273]. Note that this method is analogous to the individual-based mean-field method [118, 298, 302], which is often employed to study stochastic epidemic dynamics. This method enables us to predict the transition point of PT and the critical phenomena in the classical stochastic process in static and temporal networks [118, 298, 302, 324]. The effect of the power-law degree distribution does not manifest itself notably unless the number of the nodes in the network is at least 1000. Therefore, an exact numerical simulation method such as the quantum-jump Monte Carlo method [276] or exact diagonalization cannot be used for these two-state systems owing to their exponential numerical complexity.

We perform numerical simulations in the static model network. We choose three values of the degree exponent: $\lambda = 2.2 < \lambda_c$, $\lambda = \lambda_c = 3$, and $\lambda = 3.5 > \lambda_c$. The density of active sites and the susceptibility for these degree exponents are presented in

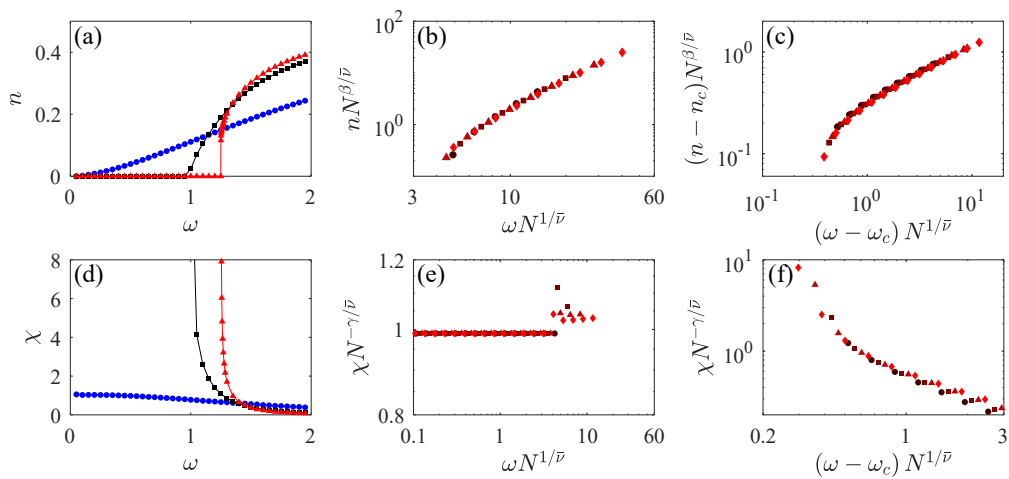


Figure 5.12: Numerical simulation results for the PTs of the QCP model on the static model. Plots of (a) the density of active sites $\langle n \rangle$ and (d) the susceptibility versus the control parameter ω for $\lambda = 2.2$ (\bullet), 3.0 (\blacksquare), and 3.5 (\blacktriangle). Note that ω_c s for $\lambda = 3.0$ and $\lambda = 3.5$ are estimated to be 0.900316 and 1.246471 , respectively. (b) Scaling plot of the order parameter $nN^{\beta/\bar{\nu}}$ versus $\omega N^{1/\bar{\nu}}$ for $\lambda = 2.2$. (c) Scaling plot of order parameter $(n - n_c)N^{\beta/\bar{\nu}}$ versus $(\omega - \omega_c)N^{1/\bar{\nu}}$ for $\lambda = 3.5$. (e) Scaling plot of susceptibility $\chi N^{-\gamma/\bar{\nu}}$ versus $\omega N^{1/\bar{\nu}}$ for $\lambda = 2.2$. (f) Scaling plot of order parameter $\chi N^{-\gamma/\bar{\nu}}$ versus $(\omega - \omega_c)N^{1/\bar{\nu}}$ for $\lambda = 3.5$. The critical exponents $\beta = 0.5$, $\gamma = 0.5$, $\bar{\nu} = 2.05$, $\omega_c = 1.246471$, and $n_c = n(\omega_c) = 0.167748$ are used. The data points for different system sizes collapse onto a single curve. Finite-size scaling analysis is not feasible for $\lambda = \lambda_c$, because logarithmic corrections are applied to both the order parameter and the susceptibility: $n \sim (\omega - \omega_c)^2 \ln\left(\frac{1}{\omega - \omega_c}\right)$ and $\chi \sim \ln\left(\frac{1}{\omega - \omega_c}\right)$.

Fig. 5.12(a) and (d), respectively. The order parameter is continuous near the transition point for $\lambda = 2.2$ and $\lambda = 3$ and discontinuous for $\lambda = 3.5$. In addition, the transition point ω_c is zero for $\lambda = 2.2$, whereas it is nonzero for $\lambda = 3$ and $\lambda = 3.5$. The susceptibility converges to unity for $\lambda = 2.2$, and it diverges for $\lambda = 3$ and $\lambda = 3.5$. The numerical results confirm these analytical predictions.

We also perform finite-size scaling analysis to measure the critical exponent $\bar{\nu}$ for $\lambda = 2.2$ and $\lambda = 3.5$. When the degree exponent is $\lambda_c = 3$, the order parameter increases continuously from zero with the critical exponent $\beta = 2$, but with a logarithmic correction as $n \sim (\omega - \omega_c)^2 \ln\left(\frac{1}{\omega - \omega_c}\right)$. Moreover, the susceptibility diverges logarithmically: $\chi \sim -\ln(\omega - \omega_c)$. Therefore, finite-size scaling analysis may not be feasible for $\lambda = \lambda_c$.

For $\lambda < \lambda_c$, we choose $\lambda = 2.2$, the effect of the logarithmic correction is so large that FSS analysis may not be feasible. We plot $nN^{\beta/\bar{\nu}}$ versus $\omega N^{1/\bar{\nu}}$ for various system sizes in Fig. 5.12(b) for $\lambda = 2.2$. The data points for various system sizes collapse onto a single curve with the critical exponents $\beta = 1.5$ and $\bar{\nu} = 2.0$.

For $\lambda = 3.5$, in Fig. 5.12(c) we plot $[n(\omega) - n(\omega_c)]N^{\beta/\bar{\nu}}$ versus $(\omega - \omega_c)N^{1/\bar{\nu}}$ with the obtained $n(\omega_c)$, because the transition is discontinuous at finite ω_c . The transition points $\omega_c = 1.246471$ and $n_c = n(\omega_c) = 0.167748$ are numerically estimated using the annealed approximation. The data points collapse onto a single curve for $\beta = 0.5$ and $\bar{\nu} = 1.95$. This β value is consistent with the analytical solution.

For the susceptibility, we plot $\chi N^{-\gamma/\bar{\nu}}$ versus $(\omega - \omega_c)N^{1/\bar{\nu}}$ for $\omega > \omega_c$. For $\lambda = 2.2$, the susceptibility converges to unity [Fig. 5.12(e)]. For $\lambda = 3.5$, the data points collapse onto a single curve with $\gamma = 0.5$ and the previously obtained $\bar{\nu} = 1.95$ [Fig. 5.12(f)]. Indeed, this result is consistent with the analytical prediction using the annealed approximation.

5.7 Summary and Discussion

Several analytical approaches have exploited phase transitions from an absorbing state to an active state in the mean-field (MF) limit in dissipative quantum systems such as the quantum contact process (QCP) and dissipative transverse Ising (DTI) model. However, their results are not consistent to each other. Thus, it is necessary to confirm the analytical results numerically. However, the numerical check is not feasible in higher dimensions because the computational complexity increases exponentially as the dimensionality is increased. Here, we numerically exploited the critical behaviors in such quantum phase transitions using the property in infinite dimensions (d_∞) that spin indices are permutation invariant (PI). Assuming that the MF solution is equivalent to the solution above the upper critical dimension d_c including d_∞ , we considered the critical behavior at d_∞ . The system at d_∞ is regarded as the all-to-all graph, on which spin indices are PI. The quantum states that are PI can be contracted to a single state. This contraction reduces the computational complexity considerably, from $\mathcal{O}(2^{2N})$ to $\mathcal{O}(N^3)$. Thus numerical simulations are feasible in relatively large system sizes (up to $N = 1024$). The critical behavior was obtained using finite-size scaling (FSS) analysis, which are consistent with those obtained using the fluctuationless MF approach.

We first considered the quantum contact process (QCP), where a previous result based on the semiclassical MF solution showed that the continuous transition belongs to the directed percolation (DP) universality class and the tricritical point (TP) belongs to the tricritical DP class (Fig. 5.9). Using our approach, we find that the transition lines are the same as those obtained using the semiclassical approach with an upper critical dimension $d_c = 3$ [160]. Furthermore, a crossover region exists along which the exponent α (associated with the density of active sites) decreases continuously from the tricritical DP value to the DP value, which is reminiscent of the one-dimensional QCP [159].

Next, both the transverse Ising (TI) and DTI models are characterized by \mathbb{Z}_2 symmetry; thus, the universality class in the steady state should belong to the Ising universality class with $\beta = 0.5$, $\gamma = 1.0$, and $\nu = 0.5$. Using this analytical transition line obtained from the fluctuationless MF results, we successfully performed FSS analysis. For the TI model, the critical exponents $\beta \approx 0.5$, $\gamma \approx 1.0$, $\bar{\nu} \approx 1.5$, and $\bar{z} \approx 0.33$ are obtained. Thus, the upper critical dimension and dynamic critical exponent are found as $d_c = 3$ and $z = 1$, respectively; these values are important for quantum phase transitions because the upper critical dimension is smaller by z than that of the classical transition [189]. By contrast, for the DTI model, the critical exponents $\beta \approx 0.5$, $\gamma \approx 1.0$, $\bar{\nu} \approx 1.75$, and $\bar{z} \approx 0.14$ are obtained. Inserting these values into $d_c + z = 4$, we obtained $d_c = 3.5 \pm 0.02$ and $z = 0.5 \pm 0.03$. Thus, both models satisfy the hyperscaling relation $2\beta + \gamma = \nu(d_c + z)$, or equivalently, $2\beta + \gamma = \bar{\nu}(1 + \bar{z})$ [83]. The MF universality behavior of the three Ising-type models is summarized in Table 5.3.

When the Keldysh formalism is applied to describe the dissipative transverse Ising (DTI) model, the spins in the DTI model are transformed to bosonic operators so that the mean-field functional integral can be applied. The Keldysh formalism is valid for bosonic systems; however, its validity is not completely warranted when applied to spin systems where spins are mapped into hard-core bosons using intense potentials on spin sites.

We remark that the upper critical dimension $d_c \approx 3.5$ is fractional, which may be unexpected. Thus, we show another example showing a fractional upper critical dimension: the 3-state Potts model. An analytic solution for this model exhibits a continuous transition in $d = 2$. For $d > 2$, using the Kadanoff variational renormalization group method, it was shown that the phase transition is discontinuous in $d = 3$. However, it was formidable to identify d_c , which remains a challenging task. Using the numerical conformal bootstrap and extensive Monte Carlo simulations, d_c was obtained approximately as 2.4 [54]. Thus, the upper critical dimension for the 3-state Potts model is fractional. Finally, we think the PI property can be used for other problems, for in-

stance, the quantum synchronizations arising in all-to-all networks [128].

Moreover, we investigated the PTs of the QCP model on SF networks. Using the annealed approximation, which is valid in the network with no degree-degree correlation, we derived the analytical formulae for the PTs as a function of the degree exponent of SF networks. The highly heterogeneous degree distribution characterized by the power-law degree distribution results in rich critical behaviors, including the vanishing transition point, second-order PT, and discontinuous PT, that are not observed in low dimensional systems [31]. When the degree exponent $\lambda < \lambda_c = 3$, the transition point ω_c vanishes, and there is a nontrivial stationary active state for $\omega > 0$. At λ_c , the system undergoes a second-order PT at finite ω_c , and the susceptibility diverges logarithmically. When $\lambda > 3$, a hybrid PT occurs at a finite ω_c . While the order parameter jumps, the susceptibility diverges at the transition point.

We performed numerical simulations on the static model network to confirm the theoretical predictions. The numerical results for the density of active sites and susceptibility were consistent with the analytical predictions. We further investigated the finite-size scaling behavior near the transition point. The critical exponent $\bar{\nu}$ for the correlation length was obtained.

The classical contact process and epidemic susceptible-infected-susceptible (SIS) model are known to belong to the same universality class, which is the DP class. Consequently, one may wonder if the critical exponent values of the QCP in the quantum limit and the previously studied simplicial SIS (s -SIS) model [149] are the same. The s -SIS model was introduced in SF hypergraphs to study the epidemic process in communities with higher-order interactions. Note that the QCP includes the quantum coherent effect, which may be regarded as a consequence of the higher-order interactions in the semiclassical action [31, 160]. Here, we found that the two systems commonly exhibit a discontinuous PT for $\lambda > \lambda_c$ with the same critical exponent values β and γ . However, λ_c is 3 for the QCP and 2.5 for the s -SIS model. For $\lambda < \lambda_c$, the transition is second-order, and the transition point is zero in both cases. Moreover, the values of the

critical exponent β are different; $\beta = (\lambda - 1)/(3 - \lambda)$ for the QCP, and $\beta = 1/(5 - 2\lambda)$ for the s -SIS model. This difference is apparently attributable to the different roles of hubs in the SF network for each model. In the classical case, the various types of phase transitions stems from the higher-order interaction mediated by hyperedges; however, in the quantum case, there is no higher-order interaction between more-than-two nodes — the interaction is purely dyadic. Instead, the complex critical behaviors are driven by mutually related non-commuting observables of the system.

Chapter 6

Conclusion

In this dissertation, we identified that the hybrid phase transition occurs universally in complex contagion processes. We also discovered a novel phenomenon where the type of phase transition is controlled by the degree exponent of the network or hypergraph. When the exponent of the degree distribution is below a certain value, the threshold of the phase transition vanishes. When the exponent is exactly the certain value, the system undergoes a continuous phase transition at finite threshold. When the exponent is larger than the certain value, the system undergoes a hybrid phase transition. We also investigated control strategies to contain complex contagion processes. We implemented the pair-based mean-field theory to resolve the issue of stochastic fluctuations to calculate the appropriateness of each hyperedge to be removed to minimize the epidemic prevalence. For nonlocal spreading processes where the pair-based mean-field theory cannot be applied, we introduced machine learning to calculate a centrality measure tailored to the process. For Further research, we can investigate how prevalent hybrid phase transition is in other types of complex spreading processes. Moreover, for nonlocal contagion processes, we can identify a new network where the contagion occurs locally.

Bibliography

- [1] Milton Abramowitz and Irene A Stegun. *Handbook of mathematical functions: with formulas, graphs, and mathematical tables*, volume 55. Courier Corporation, 1965.
- [2] Sami Abu-El-Haija, Bryan Perozzi, Amol Kapoor, Nazanin Alipourfard, Kristina Lerman, Hrayr Harutyunyan, Greg Ver Steeg, and Aram Galstyan. Mixhop: Higher-order graph convolutional architectures via sparsified neighborhood mixing. pages 21–29. PMLR, 2019.
- [3] Daron Acemođlu, Giacomo Como, Fabio Fagnani, and Asuman Ozdaglar. Opinion fluctuations and disagreement in social networks. *Math. Oper. Res.*, 38(1):1–27, 2013.
- [4] Ricard Alert, Pietro Tierno, and Jaume Casademunt. Mixed-order phase transition in a colloidal crystal. *Proc. Natl. Acad. Sci.*, 114(49):12906–12909, dec 2017.
- [5] Alberto Aleta, Guilherme Ferraz de Arruda, and Yamir Moreno. Data-driven contact structures: From homogeneous mixing to multilayer networks. *PLOS Computational Biology*, 16(7):1–16, 07 2020.
- [6] F. Altarelli, A. Braunstein, L. Dall’Asta, J. R. Wakeling, and R. Zecchina. Containing Epidemic Outbreaks by Message-Passing Techniques. *Phys. Rev. X*, 4(2):021024, may 2014.
- [7] Unai Alvarez-Rodriguez, Federico Battiston, Guilherme Ferraz de Arruda, Yamir Moreno, Matjaž Perc, and Vito Latora. Evolutionary dynamics of higher-order interactions in social networks. *Nat. Hum. Behav.*, jan 2021.

- [8] Cleo Anastassopoulou, Lucia Russo, Athanasios Tsakris, and Constantinos Siettos. Data-based analysis, modelling and forecasting of the COVID-19 outbreak. *PLoS One*, 15(3):1–21, 2020.
- [9] Roy M Anderson and Robert M May. *Infectious diseases of humans: dynamics and control*. Oxford university press, 1992.
- [10] C. Ates, B. Olmos, W. Li, and I. Lesanovsky. Dissipative binding of lattice bosons through distance-selective pair loss. *Phys. Rev. Lett.*, 109(23):233003, 2012.
- [11] Amir Bar and David Mukamel. Mixed-Order Phase Transition in a One-Dimensional Model. *Phys. Rev. Lett.*, 112(1):015701, jan 2014.
- [12] Albert-László Barabási. Scale-free networks: a decade and beyond. *Science*, 325(5939):412–413, 2009.
- [13] Francesco Barone-Adesi, Luca Ragazzoni, and Maurizio Schmid. Investigating the Determinants of High Case-Fatality Rate for Coronavirus Disease 2019 in Italy. *Disaster Med. Public Health Prep.*, 14(4):E1–E2, 2020.
- [14] Ghassan George Batrouni, Alex Hansen, and Mark Nelkin. Fourier acceleration of relaxation processes in disordered systems. *Phys. Rev. Lett.*, 57(11):1336, 1986.
- [15] Federico Battiston, Enrico Amico, Alain Barrat, Ginestra Bianconi, Guilherme Ferraz de Arruda, Benedetta Franceschiello, Iacopo Iacopini, Sonia Kéfi, Vito Latora, Yamir Moreno, Micah M. Murray, Tiago P. Peixoto, Francesco Vaccarino, and Giovanni Petri. The physics of higher-order interactions in complex systems. *Nat. Phys.*, 17(10):1093–1098, oct 2021.
- [16] Federico Battiston, Giulia Cencetti, Iacopo Iacopini, Vito Latora, Maxime Lucas, Alice Patania, Jean-Gabriel Young, and Giovanni Petri. Networks beyond

- pairwise interactions: Structure and dynamics. *Phys. Rep.*, 874(June):1–92, aug 2020.
- [17] K. Baumann, R. Mottl, F. Brennecke, and T. Esslinger. Exploring symmetry breaking at the dicke quantum phase transition. *Phys. Rev. Lett.*, 107:140402, Sep 2011.
- [18] Kristian Baumann, Christine Guerlin, Ferdinand Brennecke, and Tilman Esslinger. Dicke quantum phase transition with a superfluid gas in an optical cavity. *Nature*, 464(7293):1301–1306, Apr 2010.
- [19] G. J. Baxter, S. N. Dorogovtsev, A. V. Goltsev, and J. F. F. Mendes. Avalanche Collapse of Interdependent Networks. *Phys. Rev. Lett.*, 109(24):248701, dec 2012.
- [20] G. J. Baxter, S. N. Dorogovtsev, K.-E. Lee, J. F. F. Mendes, and A. V. Goltsev. Critical Dynamics of the $\langle k \rangle$ -Core Pruning Process. *Phys. Rev. X*, 5(3):031017, aug 2015.
- [21] Austin R. Benson, Rediet Abebe, Michael T. Schaub, Ali Jadbabaie, and Jon Kleinberg. Simplicial closure and higher-order link prediction. *Proc. Natl. Acad. Sci. U.S.A.*, 115(48):E11221–E11230, nov 2018.
- [22] Tanuj Bhatt, Vimal Kumar, Sagar Pande, Rahul Malik, Aditya Khamparia, and Deepak Gupta. A Review on COVID-19. *Stud. Comput. Intell.*, 924(April):25–42, 2021.
- [23] Ginestra Bianconi and P. L. Krapivsky. Epidemics with containment measures. *Phys. Rev. E*, 102(3):1–14, 2020.

- [24] Ginestra Bianconi, Hanlin Sun, Giacomo Rapisardi, and Alex Arenas. Message-passing approach to epidemic tracing and mitigation with apps. *Phys. Rev. Research*, 3(1):L012014, feb 2021.
- [25] Immanuel Bloch. Ultracold quantum gases in optical lattices. *Nature Physics*, 1(1):23–30, Oct 2005.
- [26] S. Boccaletti, G. Bianconi, R. Criado, C. I. del Genio, J. Gómez-Gardeñes, M. Romance, I. Sendiña-Nadal, Z. Wang, and M. Zanin. The structure and dynamics of multilayer networks. *Phys. Rep.*, 544(1):1–122, 2014.
- [27] Stefano Boccaletti, Vito Latora, Yamir Moreno, Martin Chavez, and D-U Hwang. Complex networks: Structure and dynamics. *Phys. Rep.*, 424(4-5):175–308, 2006.
- [28] Désiré Bollé and Rob Heylen. Small-world hypergraphs on a bond-disordered bethe lattice. *Phys. Rev. E*, 77(4):046104, 2008.
- [29] Désiré Bollé, Rob Heylen, and NS Skantzos. Thermodynamics of spin systems on small-world hypergraphs. *Phys. Rev. E*, 74(5):056111, 2006.
- [30] Stephen P Borgatti and Pacey C Foster. The network paradigm in organizational research: A review and typology. *J. Manag.*, 29(6):991–1013, 2003.
- [31] Michael Buchhold, Benjamin Everest, Matteo Marcuzzi, Igor Lesanovsky, and Sebastian Diehl. Nonequilibrium effective field theory for absorbing state phase transitions in driven open quantum spin systems. *Phys. Rev. B*, 95:014308, Jan 2017.
- [32] Khac-Hoai Nam Bui, Jiho Cho, and Hongsuk Yi. Spatial-temporal graph neural network for traffic forecasting: An overview and open research issues. *Appl. Intell.*, jun 2021.

- [33] Sergey V. Buldyrev, Roni Parshani, Gerald Paul, H. Eugene Stanley, and Shlomo Havlin. Catastrophic cascade of failures in interdependent networks. *Nature*, 464(7291):1025–1028, apr 2010.
- [34] Giulio Burgio, Alex Arenas, Sergio Gómez, and Joan T. Matamalas. Network clique cover approximation to analyze complex contagions through group interactions. *Commun. Phys.*, 4(1):111, dec 2021.
- [35] Giulio Burgio, Joan T. Matamalas, Sergio Gómez, and Alex Arenas. Evolution of Cooperation in the Presence of Higher-Order Interactions: From Networks to Hypergraphs. *Entropy*, 22(7):744, jul 2020.
- [36] Weiran Cai, Li Chen, Fakhteh Ghanbarnejad, and Peter Grassberger. Avalanche outbreaks emerging in cooperative contagions. *Nat. Phys.*, 11(11):936–940, 2015.
- [37] J L Cardy and R L Sugar. Directed percolation and reggeon field theory. *Journal of Physics A: Mathematical and General*, 13(12):L423–L427, dec 1980.
- [38] Timoteo Carletti, Federico Battiston, Giulia Cencetti, and Duccio Fanelli. Random walks on hypergraphs. *Phys. Rev. E*, 101(2):022308, feb 2020.
- [39] H. J. Carmichael. Breakdown of photon blockade: A dissipative quantum phase transition in zero dimensions. *Phys. Rev. X*, 5:031028, Sep 2015.
- [40] Federico Carollo, Edward Gillman, Hendrik Weimer, and Igor Lesanovsky. Critical behavior of the quantum contact process in one dimension. *Phys. Rev. Lett.*, 123:100604, Sep 2019.
- [41] C. Carr, R. Ritter, C. G. Wade, C. S. Adams, and K. J. Weatherill. Nonequilibrium phase transition in a dilute rydberg ensemble. *Phys. Rev. Lett.*, 111(11):113901, 2013.

- [42] B. A. Carreras, V. E. Lynch, I. Dobson, and D. E. Newman. Critical points and transitions in an electric power transmission model for cascading failure blackouts. *Chaos: An Interdisciplinary Journal of Nonlinear Science*, 12(4):985–994, 2002.
- [43] B. A. Carreras, V. E. Lynch, I. Dobson, and D. E. Newman. Complex dynamics of blackouts in power transmission systems. *Chaos An Interdiscip. J. Nonlinear Sci.*, 14(3):643–652, sep 2004.
- [44] B.A. Carreras, D.E. Newman, Ian Dobson, and A.B. Poole. Evidence for Self-Organized Criticality in a Time Series of Electric Power System Blackouts. *IEEE Trans. Circuits Syst. I Regul. Pap.*, 51(9):1733–1740, sep 2004.
- [45] Benjamin A. Carreras, David E. Newman, and Ian Dobson. North American Blackout Time Series Statistics and Implications for Blackout Risk. *IEEE Trans. Power Syst.*, 31(6):4406–4414, nov 2016.
- [46] Iacopo Carusotto and Cristiano Ciuti. Quantum fluids of light. *Rev. Mod. Phys.*, 85:299–366, Feb 2013.
- [47] Claudio Castellano and Romualdo Pastor-Satorras. Routes to thermodynamic limit on scale-free networks. *Phys. Rev. Lett.*, 100(14):148701, 2008.
- [48] Davide Cellai, Eduardo López, Jie Zhou, James P. Gleeson, and Ginestra Bianconi. Percolation in multiplex networks with overlap. *Phys. Rev. E*, 88(5):1–9, nov 2013.
- [49] Duanbing Chen, Linyuan Lü, Ming-Sheng Shang, Yi-Cheng Zhang, and Tao Zhou. Identifying influential nodes in complex networks. *Phys. A Stat. Mech. its Appl.*, 391(4):1777–1787, feb 2012.

- [50] Hanshuang Chen, Shuang Wang, Chuansheng Shen, Haifeng Zhang, and Ginestra Bianconi. Non-Markovian majority-vote model. *Phys. Rev. E*, 102(6):062311, dec 2020.
- [51] Li Chen, Fakhteh Ghanbarnejad, Weiran Cai, and Peter Grassberger. Outbreaks of coinfections: The critical role of cooperativity. *EPL*, 104(5), 2013.
- [52] Yiping Chen, Gerald Paul, Shlomo Havlin, Fredrik Liljeros, and H. Eugene Stanley. Finding a Better Immunization Strategy. *Phys. Rev. Lett.*, 101(5):058701, jul 2008.
- [53] Ziqi Chen and David B. Smith. Heterogeneous machine-type communications in cellular networks: Random access optimization by deep reinforcement learning. In *2018 IEEE International Conference on Communications (ICC)*, pages 1–6, 2018.
- [54] Shai M Chester and Ning Su. Upper critical dimension of the 3-state potts model. *arXiv preprint arXiv:2210.09091*, 2022.
- [55] Y S Cho, J S Kim, J Park, B Kahng, and D Kim. Percolation Transitions in Scale-Free Networks under the Achlioptas Process. *Phys. Rev. Lett.*, 103(13):135702, 2009.
- [56] K. Choi, Hoyun Choi, and B. Kahng. COVID-19 epidemic under the K-quarantine model: Network approach. *Chaos, Solitons & Fractals*, 157:111904, apr 2022.
- [57] Soonwon Choi, Joonhee Choi, Renate Landig, Georg Kucsko, Hengyun Zhou, Junichi Isoya, Fedor Jelezko, Shinobu Onoda, Hitoshi Sumiya, Vedika Khemani, Curt von Keyserlingk, Norman Y. Yao, Eugene Demler, and Mikhail D. Lukin. Observation of discrete time-crystalline order in a disordered dipolar many-body system. *Nature*, 543(7644):221–225, 2017.

- [58] Wonjun Choi, Deokjae Lee, and B Kahng. Mixed-order phase transition in a two-step contagion model with a single infectious seed. *Phys. Rev. E*, 95(2):022304, 2017.
- [59] Wonjun Choi, Deokjae Lee, and B. Kahng. Mixed-order phase transition in a two-step contagion model with a single infectious seed. *Phys. Rev. E*, 95(2):022304, feb 2017.
- [60] Sandeep Chowdhary, Aanjaneya Kumar, Giulia Cencetti, Iacopo Iacopini, and Federico Battiston. Simplicial contagion in temporal higher-order networks. *J. Phys. Complex.*, 2(3):035019, sep 2021.
- [61] Ertugrul Necdet Ciftcioglu, Ram Ramanathan, and Prithwish Basu. Generative models for global collaboration relationships. *Sci. Rep.*, 7(1):11160, 2017.
- [62] Pau Clusella, Peter Grassberger, Francisco J. Pérez-Reche, and Antonio Politi. Immunization and targeted destruction of networks using explosive percolation. *Phys. Rev. Lett.*, 117(20):1–5, 2016.
- [63] Reuven Cohen, Shlomo Havlin, and Daniel ben Avraham. Efficient immunization strategies for computer networks and populations. *Phys. Rev. Lett.*, 91:247901, Dec 2003.
- [64] James Samuel Coleman, Elihu Katz, and Herbert Menzel. *Medical innovation: A diffusion study*. Bobbs-Merrill Co, 1966.
- [65] Vittoria Colizza and Alessandro Vespignani. Invasion threshold in heterogeneous metapopulation networks. *Phys. Rev. Lett.*, 99(14):1–4, 2007.
- [66] Vittoria Colizza and Alessandro Vespignani. Epidemic modeling in metapopulation systems with heterogeneous coupling pattern: Theory and simulations. *J. Theor. Biol.*, 251(3):450–467, 2008.

- [67] Pierre Comon, Gene Golub, Lek-Heng Lim, and Bernard Mourrain. Symmetric tensors and symmetric tensor rank. *SIAM J. Matrix Anal. Appl.*, 30(3):1254–1279, 2008.
- [68] Guilherme S. Costa and Silvio C. Ferreira. Nonmassive immunization to contain spreading on complex networks. *Phys. Rev. E*, 101:022311, Feb 2020.
- [69] Owen T Courtney and Ginestra Bianconi. Generalized network structures: The configuration model and the canonical ensemble of simplicial complexes. *Phys. Rev. E*, 93(6):062311, 2016.
- [70] Diana Crane. Diffusion models and fashion: a reassessment. *The Annals of the American Academy of Political and Social Science*, 566(1):13–24, 1999.
- [71] Paolo Crucitti, Vito Latora, and Massimo Marchiori. Model for cascading failures in complex networks. *Phys. Rev. E - Stat. Physics, Plasmas, Fluids, Relat. Interdiscip. Top.*, 69(4):4, 2004.
- [72] Emanuele G. Dalla Torre, Eugene Demler, Thierry Giamarchi, and Ehud Altman. Quantum critical states and phase transitions in the presence of non-equilibrium noise. *Nature Physics*, 6(10):806–810, Oct 2010.
- [73] Emanuele G. Dalla Torre, Eugene Demler, Thierry Giamarchi, and Ehud Altman. Dynamics and universality in noise-driven dissipative systems. *Phys. Rev. B*, 85:184302, May 2012.
- [74] L de Arcangelis, S Redner, and A Coniglio. Anomalous voltage distribution of random resistor networks and a new model for the backbone at the percolation threshold. *Phys. Rev. B*, 31(7):4725–4727, Apr 1985.
- [75] Songgaojun Deng, Shusen Wang, Huzefa Rangwala, Lijing Wang, and Yue Ning. Cola-GNN: Cross-location Attention based Graph Neural Networks for

- Long-term ILI Prediction. In *Proc. 29th ACM Int. Conf. Inf. Knowl. Manag.*, pages 245–254, New York, NY, USA, oct 2020. ACM.
- [76] Sebastian Diehl, Andrea Tomadin, Andrea Micheli, Rosario Fazio, and Peter Zoller. Dynamical phase transitions and instabilities in open atomic many-body systems. *Phys. Rev. Lett.*, 105:015702, Jul 2010.
- [77] Ian Dobson, Benjamin A. Carreras, Vickie E. Lynch, and David E. Newman. Complex systems analysis of series of blackouts: Cascading failure, critical points, and self-organization. *Chaos An Interdiscip. J. Nonlinear Sci.*, 17(2):026103, jun 2007.
- [78] Zhihao Dong, Yuanzhu Chen, Terrence S Tricco, Cheng Li, and Ting Hu. Practical Strategy of Acquaintance Immunization without Contact Tracing. In *2020 IEEE Intl Conf Parallel Distrib. Process. with Appl. Big Data Cloud Comput. Sustain. Comput. Commun. Soc. Comput. Netw.*, pages 845–851. IEEE, dec 2020.
- [79] S. N. Dorogovtsev, A. V. Goltsev, and J. F. F. Mendes. K-core organization of complex networks. *Phys. Rev. Lett.*, 96(4):040601, feb 2006.
- [80] S. N. Dorogovtsev, A. V. Goltsev, and J. F. F. Mendes. Critical phenomena in complex networks. *Rev. Mod. Phys.*, 80(4):1275–1335, 2008.
- [81] S. N. Dorogovtsev and J. F.F. Mendes. Evolution of networks. *Adv. Phys.*, 51(4):1079–1187, 2002.
- [82] Krzysztof Drewniak, Joseph Helsing, and Armin R. Mikler. A method for reducing the severity of epidemics by allocating vaccines according to centrality. In *Proc. 5th ACM Conf. Bioinformatics, Comput. Biol. Heal. Informatics*, pages 341–350, New York, NY, USA, sep 2014. ACM.

- [83] Amit Dutta, Gabriel Aeppli, Bikas K. Chakrabarti, Uma Divakaran, Thomas F. Rosenbaum, and Diptiman Sen. *Quantum Phase Transitions in Transverse Field Spin Models: From Statistical Physics to Quantum Information*. Cambridge University Press, 2015.
- [84] Ernesto Estrada and Juan A. Rodríguez-Velázquez. Subgraph centrality and clustering in complex hyper-networks. *Physica A*, 364:581–594, may 2006.
- [85] Ernesto Estrada and Grant J Ross. Centralities in simplicial complexes. applications to protein interaction networks. *J. Theor. Biol.*, 438:46–60, 2018.
- [86] D. N. Ewart. Power: Whys and wherefores of power system blackouts: An examination of the factors that increase the likelihood and the frequency of system failure. *IEEE Spectr.*, 15(4):36–41, apr 1978.
- [87] Yiping Fang, Nicola Pedroni, and Enrico Zio. Optimization of Cascade-Resilient Electrical Infrastructures and its Validation by Power Flow Modeling. *Risk Anal.*, 35(4):594–607, apr 2015.
- [88] Juan Fernández-Gracia, Krzysztof Suchecki, José J. Ramasco, Maxi San Miguel, and Víctor M. Eguíluz. Is the Voter Model a Model for Voters? *Phys. Rev. Lett.*, 112(15):158701, apr 2014.
- [89] Guilherme Ferraz de Arruda, Michele Tizzani, and Yamir Moreno. Phase transitions and stability of dynamical processes on hypergraphs. *Commun. Phys.*, 4(1):24, dec 2021.
- [90] Silvio C Ferreira, Claudio Castellano, and Romualdo Pastor-Satorras. Epidemic thresholds of the susceptible-infected-susceptible model on networks: A comparison of numerical and theoretical results. *Phys. Rev. E*, 86(4):041125, 2012.

- [91] Silvio C Ferreira, Ronan S Ferreira, and Romualdo Pastor-Satorras. Quasistationary analysis of the contact process on annealed scale-free networks. *Phys. Rev. E*, 83(6):066113, 2011.
- [92] J. M. Fink, A. Dombi, A. Vukics, A. Wallraff, and P. Domokos. Observation of the photon-blockade breakdown phase transition. *Phys. Rev. X*, 7:011012, Jan 2017.
- [93] Thomas Fink, Anne Schade, Sven Höfling, Christian Schneider, and Ataç Imamoglu. Signatures of a dissipative phase transition in photon correlation measurements. *Nature Physics*, 14(4):365–369, Apr 2018.
- [94] Mattias Fitzpatrick, Neereja M. Sundaresan, Andy C. Y. Li, Jens Koch, and Andrew A. Houck. Observation of a dissipative phase transition in a one-dimensional circuit qed lattice. *Phys. Rev. X*, 7:011016, Feb 2017.
- [95] James H. Fowler. Connecting the Congress: A Study of Cosponsorship Networks. *Polit. Anal.*, 14(4):456–487, jan 2006.
- [96] F. M. Gambetta, F. Carollo, M. Marcuzzi, J. P. Garrahan, and I. Lesanovsky. Discrete time crystals in the absence of manifest symmetries or disorder in open quantum systems. *Phys. Rev. Lett.*, 122:015701, Jan 2019.
- [97] Zakariya Ghalmane, Mohammed El Hassouni, and Hocine Cherifi. Immunization of networks with non-overlapping community structure. *Soc. Netw. Anal. Min.*, 9(1):1–22, 2019.
- [98] C-M Ghim, E Oh, K-I Goh, B Kahng, and D Kim. Packet transport along the shortest pathways in scale-free networks. *Eur. Phys. J. B*, 38(2):193–199, 2004.
- [99] Gourab Ghoshal, Vinko Zlatić, Guido Caldarelli, and Mark EJ Newman. Random hypergraphs and their applications. *Phys. Rev. E*, 79(6):066118, 2009.

- [100] Philip E. Gill, Walter Murray, and Michael A. Saunders. SNOPT: An SQP Algorithm for Large-Scale Constrained Optimization. *SIAM Rev.*, 47(1):99–131, jan 2005.
- [101] Edward Gillman, Federico Carollo, and Igor Lesanovsky. Numerical simulation of critical dissipative non-equilibrium quantum systems with an absorbing state. *New J. Phys.*, 21(9):93064, 2019.
- [102] Edward Gillman, Federico Carollo, and Igor Lesanovsky. Nonequilibrium phase transitions in $(1 + 1)$ -dimensional quantum cellular automata with controllable quantum correlations. *Phys. Rev. Lett.*, 125:100403, Sep 2020.
- [103] Edward Gillman, Federico Carollo, and Igor Lesanovsky. Numerical Simulation of Critical Quantum Dynamics without Finite Size Effects. *arXiv e-prints*, page arXiv:2010.10954, October 2020.
- [104] Stanton A Glantz and Bryan K Slinker. *Primer of Applied Regression and Analysis of Variance*. McGraw-Hill, 1990.
- [105] K. I. Goh, B. Kahng, and D. Kim. Spectra and eigenvectors of scale-free networks. *Phys. Rev. E*, 64(5):051903, 2001.
- [106] K.-I. Goh, B. Kahng, and D. Kim. Universal Behavior of Load Distribution in Scale-Free Networks. *Phys. Rev. Lett.*, 87(27):278701, dec 2001.
- [107] K-I Goh, Byungnam Kahng, and Doochul Kim. Universal behavior of load distribution in scale-free networks. *Phys. Rev. Lett.*, 87(27):278701, 2001.
- [108] K-I Goh, D-S Lee, B Kahng, and D Kim. Sandpile on scale-free networks. *Phys. Rev. Lett.*, 91(14):148701, 2003.
- [109] A. V. Goltsev, S. N. Dorogovtsev, and J. F. F. Mendes. k -core (bootstrap) percolation on

- complex networks: Critical phenomena and nonlocal effects. *Phys. Rev. E*, 73(5):056101, may 2006.
- [110] Sergio Gómez, Alexandre Arenas, J Borge-Holthoefer, Sandro Meloni, and Yamir Moreno. Discrete-time markov chain approach to contact-based disease spreading in complex networks. *EPL*, 89(3):38009, 2010.
- [111] Sergio Gómez, Jesús Gómez-Gardeñes, Yamir Moreno, and Alex Arenas. Non-perturbative heterogeneous mean-field approach to epidemic spreading in complex networks. *Phys. Rev. E*, 84(3):036105, sep 2011.
- [112] Rafael Gómez-Bombarelli, Jennifer N. Wei, David Duvenaud, José Miguel Hernández-Lobato, Benjamín Sánchez-Lengeling, Dennis Sheberla, Jorge Aguilera-Iparraguirre, Timothy D. Hirzel, Ryan P. Adams, and Alán Aspuru-Guzik. Automatic Chemical Design Using a Data-Driven Continuous Representation of Molecules. *ACS Cent. Sci.*, 4(2):268–276, feb 2018.
- [113] Andrzej Grabowski and RA Kosiński. Ising-based model of opinion formation in a complex network of interpersonal interactions. *Physica A: Statistical Mechanics and its Applications*, 361(2):651–664, 2006.
- [114] Mark Granovetter. Threshold models of collective behavior. *Am. J. Sociol.*, 83(6):1420–1443, 1978.
- [115] Peter Grassberger. Tricritical directed percolation in $2+1$ dimensions. *J. Stat. Mech.: Theory Exp.*, 2006(01):P01004, 2006.
- [116] Aditya Grover and Jure Leskovec. Node2vec: Scalable feature learning for networks. In *Proc. 22nd ACM SIGKDD Int. Conf. Knowl. Discov. Data Min.*, KDD '16, page 855–864, New York, NY, USA, 2016. Association for Computing Machinery.

- [117] R. Guimerà, L. Danon, A. Díaz-Guilera, F. Giralt, and A. Arenas. Self-similar community structure in a network of human interactions. *Phys. Rev. E - Stat. Physics, Plasmas, Fluids, Relat. Interdiscip. Top.*, 68(6):065103(R), 2003.
- [118] Dongchao Guo, Stojan Trajanovski, Ruud van de Bovenkamp, Huijuan Wang, and Piet Van Mieghem. Epidemic threshold and topological structure of susceptible-infectious-susceptible epidemics in adaptive networks. *Phys. Rev. E*, 88(4):042802, oct 2013.
- [119] Ricardo Gutiérrez, Cristiano Simonelli, Matteo Archimi, Francesco Castellucci, Ennio Arimondo, Donatella Ciampini, Matteo Marcuzzi, Igor Lesanovsky, and Oliver Morsch. Experimental signatures of an absorbing-state phase transition in an open driven many-body quantum system. *Phys. Rev. A*, 96:041602(R), Oct 2017.
- [120] William L Hamilton, Rex Ying, and Jure Leskovec. Inductive representation learning on large graphs. In *Proc. 31st Int. Conf. Neural Inf. Process. Syst.*, pages 1025–1035, 2017.
- [121] Zhongkai Hao, Chengqiang Lu, Zhenya Huang, Hao Wang, Zheyuan Hu, Qi Liu, Enhong Chen, and Cheekong Lee. ASGN: An Active Semi-supervised Graph Neural Network for Molecular Property Prediction. In *Proc. 26th ACM SIGKDD Int. Conf. Knowl. Discov. Data Min.*, pages 731–752, New York, NY, USA, aug 2020. ACM.
- [122] Frank Harary and Helene J. Kimmel. Matrix measures for transitivity and balance*. *J. Math. Sociol.*, 6(2):199–210, jan 1979.
- [123] Yukio Hayashi and Toshiyuki Miyazaki. Emergent rewirings for cascades on correlated networks. *arXiv Prepr. cond-mat/0503615*, mar 2005.

- [124] Kaiming He, Xiangyu Zhang, Shaoqing Ren, and Jian Sun. Deep residual learning for image recognition. In *Proceedings of the IEEE conference on computer vision and pattern recognition*, pages 770–778. IEEE, 2016.
- [125] Chip Heath, Chris Bell, and Emily Sternberg. Emotional selection in memes: the case of urban legends. *J. Pers. Soc. Psychol.*, 81(6):1028, 2001.
- [126] Laurent Hébert-Dufresne, Antoine Allard, Jean-Gabriel Young, and Louis J. Dubé. Global efficiency of local immunization on complex networks. *Sci. Rep.*, 3(1):2171, dec 2013.
- [127] S. Helmrich, A. Arias, G. Lochead, T. M. Wintermantel, M. Buchhold, S. Diehl, and S. Whitlock. Signatures of self-organized criticality in an ultracold atomic gas. *Nature*, 577(7791):481–486, Jan 2020.
- [128] Ignacio Hermoso de Mendoza, Leonardo A. Pachón, Jesús Gómez-Gardeñes, and David Zueco. Synchronization in a semiclassical kuramoto model. *Phys. Rev. E*, 90:052904, Nov 2014.
- [129] Daniel Hernández Serrano and Darío Sánchez Gómez. Centrality measures in simplicial complexes: Applications of topological data analysis to network science. *Appl. Math. Comput.*, 382:125331, oct 2020.
- [130] Paul Hines, Karthikeyan Balasubramaniam, and E.C. Sanchez. Cascading failures in power grids. *IEEE Potentials*, 28(5):24–30, sep 2009.
- [131] Paul Hines, Ian Dobson, and Pooya Rezaei. Cascading Power Outages Propagate Locally in an Influence Graph that is not the Actual Grid Topology. *IEEE Trans. Power Syst.*, 32(2):1–1, 2016.
- [132] Ha Hoang and Bostjan Antoncic. Network-based research in entrepreneurship: A critical review. *J. Bus. Ventur.*, 18(2):165–187, 2003.

- [133] Petter Holme and Beom Jun Kim. Growing scale-free networks with tunable clustering. *Phys. Rev. E*, 65(2):026107, jan 2002.
- [134] Petter Holme and Beom Jun Kim. Vertex overload breakdown in evolving networks. *Phys. Rev. E*, 65(6):066109, jun 2002.
- [135] Andrew A. Houck, Hakan E. Türeci, and Jens Koch. On-chip quantum simulation with superconducting circuits. *Nature Physics*, 8(4):292–299, Apr 2012.
- [136] Anzi Hu, Tony E. Lee, and Charles W. Clark. Spatial correlations of one-dimensional driven-dissipative systems of rydberg atoms. *Phys. Rev. A*, 88:053627, Nov 2013.
- [137] Iacopo Iacopini, Giovanni Petri, Alain Barrat, and Vito Latora. Simplicial models of social contagion. *Nat. Commun.*, 10(1):2485, 2019.
- [138] Yoon Seok Im and B. Kahng. Dismantling efficiency and network fractality. *Phys. Rev. E*, 98(1):12316, 2018.
- [139] Sergey Ioffe and Christian Szegedy. Batch normalization: Accelerating deep network training by reducing internal covariate shift. *CoRR*, abs/1502.03167, 2015.
- [140] S. Jang, J. S. Lee, S. Hwang, and B. Kahng. Ashkin-Teller model and diverse opinion phase transitions on multiplex networks. *Phys. Rev. E - Stat. Nonlinear, Soft Matter Phys.*, 92(2):022110, aug 2015.
- [141] Hans-Karl Janssen, Martin Müller, and Olaf Stenull. Generalized epidemic process and tricritical dynamic percolation. *Phys. Rev. E*, 70(2):026114, 2004.
- [142] Yeonsu Jeong, Soo Min Oh, and Young Sul Cho. Discontinuous emergence of a giant cluster in assortative scale-free networks. *Journal of the Korean Physical Society*, 81(7):608–614, 2022.

- [143] Bukyoung Jhun. Effective epidemic containment strategy in hypergraphs. *Phys. Rev. Res.*, 3(3):033282, sep 2021.
- [144] Bukyoung Jhun. Effective vaccination strategy using graph neural network ansatz. *arXiv preprint arXiv:2111.00920*, 2021.
- [145] Bukyoung Jhun. Topological analysis of the latent geometry of a complex network. *Chaos An Interdiscip. J. Nonlinear Sci.*, 32(1):013116, jan 2022.
- [146] Bukyoung Jhun and Hoyun Choi. Abrupt transition of the efficient vaccination strategy in a population with heterogeneous fatality rates. *Chaos: An Interdisciplinary Journal of Nonlinear Science*, 32(9):093140, 09 2022.
- [147] Bukyoung Jhun, Hoyun Choi, Yongsun Lee, Jongshin Lee, Cook Hyun Kim, and B. Kahng. Prediction and mitigation of nonlocal cascading failures using graph neural networks. *Chaos: An Interdisciplinary Journal of Nonlinear Science*, 33(1):013115, 01 2023.
- [148] Bukyoung Jhun, Youngseok Jhun, Seung wook Kim, and Jung Hyun Han. Numerical Calculation of Non-uniform Magnetization Using Experimental Magnetic Field Data. *J. Korean Phys. Soc.*, 72(9):1058–1062, may 2018.
- [149] Bukyoung Jhun, Minjae Jo, and B. Kahng. Simplicial SIS model in scale-free uniform hypergraph. *J. Stat. Mech.*, 2019(12):123207, dec 2019.
- [150] Bukyoung Jhun, Minjae Jo, and B. Kahng. Quantum contact process on scale-free networks. *Chaos, Solitons & Fractals*, 160:112262, jul 2022.
- [151] Bukyoung Jhun and Cheol Hwan Park. Electronic structure of charged bilayer and trilayer phosphorene. *Phys. Rev. B*, 96(8):4–7, 2017.
- [152] Chunyan Ji and Daqing Jiang. Threshold behaviour of a stochastic SIR model. *Appl. Math. Model.*, 38(21-22):5067–5079, 2014.

- [153] Junteng Jia and Austin R. Benson. Random Spatial Network Models for Core-Periphery Structure. In *Proc. Twelfth ACM Int. Conf. Web Search Data Min.*, pages 366–374, New York, NY, USA, jan 2019. ACM.
- [154] Jie Chen, J.S. Thorp, and Manu Parashar. Analysis of electric power system disturbance data. In *Proc. 34th Annu. Hawaii Int. Conf. Syst. Sci.*, volume 00, pages 738–744. IEEE Comput. Soc, 2001.
- [155] Jiasen Jin, Alberto Biella, Oscar Viyuela, Cristiano Ciuti, Rosario Fazio, and Davide Rossini. Phase diagram of the dissipative quantum ising model on a square lattice. *Phys. Rev. B*, 98:241108, Dec 2018.
- [156] Jiasen Jin, Alberto Biella, Oscar Viyuela, Leonardo Mazza, Jonathan Keeling, Rosario Fazio, and Davide Rossini. Cluster mean-field approach to the steady-state phase diagram of dissipative spin systems. *Phys. Rev. X*, 6(3):1–18, 2016.
- [157] Minjae Jo, Bukyoung Jhun, and B. Kahng. Resolving mean-field solutions of dissipative phase transitions using permutational symmetry. *Chaos, Solitons & Fractals*, 173:113705, 2023.
- [158] Minjae Jo and B. Kahng. Tricritical directed percolation with long-range interaction in one and two dimensions. *Phys. Rev. E*, 101(2):022121, feb 2020.
- [159] Minjae Jo, Jongshin Lee, K. Choi, and B. Kahng. Absorbing phase transition with a continuously varying exponent in a quantum contact process: A neural network approach. *Phys. Rev. Res.*, 3(1):013238, mar 2021.
- [160] Minjae Jo, Jaegon Um, and B. Kahng. Nonequilibrium phase transition in an open quantum spin system with long-range interaction. *Phys. Rev. E*, 99(3):32131, 2019.
- [161] Rachel E. Jordan, Peymane Adab, and K. K. Cheng. Covid-19: risk factors for severe disease and death. *BMJ*, 368(March):m1198, mar 2020.

- [162] Róbert Juhász and Ferenc Iglói. Mixed-order phase transition of the contact process near multiple junctions. *Phys. Rev. E*, 95(2):1–8, 2017.
- [163] Alex Kamenev. *Field theory of non-equilibrium systems*. Cambridge University Press, 2011.
- [164] Zsolt Katona, Peter Pal Zubcsek, and Miklos Sarvary. Network effects and personal influences: The diffusion of an online social network. *J. Mark. Res.*, 48(3):425–443, 2011.
- [165] Matt J. Keeling and Pejman Rohani. *Modeling infectious diseases in humans and animals*. Princeton university press, 2011.
- [166] M. G. Kendall. a New Measure of Rank Correlation. *Biometrika*, 30(1-2):81–93, jun 1938.
- [167] Cook Hyun Kim, Minjae Jo, J. S. Lee, G. Bianconi, and B. Kahng. Link overlap influences opinion dynamics on multiplex networks of Ashkin-Teller spins. *Phys. Rev. E*, 104(6):064304, dec 2021.
- [168] D-H Kim, GJ Rodgers, B Kahng, and D Kim. Spin-glass phase transition on scale-free networks. *Phys. Rev. E*, 71(5):056115, 2005.
- [169] Dong Hyun Kim, Young June Choe, and Jin Young Jeong. Understanding and interpretation of case fatality rate of coronavirus disease 2019. *J. Korean Med. Sci.*, 35(12):1–3, 2020.
- [170] Heetae Kim. How modular structure determines operational resilience of power grids. *New J. Phys.*, 23(6):063029, jun 2021.
- [171] J.-H. Kim, K.-I. Goh, B. Kahng, and D. Kim. Probabilistic prediction in scale-free networks: Diameter changes. *Phys. Rev. Lett.*, 91:058701, Aug 2003.
- [172] R. Kinney, P. Crucitti, R. Albert, and V. Latora. Modeling cascading failures in the North American power grid. *Eur. Phys. J. B*, 46(1):101–107, jul 2005.

- [173] Thomas N. Kipf and Max Welling. Semi-supervised classification with graph convolutional networks. In *5th Int. Conf. Learn. Represent. ICLR 2017 - Conf. Track Proc.*, pages 1–14, sep 2017.
- [174] S. Kirkpatrick, C.D. Gelatt, and M.P. Vecchi. Optimization by Simulated Annealing. In *Readings Comput. Vis.*, number 4598, pages 606–615. Elsevier, Berlin, Heidelberg, 1987.
- [175] Maksim Kitsak, Lazaros K. Gallos, Shlomo Havlin, Fredrik Liljeros, Lev Muchnik, H. Eugene Stanley, and Hernán A. Makse. Identification of influential spreaders in complex networks. *Nat. Phys.*, 6(11):888–893, 2010.
- [176] Steffen Klamt, Utz-Uwe Haus, and Fabian Theis. Hypergraphs and cellular networks. *PLOS Comput. Biol.*, 5(5):e1000385, 2009.
- [177] Konstantin Klemm, Víctor M. Eguíluz, Raúl Toral, and Maxi San Miguel. Nonequilibrium transitions in complex networks: A model of social interaction. *Phys. Rev. E*, 67:026120, Feb 2003.
- [178] Konstantin Klemm, M. Ángeles Serrano, Víctor M. Eguíluz, and Maxi San Miguel. A measure of individual role in collective dynamics. *Sci. Rep.*, 2(1):292, dec 2012.
- [179] Florian Klimm, Charlotte M Deane, and Gesine Reinert. Hypergraphs for predicting essential genes using multiprotein complex data. *J. Complex Networks*, 9(2):2020.04.03.023937, may 2021.
- [180] Jens Klinder, Hans Keßler, Matthias Wolke, Ludwig Mathey, and Andreas Hemmerich. Dynamical phase transition in the open dicke model. *Proceedings of the National Academy of Sciences*, 112(11):3290–3295, 2015.

- [181] Yosef Kornbluth, Gabriel Cwilich, Sergey V. Buldyrev, Saleh Soltan, and Gil Zussman. Distribution of blackouts in the power grid and the Motter and Lai model. *Phys. Rev. E*, 103(3):032309, mar 2021.
- [182] B. Kraus, H. P. Büchler, S. Diehl, A. Kantian, A. Micheli, and P. Zoller. Preparation of entangled states by quantum Markov processes. *Phys. Rev. A - At. Mol. Opt. Phys.*, 78(4):42307, 2008.
- [183] Augustine Kshetrimayum, Hendrik Weimer, and Román Orús. A simple tensor network algorithm for two-dimensional steady states. *Nature Communications*, 8(1):1291, Nov 2017.
- [184] Rajesh Kumar and Edith A. Burns. Age-related decline in immunity: implications for vaccine responsiveness. *Expert Rev. Vaccines*, 7(4):467–479, may 2008.
- [185] W Kutta. Beitrag zur näherungsweise Integration von Differentialgleichungen. *Zeit. Math. Phys.*, 46:435–453, 1901.
- [186] Ying-Cheng Lai, Adilson E. Motter, and Takashi Nishikawa. *Attacks and Cascades in Complex Networks*, pages 299–310. Springer Berlin Heidelberg, Berlin, Heidelberg, 2004.
- [187] Renaud Lambiotte, Martin Rosvall, and Ingo Scholtes. From networks to optimal higher-order models of complex systems. *Nat. Phys.*, 15(4):313–320, apr 2019.
- [188] Nicholas W. Landry and Juan G. Restrepo. The effect of heterogeneity on hypergraph contagion models. *Chaos*, 30(10):103117, oct 2020.
- [189] Alexandre Le Boité, Giuliano Orso, and Cristiano Ciuti. Steady-state phases and tunneling-induced instabilities in the driven dissipative bose-hubbard model. *Phys. Rev. Lett.*, 110:233601, Jun 2013.

- [190] D-S Lee, K-I Goh, B Kahng, and D Kim. Scale-free random graphs and potts model. *Pramana*, 64(6):1149–1159, 2005.
- [191] Deokjae Lee, S. Choi, M. Stippinger, J. Kertész, and B. Kahng. Hybrid phase transition into an absorbing state: Percolation and avalanches. *Phys. Rev. E*, 93(4):42109, 2016.
- [192] Deokjae Lee, Wonjun Choi, Janos Kertész, and Byungnam Kahng. Universal mechanism for hybrid percolation transitions. *Sci. Rep.*, 7(1):5723, 2017.
- [193] Deokjae Lee, Minjae Jo, and B. Kahng. Critical behavior of k -core percolation: Numerical studies. *Phys. Rev. E*, 94(6):062307, dec 2016.
- [194] Deokjae Lee, Minjae Jo, and B. Kahng. Critical behavior of k -core percolation: Numerical studies. *Phys. Rev. E*, 94:062307, Dec 2016.
- [195] E. J. Lee, K.-I. Goh, B. Kahng, and D. Kim. Robustness of the avalanche dynamics in data-packet transport on scale-free networks. *Phys. Rev. E*, 71(5):056108, may 2005.
- [196] Hyekeyoung Lee, Hyejin Kang, Moo K Chung, Bung-Nyun Kim, and Dong Soo Lee. Persistent brain network homology from the perspective of dendrogram. *IEEE Trans. Med. Imaging*, 31(12):2267–2277, 2012.
- [197] Hyun Keun Lee, Pyoung-Seop Shim, and Jae Dong Noh. Epidemic threshold of the susceptible-infected-susceptible model on complex networks. *Phys. Rev. E*, 87(6):062812, 2013.
- [198] J-S Lee, K-I Goh, B Kahng, and D Kim. Intrinsic degree-correlations in the static model of scale-free networks. *Eur. Phys. J. B*, 49(2):231–238, 2006.
- [199] J.-S. Lee, K.-I. Goh, B. Kahng, and D. Kim. Intrinsic degree-correlations in the static model of scale-free networks. *Eur. Phys. J. B*, 49(2):231–238, jan 2006.

- [200] Jongshin Lee, Kwang-Il Goh, Deok-Sun Lee, and B Kahng. (k, q)-core decomposition of hypergraphs. *Chaos, Solitons & Fractals*, 173:113645, 2023.
- [201] Jongshin Lee, Yongsun Lee, Soo Min Oh, and B. Kahng. Betweenness centrality of teams in social networks. *Chaos An Interdiscip. J. Nonlinear Sci.*, 31(6):061108, jun 2021.
- [202] Sang Hoon Lee, Meesoon Ha, Hawoong Jeong, Jae Dong Noh, and Hyunggyu Park. Critical behavior of the ising model in annealed scale-free networks. *Phys. Rev. E*, 80(5):051127, 2009.
- [203] Sang Hoon Lee, Hawoong Jeong, and Jae Dong Noh. Random field ising model on networks with inhomogeneous connections. *Phys. Rev. E*, 74(3):031118, 2006.
- [204] Y. Lee, J. Lee, Soo Min Oh, Deokjae Lee, and B. Kahng. Homological percolation transitions in growing simplicial complexes. *Chaos*, 31(4):041102, apr 2021.
- [205] Jure Leskovec, Jon Kleinberg, and Christos Faloutsos. Graph evolution. *ACM Trans. Knowl. Discov. Data*, 1(1):2, mar 2007.
- [206] Andrew T. Levin, William P. Hanage, Nana Owusu-Boaitey, Kensington B. Cochran, Seamus P. Walsh, and Gideon Meyerowitz-Katz. Assessing the age specificity of infection fatality rates for COVID-19: systematic review, meta-analysis, and public policy implications. *Eur. J. Epidemiol.*, 35(12):1123–1138, 2020.
- [207] Hao Li, Zheng Xu, Gavin Taylor, Christoph Studer, and Tom Goldstein. Visualizing the loss landscape of neural nets. *Adv. Neural Inf. Process. Syst.*, 2018-Decem(Nips 2018):6389–6399, 2018.

- [208] WenYao Li, Xiaoyu Xue, Liming Pan, Tao Lin, and Wei Wang. Competing spreading dynamics in simplicial complex. *Appl. Math. Comput.*, 412:126595, jan 2022.
- [209] Wenzhao Li, Rejoice Thomas, Hesham El-Askary, Thomas Piechota, Daniele Struppa, and Khaled A. Abdel Ghaffar. Investigating the Significance of Aerosols in Determining the Coronavirus Fatality Rate Among Three European Countries. *Earth Syst. Environ.*, 4(3):513–522, 2020.
- [210] Xiaochen Li, Shuyun Xu, Muqing Yu, Ke Wang, Yu Tao, Ying Zhou, Jing Shi, Min Zhou, Bo Wu, Zhenyu Yang, Cong Zhang, Junqing Yue, Zhiguo Zhang, Harald Renz, Xiansheng Liu, Jungang Xie, Min Xie, and Jianping Zhao. Risk factors for severity and mortality in adult COVID-19 inpatients in Wuhan. *J. Allergy Clin. Immunol.*, 146(1):110–118, jul 2020.
- [211] Lek-Heng Lim. Singular values and eigenvalues of tensors: a variational approach. In *1st IEEE Int. Work. Comput. Adv. Multi-Sensor Adapt. Process. 2005.*, pages 129–132, 2005.
- [212] Yang Liu, Bingrui Liu, Yi Deng, and Jia Liu. Quantitative Analysis of COVID-19 Pandemic Responses Based on an Improved SEIR-SD Model. *Complexity*, 2022:1–18, feb 2022.
- [213] Alun L. Lloyd and Vincent A.A. Jansen. Spatiotemporal dynamics of epidemics: Synchrony in metapopulation models. *Math. Biosci.*, 188(1-2):1–16, 2004.
- [214] Dan Lu, Alberto Aleta, Marco Ajelli, Romualdo Pastor-Satorras, Alessandro Vespignani, and Yamir Moreno. Data-driven estimate of SARS-CoV-2 herd immunity threshold in populations with individual contact pattern variations. *medRxiv*, page 2021.03.19.21253974, 2021.
- [215] S Lübeck. Tricritical directed percolation. *J. Stat. Phys.*, 123(1):193–221, 2006.

- [216] S. Lübeck and R. D. Willmann. Universal scaling behaviour of directed percolation and the pair contact process in an external field. *J. Phys. A*, 35(48):10205–10217, 2002.
- [217] Sven Lübeck. Universal scaling behavior of non-equilibrium phase transitions. *Int. J. Mod. Phys. B*, 18(31-32):3977–4118, dec 2004.
- [218] Ruichao Ma, Brendan Saxberg, Clai Owens, Nelson Leung, Yao Lu, Jonathan Simon, and David I. Schuster. A dissipatively stabilized mott insulator of photons. *Nature*, 566(7742):51–57, Feb 2019.
- [219] John S MacDonald and Leatrice D MacDonald. Chain migration ethnic neighborhood formation and social networks. *Milbank Q.*, 42(1):82–97, 1964.
- [220] N. Madar, T. Kalisky, R. Cohen, D. Ben-Avraham, and S. Havlin. Immunization and epidemic dynamics in complex networks. *Eur. Phys. J. B*, 38(2):269–276, mar 2004.
- [221] Mohammad F. Maghrebi and Alexey V. Gorshkov. Nonequilibrium many-body steady states via keldysh formalism. *Phys. Rev. B*, 93:014307, Jan 2016.
- [222] N. Malossi, M. M. Valado, S. Scotto, P. Huillery, P. Pillet, D. Ciampini, E. Arimondo, and O. Morsch. Full counting statistics and phase diagram of a dissipative rydberg gas. *Phys. Rev. Lett.*, 113(2):23006, 2014.
- [223] Battegay Manuel, Kuehl Richard, Tschudin-sutter Sarah, Hirsch Hans H, Widmer Andreas F, and Neher Richard A. Estimating the Case Fatality Rate – a Word of Caution. *Swiss Med Wkly*, 150(February):2019–2021, 2020.
- [224] Matteo Marcuzzi, Michael Buchhold, Sebastian Diehl, and Igor Lesanovsky. Absorbing State Phase Transition with Competing Quantum and Classical Fluctuations. *Phys. Rev. Lett.*, 116(24):245701, 2016.

- [225] Jamir Marino and Sebastian Diehl. Driven Markovian Quantum Criticality. *Phys. Rev. Lett.*, 116(7):70407, 2016.
- [226] Joaquín Marro and Ronald Dickman. *Nonequilibrium phase transitions in lattice models*. Cambridge University Press, 2005.
- [227] Naoki Masuda. Immunization of networks with community structure. *New J. Phys.*, 11(12):123018, dec 2009.
- [228] Naoki Masuda. Effects of diffusion rates on epidemic spreads in metapopulation networks. *New J. Phys.*, 12, 2010.
- [229] Angélica S. Mata and Silvio C. Ferreira. Pair quenched mean-field theory for the susceptible-infected-susceptible model on complex networks. *EPL*, 103(4):48003, 2013.
- [230] Joan T. Matamalas, Alex Arenas, and Sergio Gómez. Effective approach to epidemic containment using link equations in complex networks. *Sci. Adv.*, 4(12):eaau4212, dec 2018.
- [231] Joan T. Matamalas, Alex Arenas, and Sergio Gómez. Effective approach to epidemic containment using link equations in complex networks. *Sci. Adv.*, 4(12):eaau4212, 2018.
- [232] Joan T. Matamalas, Sergio Gómez, and Alex Arenas. Abrupt phase transition of epidemic spreading in simplicial complexes. *Phys. Rev. Research*, 2:012049(R), Feb 2020.
- [233] Eli A. Meir, Haggai Maron, Shie Mannor, and Gal Chechik. Controlling Graph Dynamics with Reinforcement Learning and Graph Neural Networks. *arXiv Prepr. arXiv2010.05313*, 2020.
- [234] Dina Mistry, Maria Litvinova, Ana Pastore y Piontti, Matteo Chinazzi, Laura Fumanelli, Marcelo F.C. Gomes, Syed A. Haque, Quan Hui Liu, Kunpeng Mu,

- Xinyue Xiong, M. Elizabeth Halloran, Ira M. Longini, Stefano Merler, Marco Ajelli, and Alessandro Vespignani. Inferring high-resolution human mixing patterns for disease modeling. *Nat. Commun.*, 12(1):1–12, 2021.
- [235] Y. Moreno, R. Pastor-Satorras, and A. Vespignani. Epidemic outbreaks in complex heterogeneous networks. *Eur. Phys. J. B*, 26(4):521–529, 2002.
- [236] Y. Moreno, R. Pastor-Satorras, and A. Vespignani. Epidemic outbreaks in complex heterogeneous networks. *Eur. Phys. J. B*, 26(4):521–529, apr 2002.
- [237] Yamir Moreno, Maziar Nekovee, and Amalio F. Pacheco. Dynamics of rumor spreading in complex networks. *Phys. Rev. E*, 69(6):066130, jun 2004.
- [238] Flaviano Morone and Hernán A. Makse. Influence maximization in complex networks through optimal percolation. *Nature*, 524(7563):65–68, 2015.
- [239] Joël Mossong, Niel Hens, Mark Jit, Philippe Beutels, Kari Auranen, Rafael Mikolajczyk, Marco Massari, Stefania Salmaso, Gianpaolo Scalia Tomba, Jacco Wallinga, Janneke Heijne, Malgorzata Sadkowska-Todys, Magdalena Rosinska, and W. John Edmunds. Social Contacts and Mixing Patterns Relevant to the Spread of Infectious Diseases. *PLoS Med.*, 5(3):e74, mar 2008.
- [240] Adilson E. Motter. Cascade Control and Defense in Complex Networks. *Phys. Rev. Lett.*, 93(9):098701, aug 2004.
- [241] Adilson E. Motter and Ying-Cheng Lai. Cascade-based attacks on complex networks. *Phys. Rev. E*, 66(6):065102, dec 2002.
- [242] Charles Murphy, Edward Laurence, and Antoine Allard. Deep learning of contagion dynamics on complex networks. *Nat. Commun.*, 12(1):4720, dec 2021.
- [243] D. Nagy and P. Domokos. Nonequilibrium quantum criticality and non-markovian environment: Critical exponent of a quantum phase transition. *Phys. Rev. Lett.*, 115:043601, Jul 2015.

- [244] M. Nekovee, Y. Moreno, G. Bianconi, and M. Marsili. Theory of rumour spreading in complex social networks. *Physica A*, 374(1):457–470, 2007.
- [245] J. A. Nelder and R. Mead. A Simplex Method for Function Minimization. *Comput. J.*, 7(4):308–313, jan 1965.
- [246] M. E. J. Newman. Scientific collaboration networks. II. Shortest paths, weighted networks, and centrality. *Phys. Rev. E*, 64(1):016132, jun 2001.
- [247] M. E. J. Newman. The Structure and Function of Complex Networks. *SIAM Rev.*, 45(2):167–256, jan 2003.
- [248] Mark EJ Newman. The structure and function of complex networks. *SIAM Rev.*, 45(2):167–256, 2003.
- [249] J. Nitzbon, P. Schultz, J. Heitzig, J. Kurths, and F. Hellmann. Deciphering the imprint of topology on nonlinear dynamical network stability. *New J. Phys.*, 19(3), 2017.
- [250] Changsuk Noh and Dimitris G Angelakis. Quantum simulations and many-body physics with light. *Reports on Progress in Physics*, 80(1):016401, nov 2016.
- [251] Elaine O Nsoesie, John S Brownstein, Naren Ramakrishnan, and Madhav V Marathe. A systematic review of studies on forecasting the dynamics of influenza outbreaks. *Influenza Other Resp.*, 8(3):309–316, 2014.
- [252] Kento Okuwa, Hisashi Inaba, and Toshikazu Kuniya. Mathematical analysis for an age-structured sirs epidemic model. *Math. Biosci. Eng.*, 16(5):6071–6102, 2019.
- [253] Saeed Osat, Ali Faqeeh, and Filippo Radicchi. Optimal percolation on multiplex networks. *Nat. Commun.*, 8(1):1–6, 2017.

- [254] Vincent R. Overbeck, Mohammad F. Maghrebi, Alexey V. Gorshkov, and Hendrik Weimer. Multicritical behavior in dissipative Ising models. *Phys. Rev. A*, 95(4):042133, apr 2017.
- [255] Laurent Pagnier and Philippe Jacquod. Inertia location and slow network modes determine disturbance propagation in large-scale power grids. *PLoS One*, 14(3):e0213550, mar 2019.
- [256] George Panagopoulos, Giannis Nikolentzos, and Michalis Vazirgiannis. Transfer Graph Neural Networks for Pandemic Forecasting. *arXiv Prepr. arXiv2009.08388*, sep 2020.
- [257] S. Y. Pang, S. V. Muniandy, and M. Z. M. Kamali. Critical dynamics of transverse-field quantum ising model using finite-size scaling and matrix product states. *International Journal of Theoretical Physics*, 58(12):4139–4151, Dec 2019.
- [258] Fragkiskos Papadopoulos, Maksim Kitsak, M. Ángeles Serrano, Marián Boguñá, and Dmitri Krioukov. Popularity versus similarity in growing networks. *Nature*, 489(7417):537–540, sep 2012.
- [259] Fragkiskos Papadopoulos, Constantinos Psomas, and Dmitri Krioukov. Network Mapping by Replaying Hyperbolic Growth. *IEEE/ACM Trans. Netw.*, 23(1):198–211, feb 2015.
- [260] Jinha Park, Sudo Yi, K. Choi, Deokjae Lee, and B. Kahng. Interevent time distribution, burst, and hybrid percolation transition. *Chaos*, 29(9), 2019.
- [261] Youngjoon Park, Youngjune Choe, Ok Park, Shin Young Park, Young Man Kim, Jieun Kim, Sanghui Kweon, Yeonhee Woo, Jin Gwack, Seong Sun Kim, Jin Leejunghye Hyun, Boyeong Ryu, Yoon Sukjang, Hwami Kim, Seung Hwan Shin, Seonju Yi, Sangeun Lee, Hee Kyoung Kim, Hyeyoung Lee, Yeowon Jin,

- Eunmi Park, Seung Woo Choi, Miyoung Kim, Jeongsuk Song, Si Won Choi, Dongwook Kim, Byoung Hak Jeon, Hyosoon Yoo, and Eun Kyeongjeongm. Contact Tracing during Coronavirus Disease Outbreak, South Korea, 2020. *Emerg. Infect. Dis.*, 26(10):2465–2468, 2020.
- [262] Romualdo Pastor-Satorras, Claudio Castellano, Piet Van Mieghem, and Alessandro Vespignani. Epidemic processes in complex networks. *Rev. Mod. Phys.*, 87(3):925, 2015.
- [263] Romualdo Pastor-Satorras, Claudio Castellano, Piet Van Mieghem, and Alessandro Vespignani. Epidemic processes in complex networks. *Rev. Mod. Phys.*, 87(3):925–979, aug 2015.
- [264] Romualdo Pastor-Satorras and Alessandro Vespignani. Epidemic dynamics and endemic states in complex networks. *Phys. Rev. E*, 63(6):066117, 2001.
- [265] Romualdo Pastor-Satorras and Alessandro Vespignani. Epidemic dynamics and endemic states in complex networks. *Phys. Rev. E*, 63(6):066117, may 2001.
- [266] Romualdo Pastor-Satorras and Alessandro Vespignani. Epidemic spreading in scale-free networks. *Phys. Rev. Lett.*, 86(14):3200, 2001.
- [267] Romualdo Pastor-Satorras and Alessandro Vespignani. Epidemic spreading in scale-free networks. *Phys. Rev. Lett.*, 86(14):3200–3203, 2001.
- [268] Romualdo Pastor-Satorras and Alessandro Vespignani. Immunization of complex networks. *Phys. Rev. E*, 65(3):036104, feb 2002.
- [269] Alice Patania, Giovanni Petri, and Francesco Vaccarino. The shape of collaborations. *Eur. Phys. J. DS*, 6(1):18, 2017.
- [270] Debora Pedrazzoli, Katharina Kranzer, H. Lucy Thomas, and Maeve K. Lalor. Trends and risk factors for death and excess all-cause mortality among noti-

- fied tuberculosis patients in the uk: an analysis of surveillance data. *ERJ Open Research*, 5(4), 2019.
- [271] Carlos Pérez-Espigares, Matteo Marcuzzi, Ricardo Gutiérrez, and Igor Lesanovsky. Epidemic Dynamics in Open Quantum Spin Systems. *Phys. Rev. Lett.*, 119(14):140401, oct 2017.
- [272] Carlos Pérez-Espigares, Matteo Marcuzzi, Ricardo Gutiérrez, and Igor Lesanovsky. Epidemic dynamics in open quantum spin systems. *Phys. Rev. Lett.*, 119:140401, Oct 2017.
- [273] Carlos Pérez-Espigares, Matteo Marcuzzi, Ricardo Gutiérrez, and Igor Lesanovsky. Epidemic Dynamics in Open Quantum Spin Systems. *Phys. Rev. Lett.*, 119(14):140401, 2017.
- [274] Bryan Perozzi, Rami Al-Rfou, and Steven Skiena. DeepWalk. In *Proc. 20th ACM SIGKDD Int. Conf. Knowl. Discov. data Min.*, pages 701–710, New York, NY, USA, aug 2014. ACM.
- [275] Giovanni Petri, Paul Expert, Federico Turkheimer, Robin Carhart-Harris, David Nutt, Peter J Hellyer, and Francesco Vaccarino. Homological scaffolds of brain functional networks. *J. Royal Soc. Interface*, 11(101):20140873, 2014.
- [276] M. B. Plenio and P. L. Knight. The quantum-jump approach to dissipative dynamics in quantum optics. *Rev. Mod. Phys.*, 70:101–144, Jan 1998.
- [277] Keith G Provan, Amy Fish, and Joerg Sydow. Interorganizational networks at the network level: A review of the empirical literature on whole networks. *J. Manag.*, 33(3):479–516, 2007.
- [278] Liqun Qi. Eigenvalues of a real supersymmetric tensor. *J. Symb. Comput.*, 40(6):1302–1324, dec 2005.

- [279] Bo Qu and Huijuan Wang. Sis epidemic spreading with heterogeneous infection rates. *IEEE Transactions on Network Science and Engineering*, 4(3):177–186, 2017.
- [280] Arthur L. Reingold, Allen W. Hightower, Gail A. Bolan, Ellen E. Jones, Hilaire Tiendrebeogo, Claire V. Broome, Gloria W. Ajello, Catherine Adamsbaum, Catherine Phillips, and Adamou Yada. Age-Specific Differences in Duration of Clinical Protection After Vaccination With Meningococcal Polysaccharide a Vaccine. *Lancet*, 326(8447):114–118, jul 1985.
- [281] Saulo D. S. Reis, Yanqing Hu, Andrés Babino, José S. Andrade Jr, Santiago Canals, Mariano Sigman, and Hernán A. Makse. Avoiding catastrophic failure in correlated networks of networks. *Nat. Phys.*, 10(10):762–767, oct 2014.
- [282] Everett M Rogers. A prospective and retrospective look at the diffusion model. *J. Health Commun.*, 9(S1):13–19, 2004.
- [283] Everett M Rogers, Una E Medina, Mario A Rivera, and Cody J Wiley. Complex adaptive systems and the diffusion of innovations. *Innov. J. Public Sect. Innov. J.*, 10(3):1–26, 2005.
- [284] Dominic C. Rose, Katarzyna Macieszczak, Igor Lesanovsky, and Juan P. Garrahan. Metastability in an open quantum ising model. *Phys. Rev. E*, 94:052132, Nov 2016.
- [285] Amit Roy, Kashob Kumar Roy, Amin Ahsan Ali, M. Ashraful Amin, and A. K. M. Mahbubur Rahman. SST-GNN: Simplified Spatio-Temporal Traffic Forecasting Model Using Graph Neural Network. In *Lect. Notes Comput. Sci. (including Subser. Lect. Notes Artif. Intell. Lect. Notes Bioinformatics)*, volume 12714 LNAI, pages 90–102, 2021.
- [286] C. Runge. Ueber die numerische Auflösung von Differentialgleichungen. *Math. Ann.*, 46(2):167–178, 1895.

- [287] Subir Sachdev. *Quantum Phase Transitions*. Cambridge University Press, 2 edition, 2011.
- [288] M. Ali Saif. Epidemic threshold for the sirs model on the networks. *Physica A: Statistical Mechanics and its Applications*, 535:122251, 2019.
- [289] Marcel Salathé and James H. Jones. Dynamics and Control of Diseases in Networks with Community Structure. *PLoS Comput. Biol.*, 6(4):e1000736, apr 2010.
- [290] Amer M. Salman, Issam Ahmed, Mohd Hafiz Mohd, Mohammad Subhi Jamiluddin, and Mohammed Ali Dheyab. Scenario analysis of covid-19 transmission dynamics in malaysia with the possibility of reinfection and limited medical resources scenarios. *Computers in Biology and Medicine*, 133:104372, 2021.
- [291] Samuel V. Scarpino and Giovanni Petri. On the predictability of infectious disease outbreaks. *Nat. Commun.*, 10(1), 2019.
- [292] Davide Scarselli, Nazmi Burak Budanur, Marc Timme, and Björn Hof. Discontinuous epidemic transition due to limited testing. *Nat. Commun.*, 12(1), 2021.
- [293] Franco Scarselli, Marco Gori, Ah Chung Tsoi, Markus Hagenbuchner, and Gabriele Monfardini. The graph neural network model. *IEEE Trans. Neural Netw. Learn. Syst.*, 20(1):61–80, 2008.
- [294] Benjamin Schäfer, Dirk Witthaut, Marc Timme, and Vito Latora. Dynamically induced cascading failures in power grids. *Nat. Commun.*, 9(1):1975, dec 2018.
- [295] Mirko Schäfer, Jan Scholz, and Martin Greiner. Proactive Robustness Control of Heterogeneously Loaded Networks. *Phys. Rev. Lett.*, 96(10):108701, mar 2006.

- [296] Christian M. Schneider, Tamara Mihaljev, Shlomo Havlin, and Hans J. Herrmann. Suppressing epidemics with a limited amount of immunization units. *Phys. Rev. E*, 84(6):061911, dec 2011.
- [297] Paul Schultz, Jobst Heitzig, and Jürgen Kurths. A random growth model for power grids and other spatially embedded infrastructure networks. *Eur. Phys. J. Spec. Top.*, 223(12):2593–2610, oct 2014.
- [298] Nehemia Schwartz and Lewi Stone. Exact epidemic analysis for the star topology. *Phys. Rev. E*, 87(4):042815, apr 2013.
- [299] Devosmita Sen and Debasis Sen. Use of a Modified SIRD Model to Analyze COVID-19 Data. *Ind. Eng. Chem. Res.*, 60(11):4251–4260, mar 2021.
- [300] Chintan Shah, Nima Dehmamy, Nicola Perra, Matteo Chinazzi, Albert-László Barabási, Alessandro Vespignani, and Rose Yu. Finding Patient Zero: Learning Contagion Source with Graph Neural Networks. *arXiv Prepr. arXiv2006.11913*, pages 1–18, 2020.
- [301] Nathan Shammah, Shahnawaz Ahmed, Neill Lambert, Simone De Liberato, and Franco Nori. Open quantum systems with local and collective incoherent processes: Efficient numerical simulations using permutational invariance. *Phys. Rev. A*, 98:063815, Dec 2018.
- [302] Kieran J. Sharkey. Deterministic epidemic models on contact networks: Correlations and unbiological terms. *Theor. Popul. Biol.*, 79(4):115–129, jun 2011.
- [303] Eunha Shim. Delay-adjusted age-specific covid-19 case fatality rates in a high testing setting: South korea, february 2020 to february 2021. *Int. J. Environ. Res. Public Health*, 18(10), 2021.
- [304] Eunha Shim. Optimal Allocation of the Limited COVID-19 Vaccine Supply in South Korea. *J. Clin. Med.*, 10(4):591, 2021.

- [305] L M Sieberer, M Buchhold, and S Diehl. Keldysh field theory for driven open quantum systems. *Reports on Progress in Physics*, 79(9):096001, aug 2016.
- [306] L. M. Sieberer, S. D. Huber, E. Altman, and S. Diehl. Dynamical critical phenomena in driven-dissipative systems. *Phys. Rev. Lett.*, 110:195301, May 2013.
- [307] L. M. Sieberer, S. D. Huber, E. Altman, and S. Diehl. Nonequilibrium functional renormalization for driven-dissipative bose-einstein condensation. *Phys. Rev. B*, 89:134310, Apr 2014.
- [308] Piotr Sierant, Giuliano Chiriacò, Federica M. Surace, Shraddha Sharma, Xhek Turkeshi, Marcello Dalmonte, Rosario Fazio, and Guido Pagano. Dissipative floquet dynamics: from steady state to measurement induced criticality in trapped-ion chains, 2021.
- [309] Karen Simonyan and Andrew Zisserman. Very deep convolutional networks for large-scale image recognition. *3rd Int. Conf. Learn. Represent. ICLR 2015 - Conf. Track Proc.*, 2015.
- [310] Ann E Sizemore, Elisabeth A Karuza, Chad Giusti, and Danielle S Bassett. Knowledge gaps in the early growth of semantic networks. *arXiv:1709.00133*, 2017.
- [311] Je Ung Song, Kwangjong Choi, Soo Min Oh, and B. Kahng. Exploring non-linear dynamics and network structures in Kuramoto systems using machine learning approaches. *Chaos: An Interdisciplinary Journal of Nonlinear Science*, 33(7):073148, 07 2023.
- [312] Je Ung Song, Jaegon Um, Jinha Park, and B. Kahng. Effective-potential approach to hybrid synchronization transitions. *Phys. Rev. E*, 101(5):052313, may 2020.

- [313] Sirui Song, Zefang Zong, Yong Li, Xue Liu, and Yang Yu. Reinforced Epidemic Control: Saving Both Lives and Economy. *arXiv Prepr. arXiv2008.01257*, 2020.
- [314] Guillaume St-Onge, Iacopo Iacopini, Vito Latora, Alain Barrat, Giovanni Petri, Antoine Allard, and Laurent Hébert-Dufresne. Influential groups for seeding and sustaining nonlinear contagion in heterogeneous hypergraphs. *Commun. Phys.*, 5(1):25, dec 2022.
- [315] Guillaume St-Onge, Vincent Thibeault, Antoine Allard, Louis J. Dubé, and Laurent Hébert-Dufresne. Master equation analysis of mesoscopic localization in contagion dynamics on higher-order networks. *Phys. Rev. E*, 103(3):032301, mar 2021.
- [316] Guillaume St-Onge, Vincent Thibeault, Antoine Allard, Louis J. Dubé, and Laurent Hébert-Dufresne. Social Confinement and Mesoscopic Localization of Epidemics on Networks. *Phys. Rev. Lett.*, 126(9):1–6, 2021.
- [317] Carla Taramasco, Jean-Philippe Cointet, and Camille Roth. Academic team formation as evolving hypergraphs. *Scientometrics*, 85(3):721–740, 2010.
- [318] Moosa Tatar, Jalal Montazeri Shoorekchali, Mohammad Reza Faraji, and Fernando A Wilson. International COVID-19 vaccine inequality amid the pandemic: Perpetuating a global crisis? *J. Glob. Health*, 11(3):03086, jul 2021.
- [319] Uwe C Täuber. *Critical dynamics: a field theory approach to equilibrium and non-equilibrium scaling behavior*. Cambridge University Press, 2014.
- [320] Uwe C. Täuber and Sebastian Diehl. Perturbative field-theoretical renormalization group approach to driven-dissipative bose-einstein criticality. *Phys. Rev. X*, 4:021010, Apr 2014.
- [321] Michele Tizzoni, Paolo Bajardi, Chiara Poletto, José J Ramasco, Duygu Balcan, Bruno Gonçalves, Nicola Perra, Vittoria Colizza, and Alessandro Vespignani.

- Real-time numerical forecast of global epidemic spreading: case study of 2009 a/h1n1pdm. *BMC Med.*, 10(1):165, 2012.
- [322] Takafumi Tomita, Shuta Nakajima, Ippei Danshita, Yosuke Takasu, and Yoshiro Takahashi. Observation of the mott insulator to superfluid crossover of a driven-dissipative bose-hubbard system. *Science Advances*, 3(12), 2017.
- [323] Abhishek Tomy, Matteo Razzanelli, Francesco Di Lauro, Daniela Rus, and Cosimo Della Santina. Estimating the State of Epidemics Spreading with Graph Neural Networks. *arXiv Prepr. arXiv2105.05060*, 2021.
- [324] Eugenio Valdano, Luca Ferreri, Chiara Poletto, and Vittoria Colizza. Analytical Computation of the Epidemic Threshold on Temporal Networks. *Phys. Rev. X*, 5(2):021005, apr 2015.
- [325] Thomas W Valente. Network models of the diffusion of innovations. *Comput. Math. Organ. Theory*, 2(2):163–164, 1996.
- [326] Piet Van Mieghem, Dragan Stevanović, Fernando Kuipers, Cong Li, Ruud van de Bovenkamp, Daijie Liu, and Huijuan Wang. Decreasing the spectral radius of a graph by link removals. *Phys. Rev. E*, 84(1):016101, jul 2011.
- [327] Alexei Vazquez. Population stratification using a statistical model on hypergraphs. *Phys. Rev. E*, 77(6):066106, 2008.
- [328] Andreas Veit, Michael J Wilber, and Serge Belongie. Residual networks behave like ensembles of relatively shallow networks. *Advances in neural information processing systems*, 29, 2016.
- [329] Fátima Velásquez-Rojas, Paulo Cesar Ventura, Colm Connaughton, Yamir Moreno, Francisco A. Rodrigues, and Federico Vazquez. Disease and information spreading at different speeds in multiplex networks. *Phys. Rev. E*, 102(2):022312, aug 2020.

- [330] Petar Veličković, Guillem Cucurull, Arantxa Casanova, Adriana Romero, Pietro Liò, and Yoshua Bengio. Graph Attention Networks. *6th Int. Conf. Learn. Represent. ICLR 2018 - Conf. Track Proc.*, pages 1–12, oct 2017.
- [331] F. Verstraete, J. J. García-Ripoll, and J. I. Cirac. Matrix product density operators: Simulation of finite-temperature and dissipative systems. *Phys. Rev. Lett.*, 93:207204, Nov 2004.
- [332] Frank Verstraete and J Ignacio Cirac. Renormalization algorithms for quantum-many body systems in two and higher dimensions. *arXiv preprint cond-mat/0407066*, 2004.
- [333] Frank Verstraete, Michael M. Wolf, and J. Ignacio Cirac. Quantum computation and quantum-state engineering driven by dissipation. *Nat. Phys.*, 5(9):633–636, 2009.
- [334] Guifré Vidal. Efficient classical simulation of slightly entangled quantum computations. *Phys. Rev. Lett.*, 91:147902, Oct 2003.
- [335] Erik Volz and Lauren Ancel Meyers. Epidemic thresholds in dynamic contact networks. *J. Royal Soc. Interface*, 6(32):233–241, 2008.
- [336] B. Wang and B. J. Kim. A high-robustness and low-cost model for cascading failures. *Europhys. Lett.*, 78(4):48001, may 2007.
- [337] Dong Wang, Yi Zhao, Jianfeng Luo, and Hui Leng. Simplicial SIRS epidemic models with nonlinear incidence rates. *Chaos An Interdiscip. J. Nonlinear Sci.*, 31(5):053112, may 2021.
- [338] Panpan Wang and Jianwen Jia. Stationary distribution of a stochastic SIRD epidemic model of Ebola with double saturated incidence rates and vaccination. *Adv. Differ. Equations*, 2019(1):433, dec 2019.

- [339] Zhen Wang, Chris T. Bauch, Samit Bhattacharyya, Alberto D’Onofrio, Piero Manfredi, Matjaž Perc, Nicola Perra, Marcel Salathé, and Dawei Zhao. Statistical physics of vaccination. *Phys. Rep.*, 664:1–113, dec 2016.
- [340] Zhen Wang, Yamir Moreno, Stefano Boccaletti, and Matjaž Perc. Vaccination and epidemics in networked populations—An introduction. *Chaos, Solitons & Fractals*, 103:177–183, oct 2017.
- [341] Duncan J Watts. A simple model of global cascades on random networks. *Proc. Natl. Acad. Sci.*, 99(9):5766–5771, 2002.
- [342] Duncan J Watts and Peter Sheridan Dodds. Influentials, networks, and public opinion formation. *J. Consumer Res.*, 34(4):441–458, 2007.
- [343] Duncan J. Watts, Roby Muhamad, Daniel C. Medina, and Peter S. Dodds. Multiscale, resurgent epidemics in a hierarchical metapopulation model. *Proc. Natl. Acad. Sci. U.S.A.*, 102(32):11157–11162, 2005.
- [344] A. H. Werner, D. Jaschke, P. Silvi, M. Kliesch, T. Calarco, J. Eisert, and S. Montangero. Positive tensor network approach for simulating open quantum many-body systems. *Phys. Rev. Lett.*, 116:237201, Jun 2016.
- [345] Jian-jun Wu, Zi-you Gao, and Hui-jun Sun. Cascade and breakdown in scale-free networks with community structure. *Phys. Rev. E*, 74(6):066111, dec 2006.
- [346] Zonghan Wu, Shirui Pan, Fengwen Chen, Guodong Long, Chengqi Zhang, and S Yu Philip. A comprehensive survey on graph neural networks. *IEEE Trans. Neural Netw. Learn. Syst.*, 32(1):4–24, 2020.
- [347] Zheng Xie, Zhenzheng Ouyang, and Jianping Li. A geometric graph model for coauthorship networks. *Journal of Informetrics*, 10(1):299–311, 2016.

- [348] Keyulu Xu, Weihua Hu, Jure Leskovec, and Stefanie Jegelka. How powerful are graph neural networks? In *7th Int. Conf. Learn. Represent. ICLR 2010 - Conf. Track Proc.*, 2019.
- [349] Yunjie Calvin Xu, Cheng Zhang, Ling Xue, and Lay Lan Yeo. Product adoption in online social network. *ICIS Proc.*, page 200, 2008.
- [350] Shu Yan, Shaoting Tang, Wenyi Fang, Sen Pei, and Zhiming Zheng. Global and local targeted immunization in networks with community structure. *J. Stat. Mech.*, 2015(8), 2015.
- [351] Jae-Suk Yang, Wooseop Kwak, Kwang-II Goh, and In-mook Kim. Critical behavior of the xy model on static scale-free networks. *EPL*, 84(3):36004, 2008.
- [352] Jaewon Yang and Jure Leskovec. Defining and evaluating network communities based on ground-truth. *Knowl. Inf. Syst.*, 42(1):181–213, jan 2015.
- [353] Yang Wang, Deepayan Chakrabarti, Chenxi Wang, and Christos Faloutsos. Epidemic spreading in real networks: an eigenvalue viewpoint. In *22nd Int. Symp. Reliab. Distrib. Syst. 2003. Proceedings.*, pages 25–34. IEEE Comput. Soc, 2003.
- [354] H Yi. Quantum fluctuations in a scale-free network-connected ising system. *Eur. Phys. J. B*, 61(1):89–93, 2008.
- [355] Mingli Yuan, Wen Yin, Zhaowu Tao, Weijun Tan, and Yi Hu. Association of radiologic findings with mortality of patients infected with 2019 novel coronavirus in Wuhan, China. *PLoS One*, 15(3):1–10, 2020.
- [356] Yingfang Yuan, Wenjun Wang, and Wei Pang. A systematic comparison study on hyperparameter optimisation of graph neural networks for molecular property prediction. In *Proc. Genet. Evol. Comput. Conf.*, volume 1, pages 386–394, New York, NY, USA, jun 2021. ACM.

- [357] Zi-Ke Zhang and Chuang Liu. A hypergraph model of social tagging networks. *J. Stat. Mech.: Theory Exp.*, 2010(10):P10005, 2010.
- [358] Liang Zhao, Kwangho Park, and Ying-Cheng Lai. Attack vulnerability of scale-free networks due to cascading breakdown. *Phys. Rev. E*, 70(3):035101, sep 2004.
- [359] Liang Zhao, Kwangho Park, Ying-Cheng Lai, and Nong Ye. Tolerance of scale-free networks against attack-induced cascades. *Phys. Rev. E*, 72(2):025104, aug 2005.
- [360] Martín G. Zimmermann, Víctor M. Eguíluz, and Maxi San Miguel. Coevolution of dynamical states and interactions in dynamic networks. *Phys. Rev. E*, 69:065102(R), Jun 2004.
- [361] Vinko Zlatić, Gourab Ghoshal, and Guido Caldarelli. Hypergraph topological quantities for tagged social networks. *Phys. Rev. E*, 80(3):036118, 2009.
- [362] L. J. Zou, D. Marcos, S. Diehl, S. Putz, J. Schmiedmayer, J. Majer, and P. Rabl. Implementation of the dicke lattice model in hybrid quantum system arrays. *Phys. Rev. Lett.*, 113:023603, Jul 2014.

초 록

지난 20년간 복잡계 네트워크의 창발현상에 대해 많은 연구가 이루어져왔다. 이런 현상의 예측과 제어는 복잡계 과학에서 중요한 주제이다. 복잡계 네트워크의 그래프 표현은 이런 주제를 효과적으로 다룬다. 복잡계 중에서는 두개 이상의 개체들이 동시에 상호작용하는 경우가 있다. 예를 들어 두명 이상의 연구자가 동시에 협업을 할 수 있다. 네트워크의 엣지를 통한 전파는 단순한 전파라 불린다. 단순한 전파과정으로 나타낼 수 없는 많은 현상들이 있다. 그 예로는 하이퍼그래프 전파과정, 양자 전파과정, 그리고 사회기반시설에서의 연쇄파멸현상이 있다.

구체적으로 이 학위논문에서는 복잡한 전파과정의 예측과 제어를 다룬다. 하이퍼그래프에서의 전염병 전파 모델인 simplicial SIS 모델의 상전이와 제어 전략을 다룬다. 또한 불균일한 치명률을 가진 인구분포에서 최적 백신 전략의 상전이에 대해서도 다룬다. 추가로 degree 분포가 균일한 네트워크와 불균일한 네트워크에서의 양자 상전이에 대해서도 연구한다. 마지막으로 기계학습을 적용하여 전염병 전파와 연쇄파멸현상을 예측하고 제어한 연구에 대해 소개한다.

주요어: 전염병 확산과정, 복잡한 전염, 하이퍼그래프, 비평형 상전이, 백신 전략, 연쇄파멸, 그래프 신경망, 열린 양자계, 하이브리드 상전이

학번: 2020-34297